Spins in Josephson Junctions

Bouman, D.

DOI
10.4233/uuid:ff2ffac0-c76a-4a3d-af22-88f2151f6133

Publication date
2021

Document Version
Final published version

Citation (APA)
Bouman, D. (2021). *Spins in Josephson Junctions*. [Dissertation (TU Delft), Delft University of Technology].
https://doi.org/10.4233/uuid:ff2ffac0-c76a-4a3d-af22-88f2151f6133

SPINS IN JOSEPHSON JUNCTIONS

SPINS IN JOSEPHSON JUNCTIONS

Proefschrift

ter verkrijging van de graad van doctor
aan de Technische Universiteit Delft,
op gezag van de Rector Magnificus Prof. dr. ir. T. H. J. J. van der Hagen,
voorzitter van het College voor Promoties,
in het openbaar te verdedigen op vrijdag 15 januari 2021 om 10:00 uur

door

Daniël BOUMAN

Natuurkundig ingenieur, Technische Universiteit Delft, Nederland
geboren te Amstelveen, Nederland.

Dit proefschrift is goedgekeurd door de promotoren.

Samenstelling promotiecommissie:

Rector Magnificus,	voorzitter
Prof. dr. ir. L. P. Kouwenhoven	Technische Universiteit Delft, promotor
Dr. A. Geresdi	Technische Universiteit Delft, copromotor
Onafhankelijke leden:	
Prof. dr. J. Klinovaja	University of Basel, Switzerland
Prof. dr. ir. L. M. K. Vandersypen	Technische Universiteit Delft
Prof. dr. Y. V. Nazarov	Technische Universiteit Delft
Dr. ir. M. Veldhorst	Technische Universiteit Delft
Dr. S. De Franceschi	CEA Grenoble, France

Printed by: Gildeprint, Enschede

Cover: Artistic version of a transport measurement of Triplet-blockaded Josephson supercurrent through a double quantum, by Ilse Modder.

Casimir PhD Series, Delft-Leiden 2020-32

ISBN 978-90-8593-458-5

CONTENTS

Summary

Quantum technology is an exciting research area that has gained a lot of interest in the past few decades with the advances made in quantum computing. The quantum computer promises speedups that are impossible to achieve with classical computers. It does so by exploiting quantum mechanical properties such as entanglement and superposition with the quantum bit, or qubit, as its main building block.

Today, quantum computers are in their infancy and realizing a computer powerful enough to perform useful calculations poses major challenges. The fragility of qubits being the main difficulty. Approaches to mitigate this include implementing error correction schemes or alternative qubit designs. Topological qubits are part of the latter category and exploit the robustness of topologically invariant states to small perturbations to create more stable qubits.

In this thesis we explore semiconductor-superconductor hybrid nanowire structures and in particular the interaction of electron spins in quantum dots with superconductivity. When connected to superconductors, arrays of superconductor quantum dot hybrids can host Majorana states, a promising approach to realizing topological qubits. Creating Majoranas in quantum dots, as opposed to traditional methods, offers greater control over their properties. Additionally, understanding the interaction between spins in these quantum dots superconductor hybrids could enable new readout methods or coupling mechanisms between superconducting and spin qubits.

We start by investigating a nanowire SNS Josephson junction with signatures of Majorana states. A nanowire junction is capacitively coupled to an on-chip microwave detector made from a Josephson tunnel junction. We monitor the Josephson radiation frequency as a function of magnetic field and find a transition from a 2π to a 4π-periodic Josephson current-phase relation, consistent with a topological transition.

In a different device, we investigate a multi-orbital double quantum dot Josephson junction. We measure the excitations between doublet and singlet states that arise in a quantum dot weakly coupled to a superconducting lead, also known as Yu-Shiba-Rusinov (YSR) states. With increased dot-lead coupling we observe a supercurrent and reveal its current-phase relation, both in the single and multi-orbit regime. We show that in the single-orbital regime the supercurrent sign follows an even-odd charge occupation effects. In the even charge parity sector, we observe a supercurrent blockade when the spin ground state transitions to a triplet – demonstrating a direct spin to supercurrent conversion. For yet stronger dot-lead coupling we find a rectified current-phase relation at the transition between even and odd charge states. We investigate this apparent non-equilibrium effect and think about possible explanations.

To conclude, we discuss possible applications in spin qubit state readout and extensions of the device geometry towards realizing a Kiteav chain able to host Majorana states.

SAMENVATTING

Kwantum technologie is een spannend onderzoeksgebied dat door de vooruitgang op het gebied van kwantumcomputers de afgelopen decennia veel belangstelling heeft gekregen. De kwantumcomputer belooft versnellingen die onmogelijk zijn met de klassieke computer. Dit kan door gebruik te maken van kwantum mechanische eigenschappen zoals verstrengeling en superpositie met de kwantum bit, of qubit, als bouwsteen.

Vandaag de dag staat de kwantumcomputer nog in de kinderschoenen en het maken van een computer die krachtig genoeg is om bruikbaar te zijn, stelt een aantal grote uitdaging. Qubits zijn namelijk erg vatbaar voor verstoringen. Oplossingen kunnen gevonden worden in foutcorrectieschema's of alternatieve qubit ontwerpen. Topologische qubits vallen onder de laatste categorie, ze benutten de robuustheid van topologische toestanden tegen kleine verstoringen.

In dit proefschrift onderzoeken we de interactie van elektronen spins in kwantum dots met supergeleiding in halfgeleider-supergeleider hybride nanodraadstructuren. Wanneer ze zijn verbonden met supergeleiders, kan een serie geschakelde rij kwantum dots met supergeleiding Majorana toestanden vormen, een veelbelovende kandidaat voor topologische qubits. Het maken van Majorana's in kwantum dots biedt meer controle over hun eigenschappen dan traditionele methoden. Bovendien kan het begrijpen van de interactie tussen spins in kwantum dots en supergeleiders nieuwe uitleesmethoden of koppel mechanismen met supergeleidende qubits mogelijk maken.

We beginnen met een nanodraad Josephson junctie met kenmerken van Majorana's. De nanodraad is op de chip via een condensator gekoppeld aan een microgolfdetector gemaakt van een Josephson tunnel junctie. We meten de Josephson stralingsfrequentie in een magnetisch veld en vinden een overgang van een 2π naar een 4π periode in de Josephson stroom-faserelatie, wat kan duiden op een topologische transitie.

In een ander apparaat onderzoeken we een multi-orbitale dubbele kwantum dots in een Josephson junctie. We meten de excitaties tussen doublet- en singlet toestanden die ontstaan in een kwantum dot met een zwakke koppeling naar het supergeleidende contact, ook wel bekend als Yu-Shiba-Rusinov (YSR) toestanden. Met verhoogde contact koppeling observeren we een superstroom en meten we de stroom-faserelatie, zowel met een enkele als met meerdere orbitalen. We laten zien dat bij een enkel orbitaal de richting van de superstroom een even-oneven ladingseffect heeft. Met een even aantal ladingen zien we een superstroom blokkade bij de overgang naar een triplet grondtoestand – dit maakt een directe conversie van spin naar superstroom mogelijk. Bij een nog sterkere koppeling met de contacten vinden we een gelijkgerichte stroom-faserelatie bij de overgang tussen even en oneven ladingstoestanden. We onderzoeken dit opvallende effect en bespreken mogelijke verklaringen.

Tot slot stellen we een nieuwe methode voor om spin qubit toestanden uit te lezen en kijken we vooruit naar een uitbreiding van ons experiment waarmee Majorana toestanden gerealiseerd kunnen worden met behulp van een zogenaamde Kiteav chain.

1

INTRODUCTION

Een boek zegt meer dan duizend woorden.

Herman Finkers

1.1. Quantum mechanics

Quantum mechanics describes the behavior of microscopic particles – molecules, atoms and subatomic particles. The field started in the year 1900 with Max Planck's solution for black-body radiation and Einstein's photo-electric effect and was advanced by, now famous, physicists like Schrodinger, Heisenberg, Born.

The name comes from the fact that several quantities, such as electric charge and energy, only have discrete values – they are quantized. Additionally, quantum mechanics introduces the concept of wave-particle duality, where all particles can be described both as a wave and as a particle. This is distinctly different from classical mechanics where quantities are treated as continuous and particles as hard point-like objects.

Perhaps the most convincing illustration of this counter-intuitive property is from an experiment performed by Italian researchers in 1976. They performed a double-slit experiment with electrons [1]. When classical particles are send through a double slit with a screen behind it, the particles will strike the screen at two spots– directly behind the slits (blue curves in Figure 1.1a). When a wave propagates through the slits, an interference pattern forms on the screen (orange curve in Figure 1.1a). Figure 1.1b shows the results from the Italian researchers, where they send electrons, one-by-one through the slits. In the upper panels it can clearly be seen that the electrons hit the screen as if they are particles. But in the lower panels an interference pattern emerges, meaning that the electrons propagate as waves. From this observation it makes sense to describe electrons as waves. And indeed, a quantum system is described by a wave function where its value is a probability amplitude of where you will find the electron when measuring it.

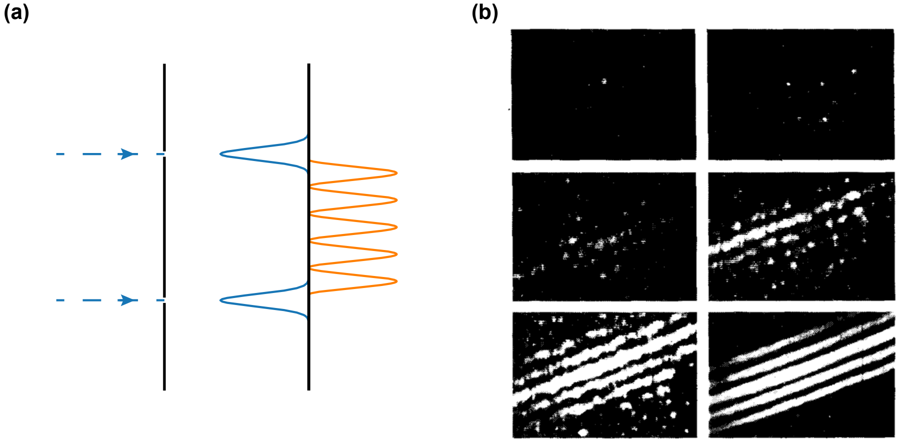

Figure 1.1: **Demonstration of wave-particle duality.** **(a)** A double-slit experiment. The curves show the patterns expected for a classical particle (blue) and a wave (orange) on the screen. **(b)** Experimental results of a double-slit experiment performed with electrons. The panels show consecutive recordings, progressing from the top left to the bottom right. Figure adapted from [1].

A great manifestation of quantum mechanics is a superconductor, a material where electrons flow without resistance. The lowest energy state of a superconductor, known as the ground state, is described by a single wave function. It is therefore an excellent system to explore quantum mechanical effects. In the field of condensed matter physics, quantum mechanical effects in superconductors such as quantum interference, superposition and entanglement are well-researched topics. In this thesis we study the quantum mechanical interactions between superconductors and single electrons in the context of quantum computing.

1.2. QUANTUM COMPUTING

Quantum mechanics lies at the heart of many modern technologies and has enabled the realization of now ubiquitous devices such as lasers, LEDs, photodetector and transistors. Transistors in particular have had a big impact on society as they form the building blocks of today's computers. The new possibilities classical computers have unlocked dramatically changed the daily life of most people over the last 70 years. Although quantum mechanics plays an important role in making today's transistors – the logic gates, the underlying mechanism of any software program, behave entirely classical. Since the 1980's people have thought about using quantum mechanical properties for computation, quantum logic gates [2].

First proposed by Paul Benioff, Richard Feynman and Yuri Manin to simulate quantum mechanical systems, the field of quantum computing really gained traction in the 1990's when it was shown that quantum computation could drastically speed up certain calculations. Most famously, Shor's algorithm for prime factorization which breaks the RSA public-key encryption [3].

In general quantum computation exploits the properties superposition and entanglement of the quantum wave functions to perform computations much faster then classical computers. At the heart of this is the quantum bit, or qubit. Unlike its classical counterpart, the bit, the qubit can be in a superposition of 0 and 1, with some probability of being in 0 and some probability of being in 1. Additionally it can be entangled with other qubits, which makes the number of possible states 2^N, instead of N^2 for N (qu)bits. The trick of a quantum algorithm is to choreograph the wavefunction of all the qubits in such a way that the probability amplitude of the correct state is much larger then for the incorrect states.

There are several qubits realizations. Currently, the two leading solid-state platforms are spin qubits in semiconductor quantum dots [4] and superconducting circuits [5]. At this point existing quantum computers are not able to perform computations faster than classical computers. A major challenge that prevents this is decoherence of the qubits. The quantum information from the delicate quantum states is lost when it interacts with its environment. Unfortunately, we cannot completely isolate the qubits because for the choreography of the quantum states, the qubits need to be manipulated. Making a useful quantum computer requires a careful balance between these opposing needs.

Currently the main approach to deal with this issue is to employ some form of error correction. For low enough rates, quantum error correction can enable reliable algorithms [6]. A different approach is to make quantum states less sensitive to decoherence to environmental interaction. One way to do that is by encoding the quantum information in topological states. This makes changing the state by accident, less likely. A simple example of topological robustness can be given with geometrical objects. Two shapes share the same topological state when they can be smoothly transformed into one another, without creating or erasing holes (Figure 1.2).

Figure 1.2: **Topology.** The doughnut and mug share the same topological state, while the pretzel is in a different state due to its two extra holes.

The same principles apply for topological states in condensed matter systems, a famous example is the quantum Hall effect [7]. More relevant for quantum computation are so-called Majorana states, the condensed matter version of the Majorana fermion predicted by Ettore Majorana [8]. Condensed matter Majorana states appear as non-local zero-energy quasiparticle state at the ends of a specific one-dimensional system [9]. This is a topological state and quantum information encoded in it, is protected by topology. There are several proposals to realize these states and to make qubits out of them [10–12]. One, so far unrealized, proposal for creating Majorana states is by simulating a Kitaev chain in array of quantum dots [13, 14]. This approach has the advantage of direct control over many of the parameters that influence the Majorana states.

2

THEORY

Tea. Earl Grey. Hot.

Jean-Luc Picard

This chapter gives a theoretical overview of the most relevant topics for the experimental chapters in this thesis. We start with an introduction to BCS superconductivity and Andreev reflections, and continue with a more detailed treatment of Josephson junctions. Next, we introduce quantum dots followed by quantum dots in close proximity to superconductors. We conclude this chapter with a toy model for Majorana states and two approaches for physical realization in condensed matter systems.

2.1. BCS SUPERCONDUCTIVITY

Superconductivity is a striking phenomenon where a metal loses all its resistance. This effect was discovered by Heike Kamerlingh Onnes when observing the resistance of mercury drop to 0 Ω at liquid helium temperatures [15]. He later received a Nobel prize for his discovery. It was later found that superconductors also expel magnetic fields, making it a perfect diamagnet [16], but only up to a certain critical magnetic field, above which superconductivity is quenched [17].

The first successful effort in giving a general description of superconductivity was provided by Ginzberg and landau [18], now known as the Ginzburg-Landau (GL) theory [19]. It does a good job in describing the macroscopic behavior of superconductors, but fails to describe a microscopic origin. Seven years later Bardeen, Cooper and Schrieffer created a theory describing a microscopic origin of superconductivity, now known as the BCS theory [20]. The trio introduced the concept of a Cooper pair, where two electrons feel an effective attraction mediated by the collective motion of phonons in the material. The electrons come in pairs with opposite momentum and spin and its size is characterized by the BCS coherence length ξ_0. The Cooper pairs are effectively bosons and condense into a condensate. This allows us to describe a superconductor with a single wave function $\Delta e^{i\phi}$, where Δ is the superconducting pairing energy and ϕ the phase of the superconducting condensate. In this section we briefly discuss the BCS theory using the Bogoluibov-de-Gennes (BdG) formalism, mostly by following the treatment from [19].

We start by writing down the so-call pairing Hamiltonian [19]:

$$H = \sum_{k,\sigma} \epsilon_k n_{k,\sigma} + \sum_{k,\mathbf{l}} V_{k,l} c^\dagger_{k,\uparrow} c^\dagger_{-k,\downarrow} c_{l,\uparrow} c_{-l,\downarrow}, \tag{2.1}$$

where the first term describes the single-particle kinetic energy with respect to the Fermi energy $\epsilon_k = \hbar^2 k^2/(2m^*) - E_\mathrm{F}$, with Fermi energy E_F and $V_{k,l}$ the pairwise interaction matrix element. The Hamiltonian is written in the language of second quantization, where $c^\dagger_{k,\sigma}$ and $c_{k,\sigma}$ are creation and annihilation operators and $n_{k,\sigma} = c^\dagger_{k,\sigma} c_{k,\sigma}$ the number operator which gives the number of fermions with momentum $\hbar k$ and spin σ.

We simplify this Hamiltonian by using the mean-field approximation, which assumes that fluctuations of $c_{-k,\downarrow} c_{k,\uparrow}$ are small and around their mean value and can therefore be neglected. This makes it convenient to write the product of the operators as the sum of the mean value b_k and the fluctuation:

$$c_{-k,\downarrow} c_{k,\uparrow} = b_k + \left(c_{-k,\downarrow} c_{k,\uparrow} - b_k\right), \tag{2.2}$$

where $b_k \equiv \langle c_{-k,\downarrow} c_{k,\uparrow} \rangle$. We substitute this into Equation 2.1 and ignore the higher order fluctuations terms due to the earlier mentioned assumption of their negligible contribution. We then retrieve the mean-field approximated Hamiltonian, also known as the BCS Hamiltonian:

$$H_\mathrm{BCS} = \sum_{k,\sigma} \epsilon_k n_{k,\sigma} + \sum_{k,l} \left(\Delta_k c^\dagger_{k,\uparrow} c^\dagger_{-k,\downarrow} + \Delta^*_k c_{-l,\downarrow} c_{l,\uparrow} \right), \tag{2.3}$$

with the pairing energy $\Delta_k = -\sum_l V_{k,l} b_l$, for simplicity we have omitted an irrelevant constant. Note that due to the mean-field approximation, particle number is no longer conserved. Parity however, is a conserved quantity.

To find the excitation spectrum, we rewrite the BCS Hamiltonian as

$$H_{\mathrm{BCS}} = \sum_k \Psi_k^\dagger H_{\mathrm{BdG}} \Psi_k, \tag{2.4}$$

where H_{BdG} is known as the Bogoliubov-deGennes Hamiltonian (BdG) and Ψ_k the spinor field operator, defined as

$$H_{\mathrm{BdG}} = \begin{pmatrix} \epsilon_k & \Delta \\ \Delta^* & -\epsilon_k^* \end{pmatrix}, \quad \Psi_k = \begin{pmatrix} c_{k\uparrow} \\ c_{-k\downarrow}^\dagger \end{pmatrix}. \tag{2.5}$$

We look for excitations in the form of quasiparticles, superpositions of a spin-up electrons and spin-down holes. We can describe these quasiparticles with the BdG equation [21]:

$$H_{\mathrm{BdG}} \begin{pmatrix} u_k \\ v_k \end{pmatrix} = E_k \begin{pmatrix} u_k \\ v_k \end{pmatrix}, \tag{2.6}$$

where the u_k and v_k are spin-up electron and spin-down hole probability amplitudes respectively. For plane wave solutions the eigenenergy is given as $E_k = \sqrt{\epsilon_k^2 + \Delta_k^2}$. Note that u_k and v_k are complex number with the normalization constraint $|u_k|^2 + |v_k|^2 = 1$. Given this constraint, we find that

$$u_k^2 = \frac{1}{2}\left(1 + \frac{\epsilon}{\epsilon_k^2 + \Delta_k^2}\right), \qquad v_k^2 = \frac{1}{2}\left(1 - \frac{\epsilon}{\epsilon_k^2 + \Delta_k^2}\right), \qquad \psi_{\mathrm{S}} = \begin{pmatrix} u_k \\ v_k \end{pmatrix} e^{ikr}. \tag{2.7}$$

with ψ_{S} the quasiparticle vector. We can now define new operators for these Bogoliubov quasiparticles:

$$\begin{aligned} \gamma_{k,\uparrow} &= u_k c_{k\uparrow} - v_k a_{-k\downarrow}^\dagger \\ \gamma_{k,\downarrow}^\dagger &= v_k c_{k\uparrow} + u_k a_{-k\downarrow}^\dagger. \end{aligned} \tag{2.8}$$

Now that we have determined the quasiparticle excitations, we can calculate the density of states. There is a direct correspondence between γ and c, which means we can write the density of states of the superconductor with

$$N_{\mathrm{S}}(E)\mathrm{d}E = N_{\mathrm{N}}(\epsilon)\mathrm{d}\epsilon. \tag{2.9}$$

We restrict ourselves to energies in the meV range and so we can take $N(\epsilon)$ to be constant and so

$$\frac{N_{\mathrm{S}}(E)}{N_{\mathrm{N}}(\epsilon)} = \begin{cases} \frac{E}{\sqrt{E^2+\Delta^2}}, & E > \Delta \\ 0, & E < \Delta. \end{cases} \tag{2.10}$$

2.2. ANDREEV REFLECTION

When a normal conductor is attached to a superconductor, it is not immediately apparent what happens with electrons that are incident on the normal-super interface. For energies $E > \Delta$ it is relatively easy to see that an incident electron is transmitted as a Bogoluibov quasiparticle with energy E. For energies $E < \Delta$ one might expect that the electron is always reflected due to a lack of quasiparticle states below the gap. It turns out however that the electron can also be reflected as a hole in a process known as Andreev reflection [22]. Due to the hole's positive charge, effectively two electron are transferred to the superconductor, which implies that a Cooper pair is added to the superconductor in the process (see Figure 2.1).

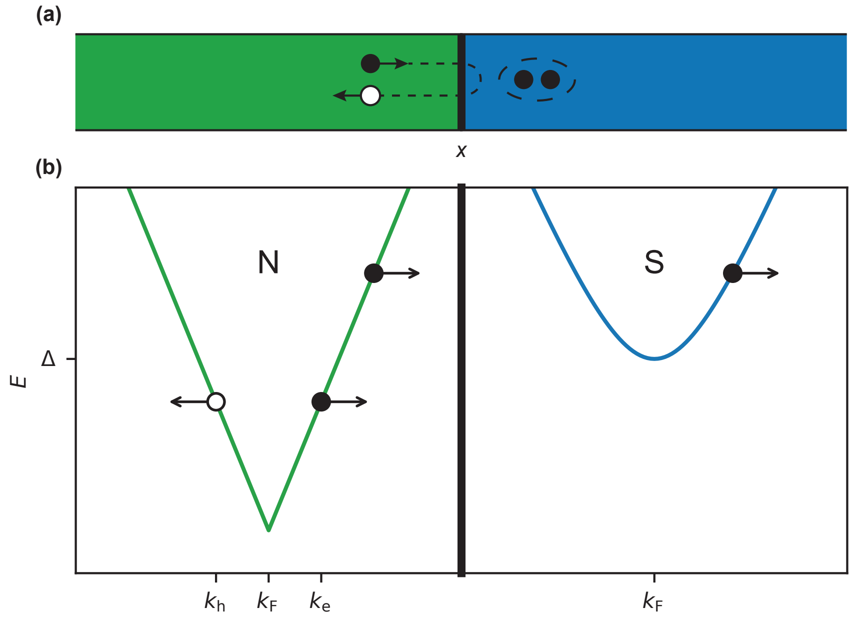

Figure 2.1: **Normal and superconducting interface.** **(a)** Schematic representation of Andreev reflection. A electron from the normal metal incident on the interface is retro reflected as a hole. A charge of $2e$ is transferred to the superconductor in the form of a Cooper pair. **(b)** Bandstructure representation. The left side shows a linear normal dispersion $E(k) = \hbar v_\mathrm{F} k - E_\mathrm{F}$, with two incident electrons for $E > \Delta$ and $E < \Delta$. The high-energy electron is transmitted as Bogoliubov quasiparticle in the superconductor, while the low-energy electron is Andreev reflected as hole as with opposite momentum.

Using the BdG formalism we can calculate what happens at the interface, using the approach introduced by Blonder, Tinkham and Klapwijk (BTK) [23]. To account for any scattering at the interface, the BTK model includes a potential barrier $V_0\delta(x)$, with amplitude V_0 and its strength described by the dimensionless parameter $Z = V_0/(\hbar v_\mathrm{F})$, with v_F the Fermi velocity. The wavefunction for the incident electron in the normal metal can be written as

$$\psi_\mathrm{N} = \begin{pmatrix}1\\0\end{pmatrix} e^{ik_\mathrm{N}^e x} + r_\mathrm{A}\begin{pmatrix}0\\1\end{pmatrix} e^{ik_\mathrm{N}^h x} + r_\mathrm{N}\begin{pmatrix}1\\0\end{pmatrix} e^{-ik_\mathrm{N}^e x}, \tag{2.11}$$

where r_N is the amplitude for normal reflection of the incident electron and r_A, the superscript of the wave vectors denotes if it is for an electron or hole. In the superconductor excitations are Bogoluibov quasiparticles, excitations of electron-holes pairs

$$\psi_\mathrm{S} = t_\mathrm{e}\begin{pmatrix}u\\v\end{pmatrix} e^{-ik_\mathrm{S}^e x} + t_\mathrm{h}\begin{pmatrix}u\\v\end{pmatrix} e^{ik_\mathrm{S}^h x}, \tag{2.12}$$

with t_e and t_h are the electron and hole-like amplitudes, respectively. We can obtain expressions for the probabilities by matching Equations 2.11 and 2.12 at the interface. Since $k_{\mathrm{S}}^{e,h} = \left(k_{\mathrm{F}} \pm 2m^*/\hbar\sqrt{E^2-\Delta^2}\right)^{1/2}$, there are no solutions for in the superconductor for $E < \Delta$ apart from an evanescent solution decreasing in amplitude away from the interface [24, 25]. For $E > \Delta$ there is a solution and electrons can be transmitted as Bogoliubov quasiparticles into the superconductor. Here, we will focus only on the solutions for the normal metal:

$$|r_A|^2 = \begin{cases} \frac{\Delta^2}{E^2+(\Delta^2-E^2)(1+2Z)^2} \\ \frac{u^2v^2}{\gamma^2} \end{cases}, \qquad |r_N|^2 = \begin{cases} 1-|r_A|^2 & \text{for } E<\Delta \\ \frac{(u^2-v^2)^2 Z^2(1+Z^2)}{\gamma^2} & \text{for } E>\Delta \end{cases}, \tag{2.13}$$

with $\gamma = (u^2 + Z^2(u^2 - v^2))^2$. Note that for energies below the gap, in the absence of a barrier $Z = 0$ we get full Andreev reflection and no normal reflection. With these results, the current through the interface can be calculated with

$$I(V) = \frac{2e}{h}\int \mathrm{d}E\left(f(E-eV)-f(E)\right)\left(1+|r_{\mathrm{A}}|^2-|r_{\mathrm{N}}|^2\right), \tag{2.14}$$

where f is the Fermi distribution and V the voltage over the interface. For small voltages $eV \ll \Delta$ a simple solution can be found for the Andreev conductance $G = \mathrm{d}I/\mathrm{d}V$ [24]:

$$G_{\mathrm{A}} = 2G_{\mathrm{Q}}\frac{T^2}{(2-T)^2}, \tag{2.15}$$

with $G_{\mathrm{Q}} = 2e^2/h$ the conductance quantum and the transmission probability $T = 1/(1+Z^2)$. Note the factor of two, coming from the fact that a $1e$ charge in the normal conductor becomes a Cooper pair with a charge $2e$ in the superconductor. In the other limit $eV \gg \Delta$, the the conductance $G = G_{\mathrm{Q}}T$.

2.3. JOSEPHSON JUNCTIONS

When superconductors are placed on both sides of the normal metal, a structure known as a Josephson junction is formed (Figure 2.2a), named after Brian Josephson who first predicted the effect of a dissipationless dc current at zero voltage, a supercurrent, in such a structure [26].

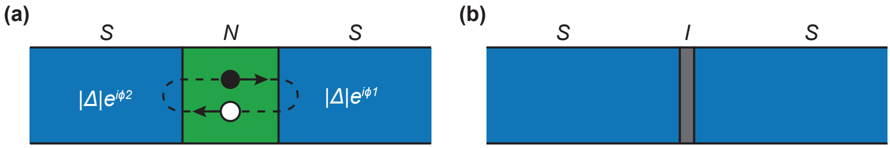

Figure 2.2: **Josephson junctions.** **(a)** Junction consisting of a superconducting-normal-superconducting (SNS) interface. The supercurrent is carried by Andreev Bound states. **(b)** Tunnel junction, where the weak link is replaced an insulating barrier, making an superconducting-insulator-superconducting (SIS) junction. Cooper pairs tunnel through the barrier.

In general, a Josephson junction is a device with two or more superconducting leads, separated by a weak link. This weak link can indeed be a normal metal as in the SNS junction shown in Figure 2.2a, but it can also be a constriction or, a thin insulation barrier (Figure 2.2b). We refer to the latter option as a Josephson tunnel junction. In fact, this type of junction was used in the first experimental observation of the Josephson effect – reported just one year after its prediction [27]. Here, we derive the Josephson effect for an SNS junction from the Andreev reflections.

Andreev reflection can occur at both the SN and the NS interfaces of the junction in Figure 2.2a. An electron incident on the right NS interface retro reflects as a hole, the hole travels in the opposite direction and reflects of the left SN interface back to an electron, which travels to the right and so on and so forth. Constructive interference of these reflections gives rise to a fermionic mode called an Andreev bound state (ABS). The energy of this state E_A can be found by matching the electron and hole wavefunctions at the interfaces and solving the boundary-value problem. If the length of the weak link d is sufficiently short $d \ll \xi$ and we assume ballistic propagation $\xi = \hbar v_\mathrm{F}/\Delta$, the energy of a single-channel Andreev state is given by [28]

$$E_\mathrm{A} = \pm\Delta\sqrt{1 - T\sin^2\frac{\varphi}{2}}, \tag{2.16}$$

where $\varphi = \phi_2 - \phi_1$ is the phase difference between the superconducting condensates. Figure 2.3a shows the ABS spectra for different T.

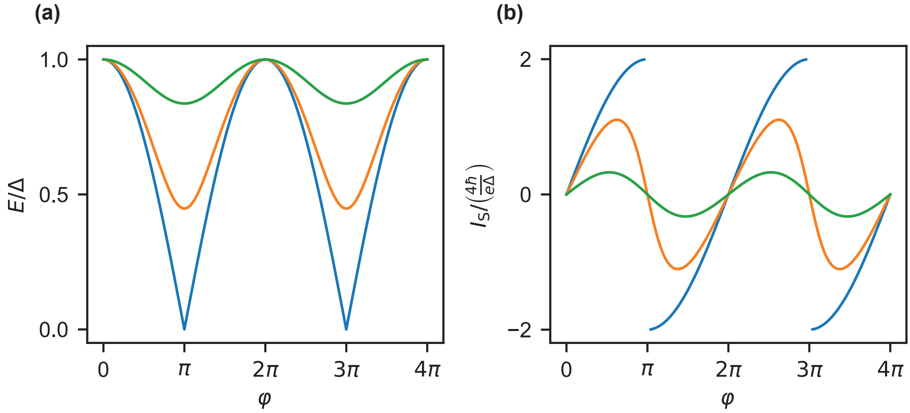

Figure 2.3: **Andreev energy spectrum and current.** **(a)** Energy spectrum of a single band, positive parity andreev bound state for different transmission probabilities; $T = 1$ (blue), $T = 0.8$ (orange), $T = 0.3$ (green). With perfect transmission the bound state energy reaches zero at $\varphi = n\pi$. The minimum moves to higher energies for lower transmission. **(b)** Supercurrent carried by the Andreev bound states of the respective transmissions. For high transmission the current-phase relation is skewed, while for low T the current-phase relation becomes sinusoidal.

An ABS effectively transports Cooper pairs between the leads and gives rise to the earlier mentioned supercurrent. We can derive the amplitude of this supercurrent by looking at the electrical power related to the Andreev bound state energy and applying the chain rule [25]

$$P = \frac{\mathrm{d}E_\mathrm{A}}{\mathrm{d}t} = \frac{\partial E_\mathrm{A}}{\partial\varphi}\frac{\mathrm{d}\varphi}{\mathrm{d}t}. \tag{2.17}$$

Next, we use the fact that the time derivative of the phase is related to voltage over the junction by [26]

$$\dot{\varphi} = 2eV/\hbar, \tag{2.18}$$

known as the ac Josephson relation. Since $P = IV$, we find that the supercurrent

$$I_S(\varphi) = -\frac{2e}{\hbar}\sum_p \frac{\partial E_{A,p}}{\partial\varphi} = \frac{e\Delta}{2\hbar}\sum_p \frac{T_p \sin\varphi}{\sqrt{1 - T_p \sin\varphi/2^2}}, \tag{2.19}$$

where p denotes a transport channel. The Josephson tunnel is effectively in the limit of many channels with low transmission T_p. The supercurrent in that case reduces to

$$I_S(\varphi) = I_C \sin\varphi, \tag{2.20}$$

where $I_C = \pi\Delta/(2eR_N)$ is the critical current with $R_N = 1/(G_Q\sum_p T_p)$. The critical current is the maximum supercurrent a junction can sustain. This effect is known as the dc Josephson relation.

When the current through a Josephson junction changes, it will induces a voltage over the junction. This means that there is an inductance associated with the junction, given by

$$L(\varphi) = \frac{L_J}{\cos\varphi}, \qquad L_J = \frac{\Phi_0}{2\pi I_C}, \tag{2.21}$$

with $\Phi_0 = h/(2e)$ the magnetic flux quantum. A related and often used quantity is the Josephson energy $E_J = L_J I_C^2$.

Josephson junctions are surprisingly versatile and have a wide range of applications. It is an essential part of the superconducting Transmon qubit [29] and due to its fundamental relation between frequency and voltage (Equation 2.18), it is used to define the international Voltage standard [30]. In the following sections we will discuss how the Josephson junctions can be used as a spectrometer or to gain control over the phase of a parallel junction.

2.3.1. SQUID

When configured correctly, a SQUID can be used to control the phase of a Josephson junction. The name stands for Superconducting Quantum Interference Device and it is build around quantum interference of supercurrents through two parallel arms. In this section we only consider the dc-SQUID variant which has a junction in both arms. In general the dc current through a SQUID is the sum of the current through the two arms:

$$I_{SQUID} = I_{S1}(\varphi_1) + I_{S2}(\varphi_2), \tag{2.22}$$

where $I_{S1}(\varphi_1)$ is the phase-dependent supercurrent through junction 1. Threading a magnetic flux through the SQUID loop area constraints the phase over both junctions via [19]:

$$\varphi_1 - \varphi_2 = 2\pi\frac{\Phi}{\Phi_0} \bmod 2\pi, \tag{2.23}$$

where Φ is the magnetic flux through the loop and $\Phi_0 = h/(2e)$, the magnetic flux quantum.

When both junctions have a sinusoidal current-phase relation and have the same critical current $I_{C,1} = I_{C,2}$, it can be shown that the maximum supercurrent for the SQUID becomes:

$$I_{C,S}(\Phi) = 2I_C \left|\cos\left(\frac{\pi\Phi}{\Phi_0}\right)\right|^2. \tag{2.24}$$

This is the maximum current for which Equation 2.22 has a solution and is therefore the critical current of the SQUID. This type of SQUID, with symmetric arms, is often used in mesoscopic devices as a tunable Josephson element [31–34]. The flux-current relation is plotted in Figure 2.4a. It is important to note that we neglect any kinetic or geometrical inductance.

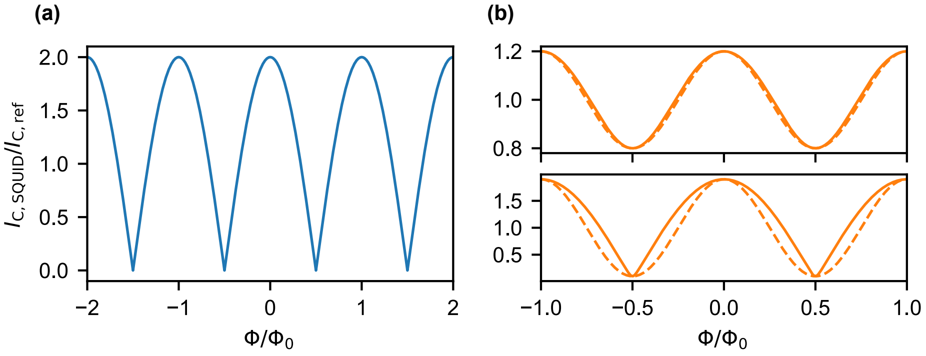

Figure 2.4: **(a)** Critical current of symmetric SQUID as a function of magnetic flux. **(b)** Critical current of a highly asymmetric SQUID. The upper panel compares the approximation of Equation 2.26 (dashed) with the exact shape (solid) of a SQUID with $I_{C,ref}/I_{C2} = 5$. The lower panel shows this for $I_{C,ref}/I_{C2} = 1.1$

Another use for a SQUID is to apply a phase bias over one of the junctions through Φ. For this use we consider another limit where one junction, the reference, has a much larger critical current then the other junction: $I_{C,ref} \gg I_{C2}$. For simplicity we assume that the reference junction has a sinusoidal CPR and by substituting Equation 2.23, the dc current through the SQUID becomes

$$I_{SQUID} = I_{C,ref}\sin(\varphi_2) + I_{S2}\left(\frac{2\pi\Phi}{\Phi_0} + \varphi_1\right). \tag{2.25}$$

Since $I_{C,ref} \gg I_{C2}$, the maximum current for which Equation 2.25 has a solution will always be close to $I_{C,ref}$. Therefore we can approximate the critical current with

$$I_{C,S}(\Phi) \approx I_{C,ref} + I_{S2}\left(\frac{2\pi\Phi}{\Phi_0} + \frac{\pi}{2}\right). \tag{2.26}$$

The CPR of the SQUID now has the shape of that of junction 2, offset by $I_{C,ref}$. This means that we can directly control the phase over junction 2 and measure its CPR. The validity of this approximation for different asymmetries is shown in Figure 2.4b.

2.3.2. RCSJ MODEL

To properly describe the behavior of a Josephson junction in an electromagnetic environment, we start with a more realistic description of its dynamics by shunting the idealized junction with a resistor and a capacitor (see Figure 2.5a). This is known as the restively and capacitively shunted Josephson junction (RCSJ) model and is required to accurately describe the current and voltage characteristics when a finite voltage drops over the junction. We follow mostly follow the treatment of Tinkham [19] and Chauvin [35].

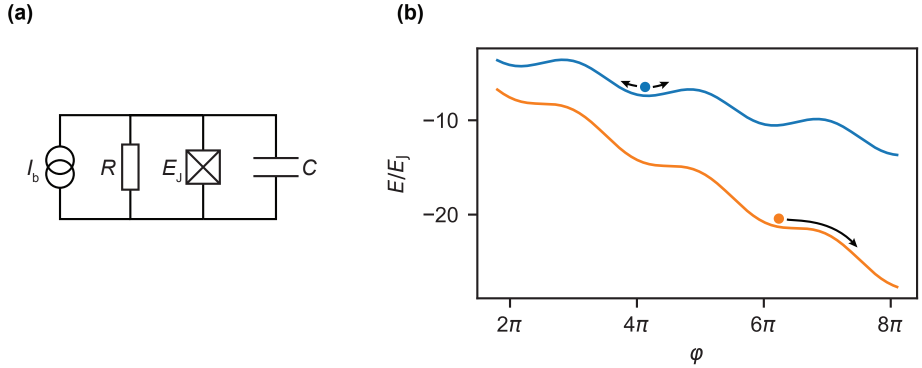

Figure 2.5: **(a)** RCSJ model circuit, with a current bias I_b, resistor R, Josephson energy EJ and capacitor C. **(b)** Washboard potential with the phase particle in the trapped state $I_b < I_C$ (blue) and in the running state $I_b > I_C$ (orange).

From the dc Josephson relation (Equation 2.20) we know the current through the junction and with Kirchhoff's current law we find the total current through the circuit:

$$I_b = I_C \sin(\varphi) + \frac{V}{R} + C\frac{\mathrm{d}V}{\mathrm{d}t}, \tag{2.27}$$

where V is the voltage over the circuit. Note that we limit ourselves to a sinusoidal current-phase relation for simplicity, sufficient for the purpose of this thesis [1].

Next, we substitute in the ac Josephson relation (Equation 2.20) and rewrite the equation to obtain a second-order differential equation

$$\left(\frac{\hbar}{2e}\right) C \frac{\mathrm{d}^2\varphi}{\mathrm{d}t^2} + \left(\frac{\hbar}{2e}\right) \frac{1}{R}\frac{\mathrm{d}\varphi}{\mathrm{d}t} + I_C \sin(\varphi) - I = 0. \tag{2.28}$$

This is similar to an equation of motion for a particle in a one-dimensional potential

$$U(\varphi) = -E_J \cos(\varphi) - \frac{\hbar I}{2e}\varphi, \tag{2.29}$$

where $E_J = \frac{\hbar I_C}{2e}$ is the Josephson energy. The phase particle has a mass $M = \left(\frac{\hbar}{2e}\right)^2 C$ and is subject to a damping proportional to the velocity $\eta = \left(\frac{\hbar}{2e}\right)^2 \frac{1}{R}$. $U(\varphi)$ is known as the

---

[1] A more general solution that includes arbitrary current-phase relations was developed by Ambegaokar and Halperin [36, 37].

washboard potential, named for its characteristic shape (Figure 2.5b). The tilt of the potential is set by the current bias I and according to Equation 2.28, the phase particle is 'trapped' in one of the local minima as long as $I < I_\mathrm{C}$. When I exceeds I_C, the phase particle rolls down the potential, generating a finite $\dot{\varphi}$ and thus 'switching' to a finite voltage.

We can now extract two characteristic quantities of the RCSJ circuit, its quality factor Q and plasma frequency ω_p. By replacing the time variable t with $\tau = t\omega_\mathrm{p}$ and dividing everything by I_C we obtain the following dimensionless equation.

$$\frac{I}{I_\mathrm{C}} = \frac{\mathrm{d}^2\varphi}{\mathrm{d}\tau^2} + \frac{1}{Q}\frac{\mathrm{d}\varphi}{\mathrm{d}\tau} + \sin(\varphi). \tag{2.30}$$

We find $\omega_\mathrm{p} = \sqrt{\frac{2eI_\mathrm{C}}{\hbar C}}$ and $Q = \omega_\mathrm{p} RC$. The quality factor describes the amount of damping the phase particle experiences and is equal to $\sqrt{\beta_c}$, known as the McCumber Stewart parameter [38, 39]. When in the potential minimum, the phase particle oscillates around the center with the plasma frequency.

So far we have ignored temperature effects. Temperature effects are usually responsible for observing a maximum supercurrent that is always lower than I_C, we therefore refer to this experimentally obtained quantity as the switching current I_SW. We model the effects of temperature as an Johnson Nyquist noise current term $I_\mathrm{n}(t)$. This term is equivalent to a random force acting on the phase particle with a Gaussian probability distribution and is described by the current-current correlation function:

$$\left\langle I_\mathrm{n}(t) I_\mathrm{n}(t') \right\rangle = \frac{2k_\mathrm{B}T}{R}\delta(t-t'), \tag{2.31}$$

with an expectation value $\langle I_\mathrm{n}(t)\rangle = 0$.

This extra current term changes the tilt of the washboard potential and is responsible for $I_\mathrm{SW} < I_\mathrm{C}$. Due to the stochastic nature of the noise, a distribution of switching currents will be observed (see Figure 2.6a). For a tunnel junction the mean switching current can be approximated by

$$\langle I_\mathrm{SW}\rangle = I_\mathrm{C}\left(1 - \left[\frac{k_\mathrm{B}T}{2E_\mathrm{J}}\ln\left(\frac{\omega_\mathrm{p}\Delta t}{2\pi}\right)\right]^{2/3}\right), \tag{2.32}$$

where Δt is time required for the current bias sweep [40]. For example, a typical small Al-AlO$_x$-Al tunnel junction with $C = 2\,\mathrm{fF}$, $I_\mathrm{C} = 20\,\mathrm{nA}$, $T = 20\,\mathrm{mK}$ and $\delta t = 0.1\,\mathrm{s}$, has $\langle I_\mathrm{SW}\rangle = 8.1\,\mathrm{nA}$ [41]. Clearly, even at low temperatures the I_SW is significantly lower than the critical current and thus important to keep in mind. Figure 2.6a shows a qualitative image of an IV curve, of a zero-temperature (dashed) and a finite-temperature (solid) junction.

Ivanchenko and Zil'Berman calculated the dc current-voltage behavior for a tunnel junction [42]. Figure 2.6b shows current-voltage curves for the zero temperature (dashed) and non-zero temperature case (solid). The blue and orange dots indicate if the phase particle is in a potential minimum (blue) or in the running state (orange).

For the zero temperature case, as long as $I < I_\mathrm{SW}$, the phase particle will sit in a local minimum of the washboard potential (blue curve in Figure 2.5). Since there are no

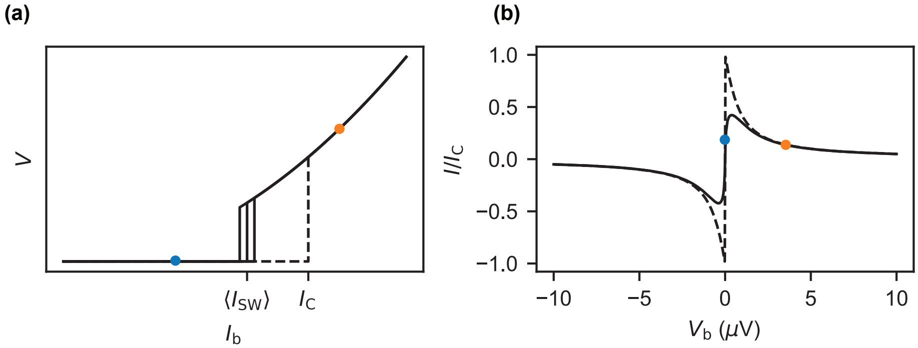

Figure 2.6: **Current-voltage characteristics of a Josephson junction.** **(a)** Qualitative description of a current-biased junction at finite temperature (solid) and zero temperature (dashed). The dots indicate if the junction is in the trapped (blue) or in the running (orange) state. **(b)** Ivanchenko Zil'Berman calculations for a voltage-biased junction.

thermal fluctuations, the measured voltage $\langle V\rangle = 0$. When $I > I_{SW}$, the minima of the potential disappear and the junction goes into the running state (orange curve in Figure 2.5). The phase particle moves with a constant velocity set by R, creating a finite voltage $\dot{\varphi}\hbar/(2e)$ over the junction.

At finite temperature the thermal fluctuations generate phase diffusion. In the washboard potential picture, the phase particle is moving back and forth – sometimes enough to escape a potential minimum, generating a finite voltage. When in a running state, energy will be dissipated and so the particle can be re-trapped in a minimum when enough is lost. As a result, the average phase velocity $\langle\dot{\varphi}\rangle$ will be non zero – generating a small voltage which grows with increasing current bias.

2.3.3. GENERAL ELECTROMAGNETIC ENVIRONMENT

A junction can be subject to range of different environments such as unintended stray inductances and capacitances in the circuit or by something purposely coupled to the junction. In the latter case one can, in fact, use the Josephson junction as a spectrometer.

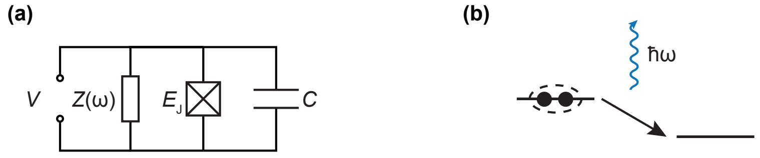

Figure 2.7: **(a)** Circuit for a general environment. **(b)** Inelastic Cooper pair tunneling process, where a photon with energy difference is absorbed by the environment $Z(\omega)$.

To generalize the RCSJ model, we replace the resistor R in the circuit of Figure 2.5 with a complex impedance $Z_{\mathrm{env}}(\omega)$ that describes the environment (Figure 2.7a). This is valid when $R \gg \mathrm{Re}\{Z_{\mathrm{env}}(\omega)\}$, which is the case if we voltage bias the junction inside the superconducting gap. The complex impedance of the circuit then becomes

$$Z(\omega) = \frac{1}{Z_{\text{env}}^{-1}(\omega) + i\omega C}. \tag{2.33}$$

We can then determine the current through the circuit by realizing that the Josephson junction is an ac current source at finite V with $I(t) = I_{\text{C}}e^{i\omega t}$ and $V(t) = Z(\omega)I(t)$. The real dissipated power is then

$$P = \frac{1}{2}\text{Re}\{VI^*\} = \frac{I_{\text{C}}^2\,\text{Re}\{Z(\omega)\}}{2}. \tag{2.34}$$

When then find that the dc current through junction at finite voltage is given by [31]

$$I = \frac{I_{\text{C}}^2}{2}\frac{\text{Re}\{Z(\omega)\}}{V}. \tag{2.35}$$

Note that this derivation ignores the possibility of charging effects due to Coulomb blockade. Specifically, we consider only the limit $E_{\text{J}} \gg U$, where U is the charging energy. A more rigorous derivation can by found in reference [43].

Intuitively, this effect can be seen in the context of Cooper pairs tunneling between the leads. In isolation, Cooper pairs tunnel back and forth at finite voltage with a frequency set by this voltage but with a mean current of zero. When a dissipative environment is attached, the Cooper pairs can in-elastically tunnel and generate a consequently a dc current will flow (see Figure 2.7b). This allows for using the junction as a spectrometer.

2.3.4. PHOTON ASSISTED TUNNELING

The previous sections have dealt with effects related to the Josephson current in an environment. In this section we focus on the superconducting gap edge. In particular, we treat photon assisted tunneling (PAT) in a Josephson junction coupled to a radiation source.

When a Josephson tunnel junction is biased to $V = 2\Delta/e - \hbar\omega_0$, where $\hbar\omega_0$ is the radiation energy and V the voltage over the junction, quasiparticles will tunnel through the junction assisted by the radiation photons and contribute to the dc current (see Figure 2.8a). In this section we will discuss what this current looks like and how it relates to the radiation spectrum. This subject has been investigated by several authors [32, 33, 44], here we mostly follow the treatment presented in Onac [45], where more in-depth derivations can be found.

The quasiparticle current comes about from an energy exchange with its environment:

$$I_{\text{QP}}(V) = \int_0^\infty \mathrm{d}\epsilon\, P(eV - \epsilon)\, I_{\text{QP},0}\left(\frac{\epsilon}{e}\right), \tag{2.36}$$

where $P(E)$ describes the probability of an energy exchange with the environment and the junction, $I_{\text{QP},0}$ is the current through the junction in the absence of an environment. By relating $P(E)$ to the power spectrum of the voltage fluctuations across the tunnel junction $S_V(\omega)$, one can rewrite Equation 2.36 to obtain the current due to photon-assisted

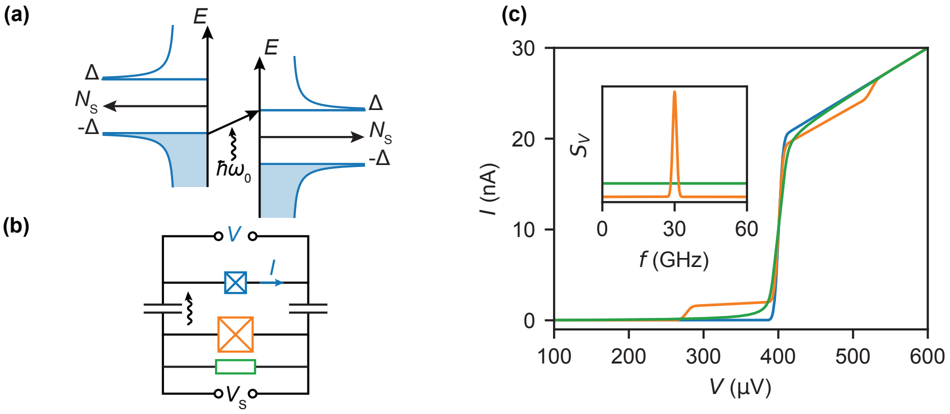

Figure 2.8: **Photon assisted tunneling (a)** Densities of states of a tunnel junction at voltage V with an incident photon (orange). Quasiparticles from the left superconducting lead tunnel to the right superconducting lead by absorbing the photon with an energy $\hbar\omega \geq 2\Delta - eV$. **(b)** Capacitively coupled PAT detection circuit with a Josephson tunnel junction as detector with voltage V (blue), a Josephson junction as a single frequency radiation source (orange) and a resistor as a shot noise source (green), at voltage V_S. **(c)** Current-voltage characteristic of an isolated tunnel junction (blue), a junction subject to single frequency radiation (orange) and to shot noise radiation (green). The inset shows the spectra for the shot noise (green), a white noise spectrum and for the single frequency centered at 30 GHz (orange). Subfigure generated with Python code from [46].

tunneling [45]:

$$I_{\mathrm{PAT}}(V) = \int_0^\infty \mathrm{d}\omega \left(\frac{e}{\hbar\omega}\right)^2 \frac{S_V(-\omega)}{2\pi} I_{\mathrm{QP},0}\left(V + \frac{\hbar\omega}{e}\right). \tag{2.37}$$

Note that we have limited ourselves to the experimentally relevant case, which assumes that $eV < 2\Delta$ and neglects any emission from the junction itself. The shape of the PAT current-voltage characteristic is thus a convolution of the voltage noise spectral density function $S_V(-\omega)$ and $I_{\mathrm{QP},0}$. The voltage spectral density function is defined as

$$S_V(\omega) = \int_{-\infty}^{\infty} \mathrm{d}\tau\, e^{i\omega\tau} \langle \delta V(\tau + t)\delta V(\tau)\rangle, \tag{2.38}$$

the Fourier transform of voltage fluctuations correlation function.

When we capacitively couple the detector junction to another Josephson junction, we can measure its noise spectrum using the PAT current. In this case, we can relate $S_V(\omega)$ in the detector to the current spectral density function of the source:

$$S_V(\omega) = S_I(\omega)|Z(\omega)|^2, \tag{2.39}$$

where $Z(\omega)$ is the transimpedance and depends on the coupling circuit [32, 33, 47]. Typical $|Z(\omega)|^2$ values for a mesoscopic on-chip circuit are on the order of a few hundred ohms.

We now consider two relevant types of noise from the source junction [48]; single-frequency noise originating from in-elastically tunneling Cooper pairs (see Figure 2.7c) and shot noise from electrons tunneling through a resistive shunt. Both are shown in the PAT circuit in Figure 2.8b, with the ideal Josephson tunnel junction as the single-frequency source in orange and the resistor as the white spectrum source in green.

In the idealized single-frequency case with $\delta V(t) = Z(\omega_0) I_C \cos\big(\omega_0 t + \varphi\big)$, the spectral density function will have two Dirac-delta peaks at $|\omega| = \omega_0$. Inserting this into Equation 2.37 results in a current

$$I_{\mathrm{PAT}}(V) = \frac{1}{8\pi}\left(\frac{e|Z(\omega_0)|I_{\mathrm{C}}}{\hbar\omega_0}\right)^2 I_{\mathrm{QP},0}\left(V + \frac{\hbar\omega_0}{e}\right). \tag{2.40}$$

We see that this case the PAT current is simply scaled copy of current-voltage characteristic of an isolated tunnel junction, offset by the $\hbar\omega_0/e$. A regular Josephson junction will have a source frequency $\omega_0 = 2eV_{\mathrm{S}}/\hbar$, due to its 2π-periodic current-phase relation. When the junction hosts MBS however, this frequency halves $\omega_0 = eV_{\mathrm{S}}/\hbar$.

When the source junction emits shot noise, the current spectral density function is frequency independent and has a constant value. This means that $S_V(\omega) = S_{I,0}|\omega|^2$ and the PAT current

$$I_{\mathrm{PAT}}(V) = \frac{S_{I,0}}{4\pi}\left(\frac{e|Z(\omega)|}{\hbar\omega}\right)^2 I_{\mathrm{QP},0}\left(V + \frac{\hbar\omega}{e}\right). \tag{2.41}$$

This results in a smooth addition to $I_{\mathrm{QP},0}$ and rounds off the otherwise sharp onset of quasiparticle current (Figure 2.8c). Measuring shot noise could be a helpful tool in measuring the transconductance [49].

2.4. QUANTUM DOTS

Quantum dots are small structures – typically nanometers up to a few micrometers in size, with a relatively small number of electrons, ranging from a single electron to thousands. Due to the small size, Coulomb repulsion becomes a significant effect and prevents electrons from flowing through the dot without paying an energy cost. When the flow of electrons is stopped, the system is said to be in Coulomb blockade. Ohm's law is no longer valid in these systems. Quantum dots show many similarities with atoms and are sometimes referred to as artificial atoms [50, 51].

The research in, and applications of, quantum dots is wide spread and includes the realm of quantum information; such as in spin qubits [4], as part of a Josephson junction [52, 53] or as a readout device for Majorana states [11, 12]. In this section we concern ourselves with single and double quantum dot properties that are most relevant when they are the weak link of a Josephson junction.

The total charge of an object is given by the integer number of charges present $Q = Ne$, where e is the elementary charge. Usually, charge appears to behave as a continuous variable. This is simply due to the large size of the conductors and the enormous number of conduction electrons that are typically involved. When dealing with small structures the charging energy $E_{\mathrm{C}} = e^2/C$, with C the capacitance of the structure, becomes an important energy scale. Consider a simple circuit for a localized charge Q and potential V_I (Figure 2.9a). It consists of a small island connected one side to a voltage source V_{g} via a capacitor with capacitance C_{g}, and on the other side to ground via tunnel junction with a capacitance C_{d} and resistance R_{d}. This resistance has to be large enough for charging

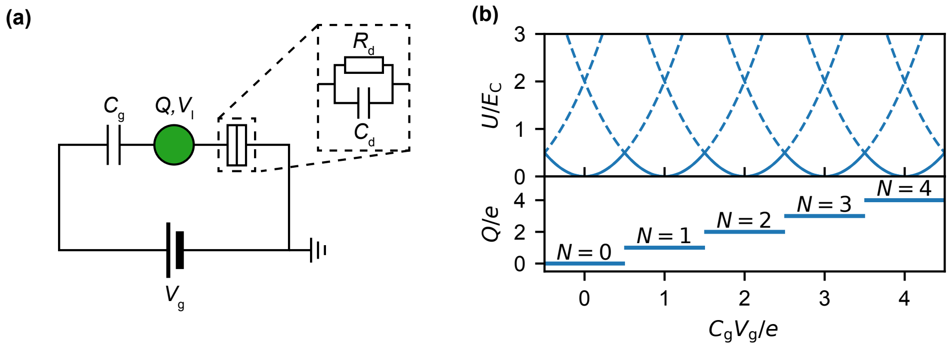

Figure 2.9: **Single-electron island (a)** Circuit diagram of a small island with Coulomb blockade effects. The island has charge Q and potential V_I, is connect to a battery V_g via capacitance C_g and to ground via a tunnel junction. The tunnel junction is a resistor R_d with a parallel capacitor C_d. **(b)** Continuous energy U of the island in the upper panel with the corresponding discreet number of charges N present on the island.

effects to manifest themselves, the condition is $R_d \gg R_Q = 2/G_Q \approx 25\,\mathrm{k}\Omega$[2]. A related quantity is the tunnel rate, which can be obtained from Fermi's golden rule [43, 54]:

$$\Gamma = \frac{\Delta E_d e V_I}{e^2} G_d \frac{1}{e^{\Delta E_d/kT} - 1}, \tag{2.42}$$

with ΔE_d the energy difference between the initial and final configurations, G_d the conductance and T the temperature.

Using the assumptions from the constant-interaction model[3] we can write down expressions for the charge and potential

$$Q = CV_I - C_g V_g, \qquad V_I = Q/C + V_{ext}, \tag{2.43}$$

where $C = C_g + C_d$ and $V_{ext} = C_g V_g / C$. The energy of the island consists of an electrostatic energy term and an energy term provided by the external voltage:

$$U(N) = \frac{(Ne)^2}{2C} - NeV_{ext} = \frac{\left(Ne - C_g V_g\right)^2}{2C}. \tag{2.44}$$

We plot equation 2.44 in the upper panel of Figure 2.9b as a function of V_g for every integer value of N. This results in a series of parabolas with a horizontal offset given by N. The actual charge on the island can be determined by finding the value of N for which U is minimal. These values plotted in the lower panel of Figure 2.9b.

2.4.1. SINGLE QUANTUM DOT

In order to do transport measurements, we modify the circuit in Figure 2.9a to a more realistic setup (see Figure 2.10a). The new expression for the electrostatic energy is given

---

[2] The charge/discharge time for an electron $\Delta t = RC$. We then arrive at this condition with the Heisenberg uncertainty relation $\Delta E \Delta T > \hbar$, where $\Delta E = E_C$.

[3] Two assumptions are made in this model: Coulomb interactions of electrons in the dot are described by the effective constant total capacitance C, the sum of capacitances surrounding the dot and the energy spectrum is independent of the number of electrons on the dot N.

by

$$U(N) = \frac{1}{2C}\left(e(N-N_0) - \sum_i C_i V_i\right)^2 + \sum_{n=1}^{N} E_n, \tag{2.45}$$

where the electron number is adjusted by an offset charge N_0, $C = C_s + C_d + C_g$, the summation in the first term sums over all capacitances and associated voltages, the second term sums over the single-particle energy levels E_N of occupied states and are determined by the confinement potential. Unlike the electron number, the effective induced charge $C_g V_g$ by the plunger gate, can be changed continuously [51, 55, 56].

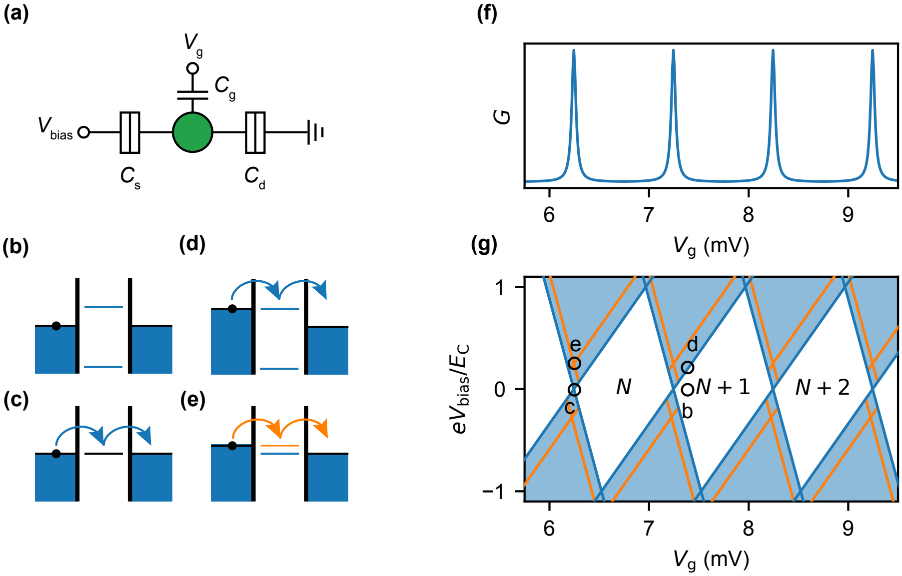

Figure 2.10: **(a)** Circuit diagram of a quantum dot capacitively coupled to a source lead (C_s), a drain lead (C_d) and plunger gate (C_g). The junctions are comprised of a (large) resistor and capacitor in parallel. **(b-e)** Schematic diagrams of electrochemical potentials μ_s, μ_{dot}, μ_d in four different configurations. **(f)** Qualitative illustration of a gate trace at $V_b \approx 0$, revealing Coulomb peaks in the conductance. **(g)** Qualitative illustration of a Coulomb diamond scan. White areas are blockaded, in blue areas the blockade is lifted. Excited states are shown in orange. The open circles indicate the locations of the diagrams in **b-e**.

The electrochemical potential of the dot $\mu(N)$ is defined as

$$\begin{aligned}\mu_{dot}(N) &\equiv U(N) - U(N-1)\\ &= E_C\left(N - N_0 - \frac{1}{2}\right) - e\alpha_g V_g + E_N,\end{aligned} \tag{2.46}$$

where we have substituted $C_g/C = \alpha_g$ which is the lever arm of the electrostatic gate. From Equation 2.46 we can retrieve the spacing between ground states, called the addition energy

$$\begin{aligned}E_{add} &= \mu_{dot}(N+1) - \mu_{dot}(N)\\ &= E_C + \Delta E_N.\end{aligned} \tag{2.47}$$

The electrostatics of quantum dots gives the electron transport through them a few unique signatures. As shown in the circuit diagram, we apply an asymmetric bias to the dot by grounding the the drain lead $V_\mathrm{d} = 0$. We apply a very small source voltage $V_\mathrm{b} \approx 0$ and the plunger gate is such that $U(N+1) > 0 > U(N)$. This scenario is depicted Figure 2.10b and is called Coulomb blockade for the reason that the Coulomb repulsion blocks the electron from tunneling to the dot – no current will flow. When the V_g is changed such that $U(N+1) = 0$ (Figure 2.10c), the chemical potential of the dot is equal to that of the source lead – the blockade is lifted and electrons can tunnel from the source to the dot, increasing N to $N+1$. The electron can tunnel further to the drain lead and decrease the electron number back to N.

By sweeping the plunger gate, we move through multiple of these cycles and find a trace similar to that shown in Figure 2.10f. The peaks are known as Coulomb peaks and their shape contains information about the coupling strength to the leads and the temperature of the electrons [57]. Recall that the distance between the peaks is determined by $\alpha_\mathrm{g} E_\mathrm{add}$.

By doing finite-bias measurements we can obtain more information about the quantum dot from its transport signatures. For a given N, when the bias voltage $-eV_\mathrm{b} < \mu(N)$ transport is blockaded. Only when $-eV_\mathrm{b} \geq \mu(N)$ blockade is lifted and current can flow (Figure 2.10d). This results in characteristic Coulomb diamonds as shown in Figure 2.10g. The height of the diamonds is equal to E_add. At bias $-eV_\mathrm{b} > \mu(N)$ transitions to excited states become allowed (Figure 2.10e)). These are visible as additional lines parallel to the Coulomb diamond boundaries (orange lines in Figure 2.10g))

2.4.2. DOUBLE QUANTUM DOT

Two quantum dots, connected in series form what is known as a double-quantum dot (DQD). Figure 2.11a shows the circuit, which is an extended version of the single dot where the two dots are coupled via a tunnel barrier. The electrostatic energy for this system is

$$U(N_1, N_2) = \frac{1}{2} N_1^2 E_\mathrm{C1} + \frac{1}{2} N_2^2 E_\mathrm{C2} + N_1 N_2 E_\mathrm{Cm} + f(V_\mathrm{g1}, V_\mathrm{g2}), \tag{2.48}$$

$$\begin{aligned} f(V_\mathrm{g1}, V_\mathrm{g2}) = {} & \frac{1}{-|e|} \big(C_\mathrm{g1} V_\mathrm{g1} (N_1 E_\mathrm{C1} + N_2 E_\mathrm{Cm}) + C_\mathrm{g2} V_\mathrm{g2} (N_1 E_\mathrm{Cm} + N_2 E_\mathrm{C2}) \big) \\ & + \frac{1}{e^2} \left(\frac{1}{2} C_\mathrm{g1}^2 V_\mathrm{g1}^2 E_\mathrm{C1} + \frac{1}{2} C_\mathrm{g2}^2 V_\mathrm{g2}^2 E_\mathrm{C2} + C_\mathrm{g1} V_\mathrm{g1} C_\mathrm{g2} V_\mathrm{g2} E_\mathrm{Cm} \right), \end{aligned} \tag{2.49}$$

where C_m is the inter-dot charging energy and $C_{1(2)} = C_{\mathrm{s(d)}} + C_{\mathrm{g1(2)}} + C_\mathrm{m}$ [58]. For the single dot case, we defined the charging energy of the dot using its total capacitance. In a DQD, each dot also has a capacitive coupling to the capacitances of the other dot. This leads to a correction factor to the charging energy compared to a single isolated dot:

$$E_{\mathrm{C1(2)}} = \frac{e^2}{C_{1(2)}} \left(\frac{1}{1 - \frac{C_\mathrm{m}^2}{C_1 C_2}} \right). \tag{2.50}$$

The electrostatic coupling is described by the inter-dot charging energy:

$$E_{\mathrm{Cm}} = \frac{e^2}{C_{\mathrm{m}}}\left(\frac{1}{\frac{C_1 C_2}{C_{\mathrm{m}}^2} - 1}\right). \tag{2.51}$$

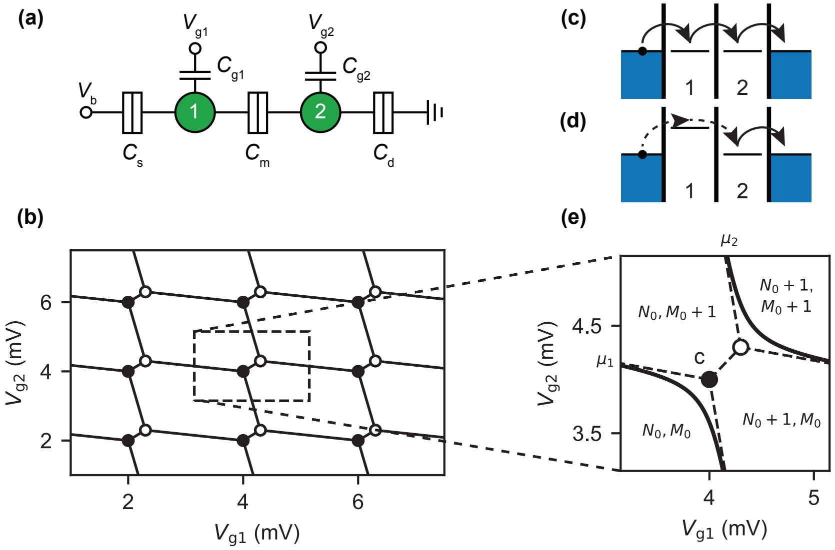

Figure 2.11: **(a)** Circuit diagram of serial double-quantum dot. **(b)** Stability diagram of a double-quantum dot, as a function of plunger gates V_{g1} and V_{g2}. **(c)** Schematic diagrams of electrochemical potentials at a triple point where electrons are shuttled from source to drain (filled circle, indicated in **e**) **(d)** Schematic diagrams of electrochemical potentials along a horizontal charge-degeneracy line. **(e)** Zoom-in around triple point, showing avoided crossing of charge boundaries μ_1, μ_2 due to coupling between charge states. Relative electron numbers N, M are written inside the charge regions.

A characteristic measurement of a DQD is the charge stability diagram (Figure 2.11b). It has hexagonal areas with stable charge configurations. Such a measurement is usually taken at $eV_{\mathrm{b}} \approx 0$. When three charge states become degenerate a conductance resonance appears (Figure 2.11c), this location in V_{g1}, V_{g2} space is called a triple point. We plot two types of triple points, filled and open circles. These correspond to different charge transfer processes, around the filled (open) circles an electron(hole) can be shuttled through the system. The spacing between these two types of triple points is determined by E_{Cm}. The (almost) horizontal vertical lines between triple points are where one of the two dots is on resonance with the leads. Naively one would expect no current to flow since one of the dots is off resonance. However, second-order processes involving an intermediate virtual state, makes it possible for an electron to tunnel through the off-resonance quantum dot in a process called co-tunneling [54]. Figure 2.11d schematically depicts such a process. For a very short time, allowed by the uncertainty principle, the electron violates energy conservation by occupying the high-energy level in dot 1. When another electron simultaneously tunnels from the high-energy level to dot 2, energy is conserved while the electron has tunneled from the left lead to dot 2.

The two dots have a finite coupling to each other, this coupling lifts the degeneracy at the triple points and causes avoided crossings of the charge boundaries. We describe the system with a one-electron Hamiltonian

$$H_{\text{coupling}} = \begin{pmatrix} \epsilon_1 & \tau \\ \tau & \epsilon_2 \end{pmatrix}, \tag{2.52}$$

where τ is the coupling strength between the dots and $\epsilon_1(2)$ the electrochemical potential of dot 1(2) [56] (not to be confused with τ in section 2.3.2). Diagonalizing this Hamiltonian gives the energy eigenvalues

$$E_\pm = \epsilon \pm \frac{1}{2}\sqrt{\delta^2 + 4|\tau|^2}, \tag{2.53}$$

where ϵ and δ defines a new coordinate system – ϵ is the equal energy axis moving through both triple points and δ the de-tuning axis, perpendicular to ϵ. The boundaries are given by the energy difference between the ground-state energies E_{N+M} of neighboring charge states.

$$\begin{aligned} \mu_1 &= E_1 - E_0 = \epsilon - \frac{1}{2}\sqrt{\delta^2 + 4|\tau|^2} \\ \mu_2 &= E_2 - E_1 = \epsilon + \frac{1}{2}\sqrt{\delta^2 + 4|\tau|^2} + E_{Cm}, \end{aligned} \tag{2.54}$$

where E_{Cm} accounts for the distance between the triple points (Figure 2.11e).

2.5. SUPERCONDUCTIVITY AND QUANTUM DOTS

Combining superconductivity and quantum dots gives rise to range of different phenomena, depending on device design and on the coupling strength [59]. In the weak coupling regime, the interaction between a superconducting lead and the single spins in the coupled quantum dot, give rise to new energy states below the gap. These states are known as Yu-Shiba-Rusinov states [60–62].

2.5.1. YU-SHIBA-RUSINOV STATES

Apart from influencing the supercurrent in a Josephson junction, a superconductor coupled to quantum dots gives rise new excitations inside the superconducting gap. These sub-gap states are known as Yu-Shiba-Rusinov (YSR) states and where first theorized by the equally named trio [63–66].

YSR states are closely related to earlier introduced sub-gap states called ABS. They are however commonly used in different regimes. ABS are usually used to describe transport in a regime of negligible charging energy $E_C \ll \Delta$, whereas YSR states offer a more suitable description for the emerging sub-gap energy states when there is strong coulomb interaction $E_C \gg \Delta$ [67].

The system we consider in this section is a single quantum dot coupled to a superconducting lead (see Figure 2.12a). For analytical insights of the ground state behavior of the quantum dot we construct an effective Hamiltonian where $\Delta \to \infty$ [68, 69]:

$$H_{\text{YSR}} = \sum_{\sigma=\uparrow,\downarrow} \xi c_\sigma^\dagger c_\sigma - \Gamma\left(c_\uparrow^\dagger c_\downarrow^\dagger + \text{h.c.}\right) + \frac{E_C}{2}\left(\sum_{\sigma=\uparrow,\downarrow} c_\sigma^\dagger c_\sigma\right)^2. \tag{2.55}$$

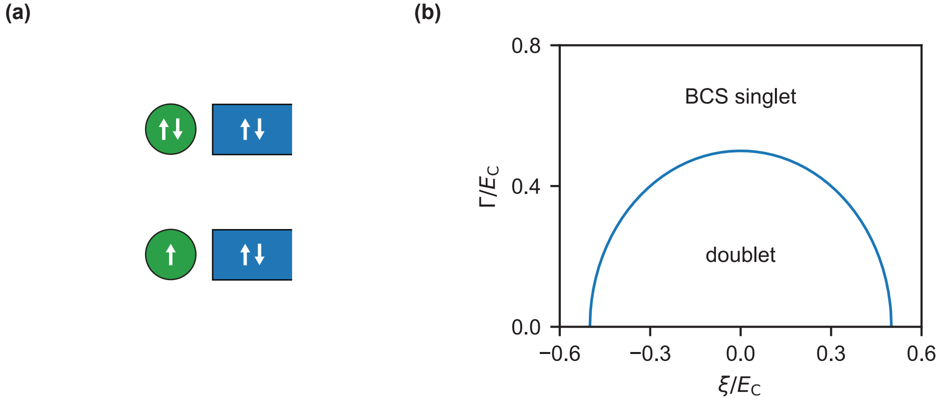

Figure 2.12: **(a)** Schematic diagram of the YSR model system, with a quantum dot shown as a green circle and a superconducting lead in blue. In the upper version the quantum dot is in a singlet ground state, whereas the lower version is in a doublet configuration. **(b)** Phase diagram of the YSR system showing the two different ground states as a function of quantum dot potential $\epsilon + E_C/2$ and coupling Γ.

The hybridization parameter Γ between the dot and the superconducting lead now acts as an effective Δ and we have shifted the dot energy level with $\xi = \epsilon + \frac{E_C}{2}$ to make the Hamiltonian particle-hole symmetric around $\xi = 0$.

Through a Bogoliubov transformation we can find that H_{YSR} has four eigen states; two single spin-1/2 (doublet) states $|\uparrow\rangle$ and $|\downarrow\rangle$, with eigenenergies $E_\downarrow = E_\uparrow = 0$ in addition to two BCS-type (singlet) eigenstates [68] :

$$|+\rangle = u\,|\uparrow\downarrow\rangle + v\,|0\rangle\,, \qquad |-\rangle = -v\,|\uparrow\downarrow\rangle + u\,|0\rangle\,, \tag{2.56}$$

with eigenenergies $E_\pm = \pm\sqrt{\xi^2 + \Gamma^2} + E_C/2$ and coefficients

$$u^2 = \frac{1}{2}\left(1 + \frac{\xi}{\sqrt{xi^2 + \gamma^2}}\right), \qquad v^2 = \frac{1}{2}\left(1 - \frac{\xi}{\sqrt{xi^2 + \gamma^2}}\right). \tag{2.57}$$

It is clear that of the two BCS singlet states, E_- has a lower energy, which means that H_{YSR} has two possible ground states – a singlet or a degenerate doublet configuration. Whenever $\xi > 0$ the ground state is a doublet and a singlet otherwise. By setting $E_- = 0$, we can find the phase boundary of the transition between the two configurations and find it to be

$$\xi^2 + \Gamma^2 = \frac{U^2}{4}. \tag{2.58}$$

The resulting phase diagram is shown in Figure 2.12b. When the coupling between the superconducting lead and the dot $\Gamma > E_C/2$, the quantum dot will always be in a singlet configuration. In this case, superconductivity has broken conservation of charge in the quantum dot. The phase diagram for a finite Δ looks qualitatively similar and calculations for that regime can be found in Reference [68].

Next, we discuss the shape of the sub-gap states. Unfortunately, there are no known analytical approaches to properly describe the sub-gap states of the system. Numerical

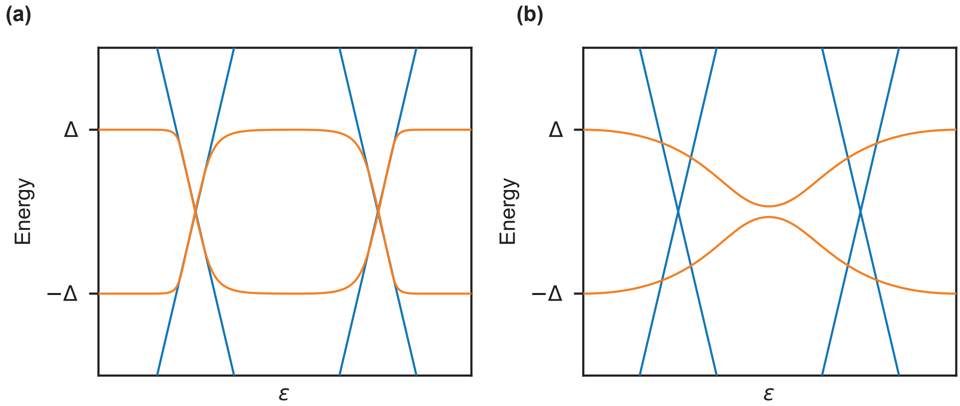

Figure 2.13: Qualitative depiction of YSR sub-gap states. **(a)** Weak coupling limit, the system moves between a doublet and a singlet ground state as a function of dot potential. **(b)** Strong coupling limit, the system is always in a singlet ground state. Conservation of charge is broken.

re-normalization group does a good job in describing the states, but is beyond the scope of this thesis [4]. We therefore limit ourselves here to a qualitative discussion.

In weak coupling limit (see Figure 2.13), the energy cost for going from singlet to doublet is maximum Δ when in even state and minimal Δ when in odd state, with smooth transition around degeneracy points. When the coupling increases, the shape becomes more asymmetric as the energy cost for a doublet state increases as the superconductivity in the dot becomes stronger. At a certain point the coupling becomes so strong that the system always stays in a singlet ground state. In this scenario the YSR states no longer go below 0 in the odd occupation (see Figure 2.13b). At this point, conservation of charge is broken.

2.5.2. SUPERCURRENT

When the coupling to the quantum dot(s) is strong and superconducting leads are on both sides, a supercurrent can flow – creating a special type of Josephson junction [52, 53, 71–73]. Although Cooper pairs cannot tunnel at once though a quantum dot, single electrons can tunnel coherently to transfer Cooper pairs. The occupation of the quantum dot(s) influences the supercurrent and give rise to a so-called π-junction. The supercurrent becomes negative in this type of junction, equivalent to a π phase-shift in the current-phase relation.

Here we will start with a treatment the supercurrent through a double-quantum dot Josephson junction and give an intuitive picture of the even-odd (0-π) effect. Most of this theory also holds for a single quantum dot junction. For simplicity we do not consider spin-orbit coupling and temperature. The theory and simulations in this section were developed in collaboration with András Pályi, Dávid Pataki, Gorm Steffensen and Jens Paaske. More extensive discussions can be found in the supplementary information of Chapter 6.

---

[4] References [67, 70] give an extensive overview of available analytical and numerical approaches.

We model the system as four single-orbital fermionic sites with nearest-neighbor hopping (see Figure 2.14). The outer sites are superconducting leads and the green circles are the quantum dots. The Hamiltonian reads

$$H = H_{\mathrm{L}} + H_{\mathrm{tL}} + H_{\mathrm{DQD}} + H_{\mathrm{tR}} + H_{\mathrm{R}}, \tag{2.59}$$

where H_L and H_R are the lead terms H_0 is the quantum dot system and H_t contains the tunneling between the dot(s) and the leads.

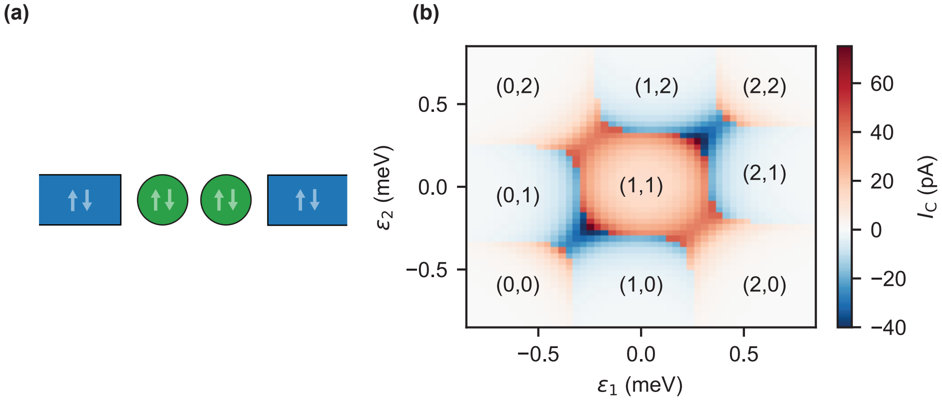

Figure 2.14: **(a)** Schematic representation of the double-quantum dot Josephson junction. The four fermionic sites are coupled to nearest neighbors only. The blue sites are superconducting leads and the green circles the dots. **(b)** Numerical simulation using the Hamiltonian in Equation 2.59 with $E_{\mathrm{C}} = 600\,\mu\mathrm{eV}$, $t_{\mathrm{L}} = t_{\mathrm{R}} = \tau = 50\,\mu\mathrm{eV}$.

The leads are modeled with the zero-bandwidth (ZBW) approximation, which has a single energy level at the superconducting gap Δ. This is the simplest model for qualitatively representative results [5]:

$$H_L = \Delta\left(e^{-i\varphi/2} c^\dagger_{L,\uparrow} c^\dagger_{L,\downarrow} + \text{h.c.}\right), \tag{2.60}$$

$$H_R = \Delta\left(e^{i\varphi/2} c^\dagger_{R,\uparrow} c^\dagger_{R,\downarrow} + \text{h.c.}\right), \tag{2.61}$$

with φ the phase difference between the leads, $c^\dagger_{l,\sigma}$ the creation operator for lead l and spin σ. Tunneling from the dot 1,2 to the lead L,R is described by

$$H_{\mathrm{tL}} = t_{\mathrm{L}} \sum_{\sigma=\uparrow,\downarrow} \left(c^\dagger_{L,\sigma} c_{1,\sigma} + \text{h.c.}\right), \tag{2.62}$$

$$H_{\mathrm{tR}} = t_{\mathrm{R}} \sum_{\sigma=\uparrow,\downarrow} \left(c^\dagger_{R,\sigma} c_{2,\sigma} + \text{h.c.}\right), \tag{2.63}$$

where $c_{m,\sigma}$ is the annihilation operator for dot m. Finally double-quantum dot term is

---

[5] A treatment using BCS leads and comparison with ZBW can be found in the supplement of reference [53]

given as

$$
\begin{aligned}
H_{\mathrm{DQD}} = {} & \epsilon_1 n_1 + \epsilon_2 n_2 + \frac{E_{\mathrm{C1}}}{2} n_1(n_1-1) + \frac{E_{\mathrm{C2}}}{2} n_2(n_2-1) + E_{\mathrm{Cm}} n_1 n_2 \\
& + \tau \sum_{\sigma=\uparrow,\downarrow} \left(c^\dagger_{1,\sigma} c_{2,\sigma} + \mathrm{h.c.} \right) + \frac{g\mu_{\mathrm{B}} B}{2} \sum_{m=1,2} \left(n_{m,\uparrow} - n_{m,\downarrow} \right),
\end{aligned}
\tag{2.64}
$$

with ϵ_m the on-site energy of dot m, particle number operator $n_m = \sum_{\sigma=\uparrow,\downarrow} c^\dagger_{m,\sigma} c_{m,\sigma}$, τ the inter-dot coupling, g the Landé g-factor, μ_{B} the Bohr magneton and B the magnetic field.

Next, we evaluate the ground state energies for different charge occupations. The ground state of a sector determines which electron transfers are allowed and that in turn determines the direction and amplitude of the supercurrent. For simplicity, we set the on-site and charging energies of both dots to be equal; $\epsilon_1 = \epsilon_2 = \epsilon$ and $E_{\mathrm{C1}} = E_{\mathrm{C2}} = E_{\mathrm{C}}$.

When the dots are empty, all terms in $H_{\mathrm{DQD},0}$ are zero and so the ground state energy $E_0 = 0$. For the one-electron sectors we consider the basis states $\{|n_{1,\uparrow}\rangle\,|n_{2,\uparrow}\rangle\,|n_{1,\downarrow}\rangle\,|n_{2,\downarrow}\rangle\}$ which gives a 4 × 4 matrix:

$$
H_{\mathrm{DQD},1} = \begin{pmatrix}
\epsilon + \frac{g\mu_{\mathrm{B}}B}{2} & \tau & 0 & 0 \\
\tau & \epsilon + \frac{g\mu_{\mathrm{B}}B}{2} & 0 & 0 \\
0 & 0 & \epsilon - \frac{g\mu_{\mathrm{B}}B}{2} & \tau \\
0 & 0 & \tau & \epsilon - \frac{g\mu_{\mathrm{B}}B}{2}
\end{pmatrix},
\tag{2.65}
$$

with eigenenergies for the four possible configurations

$$
E_{1,2} = \epsilon + \frac{g\mu_{\mathrm{B}}B}{2} \pm \tau, \qquad E_{3,4} = \epsilon - \frac{g\mu_{\mathrm{B}}B}{2} \pm \tau.
\tag{2.66}
$$

Since all quantities here are positive numbers, the ground state energy of the single electron sector is $E_{g,1} = E_4 = \epsilon - g\mu_{\mathrm{B}}B/2 - \tau$.

Using the singlet-triplet basis, the two-electron matrix becomes

$$
H_{\mathrm{DQD},1} = \begin{pmatrix}
2\epsilon+E_{\mathrm{C}} & 0 & \sqrt{2}\tau & 0 & 0 & 0 \\
0 & 2\epsilon+E_{\mathrm{C}} & \sqrt{2}\tau & 0 & 0 & 0 \\
\sqrt{2}\tau & \sqrt{2}\tau & 2\epsilon+E_{\mathrm{Cm}} & 0 & 0 & 0 \\
0 & 0 & 0 & 2\epsilon+E_{\mathrm{Cm}} & 0 & 0 \\
0 & 0 & 0 & 0 & 2\epsilon+E_{\mathrm{Cm}}-g\mu_{\mathrm{B}}B & 0 \\
0 & 0 & 0 & 0 & 0 & 2\epsilon+E_{\mathrm{Cm}}+g\mu_{\mathrm{B}}B
\end{pmatrix}.
\tag{2.67}
$$

The triplet part of the Hamiltonian is already diagonal, so we can directly read off the eigenenergies. For the singlet part, we find the eigenenergies after diagonalization and if we assume τ to be small, we find that the ground-state energies are

$$
\begin{aligned}
E_{\mathrm{g,S}} &\approx 2\epsilon + U_{\mathrm{Cm}} - \frac{4\tau^2}{E_{\mathrm{C}} - U_{\mathrm{Cm}}} \\
E_{\mathrm{g,T}} &= 2\epsilon + U_{\mathrm{Cm}} - g\mu_{\mathrm{B}}B.
\end{aligned}
$$

As expected, at zero magnetic field the ground-state configuration is a singlet. At finite magnetic field however the triplet ground state becomes lower in energy and at magnetic fields above $B/(g\mu_\mathrm{B}) = 4\tau^2/(E_\mathrm{C} - E_\mathrm{Cm})$, the ground state becomes a triplet configuration. As we will see, this has consequences for the supercurrent amplitude.

The current operator for the interface between the left lead and dot 1 is defined as

$$j_\mathrm{L} = -\frac{i}{\hbar}[n_1, H_\mathrm{tL}] = t_\mathrm{L}\frac{i}{\hbar}\sum_{\sigma=\uparrow,\downarrow}\left(c^\dagger_{L,\sigma}c_{1,\sigma} - \mathrm{h.c.}\right). \tag{2.68}$$

The supercurrent through the junction is then the expectation value of the current operator

$$I_\mathrm{S}(\varphi) \equiv \left\langle \Psi_0(\varphi)\right| j_\mathrm{L} \left|\Psi_0(\varphi)\right\rangle. \tag{2.69}$$

Because of the quantum dot barriers, the transmission will be low and so the supercurrent is sinusoidal and the critical current is $I_\mathrm{C} = I_\mathrm{S}(\pi/2)$. Figure 2.14b shows the resulting current values for up to 4 electrons. For this simulation $E_\mathrm{C} = 600\,\mu\mathrm{eV}$, $t_\mathrm{L} = t_\mathrm{R} = \tau = 50\,\mu\mathrm{eV}$.

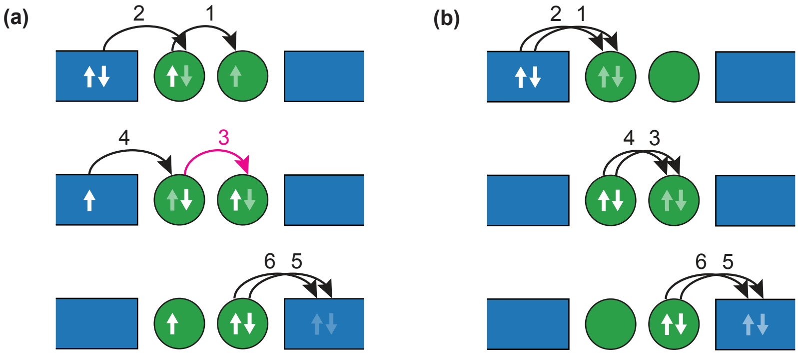

Figure 2.15: **(a)** Visual representation of a Cooper pair transfer through an odd occupied DQD. During the third transfer, the spin-down electron encounters a spin-up electron and causes a sign flip in the supercurrent. **(b)** Cooper pair transfer through an even occupied DQD. Numbers indicate the order of the transfers.

Notice that the sign of the critical current follows an even-odd pattern, for a total even number of electrons on the dots the critical current is positive and for an odd number it is negative. An intuition for this is shown in Figure 2.15. The electrons hopping from the left lead to the right lead in six tunneling events. In this representation, when an electron encounters an electron with opposite spin – when tunneling from one site to another – the current operator will be multiplied with a minus sign. In Figure 2.15a we show a process for an odd number of electrons on the dot. Here an electrons encounters an opposite spin during the third event. Since this happens an odd number of times, the resulting critical current for this configuration is negative. In Figure 2.15b a process is shown for an even number of electrons on the dot and we see an even number of opposite spin encounters, zero in total. Therefore the critical current is positive. It turns out that this even-odd effect is independent of the length the quantum dot array. As long as the dots are single orbital, the even-odd pattern remains. A formal proof for this can be found in the supplementary material of Chapter 6.

When the DQD is in a triplet ground state, the number of possible electron transfer processes is sharply decreased. This results in a suppression of the supercurrent [74, 75].

If we replace the ZBW superconducting leads with BCS leads, it can be shown that in the limit $\Delta \rightarrow \infty$ the effective Hamiltonian becomes [74]

$$H_{\mathrm{eff}} = H_{\mathrm{tL}} + H_{\mathrm{DQD}} + H_{\mathrm{tR}} + \Gamma_L e^{-i\varphi/2} c_{1,\uparrow} c_{1,\downarrow} + \Gamma_R e^{-i\varphi/2} c_{2,\uparrow} c_{2,\downarrow}, \tag{2.70}$$

where Γ_l is the coupling strength to lead l. Note that the new lead terms in Equation 2.70 couple to electrons with opposite spins from one dot only. Thus a triplet configuration does not couple to the leads, resulting in a complete suppression of supercurrent. In the limit where Δ is finite and $E_{\mathrm{C}} \rightarrow \infty$, only transport processes where no extra electrons have to be charged on the quantum dots are allowed. It turns out that these transfer processes exists for a singlet configuration, but not for a triplet. Resulting also in this limit in a complete suppression . Interestingly, in the regime in-between these two limits, a finite triplet current is possible. Numerically it can be shown that the maximum triplet supercurrent suppression is roughly a factor of 4 (See Chapter 6 for more details).

2.6. MAJORANA STATES

In this section we introduce a theoretical toy model for creating Majorana states in a condensed matter system and discuss two different approaches for realizing a physical system that can host Majorana states.

2.6.1. KITAEV CHAIN

The Kitaev chain is a one-dimensional system with p-wave superconductivity proposed by Kitaev. He showed that that Majorana states can appear at the ends of the quantum wire [9].

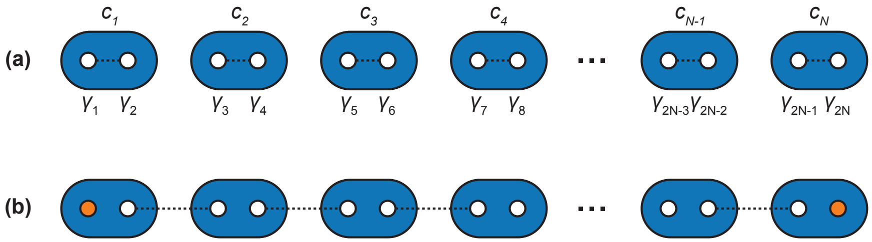

Figure 2.16: **Kiteav chain.** **(a)** Blue boxes are fermionic sites c containing with each two Majorana sites. Majorana operators γ are paired neighboring operators in the same fermionic site. This corresponds to the limit where $\Delta = t = 0$ and $\mu < 0$. **(b)** The limit where $\Delta = t > 0$ and $\mu = 0$. Majorana operators are paired with operators from neighboring fermionic sites. This leaves two unpaired Majorana operators (orange), creating a non-local fermion.

The model consist of a linear chain of fermionic sites with annihilation and creation operators $c_j, c_j^\dagger$. The chain with N fermionic sites is described by the following Hamiltonian

$$H = -\mu \sum_{j=1}^{N} \left(c_j^\dagger c_j - \frac{1}{2} \right) + -t \sum_{j=1}^{N-1} \left(c_j^\dagger c_{j+1} + c_{j+1}^\dagger c_j \right) + \sum_{j=1}^{N-1} \left(\Delta c_j c_{j+1} + \Delta^* c_{j+1}^\dagger c_j^\dagger \right), \tag{2.71}$$

with μ the chemical potential, t the hopping amplitude and superconducting gap Δ. Note that the Hamiltonian does not contain any spin parameters, meaning that we assume p-wave superconductivity. Figure 2.16 shows a depiction of a Kitaev chain with N sites in two limits. Next, we introduce Majorana operators

$$\gamma_{2j-1} = c_j + c_j^\dagger, \qquad \gamma_{2j} = \frac{c_j - c_j^\dagger}{i}. \tag{2.72}$$

We can now rewrite equation 2.71 with these operators and investigate two limits highlighting the special properties of this model.

In the limit where $\Delta = t = 0$ and $\mu < 0$

$$H = -\mu \sum_{j=1}^{N} \left(c_j^\dagger a_j - \frac{1}{2} \right) = \frac{-i\mu}{2} \sum_{j=1}^{N} \gamma_{2j-1}\gamma_{2j}. \tag{2.73}$$

This is a topologically trivial phase, the Majorana operators pair with each other on the same fermionic sites. There is a unique ground state which has zero electrons, since $\mu < 0$, and an even parity. Excitations from this ground state correspond to adding an electron with energy $|\mu|$. This situation is schematically shown in Figure 2.16a.

A different – more interesting limit is where $\Delta = t > 0$ and $\mu = 0$. The Hamiltonian in that case becomes

$$H = it \sum_{j}^{N-1} \gamma_{2j}\gamma_{2j+1}. \tag{2.74}$$

Note that now Majoranas from neighboring fermionic sites pair up, instead of in the same site. Also, the first and last Majorana from the chain do not appear in this Hamiltonian (see Figure 2.16. We can rewrite Equation 2.74 by defining new fermionic operators which pair Majoranas from neighboring sites

$$\tilde{c}_j = \frac{1}{2}(\gamma_{2j} + i\gamma_{2j+1}), \qquad \tilde{c}_j^\dagger = \frac{1}{2}(\gamma_{2j} - i\gamma_{2j+1}) \tag{2.75}$$

leading to

$$H = 2t \sum_{j=1}^{N-1} \tilde{c}_j^\dagger \tilde{c}_j. \tag{2.76}$$

Since the unpaired Majorana states do not appear in the Hamiltonian, their excitation energy is zero. This results in a zero-energy state in the density of states of the system, in contrast with conventional s-wave superconductors which have a completely gapped excitation spectrum below $|\Delta|$.

Let us define two new operators for the non-local fermions

$$\tilde{c}_0 = \frac{1}{2}(\gamma_1 + i\gamma_{2N}), \qquad \tilde{c}_0^\dagger = \frac{1}{2}(\gamma_1 - i\gamma_{2N}) \tag{2.77}$$

Using these operators we define a ground state $|0\rangle$ with zero occupancy that satisfies $\tilde{c}_0 |0\rangle = 0$. We can add one non-local fermion $\tilde{c}_0^\dagger |0\rangle = |1\rangle$, which will have the same energy due to zero energy cost of the operations. As a result the system has a two-fold degenerate ground state, characterizing the system as topological. The states are orthogonal and have a different parity. We can verify this with the parity operator

$$-i\gamma_1\gamma_{2N}. \tag{2.78}$$

The conditions that we have set above can be relaxed to $2t > |\mu|, \Delta \neq 0$, when we consider a chain of infinite length $l \to \infty$. In a realistic situation we can add an interaction term to the Hamiltonian to describe coupling between the Majorana end modes:

$$H_{\text{eff}} = \frac{i}{2} t_0 \gamma_1 \gamma_N, \tag{2.79}$$

where $t_0 \propto e^{-l/\xi}$, with Majorana localization length $\xi = \hbar v_{\text{F}}/\Delta$, with v_{F} the Fermi velocity. Due the exponentially decaying interaction strength, the ground-state degeneracy is maintained for a sufficiently long chain.

2.6.2. FRACTIONAL AC JOSEPHSON EFFECT

Apart from the zero-energy state in the excitation spectrum, another key signature of Majorana states is the fractional ac Josephson effect that arises in a Josephson junction with topological superconducting leads. In such a junction (see Figure 2.17), the unpaired fermionic sites at the ends of the topological superconducting leads give rise to a Majorana bound state (MBS). The energy of this states has a 4π periodicity as a function of phase, instead of 2π for regular ABS.

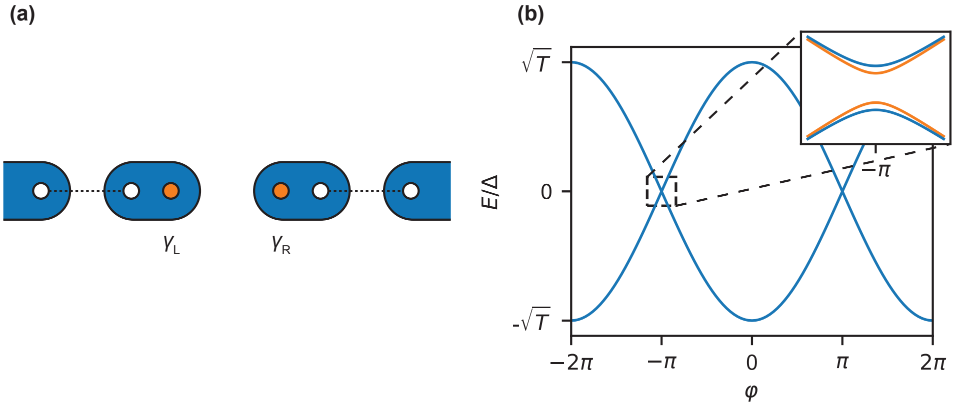

Figure 2.17: Topological Josephson junction. **(a)** Two Kiteav chains forming a Josephson junction. The Majorana states are shown in orange. **(b)** Energy spectrum of MBS as function of phase. The inset shows an avoided crossing at $\varphi = n\pi$ arising from the finite-length of the Kitaev chains.

To see how this comes about we include the, previously ignored, phases of the superconducting leads in our definition of the Majorana operators in the junction

$$\gamma_{\text{L}} = c_0^\dagger e^{i\phi_{\text{L}}/2} + c_0 e^{-i\phi_{\text{L}}/2}, \qquad \gamma_{\text{R}} = i\left(c_0^\dagger e^{-i\phi_{\text{L}}/2} + c_0 e^{i\phi_{\text{L}}/2}\right), \tag{2.80}$$

where $\phi_{\mathrm{L,R}}$ are the phases of the left and right superconductors. Combined, these states form a fermion. We can determine the occupation by writing out the number operator

$$n_0 = c_0^\dagger c_0 = \frac{1}{2}\left(1 + i\gamma_{\mathrm{L}}\gamma_{\mathrm{R}}\right) = \frac{1}{2}\left(1 - e^{i\varphi/2}\right) + c_0^\dagger c_0 \cos\frac{\varphi}{2}, \tag{2.81}$$

where $\varphi = \phi_{\mathrm{R}} - \phi_{\mathrm{L}}$. Note that when the phase is advanced by 2π, the parity of the system is changed $n_0 = 1 - c_0^\dagger c_0$. Since parity is a conserved quantity in this system, the system will wind another 2π to restore the original parity. This effectively makes the Josephson current 4π periodic [9].

The energy states of the MBS is plotted in Figure 2.17b and is given by [76, 77]:

$$E_0 = \pm\Delta\sqrt{T}\cos\frac{\varphi}{2}. \tag{2.82}$$

Note that unlike ABS, the MBS are detached from the continuum for non-ideal transmission $T < 1$ and the maximum energy is given by $\sqrt{T}$. The Josephson current is obtained by differentiating the energy with respect to phase

$$I_{\mathrm{S}} = \frac{2e}{\hbar}\frac{\mathrm{d}E}{\mathrm{d}\varphi} = \Delta\sqrt{T}\frac{e}{\hbar}\sin\frac{\varphi}{2}. \tag{2.83}$$

Apart from the 4π periodicity in the current-phase relation, the current scales with $\sqrt{T}$ (assuming $T \ll 1$) in contrast to $I \propto T$ for ABS.

In a realistic setup we have to consider the interaction term from Equation 2.79, due to the coupling of Majoranas at the other ends of the two chains. This results in an avoided crossing around $E = 0$ in the energy spectrum (inset of Figure 2.17b) and makes the junction effectively 2π periodic. It turns out however, that when the junction is voltage biased such that the phase evolves fast enough, so-called Landau-Zener tunnel processes restore 4π periodicity [78, 79].

2.6.3. PHYSICAL REALIZATIONS

Due to a lack of readily available spin-less superconductors, the Kiteav chain seems non-physical. Their are however proposals to realize Majorana states in a physical system. We will discuss two approaches in this section. Perhaps the most straightforward approach coming from the Kitaev chain, is to use a linear array of quantum dots as fermionic sites. This does leave us with the issue of spin-less superconductivity. It turns out that this can be resolved with a combination of spin-orbit interaction and an external magnetic field [13, 14, 80].

Consider the linear array of quantum dots in Figure 2.18. Each quantum dot is coupled to a superconductor that induces an s-wave pairing $\Delta_{\mathrm{ind},n}$ in dot n, the dots have tunable couplings t_n between neighboring dots. The dots are made of a semiconductor material with a strong spin-orbit interaction. Spin-orbit interaction describes the coupling between the spin and momentum of an electron and creates an effective magnetic field. When the spin propagates, its spin precesses around that field (schematically depicted in the left dot of Figure 2.18). This allows for a spin-less p-wave pairing between electrons in neighboring dots. The length along which the spin makes a 180° rotation is

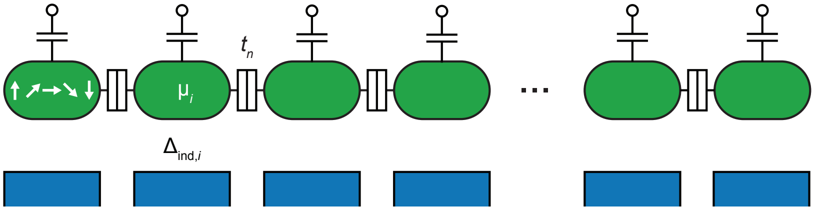

Figure 2.18: **Kiteav chain realized in a quantum dot array.** Quantum dots are depicted by green boxes with capacitively coupled plunger gates to tune electrochemical potentials μ_n. The quantum dots are single orbital and are coupled superconductors that induce an s-wave pairing $\Delta_{\text{ind},n}$. The dots are coupled to their neighbors with coupling strength t_n. Spin-orbit coupling precesses over a length l_{SO} to achieve spin-less coupling.

given by $l_{\text{SO}} = \hbar/(2m^*\alpha)$, with m^* the effective mass of the electron and α the Rashba spin-orbit strength [81].

The quantum dots are assumed to have a large level spacing such that we only to consider a single level and that it is the largest energy scale in the Hamiltonian. An external magnetic field lifts the spin degeneracy of the quantum dot levels and in combination with the spin-orbit interaction we have effectively created a spin-less chain. Here we have assumed that the dimensions of the quantum dot perpendicular to the wire length, are much smaller than the dimension along the wire $l_{y,\text{DQ}}, l_{z,\text{DQ}} \ll l_{x,\text{DQ}}$. This assures that spin-orbit direction is the same for each quantum dot and we can apply a single, global external magnetic field [13]. The spin-orbit strength should be such that $l_{\text{SO}} < l_{x,\text{DQ}}$ in order to get superconducting pairing. We have created a system equivalent to the Hamiltonian in Equation 2.76 when we tune the parameters such that

$$\epsilon_n = \sqrt{\epsilon_{\text{Z}}^2 - \Delta_{\text{ind},n}}, \tag{2.84}$$

where ϵ_{Z} is the Zeeman energy.

Another option is to use a semiconductor nanowire, also with induced superconductivity, but without quantum dots. This proposal was introduced by Lutchyn *et al.* [82] and Oreg *et al.* [83] and is the most widely used model for investigating Majorana states in condensed matter systems. The model comprises of a quasi-one-dimensional nanowire with strong spin-orbit interaction and a large Landé g-factor. The wire is coupled to a superconductor that induces superconductivity in the semiconductor material through the proximity effect. An in-depth description can be found in References [84–86].

We assume a system with a single subband and with the following Hamiltonian:

$$H_{\text{BdG}} = \left(\frac{p_x^2}{2m^*} - \mu\right)\tau_z + \frac{\alpha}{\hbar} p_x \sigma_y \tau_z + \frac{g}{2}\mu_{\text{B}} B_x \sigma_x + \Delta\tau_x, \tag{2.85}$$

where we use the BdG formalism with the Nambu spinor basis Ψ:

$$H = \int \mathrm{d}x \Psi^\dagger H_{\text{BdG}} \Psi, \qquad \Psi = \left(c_\uparrow, c_\downarrow, c_\downarrow^\dagger, -c_\uparrow^\dagger\right). \tag{2.86}$$

The first term in H_{BdG} is a kinetic energy term and describes a one-dimensional conductor with effective m^*, chemical potential μ and momentum p_x confined to the x-direction in a Cartesian coordinate system, τ_z is a Pauli matrix acting on particle-hole space. The second term describes a Rashba-type spin-orbit interaction with interaction strength α, σ_y is a Pauli matrix acting on the spin degree of freedom. The spin-orbit interaction term gives rise to an effective magnetic field B_{SO}. If we assume an electric field along the z-direction [6], B_{SO} is oriented in the y direction, perpendicular to the axis of the nanowire. The third term accounts for an external magnetic field B_x along the length of the wire, with μ_{B} the Bohr magneton. The last term adds superconductivity with pairing potential Δ. The eigenenergies of the Hamiltonian can be found to be

$$E = \left(\epsilon_k^2 + \epsilon_{\mathrm{SO}}2 + \epsilon_B^2\Delta^2 \pm 2\sqrt{\epsilon_k^2\left(\epsilon_{\mathrm{SO}}^2 + \epsilon_B^2\right) + \epsilon_{\mathrm{Z}}^2\Delta^2}\right)^{\frac{1}{2}}, \tag{2.87}$$

where $\epsilon_k = \hbar^2 k^2/(2m^*) - \mu$, $\epsilon_{\mathrm{SO}} = \alpha k$ and $\epsilon_{\mathrm{Z}} = 1/2 g\mu_{\mathrm{B}} B_x$.

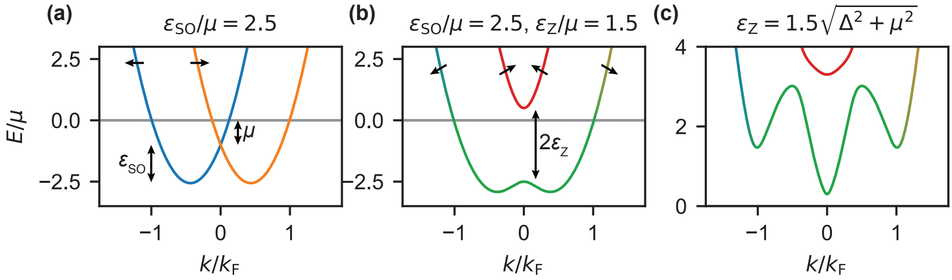

Figure 2.19: **Nanowire band structure evolution.** **(a)** Spin-orbit interaction shifts the bands along the momentum axis by $2k_{\mathrm{SO}}$. The arrows and colors denote the spin direction of each band; ← blue, → orange. The parabolic bands are shifted also down along the energy axis by an amount $\epsilon_{\mathrm{S})} = m^*\alpha^2/(2\hbar^2)$. **(b)** An external magnetic field creates a helical gap. When $|\mu| < |\epsilon_{\mathrm{Z}}|$ transport electrons only cross a single subband making them effectively spinless. The color gradients indicates the gradual spin rotation along the momentum axis. **(c)** Adding superconductivity makes the wire topological, with inverted bands.

It is instructive to add each ingredient separately, to see how they affect the bandstructure of the nanowire (Figure 2.19). Spin-orbit interaction splits the otherwise spin-degenerate conduction band and gives rise to the effective magnetic field. The spins are projected in the direction of the B_{SO}. The parabolas are shifted along the k-axis by $\pm k_{\mathrm{SO}} = \pm m^*\alpha/\hbar^2$ (Figure 2.19a). Note that this does not completely lift the spin degeneracy. When the magnetic field along the x-axis is turned on, the bands are split in along the energy axis and completely lifts the spin degeneracy (Figure 2.19b). It opens up a gap in the spectrum of size ϵ_{Z}, called the helical gap. The spins are rotated towards the magnetic field axis by a momentum-dependent amount. Around $k = 0$ the spins are completely aligned with the magnetic field since here the spin-orbit field is zero. Toward higher momentum the spins gradually rotate towards the spin-orbit field axis.

Note that if the chemical potential μ lies within the helical gap, electrons with opposite momentum see the same spin subband. And so electrons can pair with the same spin, making spin-less superconductivity a possibility. By now proximitizing the nanowire with s-wave superconductivity (Figure 2.19c), we have created topological superconducting wire with is accompanied with Majorana states at the ends of the wire.

---

[6] This is a reasonable assumption if the nanowire lies flat on a substrate.

In an experimental setting, the ingredients are usually added in a different order. All but magnetic field are present from the start and magnetic field is gradually increased until the topological phase transition is reached. To illustrate this we plot the band structure for four different Zeeman energies in Figure 2.20. At $\epsilon_Z = 0$ the induced superconductivity opens a gap in the spectrum. We keep track of two different gaps, Δ_0 and Δ_F situated at $k = 0$ and $k = k_F$ respectively. Due to spin-orbit interaction, both gaps behave different in magnetic field. At $k = 0$, where spin-orbit strength is zero, the gap decreases linearly with B_x, $\Delta_0 = \sqrt{\mu^2 + \Delta^2} - \epsilon_Z$. Δ_0 is completely closed when $\epsilon_B = \sqrt{\mu^2 + \Delta^2}$ (Figure 2.20c) and reopens (with a negative sign) when B_x is further increased (Figure 2.20d). This is the topological phase transition. The gap Δ_F hardly changes in field due to the strong spin-orbit field.

Both approaches use a clever combination of spin-orbit interaction and external magnetic field to engineer spin-less superconductivity. Although a linear quantum dot array is conceptually closer to the Kitaev chain model, the nanowire approach is easier to realize in an experimental setting and most experimental signatures of Majoranas have been obtained with this approach in InAs or InSb nanowires [87, 88].

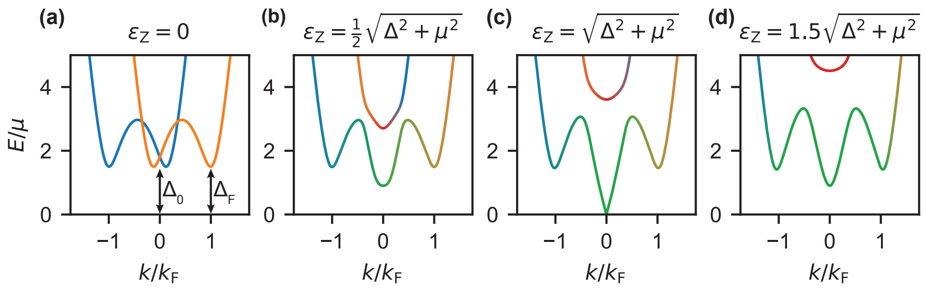

Figure 2.20: **Band structure evolution with increasing magnetic field.** **(a)** No external magnetic field. Spin split by spin-orbit interaction and gapped by superconductivity. Due to the momentum dependence of the spin-orbit interaction we keep track of two gaps Δ_0 and Δ_F. **(b)** Magnetic field turned on but below the topological transition decreases Δ_0. **(c)** At the phase transition, $\Delta_0 = 0$ while Δ_F remains almost unchanged. **(d)** The gap at $k = 0$ reopens, but $\Delta_0 < 0$. The system is now in the topological regime.

3

METHODS

The way you make an omelet reveals your character.

Anthony Bourdain

In this chapter we summarize the most important materials and fabrication techniques that are used to make the devices for the experimental chapters. Next, we discuss important details of the used measurement setup and novel superconducting interconnects.

3.1. FABRICATION

All devices in this thesis are build with Si wafer coupons as a substrate. A detailed list of all fabrication steps can be found in Appendix A.

3.1.1. NANOWIRE GROWTH AND TRANSFER

InAs-Al core-shell nanowires are at the heart of the experiments presented in this thesis. They are grown by the groups of Jesper Nygård and Peter Krogstrup using a vapor-liquid-solid method in a molecular beam epitaxy (MBE) system with an axial (0001)B wurtzite orientation [89]. The wires grow vertically on a substrate, underneath Au catalyst droplets. After growth, Al is deposited *in situ* on two or three facets using directional evaporation. The Al layer induces superconductivity in the InAs. Typical wire lengths are between 5 and 10 µm with a diameter between 60 and 100 nm. The Al layer is between 5 and 10 nm thick, providing a large critical magnetic field. Growing Al directly on the InAs without breaking the vacuum of the MBE chamber allows for a clean interface between the materials, which is crucial for inducing a hard superconducting gap in the wire and has enabled great advancements in the field of superconducting nanowires [90, 91].

Individual nanowires are manually transferred from the growth chip to a Si substrate with lithography alignment markers, shown in Figure 3.2a, using a W needle attached to a micromanipulator under an optical microscope. The wires stand up vertically on the growth chip, like trees in a forest, and are visible through the microscope as small dots. By varying the focal plane of the microscope one can estimate the vertical position of the needle with respect to the nanowires. By carefully brushing the needle past the vertical wire, the wire breaks off at its base and sticks to the needle with van der Waals forces. Next, the wire can be deposited on the Si substrate by brushing the needle with attached nanowire over the surface. The transfer from the needle tip to the substrate is possible because the contact surface area between the wire and the substrate is much larger then between the needle and the wire, resulting in a stronger van der Waals force to the substrate. A in-depth explanation with illustrations can be found in references [92, 93].

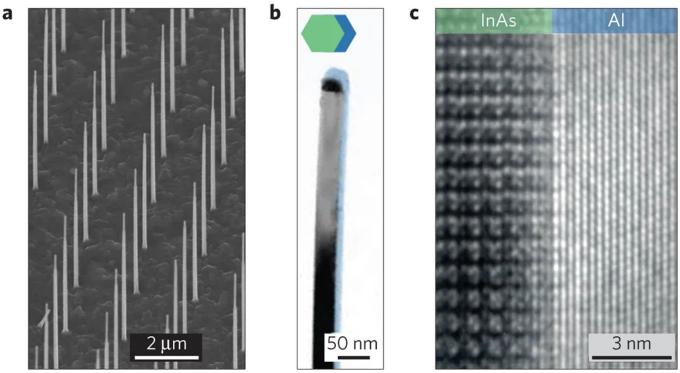

Figure 3.1: **a** Scanning electron micrograph (SEM) of a nanowire 'forest' on an InAs (111)B substrate. **b** Transmission electron micrograph (TEM) of the top part of a wire, the Al shell is marked in blue. **c** TEM highlighting the sharp and clean interface between InAs core wire and the Al shell. Figure adapted from [89].

3.1.2. SELECTIVE ALUMINUM ETCHING

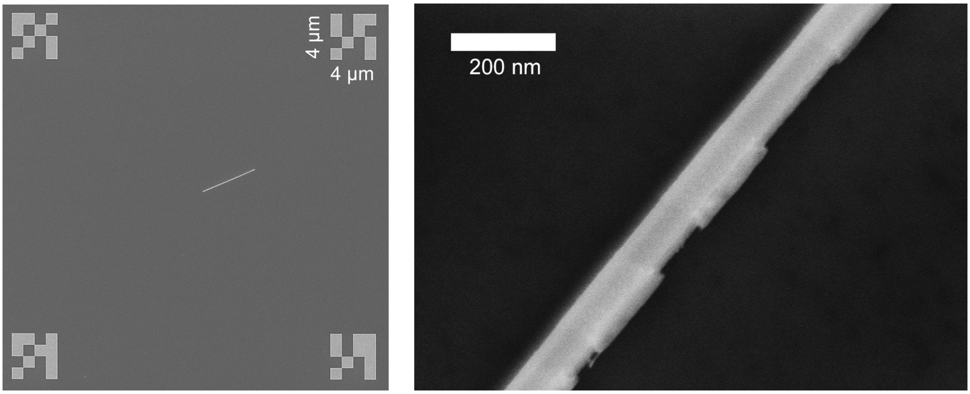

Figure 3.2: Left panel shows an SEM of a deposited InAs nanowire between unique lithography markers on a Si substrate. Each of the four marker images cover a 4 by 4 µm square. Right panel shows an SEM of selectively etched Al sections. Etch windows were designed to be 50 nm, 100 nm and 200 nm in width. The measured widths of bare InAs after etching are 63 nm, 119 nm and 219 nm respectively.

The Al shell covers the entire length of the nanowire and so to make a junction, part of this shell has to be removed. Selectively etching part of the Al is commonly done with a commercial product named Transene-D, originally developed to be selective against GaAs, Ga or GaP [94]. The process involves heating the solution to 48.2 °C submerging the wire in the solution for a period of 12 s for shell thickness on the order of 10 nm. This method is prone to over or under etching due to the short time window and the sensitivity to temperature. This is problematic since Transene-D is known to be not entirely selective against InAs and cause damage [95]. As an alternative, we use a solution with diluted Tetramethylammonium hydroxide (TMAH, 2.14% by weight) in the form of a photo developer (MF-321). TMAH has a better selectivity against InAs, can be used at room temperature and has a slower etch rate. This makes the process simpler, since we do not require heating the solution, and the longer etch time is more forgiving on timing errors. Figure 3.2b shows three junctions etched using the MF-321 etchant. The designed windows were 50, 100 and 200 nm, with resulting junction lengths 63, 119 and 219 nm respectively. Compared to the Transene-D process, the MF-321 does tend to leave more AlO_x residues as can be seen in the smallest junction in Figure 3.2b.

We cover the substrate with a thin layer (~ 200 nm) of PMMA (polymethyl methacrylate) and subsequently open a window with e-beam lithography, exposing a small part of the nanowire to the etchant. We then chemically etch the Al in those windows by submerging the chip in the etch solution. To avoid creeping of the etchant, the Si substrate with nanowire is baked on a hotplate at 175 °C for 1 min to remove moisture from the surface and improve resist adhesion. Directly after baking, a layer of PMMA is spin coated on the chip and subsequently baked at 175 °C for 5 min. After electron beam exposure, the PMMA is developed for 60 s in a solution of H_2O/IPA (1:3 ratio by volume) and dried directly with N_2. The chip is then submerged in MF-321 for 55 s without agitation, followed by a thorough H_2O rinse. The resist is stripped in heated acetone.

The use of H_2O/IPA as a developer for PMMA is relatively uncommon but has some key advantages over the traditional MIBK/IPA solution. The contrast of the PMMA for a 1:3 solution of H_2O/IPA is between 6.3 and 7 compared to 5.4 for the standard MIBK/IPA 1:3 solution. After developing, the sample can be dried directly with N_2 without the need for a rinsing step [96, 97]. Finally, a pre-mixed solution of H_2O/IPA is shelf stable at 7 °C for at least six months, unlike pre-mixed MIBK/IPA solutions which are known to produce unreliable results after being stored for a few weeks. Note that the contrast depends on the ratio of H_2O/IPA and on the rinsing method: directly drying with N_2 results in a higher contrast compared to rinsing in IPA. Additionally, H_2O/ethanol solution are reported to yield even higher contrasts of up to 10 [96, 97].

3.1.3. NANOWIRE CONTACTS

After selectively removing the Al to form junctions, the nanowire needs contacts in order to perform transport measurements. The native oxide of the InAs and the Al shell prevents ohmic contacts. We therefore use *in situ* argon milling to remove both oxides before depositing the contact metal. In the case of the SQUID devices, the superconducting material NbTiN is deposited by DC sputtering. It is important to note that the contacts are placed at least 1 µm away from the junctions. The argon milling process physically removes atoms from the surface and leaves a relative rough surface. This will negatively influence the induced superconductivity and result in a soft gap [98].

3.1.4. CONFORMAL TOP GATES

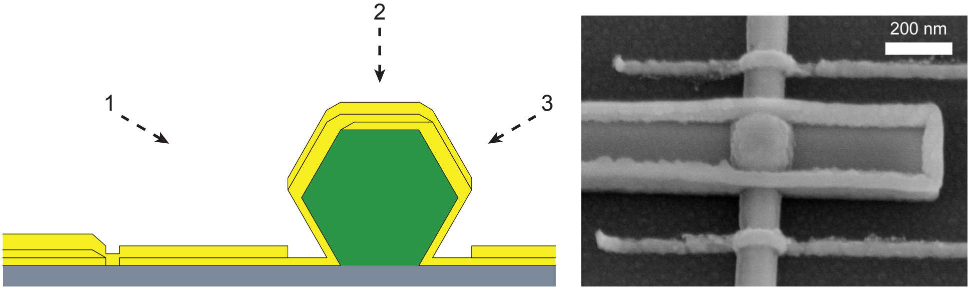

Figure 3.3: Left panel shows a schematic representation of the gate evaporation process from a cross-section point of view with the nanowire shown in green. The right panel shows an SEM of two gates made using this approach. In between the gates is a piece of NbTiN that is unrelated.

To create quantum dots, electrostatic gates are used to locally deplete the nanowire. In this thesis we use full wrap-around gates with a 10 nm AlO_x dielectric in between, deposited using atomic layer deposition (ALD). It was found that AlO_x deposited through ALD is an excellent gate dielectric for InAs: low hysteresis and higher electron mobility compared to SiN [94, 99]. The conformal coverage of AlO_x also protects the nanowire from further degradation in air.

The gate pattern design for the double quantum dot (DQD) devices consists of five parallel gates, each with a width of 40 nm and a pitch of 80 nm – covering a nanowire section (see Chapter 6). Regular evaporation at a 90° angle to the substrate would require the gate metal to have a height of approximately 140 nm to ensure a continuity over the wire. On top of that, the hexagonal shape of the nanowire creates shadows underneath the edges, weakening part of the of gate. This height results in a high aspect ratio of 3.5 that is difficult to obtain with a PMMA resist since they will almost certainly fall over during processing.

Instead, we evaporate the gate metal (Ti/Au) under an angle to achieve a continuous line with a thin layer. Figure 3.3a shows a schematic representation of the evaporation procedure. The first layer is evaporated under a 30° angle with respect to the substrate. This step is repeated, but mirrored with respect to the wire. To ensure a fully continuous gate line, we finish with a layer from a 90° angle. A 50 nm thick layer is now enough for a reliable gate with a resist layer with a thickness of approximately 150 nm. Figure 3.3b shows an SEM of two gates made in this fashion. Due to the 30° angle, some metal is also evaporated on the walls of the resist. To minimize lift-off issues, the sample is aligned to angled along the length of the gate lines, this way only a 40 nm wide vertical wall is evaporated onto the resist wall, which easily tears of during lift off. The remaining vertical metal can be seen at the end of the gates in figure 3.3b.

The resulting gates typically have a lever arm between 0.1 and 0.5. Gate hysteresis is very low and almost negligible (see Figure 3.4a). Note that in order that in order to achieve this low level of hysteresis, any handling with electrical discharge, such as SEM imaging or dicing was avoided after deposition of the dielectric [94].

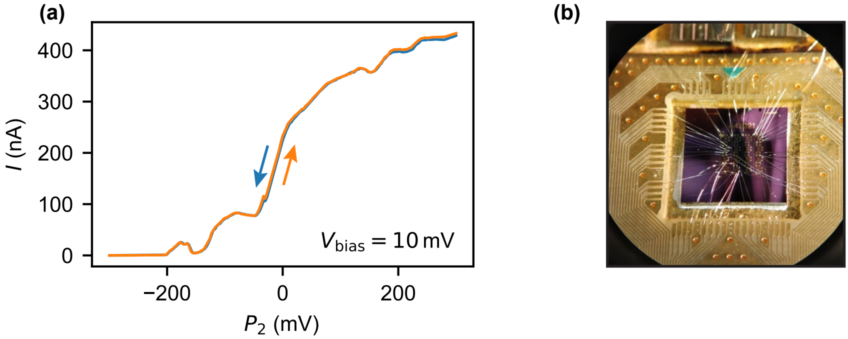

Figure 3.4: **(a)** Pinch-off (blue) and pinch-on (orange) curve of a plunger topgate P_2 for a quantum dot. Note the low hysteresis. **(b)** A finished device chip, mounted and wirebonded to a PCB.

3.1.5. POST PROCESSING

After cleanroom fabrication, the device is visually inspected under an optical microscope and electrically with probe needles. The electrical inspection aims to select the most promising devices on a chip to be measured. The 48 electrical lines limits the number of devices that can be measured in a single cool down. The chip is glued with a conductive silver paint to the cold finger of a dilution refrigerator and the on-chip devices are electrically connected to a PCB with AlSi wedgebonds (see Figure 3.4b). The PCB is connected to the electrical lines in a dilution refrigerator.

3.2. CRYOGENIC TRANSPORT MEASUREMENTS

The transport data presented in this thesis is acquired in Leiden Cryogenics cryogen-free dilution refrigerators with base temperatures between 20 and 40 mK [1], depending on the instance. Figure 3.7a shows the different cooling stages.

At room temperature we use a battery-powered, galvanically isolated electronic measurement system known as the IVVI rack [2]. This system is designed and build in-house and is build up of interchangeable modules housed in an enclosure suitable for mounting in a 19 inch rack (figure 3.5b). The system is designed and maintained by Raymond Schouten and meant for low-noise cryogenic electrical measurements. The main components are 16 bit digital-to-analog converters (DACs) that can supply an output voltage with a range of 4 V. They are digitally controllable through a fiber-optic interface for galvanic isolation. The rack has isolated input and output ports with low-pass filters, that can be connected to commercial equipment for external readout and readout, respectively. Typically these are arbitrary waveform generators (AWG), lock-in amplifiers, oscilloscopes and digital multimeters (DMMs). Common modules used in this thesis include a voltage (V), current (I) source and voltage, current measure modules.

Figure 3.5: **(a)** Photograph of a matrix module with 48 separate channels. Each channel has a toggle switch to ground, float or connect the line. **(b)** Photograph of a full IVVI rack. The S0 module (far left position) contains isolated input ports, next to that are S3b modules for voltage/current bias, M2b and M1h are voltage and current measure modules respectively.

Accompanying the IVVI rack is a matrix module, used in a way similar to an old-

---

[1] See https://leiden-cryogenics.com/products/cryogen-free/cf-cs50 for more information.

[2] More information can be found on http://qtwork.tudelft.nl/ schouten.

fashioned telephone switchboard: it allows the operator to route lines to the device through modules or DACs (Fig. 3.5a). From the matrix module, the lines go into the dilution refrigerator and pass through several passive low-pass filters before reaching the sample (see Figure 3.6b).

The first is a π-filter at room temperature, attached to the back of the matrix module that starts attenuating at 1-10 MHz. Made from a π configuration of capacitors and an inductor, mounted in a feedthrough construction with a metal enclosure to enable filtering up to 10 GHz. The output of the filter is connected to fridge lines via a 24-pin fisher cable with shielded twisted pair lines. Figure 3.6 shows the approximate attenuation ranges of the filters and a schematic layout of the measurement setup arrangement.

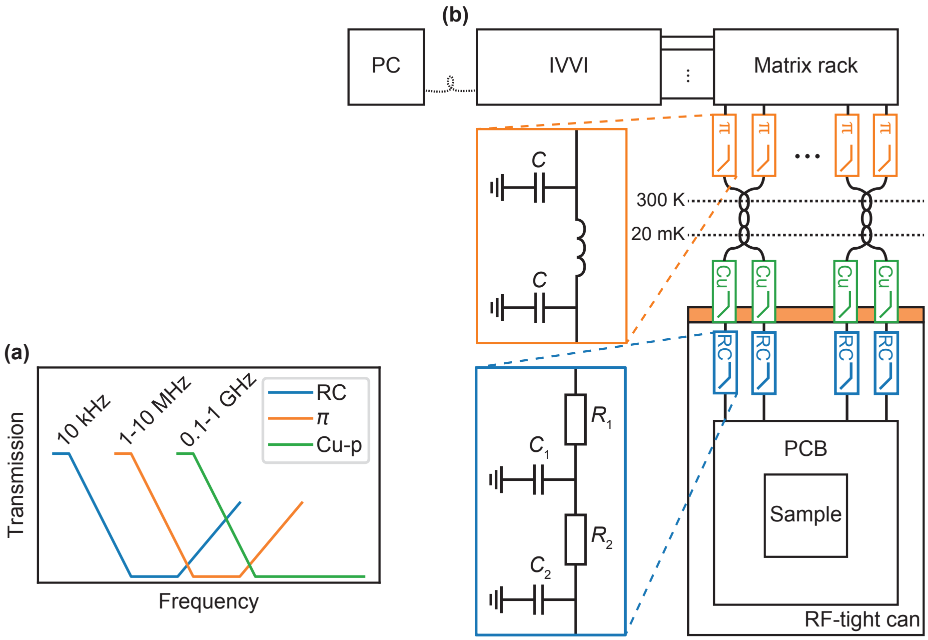

Figure 3.6: **Filter electronics (a)** Attenuation range of the different filters that used. **(b)** Schematic overview of the filtering. Enclosed in orange, the effective circuit diagram of the π filters, with $C \approx 1.5\,\text{nF}$. Enclosed in blue, second order RC filters, with $R_1 = 510\,\Omega$, $C_1 = 10\,\text{nF}$, $R_2 = 2\,\text{k}\Omega$, $C_2 = 220\,\text{pF}$.

Inside the fridge, the twisted pairs continue down to the mixing chamber stage, where the lines go through Cu-powder filters. Here, the lines are on a printed circuit board (PCB) – immersed in an epoxy with suspended Cu particles. The Cu powder acts as a lossy dielectric for high-frequency signals starting at a few GHz [100, 101]. To keep the signals clean after this filtering stage, the Cu-powder filters are directly attached to the entrance of an RF-tight Cu can. Inside the can, the lines are filtered one final time by second-order *RC* filters with an attenuation elbow around 10 kHz. Throughout the dilution fridge, other measures have been taken to keep the electron temperature by adding radiation absorbing paint and broadband microwave absorbing materials [102].

3.2.1. SUPERCONDUCTING INTERCONNECTS

Running large currents, up to several tens of milliampere, through on and off-chip resistive lines generates heat which is usually detrimental to the base temperature of a dilution refrigerator as the generated heat is more than the cooling power of the fridge – warming up the mixing chamber significantly. For a magnet coil one can get around this by using superconducting wires, thus removing the resistance of the lines and eliminating the heating. But for large on-chip currents the interconnects and filters between the fridge lines and the chip, have to be continuously superconducting as well. On-chip currents are commonly used to create local magnetic fields. For example in the Transmon community, where a SQUID is used for a tunable Josephson energy for each qubit [29]. It is known that this warms up the fridge but not to an amount to become a limiting factor. For this thesis, the use case will be an on-chip spectroscopy device, which we discuss in the outlook chapter 8. It uses multiple SQUID loops that need independent flux biasing with currents of up to 5 mA, too high for acceptable base temperatures when using resistive lines.

With the approach described in this section, we introduce superconducting interconnects that reach currents up to 45 mA without any measurable heating of the fridge base temperature. The system is built into a removable probe that is hosted in a CF-1400 Leiden cryogenics dilution refrigerator and provides four superconducting lines used to control two flux bias lines [3].

A schematic drawing of the setup is shown is figure 3.7a. At room temperature, normal resistive cables enter the fridge via coaxial feedthrough connections. The lines go through the lower pulse tube plate and are soldered to a tagboard on the still plate, most of the heat generated by these normal lines will be dissipated here. We estimate a power of a few milliwatt based on the resistance of these normal lines, well within the cooling power of the fridge at this stage. On the other side of the tagboard, NbTi cables in a CuNi matrix are soldered. From here on, the NbTi lines are continuous all the way down interconnect at the mixing chamber plate.

The NbTi lines are twisted pairs and at each temperature stage wound around a Cu pole, thermally anchored to the stage. This achieves two goals: it thermalizes the lines at every stage to keep them below their critical temperature of approximately 10 K and it acts as a low-pass *LC* filter. At the mixing chamber stage the lines go trough a Cu-powder filter and pass through an RF-tight can where the chip resides. Here, the wires are soldered to specially coated Cu solder tabs. The solder consists of a superconducting tin/lead mixture and sits under a sputtered NbTiN film. Standard wedgebond AlSi bondwires with a 25 µm diameter, connect the tabs to the NbTiN lines on the chip. Figure 3.7b shows an image of an exemplary device with a superconducting line acting as a flux-bias line (highlighted in purple). In this particular design, a current of approximately 3 mA threads a single flux quantum through the SQUID loop, which allows for complete independent control using the superconducting lines at base temperature.

Figure 3.7c shows a photograph of the chip PCB with the superconducting tabs. A more detailed schematic side view is depicted in figure 3.7d. The Cu tabs sit on a thin layer of GE10 varnish, providing galvanic separation while still providing good thermal contact to the Cu chip carrier which is thermally anchored to the mixing chamber. On

---

[3] This system was developed together with Matthew Sarsby, Olaf Benningshof and Jason Mensingh

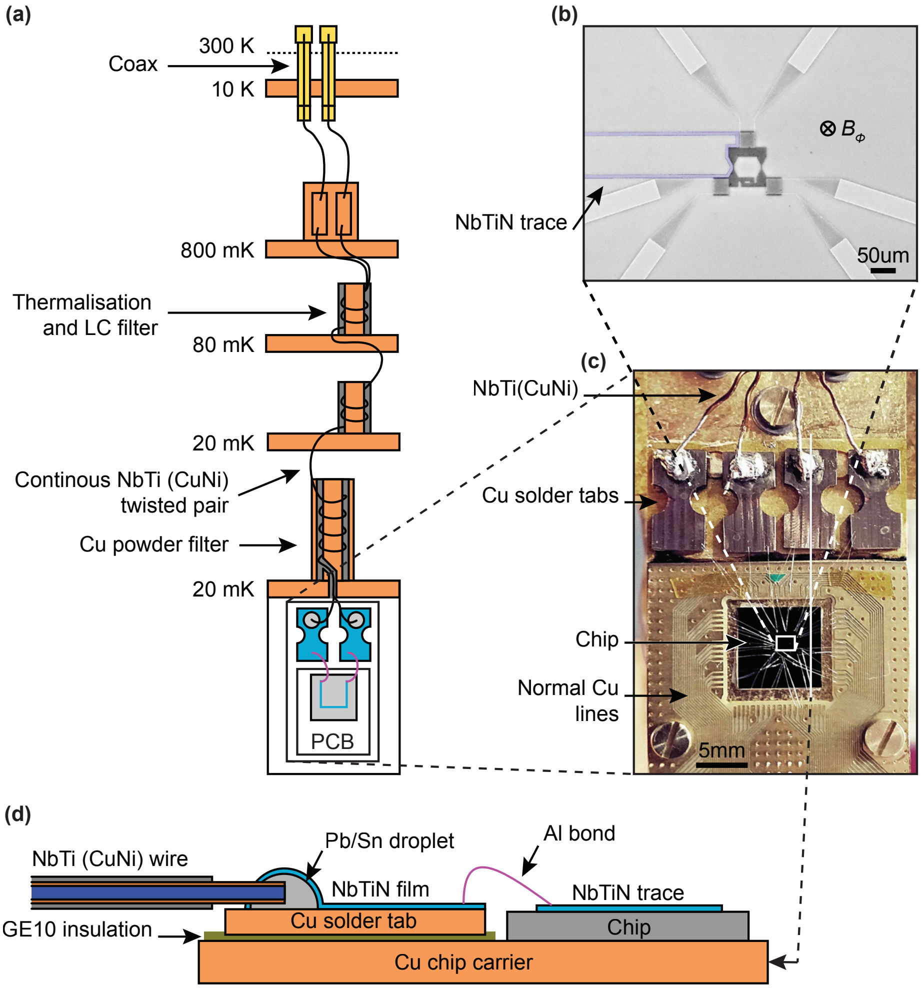

Figure 3.7: **Superconducting bias lines.** **(a)** Overview of the twisted-pair superconducting lines. The lines are thermalized and filtered at each stage of the dilution fridge and go inside the RF-tight can via a feed through. They are then connected to the chip via a superconducting solder tab. **(b)** Electron micrograph of a test device with a superconducting flux-bias line highlighted in purple. **(c)** Photograph of the chip carrier with solder tabs, PCB and chip. **(d)** Cross-sectional view of the superconducting interconnect between the NbTi fridge wire and the NbTiN trace on the chip.

top of the tab, a droplet of solder is placed and the entire top side of the tab is then sputter coated with a 200 nm thick layer of NbTiN. The NbTi wire is attached by piercing through the NbTiN shell of the solder droplet and soldered in. Al bondwires then connect the tabs to the on-chip superconducting lines.

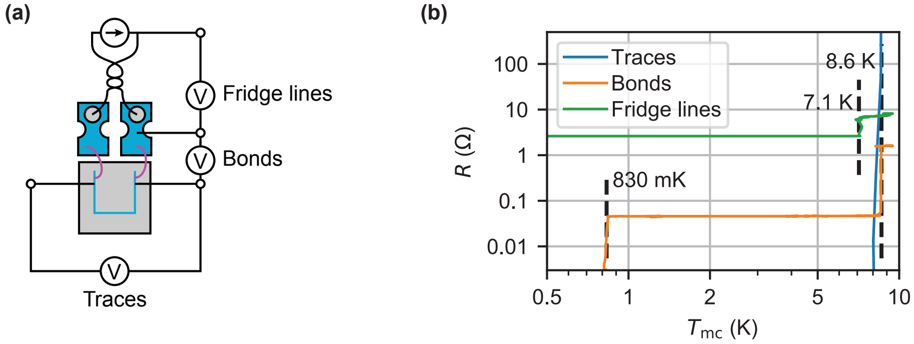

Figure 3.8: **Phase transitions of superconducting bias lines.** **(a)** Four-terminal probe setups for each section of the lines. **(b)** Line resistances of all sections as a function of temperature. Superconducting phase transitions are found of the NbTi wires, the AlSi bond wires and the on-chip NbTiN.

We qualitatively test the superconducting lines by performing a temperature sweep while measuring the resistance of each section of the lines through a four-terminal setup (figure 3.8a). A current bias is connected to one pair of superconducting lines and voltage probes are attached to measure the voltage drops over the fridge lines, bond wires and the on-chip traces. The results are plotted in figure 3.8b and show the superconducting phase transitions of each section. The thermometer is not well calibrated for this temperature range, evident from the systematically lower than the expected critical temperatures for the used materials. They do however still serve as qualitative indication. The bond wires (orange) are the first to turn normal, followed by the fridge lines (green) and finally the on-chip NbTiN traces (blue). Below the transition temperature, the fridge lines go to 2.6 Ω due to the normal lines between the still stage and room temperature (see figure 3.7a). This result shows that the superconducting interconnects are working between the tabs and the chip.

The temperature-dependent scan can not exclude resistive interconnects between the NbTi wires and the tabs via the solder droplet. To verify that this part is also superconducting, we run increasing currents through the lines while monitoring the temperature of the mixing chamber. When any part of the interconnects is resistive, the generated power will be dissipated to the mixing chamber, increase its temperature. We first turn on a magnetic field $B = 20\,\mathrm{mT}$ to quench the superconductivity in the bond wires, making them resistive with $R \approx 46\,\mathrm{m}\Omega$ (figure 3.8). We see that the temperature increases from below 20 mK without any current, to around 30 mK for a current of 20 mA. When we apply the same currents but with the bond wires superconducting by turning off the magnetic field, we find no measurable increase in the mixing chamber temperature. Implying that the interconnects are fully superconductive or resistive below 1 μΩ.

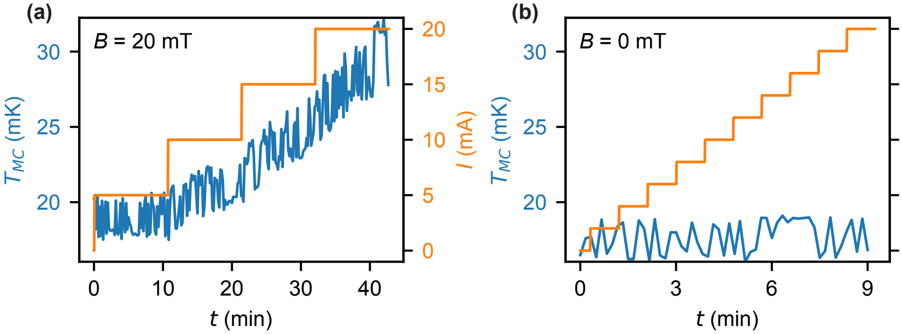

Figure 3.9: **Mixing chamber temperatures with current bias through continuous superconducting lines.** **(a)** With a magnetic field $B = 20\,\text{mT}$, turning the bondwires normal with a resistance of approximately $46\,\text{m}\Omega$. **(b)** Without magnetic field, no noticeable temperature increase.

3.2.2. MEASURING SWITCHING CURRENTS

Chapters 5, 6 and 7 rely on accurate supercurrent measurements. Although the critical current cannot be measured directly (see 2.3), we can measure the switching current I_{SW}. This experimentally obtainable value is always lower than the critical current due to thermal and noise activation.

Due to the stochastic nature of the switching current, between 20 and 100 measurements are taken to get a reliable value for a single data point. In order to keep to the measurement times practical, acquiring switching currents should be done fast. The approach used here is ramping a current bias I_{bias} with a saw-tooth waveform and recording I_{bias} at the point where the voltage V measured over the junction jumps from zero to a finite value. Figure 3.10a shows a schematic depiction of this protocol. The blue line is the I_{bias} signal and the orange line V. The dashed lines indicate a threshold value set for V, at these points I_{bias} is recorded.

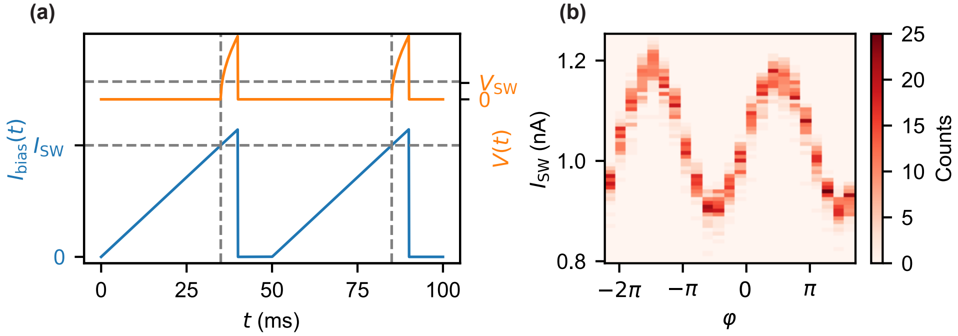

Figure 3.10: **Switching current experiment.** **(a)** Switching current protocol to obtain the switching currents. When the measured voltage (orange) reaches V_{SW} (horizontal dashed line), the current bias (blue) is recorded. **(b)** Histogram of an experimentally obtained switching currents of a current-phase relation. The color scale denotes the number of counts for a given current on the vertical axis as a function of the phase φ.

At the heart of this setup is the M3m IVVI module, it serves as interface between all the components. It monitors the four-probe voltage measured over the junction. When it reaches a set threshold value V_{SW}, the module sends the I_{bias} value to its output, connected to a DMM. At the same time the module sends an optical pulse through a fiber-optic cable to trigger the voltage readout of the DMM, this bias value is then saved as I_{SW}. The saw-tooth waveform is supplied by a Rigol DG4102 arbitrary waveform generator at a frequency of 20 Hz.

By repeating this protocol we acquire a collection of the switching currents, providing a lower limit of the critical current. We can fit the data to theoretical models and perform statistical analysis to extract properties of the supercurrent, such as amplitude and phase. Figure 3.10b shows a collection of histograms from a dataset of the current-phase relation of a nanowire SQUID with an SNS Josephson junction. The color-scale denotes the number of counts for a given switching current bin as a function of the phase over the SQUID.

It is important to be aware of the limitations of this method. Figure 3.11 shows benchmarking measurements for a range of current bias ramp frequencies. Due to the resistance and capacitors of the filters in the bias lines, the IV curve is deformed. The amount of deformation is determined by the ramping frequency. Figure 3.11a shows the curves for three different frequencies. Notice that the sharp vertical parts of curve become a gradual slope with increasing ramp frequency, additionally the entire curve shifts to the right. Both effects are caused by delays in the circuit that are more pronounced at higher frequencies. Apart from a constant offset, the gradual slope also results in a broader distribution of switching current – shown in Figure 3.11b, where the standard deviation σ is shown in the legend. On the other hand, slower ramping speeds makes the junction likelier to switch to the normal state earlier, resulting in a lower switching current on average. In the end a compromise has to be made. In this thesis we use ramping frequencies between 10 and 20 Hz where the IV curves show minimal deformation and the acquisition speed allows us to obtain enough samples within a practical time frame.

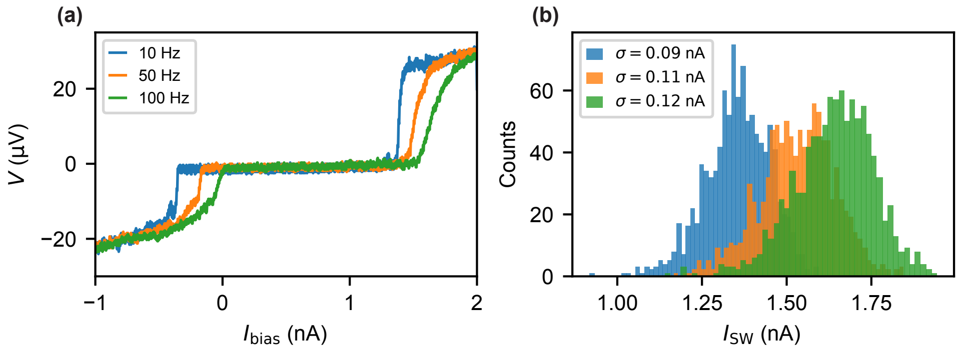

Figure 3.11: **Switching current benchmarks (a)** IV curves at current bias driving frequencies 10, 50 and 100 Hz. **(b)** Switching current distributions for the same driving frequencies as in **a**.

4

OBSERVATION OF THE 4π-PERIODIC JOSEPHSON EFFECT IN INDIUM ARSENIDE NANOWIRES

D. Laroche[†], **D. Bouman**[†], D. J. van Woerkom, A. Proutski, C. Murthy,
D .I. Pikulin, C. Nayak, R. J. J. van Gulik, J. Nygård, P. Krogstrup,
L. P. Kouwenhoven, A. Geresdi

Quantum computation by non-Abelian Majorana zero modes (MZMs) offers an approach to achieve fault tolerance by encoding quantum information in the non-local charge parity states of semiconductor nanowire networks in the topological superconductor regime. Thus far, experimental studies of MZMs chiefly relied on single electron tunneling measurements, which lead to the decoherence of the quantum information stored in the MZM. As a next step towards topological quantum computation, charge parity conserving experiments based on the Josephson effect are required, which can also help exclude suggested non-topological origins of the zero bias conductance anomaly. Here we report the direct measurement of the Josephson radiation frequency in indium arsenide (InAs) nanowires with epitaxial aluminium shells. We observe the 4π*-periodic Josephson effect above a magnetic field of* $\approx 200\,\mathrm{mT}$, *consistent with the estimated and measured topological phase transition of similar devices.*

This chapter has been published in Nature Communications 10.1 (2019): 1-7.

[†] These authors contributed equally to this work.

4.1. INTRODUCTION

The universal relation between the frequency f_J of the oscillating current and an applied DC voltage bias V across a superconducting weak link [103] is determined solely by natural constants:

$$\frac{f_\mathrm{J}}{V} = \frac{2e}{h} = \Phi_0^{-1} = 483.6\,\mathrm{MHz}\mu\mathrm{V}^{-1}, \tag{4.1}$$

where e is the single electron charge, h is the Planck constant and Φ_0 is the superconducting flux quantum. This relation, describing the conventional, 2π-periodic Josephson effect, can be understood as the tunneling of Cooper pairs with a net charge $e^\star = 2e$ coupled to photons of energy hf [104]. This coupling, referred to as the AC Josephson effect, has first been measured in superconducting tunnel junctions [105] and has been shown to persist in metallic weak links [106], carbon nanotubes [107] and semiconductor channels [108, 109], as well as in high critical temperature superconductors [110].

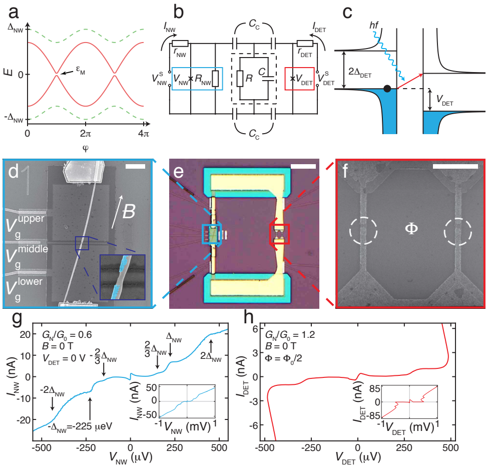

Figure 4.1: **Principles of the experiment.** **(a)** Energy dispersion of topologically trivial (dashed green line) and nontrivial (solid red line) Andreev levels inside a NW Josephson junction as a function of the phase difference across the junction. The gap ε_M arises from the finite MZMs wavefunction overlap. **(b)** Equivalent circuit diagram of the device. The NW junction (in blue box) is capacitively coupled to the superconducting tunnel junction (red box) via the capacitors C_C. The microwave losses and stray capacitance are modeled by the RC element enclosed by the dashed black box, see text. The applied DC bias voltages are V^S_NW and $V^\mathrm{S}_\mathrm{DET}$ with an effective internal resistance r_NW and r_DET, respectively. **(c)** Principle of the frequency sensitive detection based on photon-assisted tunneling: an absorbed photon with an energy hf gives rise to quasiparticle current if $hf > 2\Delta_\mathrm{DET} - eV_\mathrm{DET}$. **(d)** Scanning electron micrograph of the NW junction placed on three electrostatic gates. A false color micrograph of the junction is shown in the inset, with the epitaxial Al shell highlighted in cyan. **(e)** Bright field optical image of the coupling circuitry between the NW junction (blue box) and the detector junction (red box). **(f)** Micrograph of the split tunnel junction detector. The junctions are encircled. **(g)** Measured $I_\mathrm{NW}(V_\mathrm{NW})$ characteristics of the NW junction at zero in-plane magnetic field exhibiting a supercurrent branch and multiple Andreev reflections. **(h)** Measured $I_\mathrm{DET}(V_\mathrm{DET})$ trace of the detector split junction at zero in-plane magnetic field with a minimized switching current. The insets in panels **(g)** and **(h)** show the large scale $I(V)$ trace of each junction. The normal state conductance, G_N is given in the units of $G_0 = 2e^2/h$. All images and data were taken on device NW1. The scale bars denote 1 μm **(d)**, 10 μm **(e)** and 1 μm **(f)**, respectively.

In proximitized semiconductor nanowires, an effective superconducting gap with a p-wave symmetry arises due to the breaking of the time-reversal symmetry above a threshold magnetic field [111–118]. When a weak link is formed between two leads, the p-wave component leads to a factor of two increase in the flux periodicity, giving rise to the so-called 4π-periodic Josephson effect [119, 120]. Phenomenologically, this phase periodicity is equivalent to an effective tunneling charge $e^\star = e$ instead of $2e$ in Eq. (1). Therefore, in this MZM regime, the frequency at a given voltage bias V drops by a factor of two, $f_{\mathrm{MZM}}(V) = f_{\mathrm{J}}(V)/2$, providing a robust signature of the topological phase transition in the superconducting leads. In real devices however, the finite size of the topological regions [121], poisoning events [111, 120] and Landau-Zener tunneling to the quasiparticle continuum [122] can effectively restore the 2π-periodic, trivial state. The latter two parity-mixing effects cause the system to relax to its ground state, effectively constraining the system in the lowest topological energy branch (red solid lines in Fig. 4.1a). Nevertheless, out-of-equilibrium measurements performed at rates faster than these equilibration processes can still capture the 4π-periodic nature of topological junctions [121–123]. In contrast, finite-size effects can be avoided by biasing the junction at voltages large enough to overcome the Majorana hybridization gap ε_{M} [122].

Here, we report the direct observation of a magnetic field-induced halving of the Josephson radiation frequency [124] in InAs nanowire (NW) junctions partially covered with an epitaxially grown aluminium shell (Fig. 4.1d). In this system, possessing a hard induced superconducting gap [125], previous direct transport experiments suggest parity lifetimes above 0.1 μs [126] and hybridization energies $\varepsilon_{\mathrm{M}} \lesssim 1\,\mu\mathrm{eV}$ for leads longer than 1.5 μm [127]. Thus, a frequency-sensitive measurement in the microwave domain is expected to reveal the 4π-periodic Josephson effect [128, 129].

4.2. RESULTS

FREQUENCY-SENSITIVE DETECTION OF THE JOSEPHSON RADIATION

As a frequency-sensitive microwave detector, we utilize a superconducting tunnel junction with a quasiparticle gap of Δ_{DET}, wherein the photon-assisted electron tunneling (PAT) current contributes to the DC current above a voltage bias threshold $eV_{\mathrm{DET}} > 2\Delta_{\mathrm{DET}} - hf$ [124, 130] (Fig. 4.1c). This *on-chip* detector [131], coupled via capacitors C_{C} to the NW junction (see Fig. 4.1b for the schematics and Fig. 4.1e for an optical image of the device) is engineered to result in an overdamped microwave environment characterized by a single $f_{\mathrm{c}} = (2\pi RC)^{-1} \approx 28\,\mathrm{GHz}$ cutoff frequency with $R = 538\,\Omega$ and $C = 10.4\,\mathrm{fF}$, see Supplementary Figure 4.6. The resulting broadband coupling to the detector [109] inhibits higher order photon emission, which could mimic the 4π-periodic Josephson effect [132].

The nanowire is deterministically deposited on a set of three gates covered by 30 nm thick SiN_x dielectric as shown in Fig. 4.1d. The Josephson weak link, where the Al shell is removed by wet chemical etching, is located above the central gate (see inset of Fig. 4.1d). We investigated devices with junction lengths ranging from 86 nm to 271 nm. The high quality of the nanowire junction is apparent from the presence of distinct multiple Andreev reflection steps in its $I_{\mathrm{NW}}(V_{\mathrm{NW}})$ characteristics [133] (Fig. 4.1g), which is a signature of the hard superconducting gap in the nanowire [125]. The observed curves and

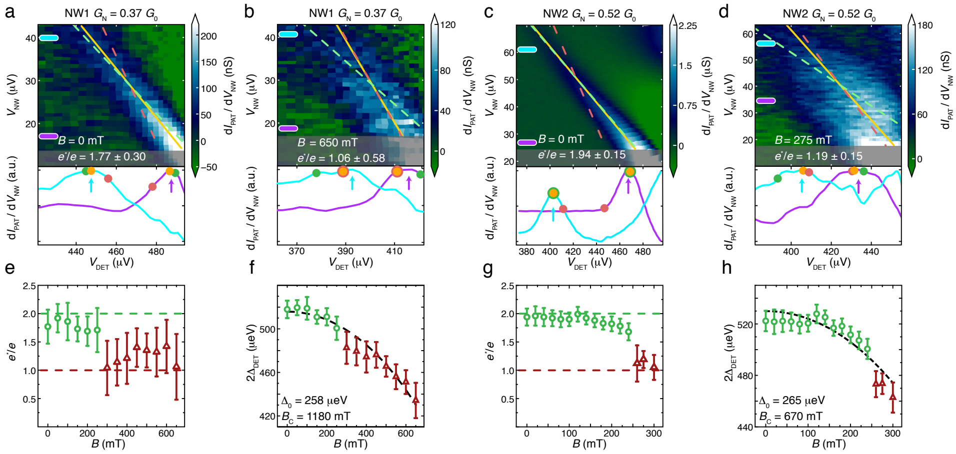

Figure 4.2: **Magnetic field-induced 4π-periodic Josephson radiation.** Differential transconductance $\mathrm{d}I_{\mathrm{PAT}}/\mathrm{d}V_{\mathrm{NW}}$ as a function of V_{NW} and V_{DET} for device NW1 (panels **(a)** and **(b)**), NW2 (panels **(c)** and **(d)**) at zero and finite magnetic fields, respectively. The position of the transconductance peak maps the frequency of the monochromatic Josephson radiation. A linear fit $e^\star V_{\mathrm{NW}} = 2\Delta_{\mathrm{DET}} - eV_{\mathrm{DET}}$ through these peaks is shown as an orange line. Dashed green and red lines show linear fits with a fixed slope corresponding to $e^\star = 2e$ and $e^\star = e$, respectively. The shaded regions show the regimes where the fit of the transconductance peak is not reliable, see text. Two normalized and smoothed horizontal linecuts are plotted, where arrows point at the position of the extracted peaks. The orange, green and red dots denote the position of the best fit, the $e^\star = 2e$ fit and the $e^\star = e$ fit, respectively. The evolution of $e^\star(B)$ and $2\Delta_{\mathrm{DET}}(B)$ are presented in panels **(e)** and **(f)** for NW1 and in panels **(g)** and **(h)** for NW2. For the calculation of the error bars, see text and Supplementary Note 4.5.3. The transition from the 2π- to 4π-periodic Josephson radiation is observed between 175 and 300 mT as $e^\star$ evolves from values near $2e$ (green circles) to values close to $1e$ (red triangles). For all devices, $2\Delta_{\mathrm{DET}}(B)$ drops monotonically (black dashed line, see text), independently of the change in $e^\star$.

linear conductance also establish that no conductive mode with a transmission close to unity exists in the channel, which could contribute to the 4π-periodic signal even in the absence of topological ordering [122].

The microwave detector, presented in Fig. 4.1f, is fabricated using two angle evaporated [134] Al/AlO$_x$/Al tunnel junctions, forming a superconducting quantum interference device (SQUID). This geometry allows us to minimize the Josephson energy of the detector by applying $\Phi = \Phi_0/2$ flux through the loop (see Fig. 4.1h) and thus to limit its backaction to the nanowire. The respectively 8 and 11 nm thick Al layers set an *in-plane* critical magnetic field of the detector in excess of 1 T, well above the measured topological transition in similar devices [127]. Nevertheless, increasing subgap currents limited our experimental field range to 325 – 650 mT for different devices. The circuit parameters and fabrication details are given in the Supplementary Tables 4.5.1 and in the Methods, respectively.

In the presence of a voltage spectral density $S_V(f)$, the DC current contribution of the PAT process is as follows [124, 130] in the subgap regime, where $eV_{\mathrm{DET}} < 2\Delta_{\mathrm{DET}}$:

$$I_{\mathrm{PAT}}(V_{\mathrm{DET}}) = \int_0^\infty \mathrm{d}f \left(\frac{e}{hf}\right)^2 S_V(f)\, I_{\mathrm{QP},0}\left(V_{\mathrm{DET}} + \frac{hf}{e}\right). \tag{4.2}$$

Here, $I_{QP,0}(V_{\mathrm{DET}})$ is the tunnel junction current in the absence of absorbed radiation, $S_V(f) = 0$ (see Fig. 4.1h). Note that the quasiparticle gap edge at $eV_{\mathrm{DET}} = 2\Delta_{\mathrm{DET}}$ results in a sharp increase of $I_{QP,0}(V_{\mathrm{DET}})$. In the presence of monochromatic radiation with a frequency f_0, $S_V(f) \sim \delta(f - f_0)$, $I_{\mathrm{PAT}}(V_{\mathrm{DET}})$ thus develops a step-like feature at $hf_0 = 2\Delta_{\mathrm{DET}} - eV_{\mathrm{DET}}$. With a phenomenological effective charge $e^\star$ of the AC Josephson effect, we write this condition in terms of the voltage drop on the nanowire, V_{NW}:

$$e^\star V_{\mathrm{NW}} = hf_0 = 2\Delta_{\mathrm{DET}} - eV_{\mathrm{DET}}, \tag{4.3}$$

where $e^\star = 2e$ for conventional junctions (see Eq. (1)) and $e^\star = e$ in the 4π-periodic regime. To extract $e^\star$ and thus determine the periodicity of the Josephson radiation, we track the transconductance peak $\mathrm{d}I_{\mathrm{PAT}}/\mathrm{d}V_{\mathrm{NW}}(V_{\mathrm{NW}}, V_{\mathrm{DET}})$ measured by standard lock-in techniques at a frequency of 17.7 Hz (see Supplementary Figure 4.5). The experiments were performed at the base temperature of a dilution refrigerator (~ 20 mK).

THE JOSEPHSON RADIATION AS A FUNCTION OF THE MAGNETIC FIELD

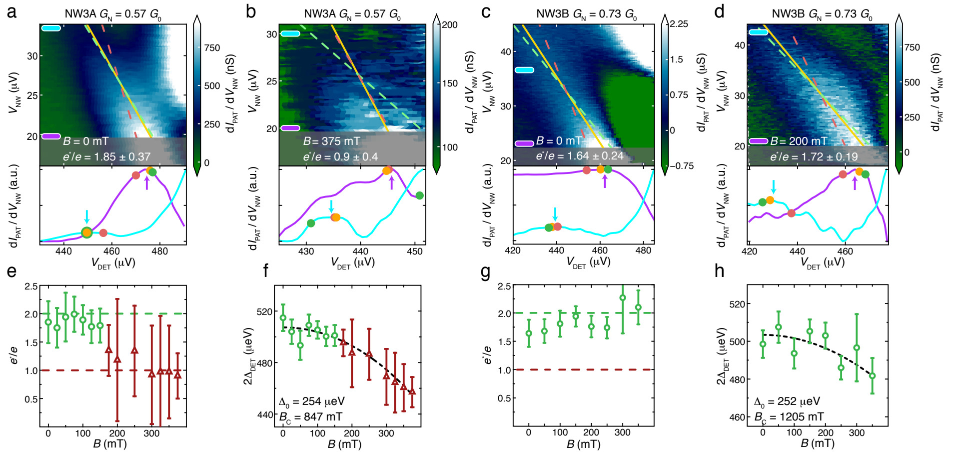

Figure 4.3: **Gate tuning of the 4π-periodic radiation regime.** Differential transconductance $\mathrm{d}I_{\mathrm{PAT}}/\mathrm{d}V_{\mathrm{NW}}$ as a function of V_{NW} and V_{DET} for device NW3 at gate setting A (panels **(a)** and **(b)**) and setting B (panels **(c)** and **(d)**) at zero and finite magnetic field, respectively. A linear fit and fits with a fixed slope $e^\star = 2e$ and $e^\star = e$ are shown as an orange line, a dashed green line and a dashed red line, respectively. Two normalized and smoothed horizontal linecuts are also presented, where arrows point at the position of the extracted peaks. The evolution of $e^\star(B)$ and $\Delta_{\mathrm{DET}}(B)$ are shown in panels **(e)** and **(f)** for setting A and in panels **(g)** and **(h)** for setting B. A transition from to 2π- to 4π-periodic Josephson radiation is observed for gate setting A, but the radiation remains 2π-periodic for setting B. The gate voltage values are shown in Supplementary Table 4.2. For the calculation of the error bars, see text and Supplementary 4.5.3.

Typical experimental datasets are shown in Fig. 4.2 for two nanowire junctions (NW1 and NW2, respectively) as the source of Josephson radiation. We limit the detector voltage range by the condition $\mathrm{d}I_{\mathrm{DET}}/\mathrm{d}V_{\mathrm{DET}} < 10\,\mu\mathrm{S}$ where the subgap quasiparticle current is still negligible, typically $I_{\mathrm{DET}} \lesssim 1\,\mathrm{nA}$. A lower limit of the emitter junction voltage is defined by the phase diffusion regime [135], characterized by periodic switching and retrapping events, which breaks the validity of Eq. (1) (see Supplementary 4.5.4). We therefore do not consider the low V_{NW} regime, within the supercurrent peak. We show this range, excluded from the linear fits, shaded in grey in Fig. 4.2 and Fig. 4.3 (see Supplementary 4.5.3 on the characterization of these limits). We fit the peak positions using Eq. (3) in order to extract $e^{\star}$ and Δ_{DET} as a function of the applied in-plane magnetic field. The typical standard deviation is 3.6 GHz for each frequency datapoint (see Supplementary 4.5.3). The error bars of the fitted parameters are determined using the bootstrapping method [136] (see Supplementary 4.5.3) and show the full width at half maximum yielding a confidence level of 75% for a Gaussian lineshape.

At zero magnetic field (Fig. 4.2a and c), the emitted Josephson radiation is always 2π-periodic with an extracted effective charge close to $e^{\star} = 2e$, as shown by the good agreement between the orange line and the dashed green line (best fit with fixed $e^{\star} = 2e$). In contrast, NW1 and NW2 exhibit the 4π-periodic Josephson effect above a threshold magnetic field (Fig. 4.2b and d), where $e^{\star} \approx e$. The full evolution is shown in Fig. 4.2e and 2g, respectively, where a sharp transition is visible from $e^{\star} \approx 2e$ (green circles) to $e^{\star} \approx e$ (red triangles). Finally, the fitted Δ_{DET} (Fig. 4.2c and f) shows a monotonic decrease described by $2\Delta_{\mathrm{DET}}(B) = 2\Delta_0\sqrt{1 - B^2/B_c^2}$ for all devices (dashed lines), with no additional feature at the transition field. In contrast with the nanowire junctions, our control device, an Al/AlO$_x$/Al tunnel junction, exhibits no transition in $e^{\star}$ over the entire magnetic field range (see Supplementary Figure 4.9).

THE JOSEPHSON RADIATION AT DIFFERENT GATE VOLTAGES

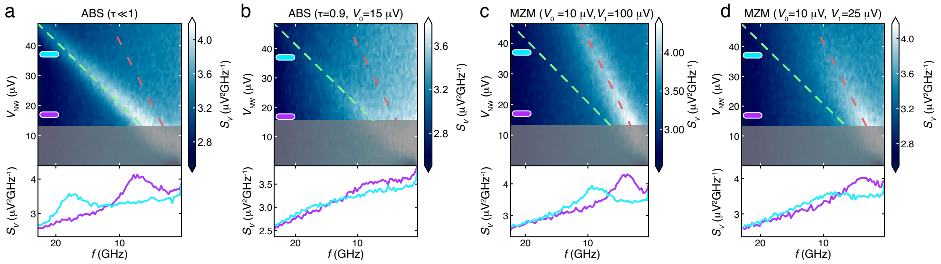

Figure 4.4: **The calculated radiation spectrum.** The voltage spectral density $S_V(f)$ incident on the detector junction, computed by numerically solving the system of stochastic differential equations shown in Supplementary 4.5.4. Panels **(a)** and **(b)** show results for a junction in the trivial regime (small transmission and large transmission, respectively), while panels **(c)** and **(d)** show the emission spectrum in the topological regime. V_0 and V_1 are voltage scales for Landau-Zener tunneling between branches of the junction bound state and for tunneling to the quasiparticle continuum, respectively, see text. Circuit parameters are set as $r_{\mathrm{NW}} = 2.4\,\mathrm{k\Omega}$, $R_{\mathrm{NW}} = 50\,\mathrm{k\Omega}$, $R = 0.5\,\mathrm{k\Omega}$, $C = 10\,\mathrm{fF}$, $C_C = 400\,\mathrm{fF}$, and $I^0_{\mathrm{NW}} = 8\,\mathrm{nA}$. The noise temperature is $T = 150\,\mathrm{mK}$ and the quasiparticle poisoning rate is $\Gamma_q = 100\,\mathrm{MHz}$. As in Fig. 4.2, the dashed green and red lines show the frequency of the Josephson radiation corresponding to $e^{\star} = 2e$ and $e^{\star} = e$, respectively. The estimated phase diffusion region is shaded in gray.

Fig. 4.3 shows the magnetic field evolution of device NW3 at two distinct gate settings with similar G_{N} and $\mathrm{d}I_{\mathrm{PAT}}/\mathrm{d}V_{\mathrm{NW}}$ corresponding to similar Josephson coupling. By tuning the chemical potential in the nanowire via changing the gate voltages, it is possible to displace the position of the onset of the 4π-periodic Josephson radiation from $\approx 175\,\mathrm{mT}$ (Fig. 4.3b) to values larger than $375\,\mathrm{mT}$ (Fig. 4.3d). Note that the additional local maximum at high V_{NW} values, also observed in earlier experiments [109], is attributed to the shot noise of the nanowire junction.

The possibility to tune the nanowire devices into the 4π-periodic Josephson radiation regime with both magnetic field and chemical potential is consistent with the predicted phase diagram of this system [111, 112, 120]. We observe the same behaviour in four distinct nanowire devices (see Supplementary Figure 4.8 for device NW4), which we can interpret within the single subband model of the topological phase transition that takes place at a magnetic field $B^\star$, where $E_z = g\mu_{\mathrm{B}}B^\star/2 = \sqrt{\Delta_{\mathrm{NW}}^2 + \mu_{\mathrm{NW}}^2}$. Here g and μ_{B} are the Landé g-factor and the Bohr magnetron, respectively. From our device parameters (see Supplementary Table 4.2), lower bounds on the g-factors ranging from $g \approx 11$ ($B^\star = 175\,\mathrm{mT}$) in device NW3 to $g \approx 35$ ($B^\star = 190\,\mathrm{mT}$) in device NW4 are obtained, in agreement with values reported in similar devices [117, 127, 137]. In contrast, an accidental crossing of a trivial Andreev bound state would be inconsistent with the observed field range of $\Delta B \sim 0.3\,\mathrm{T}$ of the 4π-periodic radiation, since within this range, a spinful Andreev level [137] would evolve over the scale of the superconducting gap, $\Delta_{\mathrm{NW}} \sim g\mu_{\mathrm{B}}\Delta B$, suppressing the 4π periodicity. We however did not observe a continuous variation of the onset magnetic field $B^\star$ as a function of the applied gate voltages. This behaviour is consistent with calculations of the topological phase diagram based on realistic device simulations including orbital effects of the magnetic field [138] and multiple spatial dimensions [139, 140] of the device.

We observe a single Josephson radiation frequency in the 4π-periodic regime, which is consistent with the supercurrent being predominantly carried by a single transmitting mode. While we were not able to reliably extract the transparency and the number of modes in our devices, the single mode regime was observed earlier in similar InAs nanowires [137, 141, 142]. We also note that an upper bound on the channel transmission of $\tau = G_{\mathrm{N}}/G_0$ can be determined from the normal state conductance $G_{\mathrm{N}} < G_0$, which is measured in the linear regime well above the superconducting gap. This value is shown in Fig. 4.2 and Fig. 4.3 for each device.

NUMERICAL SIMULATIONS OF THE JOSEPHSON RADIATION FREQUENCY

Next, we numerically evaluate the expected voltage spectral density seen by the detector junction in various regimes. We use the quasiclassical resistively and capacitively shunted junction (RCSJ) model coupled to a stochastic differential equation describing the occupation of the single pair of Andreev levels in the NW junction. The equivalent circuit of the device in the microwave domain is shown in Fig. 4.1b, where each element is experimentally characterized [109] (see Supplementary Figure 4.6 and Supplementary Tables 4.5.1). Note that we neglect the load of the detector on the circuit, which is justified by its negligible subgap conductance compared to that of all other elements in the circuit.

Our model of the nanowire junction considers Landau-Zener (LZ) tunneling between branches of the energy-phase dispersion shown in Fig. 4.1a, as well as tunneling to the continuum, and stochastic quasiparticle poisoning events [122]. The probability of LZ tunneling is determined by the voltage drop V_{NW} according to $P_{\mathrm{LZ}} = \exp(-V_0/V_{\mathrm{NW}})$, where $eV_0 = 4\pi\varepsilon_M^2/(\Delta_{NW}\sqrt{\tau})$ is the characteristic voltage above which $P_{LZ} \sim 1$. In this limit, 4π-periodicity is observed despite the gap ε_M caused by finite-size effects [127]. Similarly, LZ tunneling to the continuum close to $\varphi = 2\pi$ defines a voltage scale $eV_1 = 2\pi\Delta_{NW}(1-\sqrt{\tau})^2/\sqrt{\tau}$, above which 2π-periodicity is restored [122]. We note that a trivial Andreev bound state in the short junction limit can be modeled similarly with $eV_0 = \pi\Delta_{NW}(1-\tau)$ and $eV_1 = 0$.

Fig. 4.4 shows representative plots obtained by numerically evaluating $S_V(f, V_{NW})$ (see Supplementary section 4.5.4), which determines the photon-assisted tunneling current by Eq. (2). We observe that the numerical results agree well with the characteristic features of the experimental data. We find that the circuit equations allow for a phase diffusion regime at low V_{NW} values [135], where $e^\star V_{NW} < hf$, because the junction spends part of the time in the steady supercurrent state where the voltage drop is zero. The calculations also reproduce the absence of higher harmonics in the radiation spectrum, attributed to the low transmission of the junction and the overdamped nature of the microwave environment [132]. This confirms our expectation of the suppression of multiphoton processes due to a low quality factor, justifying the usage of the semiclassical junction model.

A key result of these simulations in a wide range of junction parameters is that, with the circuit elements taking values representative of those in the experiment, the radiation frequency always reflects the internal dynamics of the nanowire Josephson junction both in the 2π-periodic (Fig. 4.4a and b) and in the 4π-periodic emission regime (Fig. 4.4c and d). Finally, we note that our results are consistent with $V_0 \lesssim 15\,\mu\text{eV}$ translating to an avoided crossing $\varepsilon_M \lesssim 10\,\mu\text{eV}$. Using the exponential cutoff in Ref. [127], this suggests that our devices have a continuous topological region of several hundreds of nanometers on each side of the nanowire junction, which is consistent with the scanning electron microscopy images of the devices.

4.3. DISCUSSION

In conclusion, we observed the 4π-periodic Josephson effect in multiple InAs nanowires above a threshold magnetic field in a range of 175 – 300 mT. This effect, which can be suppressed by tuning the gate voltages, is consistent with the expected signatures of a topological phase transition. By observing the periodicity of the Josephson effect using an *on-chip* microwave detector, we investigated this system whilst preserving its charge parity, in line with the requirements for prospective topological quantum computers. This experimental technique may also prove instrumental in identifying more exotic non-Abelian anyon states [143, 144], due to its proven sensitivity to the periodicity of the Josephson effect, directly measuring the charge fractionalization of the anyon state [145, 146].

4.4. METHODS

DEVICE FABRICATION

The devices are fabricated on commercially available undoped Si substrates with an insulating SiO_x layer of 285 nm thick in a similar fashion to Refs. [137] and [109]. All etching and metal deposition steps are realized using standard positive tone electron-beam lithography techniques. First, three Ti/Au (5 nm/15 nm) electrostatic gates and the coupling capacitor bottom plates are deposited (see Fig. 4.1 for design details). These are subsequently covered by a ∼ 30 nm thick SiN_x dielectric layer deposited by sputtering. Eleven 100 nm wide Cr/Pt (5 nm/25 nm) tracks are then defined. These ∼ $100\,\Omega\,\mu\mathrm{m}^{-1}$ resistive lines connect the gates, the (yet to be defined) $\mathrm{Al/AlO}_x\mathrm{/Al}$ detector and the nanowire to the instrumentation setup. Next, the $\mathrm{Al/AlO}_x\mathrm{/Al}$ Josephson junctions are fabricated by evaporating 8 and 11 nm thick Al layers with an intermediate *in-situ* oxidation step at 0.5 mbar for 4 minutes using the Dolan bridge technique [134]. The nanowires are then deterministically deposited onto the electrostatic gates with a micro-manipulator setup equipped with an optical microscope. A gap in the nanowire Al shell is then created by wet etching using Transene D at a temperature of 48.2°C for 12 seconds. Next, both the nanowire and the detector junctions are connected to the resistive lines with an 80 nm thick sputtered NbTiN film after an *in-situ* Ar plasma milling step. Finally, a Ti/Au (15/100 nm) layer is evaporated to define quasiparticles traps, the upper capacitor plates and the contact pads. We note that no NbTiN film was used in device NW3. Instead, a Ti/Au (15/100 nm) layer was used to contact the nanowire and the detector. The dimensions and properties of each device are presented in Supplementary Table 4.1, and the experimental setup is described in Supplementary Figure 4.5. We note that the detector is made of narrow and thin aluminum sections (see Fig. 4.1f) to limit the presence of vortices near the $\mathrm{Al/AlO}_x\mathrm{/Al}$ junctions, and thus to decrease the subgap current in finite magnetic field.

The InAs nanowires used in this work are grown via a two-step process by molecular beam epitaxy. The InAs nanowires are grown at 420°C using the vapour-liquid-solid method with Au droplets as a catalyst. After cooling the system to −30°C, Al is epitaxially grown on two of the six nanowires facets [125].

THE MICROWAVE ENVIRONMENT OF THE INAS JOSEPHSON JUNCTION

We model the effective microwave environment of the nanowire Josephson junction with a parallel lumped resistor (R) and capacitor (C) element, which accounts for the low-pass nature of the coupling circuit (see inset of Supplementary Figure 4.6a). We determine the effective RC values by measuring a sample wherein the nanowire junction is replaced by an $\mathrm{Al/AlO}_x\mathrm{/Al}$ tunnel junction. The supercurrent peak is fitted against the Ivanchenko-Zil'berman model to find the RC values and the noise temperature of the circuit [135] at zero magnetic field (see Supplementary Figure 4.6a). The critical current as a function of the magnetic field is then found using the same model, with the R,C and the noise temperature fixed at their zero field value (Supplementary Figure 4.6b). We note that the same coupling circuit was used in [109], leading to RC and noise temperature values in good agreement with the current ones. Thus, we conclude that the reproducibility is good for all samples featured in the current study. These parameters are used to theoretically study the dynamics of the Josephson radiation.

REPRODUCIBILITY OF THE TRANSITION FOR NANOWIRE DEVICES

Supplementary Figure 4.7 shows every differential transconductance color plots from which the effective charge $e^\star$ has been extracted in Fig. 4.2e. The color plots nominally follow the same trend as the ones presented in Fig. 4.2. Supplementary Figure 4.8 shows the magnetic field evolution of $e^\star$ in device NW4. Device NW4 also exhibits a transition from to 2π- to 4π-periodic Josephson radiation at $B \sim 175\,\text{mT}$. As such, the observation of a magnetic field induced transition in the periodicity of the Josephson radiation has been observed in four distinct devices, showcasing the reproducibility of the observation.

JOSEPHSON RADIATION OF AN AL/ALO$_x$/AL TUNNEL JUNCTION

Supplementary Figure 4.9 shows our measured data with a conventional Al/AlO$_x$/Al superconducting tunnel junction as the source of Josephson radiation. Evaluating $e^\star$ as a function of magnetic field in the same range as for Fig. 4.2 and Supplementary Figure 4.8, we observe no transition in the periodicity of the Josephson effect, confirming that the 4π-periodic Josephson radiation only occurs in nanowire junctions. We note that, in order to keep the circuit behavior similar, the normal state conductance of the tunnel junction was set to $G_{\text{N,T}} = 0.26G_0$.

4.5. SUPPLEMENTARY INFORMATION

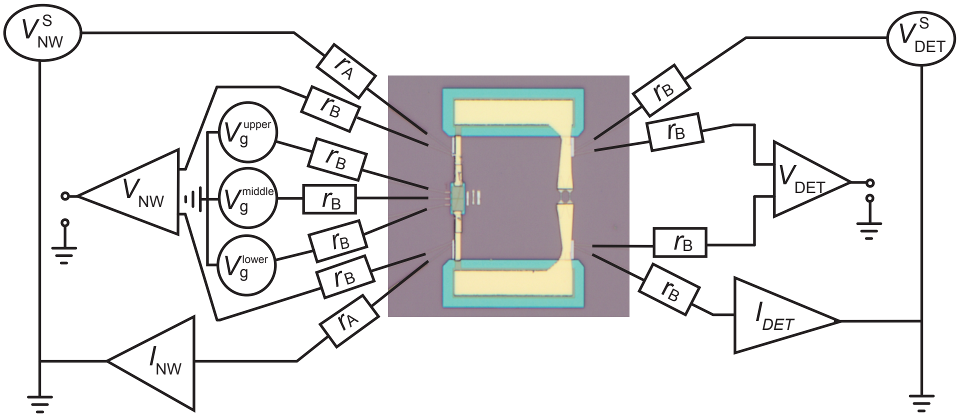

Figure 4.5: **Schematics of the PAT measurement.** The voltage V^S_{NW} is the sum of a DC voltage and a $2\,\mu\text{V}$ AC component at 17.7 Hz applied via resistive lines with $r_A = 1.2\,\text{k}\Omega$ resistances. The voltage drop over the nanowire V_{NW} is measured in a four point probe geometry via the $r_B = 12\,\text{k}\Omega$ on-chip resistors using a home-built low noise preamplifier. The current I_{NW} is measured simultaneously using a home-built current to voltage converter. The gate voltages V_g^{upper}, V_g^{middle} and V_g^{lower} are all applied via $r_B = 12\,\text{k}\Omega$ on-chip resistors. The detector junction is measured in a similar, four point probe geometry, using $r_B = 12\,\text{k}\Omega$ in all connecting lines. The DC current, originating from both the intrinsic characteristics of the detector and from PAT, and the AC component, generated solely by PAT, are measured with a home-built current to voltage converter. We note that it was not possible to perform the measurements in the 4-point geometry on the detector side of device NW4, nor on either side of device NW3. In these cases, series resistances of 116, 7.5 and 7.4 kΩ were taken into account to calculate V_{DET} from V^S_{DET} in device NW4 and NW3, and to calculate V_{NW} from V^S_{NW} in device NW3, respectively.

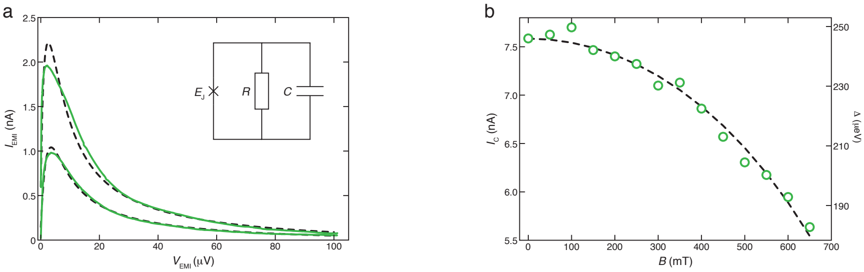

Figure 4.6: **Characterization of the microwave environment.** **(a)** Supercurrent peak of an Al/AlO$_x$/Al junction emitter device at magnetic fields $B = 0\,\mathrm{mT}$ and $B = 650\,\mathrm{mT}$ (higher and lower solid curves respectively), with the dashed lines being the best fit yielding $R = 538\,\Omega$, $C = 10.4\,\mathrm{fF}$ and $T = 133\,\mathrm{mK}$. **(b)** Extracted critical current I_C as a function of B. The right axis shows the extracted superconducting gap $\Delta = 2I_C/\pi G_N$. The dashed line shows the best fit to $\Delta(B)/\Delta(B=0) = \sqrt{1 - B^2/B_c^2}$, yielding a critical field $B_{c,\mathrm{EMI}} = 953\,\mathrm{mT}$.

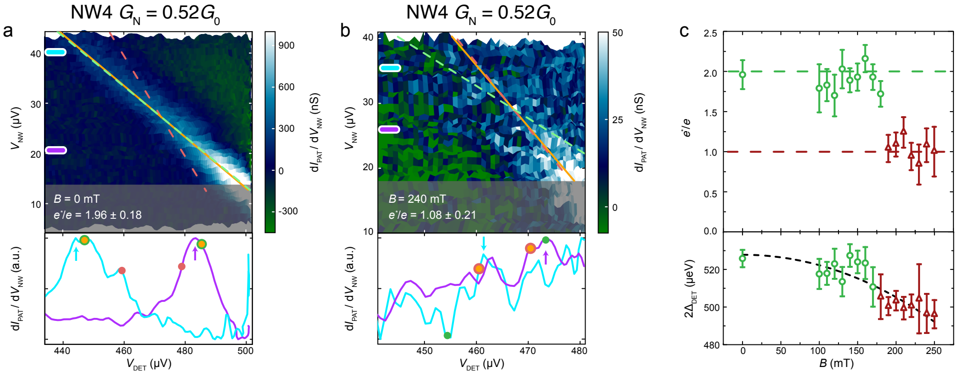

Figure 4.8: **Magnetic field evolution of $e^\star$ for device NW4.** Differential transconductance $\mathrm{d}I_{\mathrm{PAT}}/\mathrm{d}V_{\mathrm{NW}}$ as a function of V_{NW} and V_{DET} for device NW4 at **(a)** $B = 0\,\mathrm{mT}$ and **(b)** $B = 240\,\mathrm{mT}$. A linear fit $e^\star V_{\mathrm{NW}} = 2\Delta - eV_{\mathrm{DET}}$ through these peaks is shown as an orange line. Dashed green and red lines show linear fits with a fixed slope corresponding to $e^\star = 2e$ and $e^\star = e$ respectively. The shaded regions represent regimes where the fit on the transconductance peak is not reliable. Normalised and smoothed horizontal linecuts are plotted at two V_{NW} values, where arrows show the position of the extracted peaks and orange, green and red dots denote the position of the best fit, the $e^\star = 2e$ fit and the $e^\star = e$ fit, respectively. **(c)** The effective charge $e^\star$ and Δ_{DET} extracted from the linear fit as a function of magnetic field. The transition from to 2π- to 4π-periodic Josephson radiation occurs at B ≈ 175 mT.

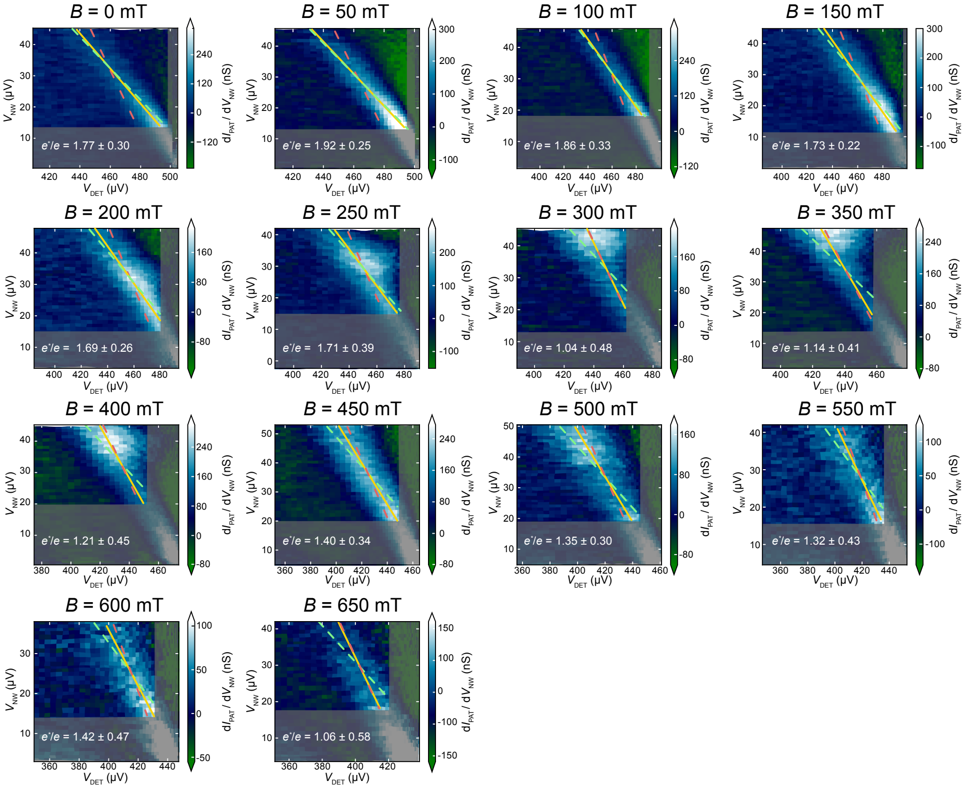

Figure 4.7: **Complete magnetic field dependence for device NW1.** Differential transconductance $\mathrm{d}I_{\mathrm{PAT}}$ / $\mathrm{d}V_{\mathrm{NW}}$ as a function of V_{NW} and V_{DET} for device NW1 at magnetic fields ranging between 0 and 650 mT. A linear fit $e^{\star} V_{\mathrm{NW}} = 2\Delta - eV_{\mathrm{DET}}$ through these peaks is shown as an orange line. Dashed green and red lines show linear fits with a fixed slope corresponding to $e^{\star} = 2e$ and $e^{\star} = e$, respectively. The shaded regions represent regimes where the fit of the transconductance peaks is not reliable either due to the phase diffusion regime at low V_{NW}, or due to high detector conductance at high V_{DET} values.

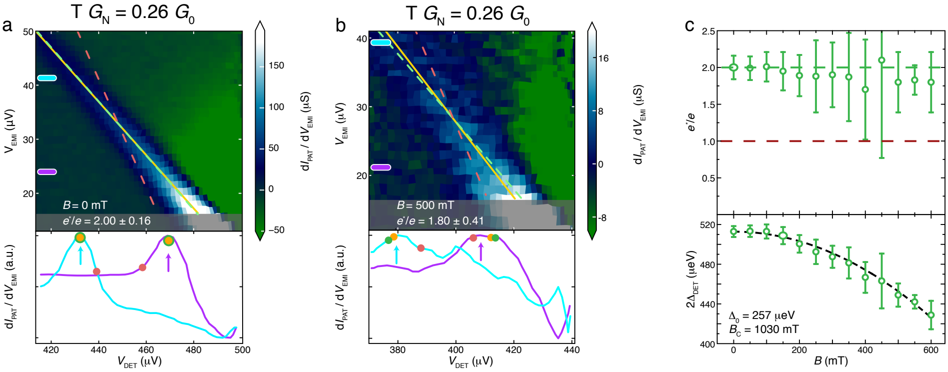

Figure 4.9: **Magnetic field evolution of $e^\star$ for the tunnel junction device, T.** Differential transconductance dI_{PAT} / dV_{EMI} as a function of V_{EMI} and V_{DET} for device T at **(a)** $B = 0\,\mathrm{mT}$ and **(b)** $B = 500\,\mathrm{mT}$. A linear fit $e^\star V_{\mathrm{EMI}} = 2\Delta - eV_{\mathrm{DET}}$ through these peaks is shown as an orange line. Dashed green and red lines show linear fits with a fixed slope corresponding to $e^\star = 2e$ and $e^\star = e$ respectively. The shaded regions represent regimes where the fit on the transconductance peak is not reliable. Normalised and smoothed horizontal linecuts are plotted at two V_{EMI} values, where arrows show the position of the extracted peaks and orange, green and red dots denote the position of the best fit, the $e^\star = 2e$ fit and the $e^\star = e$ fit, respectively. **(c)** The effective charge $e^\star$ and Δ_{DET} extracted from the linear fit as a function of magnetic field. No transition from to 2π- to 4π-periodic Josephson radiation occurs.

4.5.1. SUPPLEMENTARY TABLES

Parameter	NW1	NW2	NW3	NW4
Nanowire channel length (nm)	139	86	131	271
Total length between contacts (µm)	6.49	5.02	2.55	4.06
Detector tunnel junction area (µm^2)	0.040	0.014	0.025	0.024
Detector linear conductance, $G_{\mathrm{N,DET}}$ (G_0)	1.24	0.55	0.79	0.86
SQUID effective area, A_{SQUID} (µm^2)	5.34	3.62	5.37	5.49
Zero field detector gap, Δ_{DET} (µeV)	258	265	252	262
Detector critical field, $B_{\mathrm{C,DET}}$ (mT)	1180	670	1000	1070

Table 4.1: Geometric and electrical parameters of the devices with a nanowire junction.

	NW1	NW2	NW3A	NW3B	NW4
Upper gate voltage, $V_{\mathrm{g}}^{\mathrm{upper}}$ (V)	-4.0	-0.95	-1.8	-2.22	1.75
Middle gate voltage, $V_{\mathrm{g}}^{\mathrm{middle}}$ (V)	-7.25	2.5	0.0	0.0	0.87
Lower gate voltage, $V_{\mathrm{g}}^{\mathrm{lower}}$ (V)	-4.0	-0.95	-1.08	-1.825	1.75
Emitter linear conductance, G_{N} (G_0)	0.37	0.52	0.57	0.73	0.52
Nanowire induced gap, Δ_{NW} (µeV)	232	105	60	84	164
4π transition field, $B^\star$ (mT)	300	260	175	–	190
Estimated eV_1 (µeV)	368	71	30	13	111

Table 4.2: Electrical parameters of the nanowire junctions, specific to the gate voltage values used.

Parameter	Value
Emitter tunnel junction area (µm^2)	0.027
Emitter linear conductance, G_{N} (G_0)	0.26
Zero field gap, $\Delta(B=0)$ (µeV)	247
Zero field critical current, $I_{\mathrm{C}} = \pi\Delta_{\mathrm{EMI}}G_{\mathrm{N}}/2e$ (nA)	7.58
Emitter junction critical field, $B_{\mathrm{C,EMI}}$ (mT)	953
Detector tunnel junction area, A_{DET} (µm^2)	0.023
Detector conductance, $G_{\mathrm{N,DET}}$ (G_0)	0.26
SQUID effective area, A_{SQUID} (µm^2)	5.44
Zero field detector gap, Δ_{DET} (µeV)	257
Detector critical field, $B_{\mathrm{C,DET}}$ (mT)	1030

Table 4.3: Geometric and electrical parameters of device T with a superconducting tunnel junction as emitter, used for calibration purposes.

4.5.2. DETERMINATION OF THE SUPERCONDUCTING GAPS

This section describes the methods used to determine the superconducting gap in the nanowire and the detector. $2\Delta_{\text{NW}}$ is inferred from the position of the coherence peaks in the nanowire differential conductance observed at the largest V_{NW}, as shown in Supplementary Figure 4.10a. The position of these peaks is comparable at both negative and positive bias voltages, and these values are consistent with the additional MAR features visible at fractions of $2\Delta_{\text{NW}}$. The evolution of this gap with field for device NW1 is presented in Supplementary Figure 4.10b. Consistently with earlier tunneling spectroscopy experiments on similar devices [113, 114, 118, 127] and with the theoretical literature [147–150], no gap closing is observed.

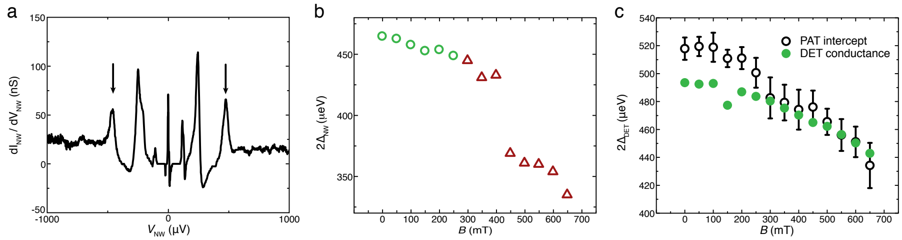

Figure 4.10: **Identification of the superconducting gaps.** **(a)** Nanowire differential conductance ($dI_{\text{NW}}/dV_{\text{NW}}$) as a function of nanowire voltage V_{NW} at B = 0 mT for device NW1. The coherence peaks at $2\Delta_{\text{NW}}$ are identified by black arrows and are located at ± 465 µeV. The large peak at zero-bias arises from the supercurrent and the additional peaks are associated with multiple Andreev reflections (MAR). **(b)** Nanowire induced gap ($2\Delta_{\text{NW}}$) as a function of magnetic field. Gaps obtained in the 2π- and the 4π-periodic regimes are shown as green circles and red triangles, respectively. **(c)** Al/AlO$_x$/Al detector gap ($2\Delta_{\text{DET}}$) as a function of magnetic field for device NW1. The gap value is either obtained from the intercept of the fitted PAT data (open black circles, same as Fig. 4.2d) or from the raw IV-trace of the detector (solid green circles).

As shown in Supplementary Figure 4.10c, the gap value of the SIS detector can be obtained either from the intercept of the fitted PAT data, as extracted in Fig. 4.2d, or from the raw IV-trace of the detector (Fig. 4.1h). Due to the limited range of the detector IV-trace, the gap is determined by the point at which the derivative of the detector IV-trace reaches 500 µS. The two methods agree well at magnetic fields larger than 250 mT. The discrepancy at lower fields is attributed to local heating effects at finite bias across the superconductor, which artificially increases the derivative of the detector IV-trace near the gap edge. Due to the unreliability of the data extracted from the IV at low magnetic fields, the gap value extracted from the fitted PAT data has been reported in Supplementary Table 4.2.

4.5.3. PEAK FINDING AND FITTING

This section describes the methodology for finding the peaks of the PAT current transconductance, and subsequently fitting them to obtain the effective charge $e^{\star}$. An example of a typical transconductance scan in shown in Supplementary Figure 4.11a. For every V_{NW} trace taken during this scan (see Supplementary Figure 4.11b for a typical line trace), the data is interpolated into 100 evenly spaced points. This interpolated data is then smoothed using a 2nd order polynomial Savitzky-Golay filter with a dynamical window length ranging between 5 and 21 points (red line in Supplementary Figure 4.11b). The window length scales linearly, with the larger window size being used at larger V_{NW}. The f^{-2} dependence of the PAT signal [124] results in a decreased signal-to-noise ratio at large V_{NW}, making additional smoothing desirable. Next, the peak from this smoothed curve is extracted. The data is then further smoothed using a 51 points dynamical window (not shown in Supplementary Figure 4.11b), and the first relative minimum reached on each side of the peak is used to define the peak minimum. The half-width at half-maximum on each side of the peak are then averaged, and used as the uncertainty on the peak position.

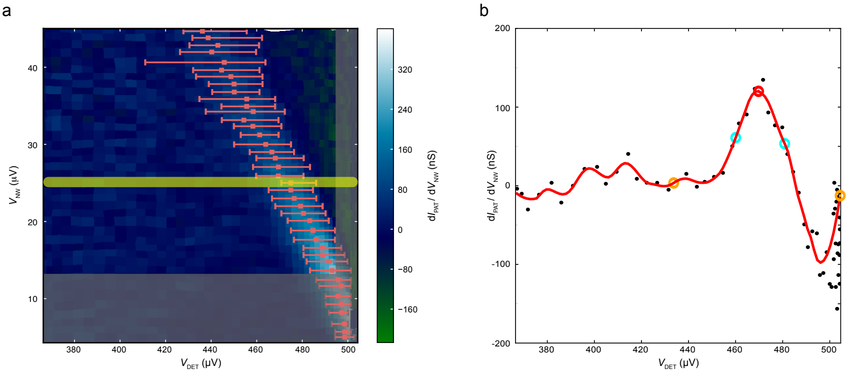

Figure 4.11: **Peak finding algorithm.** **(a)** Transconductance of the PAT current as a function of the bias across the NW junction and the detector for device NW1 at B = 0 mT. The position of the transconductance peak for each V_{NW} trace, with its uncertainty, is shown as a red dot with error bars. The shaded regions represent regimes where the position of the transconductance peak is shifted due to the large sub-gap current in the detector (x-axis) and/or due to the presence of phase-diffusion in the nanowire junction (y-axis). **(b)** Typical processed line-cut used to extract the transconductance peak. This line-cut corresponds to the yellow line in panel **(a)**. The maximum (red dot) is extracted from the smoothed curve (shown in red) and corresponds to the red dots in panel **(a)**. The estimated peak minimums (orange dots) and the corresponding half-maximum values (cyan dots, corresponding to the error bars in panel **(a)** are also shown.

The peak finding algorithm initially finds the peak for the lowest V_{NW} trace. To ensure that neither the current associated with quasiparticle tunneling at high V_{NW} values near the gap edge nor noise signals far away from the peak are inadvertently selected, all subsequent peaks are required to be located at a position in V_{DET} within a moving window $V_{\mathrm{DET}}^{\mathrm{last}} - 28\,\mu\mathrm{V} \leq V_{\mathrm{DET}}^{\mathrm{new}} \leq V_{\mathrm{DET}}^{\mathrm{last}} + 5\,\mu\mathrm{V}$.

Once the transconductance peaks are obtained, they are fitted using a Monte-Carlo bootstrap method with 10000 iterations [136]. For every iteration, the peak position of each V_{NW} trace is randomly determined from a Gaussian distribution with the average and the deviation given by the original peak position and uncertainty. These generated peaks are then linearly fitted and their slope and intercept are collected. The reported slope and intercept are given by the average results obtained over the 10000 iterations, and the uncertainty is given by their standard deviation.

The fitting procedure is carried out over a subset of the raw dataset. The lower bound of the fitting range is set so as to exclude two phenomena causing the extracted peaks to be improperly linked to the Josephson radiation, as inferred from Eq. (3). The first phenomenon stems from the assumption that the detector IV characteristics is ideal, *i.e.* that zero subgap current is present at detector voltages lower than the superconducting gap. While this assumption is realistic at V_{DET} values sufficiently far from the superconducting gap, it breaks down as V_{DET} is increased, and Eq. (2) is not expected to remain valid at these voltages. The breakdown point has been empirically determined in a trivial device (at B = 0 mT), and is reached when the derivative of the detector IV at $V_{\mathrm{NW}} = 0\ \mu\mathrm{V}$ is greater than 10 µS (see Supplementary Figure 4.12a). This regime is represented by the vertical gray-shaded area in Supplementary Figure 4.11a.

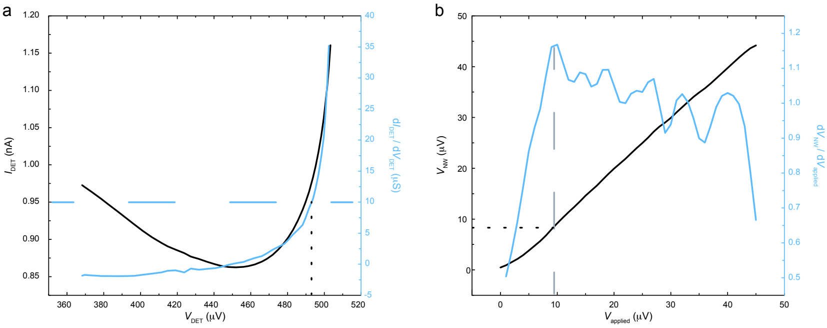

Figure 4.12: **Experimental determination of the reliable biasing regions. (a)** Detector current (left axis) and derivative of the detector current (right axis) as a function of the detector voltage. The detector voltage cut-off (black dotted line) is determined by the value at which the derivative of the detector current at $V_{\mathrm{NW}} = 0\ \mu\mathrm{V}$ reaches 10 µS (blue dashed line). **(b)** Measured voltage across the nanowire junction (left axis) and derivative of the measured voltage across the nanowire junction (right axis) as a function of the applied voltage across the nanowire side of the circuit. The nanowire voltage cutoff is 5 µV larger than the value of the first peak in the derivative of the measured nanowire voltage (gray dashed line). All data was taken on device NW1 at $B = 0$.

Phase diffusion in the nanowire junction can also induce a discrepancy between the position of the transconductance peak and the Josephson radiation extracted using Eq. (3). The dynamics of this phenomenon are presented in details later in this supplement. The phase-diffusion regime is characterized by a non-linearity between the applied voltage and the measured voltage across the nanowire junction. Experimentally, we define this regime by locating the peak in the (low-pass filtered) derivative of the measured voltage with respect to the applied voltage (see Supplementary Figure 4.12b). Only data obtained at voltages 5 µV larger than this peak are considered reliable. The excluded phase-diffusive region occurs at V_{NW} values located in the horizontal gray-shaded area in Supplementary Figure 4.11a.

4.5.4. THEORY

PROBABILISTIC MODEL OF VOLTAGE BIASED MAJORANA JOSEPHSON JUNCTION

For simplicity, we consider a single conduction channel through the proximitized nanowire. In the topological regime, four Majorana states emerge; two near the junction, and two at the far ends of the wire. Taking into account the overlaps between these Majorana states [151], one obtains two many-body levels of each parity, with energies of the form

$$E_{\pm,o/e}(\phi) = \pm\sqrt{\varepsilon_{M,o/e}^2 + \epsilon^2\cos^2(\phi/2)}\,. \tag{4.4}$$

Here ϕ is the gauge-invariant phase difference across the junction, ϵ is a typical coupling energy of the Majorana states near the junction, and $\varepsilon_{M,o/e}$ is set by the couplings of these interior Majorana states to the ones on the wire ends. The phase dependence exhibits avoided level-crossings at $\phi = (2n+1)\pi$, with minimum energy splitting $\varepsilon_{M,o/e}$ between the upper and lower branches of the odd or even parity states respectively. We make the simplifying assumption that the odd and even states have the same energy, $E_\pm(\phi)$ (i.e. that $\varepsilon_{M,o/e} = \varepsilon_M$). The supercurrent in the lower (ground state; $-$) or upper (excited; $+$) branch is

$$I_\pm(\phi) = \frac{2e}{\hbar}\frac{\partial E_\pm}{\partial\phi} \approx \mp I_m\,\mathrm{sgn}[\cos\big(\phi/2\big)]\sin\big(\phi/2\big)\,, \tag{4.5}$$

where the last formula holds in the limit $\varepsilon_M \to 0$, with $I_m = e\epsilon/\hbar$. When the junction is biased by a DC voltage V, the phase difference ϕ winds linearly with time, $\dot{\phi} = (2e/\hbar)V$. For sufficiently small bias, the system evolves adiabatically (entirely in the lower branch at $T = 0$) and the usual Josephson effect results: the supercurrent oscillates at the Josephson frequency $\omega_J = (2e/\hbar)V$. Larger bias voltages can induce Landau-Zener (LZ) tunneling [152, 153] between branches at $\phi = (2n+1)\pi$. The system can also tunnel from the upper branch to the continuum at $\phi = 2n\pi$, effectively emitting a quasiparticle and relaxing to the lower branch in the process. In addition, the quantum dynamics of the junction are affected by thermal relaxation, dephasing, and quasiparticle poisoning processes.

The appropriate model for the dynamics of the junction depends on the nature and strength of the coupling to the external circuit. We assume that this coupling is strong, and that the external circuit, which can be described classically, frequently measures the current through the junction. As a result of such a measurement, the junction collapses into a state of definite current, i.e. into either the upper or lower branch, $E_\pm(\phi)$. Motivated by this reasoning, we describe the instantaneous state of the junction by a random variable $\zeta = \pm 1$, which labels the branches. LZ tunneling between branches is described by the transition probability

$$P(\zeta \to -\zeta) = p_0(V) = \exp(-V_0/V) \tag{4.6}$$

whenever ϕ crosses $(2n+1)\pi$, where $V_0 \approx 4\pi\varepsilon_M^2/e\epsilon$ is the LZ voltage scale and V is the instantaneous voltage across the junction. Tunneling to the continuum is described by a transition probability of the same form [123, 154],

$$P(\zeta = +1 \to \zeta = -1) = p_1(V) = \exp(-V_1/V) \tag{4.7}$$

whenever ϕ crosses $2n\pi$, where $V_1 = 2\pi\Delta_{\mathrm{NW}}(1-\sqrt{\tau})^2/e\sqrt{\tau}$ is another voltage scale. We ignore thermal relaxation of the junction state, since the associated timescale is large relative to an oscillation period. Quasiparticle poisoning is described by a constant rate Γ_q for transitions from $\zeta \to -\zeta$ (independent of ϕ). Although these approximations are drastic, we expect our results to be qualitatively correct as long as decoherence is fast enough relative to other timescales. The opposite limit of very slow decoherence is discussed in [151]. Effective discrete Markov models such as ours have been used to describe the non-adiabatic dynamics of Majorana bound states in the past, for instance by [123].

POWER SPECTRUM FOR FIXED JUNCTION VOLTAGE (NO EXTERNAL CIRCUIT)

We first study the dynamics of our simplified model when the Majorana junction is biased by a constant external voltage $V > 0$, so that the phase difference across the junction increases linearly with time; $\phi(t) = \phi_0 + (2e/\hbar)Vt$. In this case, one can obtain an analytical result for the power spectral density of the supercurrent noise. The supercurrent branch of the system changes randomly due to LZ tunneling every time ϕ passes an odd multiple of π, but we temporarily ignore tunneling to the continuum.

The supercurrent power spectral density (PSD) is defined as

$$S_I(\omega; V, V_0) = \lim_{t_f\to\infty} \frac{1}{t_f} \int_0^{t_f} \mathrm{d}t \int_0^{t_f} \mathrm{d}t' \left\langle I(t) I(t') \right\rangle e^{i\omega(t-t')} \tag{4.8}$$

where $I(t)$, the supercurrent at time t, is a random variable due to LZ tunneling with associated voltage scale V_0. We show later in this Supplement that

$$S_I(\omega; V, V_0) = \left(\frac{\hbar I_m^2}{eV}\right) F\left(\frac{\hbar\omega}{2eV}, \frac{V}{V_0}\right) \tag{4.9}$$

where $F(x, y)$ is the scaled PSD,

$$F(x,y) = \left[\frac{x^2(1+\cos 2\pi x)}{\pi(x^2-1/4)^2}\right] \left[\frac{1-(1-2e^{-1/y})^2}{1+(1-2e^{-1/y})^2 - 2(1-2e^{-1/y})\cos 2\pi x}\right]. \tag{4.10}$$

Note that x is simply the frequency ω measured in units of the Josephson frequency $\omega_J = (2e/\hbar)V$. The function $F(x, y)$ is plotted in Supplementary Figure 4.13 and Supplementary Figure 4.14. We draw attention to the fact that, for V between $\sim V_0$ and $\sim 2V_0$, the spectral density is broad but has a maximum at a frequency ω_* intermediate between ω_J and $\omega_J/2$.

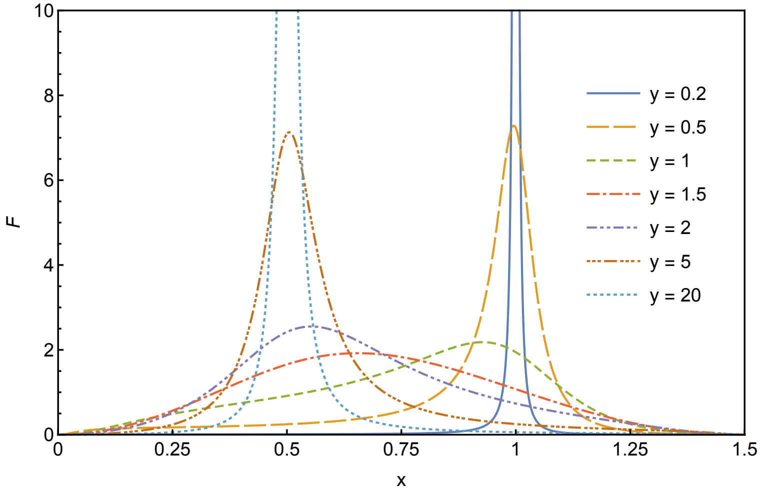

Figure 4.13: **Scaled spectral density.** The scaled spectral density $F(x, y)$, defined in Eq. (4.10), is plotted versus x for specified values of y. The variable x is frequency measured in units of Josephson frequency $\omega_J = (2e/\hbar)V$, while $y = V/V_0$ is the ratio of the bias voltage to the characteristic LZ tunneling voltage. At small bias $V/V_0 \ll 1$, the PSD exhibits a sharp peak at $\omega = \omega_J$. Over an intermediate bias range $V/V_0 \sim 1-2$, the PSD broadens, with the maximum gradually moving from $\omega = \omega_J$ to $\omega = \omega_J/2$. Finally, for large bias $V/V_0 \gg 1$, the PSD becomes sharply peaked at $\omega = \omega_J/2$. Note that the peaks for $y = 0.2$ and 20 extend far beyond the range of the plot.

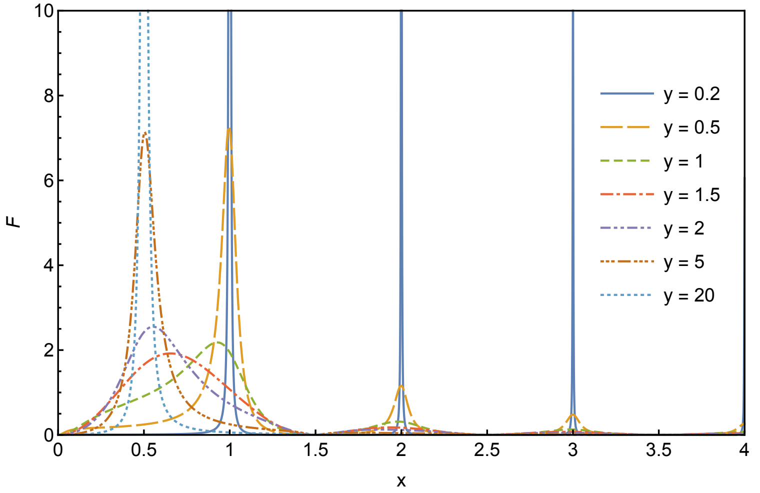

Figure 4.14: **Scaled spectral density over a larger range.** Same linecuts of $F(x, y)$ as in Supplementary Figure 4.13, but plotted over a larger range of x. The PSD is clearly peaked at all integer multiples of the Josephson frequency, $\omega = n\omega_J$. However, the weight of these peaks decreases rapidly with both increasing n and increasing y; even the $n = 2$ peak is negligible by $y = V/V_0 \approx 1.5$. The dependence on y is understood as follows: for $V \ll V_0$, the dynamics are essentially adiabatic, and the peaks at $\omega = n\omega_J$ come from higher harmonics in the expansion of the supercurrent $I(\phi) \sim I_m \,\mathrm{sgn}[\cos(\phi/2)] \sin(\phi/2)$, which changes abruptly from $+I_m$ to $-I_m$ as ϕ crosses π. When $V \geq V_0$, on the other hand, LZ transitions between the branches smooth the effective supercurrent-phase relation and wash out these higher harmonics. In the limit $V \gg V_0$, the system tracks a smooth 4π-periodic $I(\phi) \sim \sin(\phi/2)$, leading to the sharp peak at $\omega = \omega_J/2$, without any higher harmonics.

The above results are valid in the regime $V \ll V_1$, where V_1 is the voltage scale for tunneling to the continuum (Eq. (4.7)). The effect of finite V_1 on the dynamics of a perfectly 4π-periodic bound state (corresponding to $V_0 = 0$) has been studied in detail by Houzet et al. [123]. Eq. (14) in their paper gives the PSD obtained by solving an effective discrete Markov model very similar to ours, but with $V_0 = 0$ and V_1 finite. Their result may be compared with our Eqs. (4.9) and (4.10), which is for V_0 nonzero and $V_1 \to \infty$. Qualitatively, large but finite $V_1 > V$ broadens the $\omega_J/2$ peak in Figs. 4.13 and 4.14, as it provides an additional decay channel for the effective 4π-periodic state. When $V \gtrsim V_1$, the $\omega_J/2$ peak is strongly suppressed because the junction transitions out of the upper branch at $\phi = 2n\pi$ with high probability. Therefore, the ideal PSD $S_I(\omega)$ exhibits a clear peak at half the Josephson frequency only in the voltage range $2V_0 \lesssim V < V_1$.

MODELING THE JUNCTION ENVIRONMENT: EQUIVALENT CIRCUIT

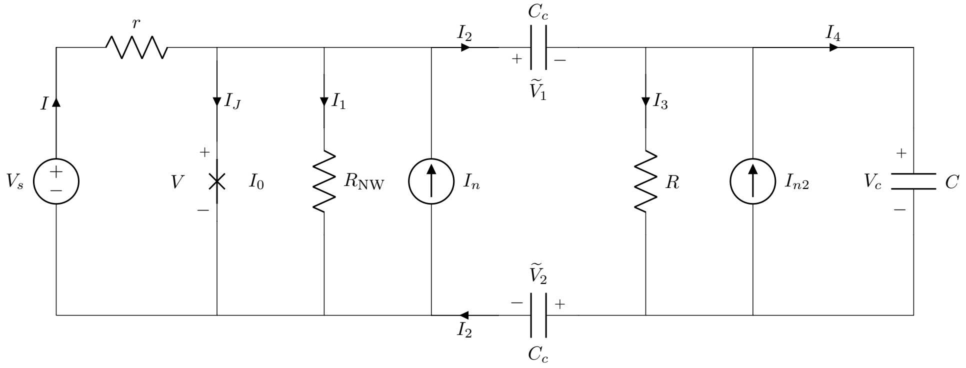

Figure 4.15: **Circuit diagram.** Physical circuit parameters are: DC source voltage V_s, resistances r, R_{NW}, R, and capacitances C, C_c. $V, V_c, \widetilde{V}_1, \widetilde{V}_2$ are time-dependent voltages across the indicated circuit elements. The current source I_{n2} describes Johnson noise of the resistance R; current source I_n describes the combined Johnson-Nyquist noise of resistances R_{NW} and r. Note that here, R_{NW} represents the sub-gap resistance in the relevant voltage range, and is in general larger than the normal-state resistance of the nanowire.

We model the dynamics of the nanowire Josephson junction, along with its RF environment, via the following equivalent circuit (this corresponds to the left half of Fig. 4.1b in the main text), which includes Johnson-Nyquist noise current sources for the various resistances. The detector part of the circuit (right half of Fig. 4.1b) is not modeled explicitly; the capacitive coupling via C_c of the emitter and detector decouple them at low-frequencies, and we assume that any high-frequency feedback from the detector can be absorbed into a renormalization of the effective environment capacitance C. The measured noise power spectral density at the detector is approximated by the PSD of the voltage $V_c(t)$ across the capacitor C.

First consider a standard Josephson tunnel junction in the non-topological regime (we will treat the topological case in the next section). The phase difference $\phi(t)$ across the ideal Josephson junction element obeys

$$\frac{\mathrm{d}\phi}{\mathrm{d}t} = \frac{2e}{\hbar} V(t) \tag{4.11}$$

and the supercurrent through the junction is given by

$$I_J(t) = I_0 \sin\phi(t)\,. \tag{4.12}$$

The current sources I_n and I_{n2} represent white Gaussian noise with zero mean and autocorrelation

$$\langle I_n(t_2) I_n(t_1)\rangle = 2k_B T\left(\frac{1}{r} + \frac{1}{R_{\mathrm{NW}}}\right)\delta(t_2 - t_1)\,, \qquad \langle I_{n2}(t_2) I_{n2}(t_1)\rangle = \frac{2k_B T}{R}\delta(t_2 - t_1) \tag{4.13}$$

respectively, where T is the effective noise temperature (assumed to be the same for all resistors). Note: if one introduces independent noise current sources I_{na}, I_{nb} for resistors r and R_{NW}, only the sum $I_{na} + I_{nb}$ appears in the equations of motion, and $I_n = I_{na} + I_{nb}$ has the specified autocorrelation function.

The quantities of interest are the instantaneous current $I(t)$, voltage $V(t)$ across the junction, and voltage $V_c(t)$ across capacitor C. It is convenient to describe the circuit dynamics in terms of dimensionless variables. If we define

$$\begin{aligned}
R_{\mathrm{eff}} &= (1/r + 1/R_{\mathrm{NW}})^{-1}\\
\omega_0 &= 2eI_0 R_{\mathrm{eff}}/\hbar\\
\tau &= \omega_0 t\\
v &= V/R_{\mathrm{eff}} I_0\\
v_c &= V_c/R I_0\\
v_s &= V_s/r I_0\\
i_n &= I_n/I_0\\
i_{n2} &= I_{n2}/I_0\\
Q^2 &= \omega_0 R_{\mathrm{eff}} C = 2eI_0 R_{\mathrm{eff}}^2 C/\hbar\\
\alpha &= R_{\mathrm{eff}}/R\\
\gamma &= 2C/C_c\\
\Gamma &= 2ek_B T/\hbar I_0,
\end{aligned} \tag{4.14}$$

then the equations of motion take the form (derivations are shown later in this Supplement)

$$\begin{aligned}
\frac{\mathrm{d}\phi}{\mathrm{d}\tau} &= v\,,\\
\frac{\mathrm{d}v}{\mathrm{d}\tau} &= Q^{-2}\Big[(1+\gamma)(v_s - v - \sin\phi + i_n) - v_c + i_{n2}\Big]\,,\\
\frac{\mathrm{d}v_c}{\mathrm{d}\tau} &= \alpha Q^{-2}\Big[v_s - v - v_c - \sin\phi + i_n + i_{n2}\Big]\,,
\end{aligned} \tag{4.15}$$

where i_n, i_{n2} represent white Gaussian noise with zero mean and autocorrelation

$$\begin{aligned}
\langle i_n(\tau_2) i_n(\tau_1)\rangle &= 2\Gamma\delta(\tau_2 - \tau_1)\,,\\
\langle i_{n2}(\tau_2) i_{n2}(\tau_1)\rangle &= 2\alpha\Gamma\delta(\tau_2 - \tau_1)\,.
\end{aligned} \tag{4.16}$$

The system of stochastic differential equations Eq. (4.15) describes a nonlinear stochastic process in the three dimensional state space spanned by the variables ϕ, v and v_c. We can gain insights into the properties of typical solutions by studying the attractors of the underlying deterministic process,

$$\begin{aligned}
\frac{\mathrm{d}\phi}{\mathrm{d}\tau} &= v\,, \\
\frac{\mathrm{d}v}{\mathrm{d}\tau} &= Q^{-2}\Big[(1+\gamma)(v_s - v - \sin\phi) - v_c\Big]\,, \\
\frac{\mathrm{d}v_c}{\mathrm{d}\tau} &= \alpha Q^{-2}\Big[v_s - v - v_c - \sin\phi\Big]\,,
\end{aligned} \tag{4.17}$$

i.e. the zero temperature limit of Eq. (4.15). For given parameters (α, γ, Q, v_s), the solution to Eq. (4.17) with initial condition (ϕ, v, v_c) defines a map

$$f_\tau : (\phi, v, v_c) \mapsto (\phi(\tau), v(\tau), v_c(\tau)). \tag{4.18}$$

We identify the attractors and their basins of attraction by numerically evaluating f_τ for large τ. The results are plotted in Figs. 4.16 and 4.17 for various parameter values. As in the simpler RCSJ model, the attractors of Eq. (4.17) come in two varieties: zero-voltage attractors, in which $v = v_c = 0$ and $\phi = \phi_*$ is constant, and a nonzero-voltage attractor, in which $v > 0$ and the phase winds. We will call these 0 and 1 states for brevity.

The low-temperature, noisy dynamics of the system can be understood in terms of diffusive motion around an attractor in state space, together with intermittent noise-induced transitions between the attractors [155]. We identify a thermally activated phase diffusion regime at low bias voltages, $v_s < v_{s1}$, in which the measured average voltage $\bar{v}$ is entirely due to the difference in transition rates for thermally activated $\phi_* \to \phi_* + 2\pi$ and $\phi_* \to \phi_* - 2\pi$ processes. At intermediate bias, $v_{s1} < v_s < v_{s2}$, the dynamics is more complicated, with the possibility of thermally activated transitions between coexisting 0 and 1 states. In this switching regime, the measured $\bar{v}$ can be interpreted as a weighted mean of the average voltage in the 1 state and the phase diffusion voltage. Finally, for $v_s > v_{s2}$, the dynamics reduces to small thermal fluctuations around the 1 state.

We conclude from this analysis that, when $v_s < v_{s2}$, the frequency of radiation emitted by the junction is not simply related to the Josephson frequency $\omega_J = (2e/\hbar)\overline{V}$. On the other hand, when $v_s > v_{s2}$, the dynamics of the external circuit does not play a major role, and the emitted radiation faithfully represents the dynamics of the junction (we verify this assertion by numerically solving the circuit equations—see Fig. 4.4 in the main text and Supplementary Figure 4.21 below).

In the $\Gamma \ll 1$ limit, $v_{s2} \approx 1$, since this is the bias voltage at which the 0 state attractors vanish. For parameter values $Q \sim 1.1$, $\alpha \sim 4.6$, and $\gamma \sim 0.05$, we find that $v_{s1} \approx 0.58$ (see Supplementary Figure 4.16). For larger Γ, the threshold bias $v_{s2}(\Gamma)$ may be estimated as the value of v_s above which $\mathrm{d}\bar{v}/\mathrm{d}v_s \approx 1$. In general, $v_{s2}(\Gamma) > v_{s2}$.

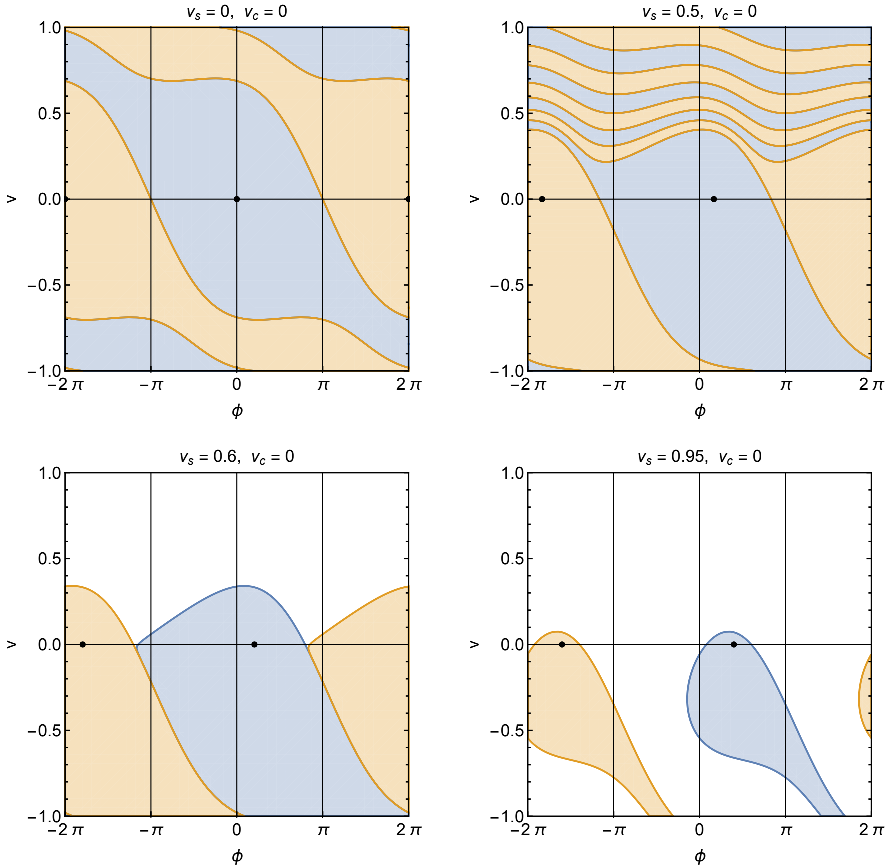

Figure 4.16: **Basins of attraction in the non-topological case.** Basins of attraction of Eq. (4.17) on a $v_c = 0$ slice through state space, for various values of dimensionless bias voltage v_s. Other dimensionless parameters are fixed at $Q = 1.1, \alpha = 4.6, \gamma = 0.05$ (these are the approximate experimental values). The blue and orange regions are stable manifolds of 0 state attractors; every point in such a region flows to the same 0 state. Two 0 state attractors are shown (black dots). The white region is the stable manifold of the 1 state; every point in this region flows to the same periodic 1 state trajectory (not shown here). Note that the state space and all attractors are 2π-periodic in ϕ.

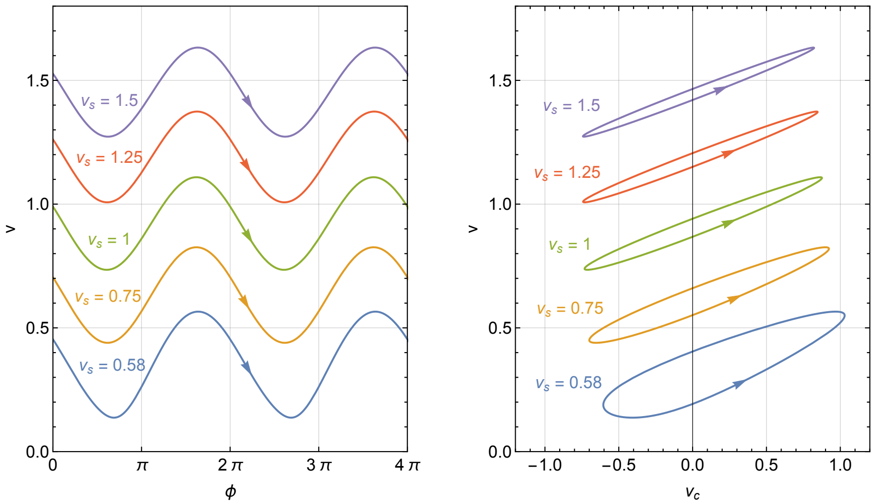

Figure 4.17: **Non-topological 1 state attractor.** Trajectories of the 1 state attractor for various values of dimensionless bias voltage v_s, in the non-topological case Eq. (4.17). The two panels show projections of the attractors onto the (ϕ, v) and (v_c, v) planes, respectively. As is clear from the left panel, ϕ increases by 2π over an orbital period. Other dimensionless parameters are fixed at $Q = 1.1$, $\alpha = 4.6$, and $\gamma = 0.05$ (these are the approximate experimental values). Note that, for these parameter values, the 1 state is only stable for $v_s \gtrsim 0.58$ (for smaller v_s, all initial points flow to a 0 state).

CIRCUIT EQUATIONS IN THE TOPOLOGICAL REGIME

In the topological regime, the Josephson current relation Eq. (4.12) is replaced, in our model of the junction, by

$$I_J(t) = I_m \zeta(t)\, \mathrm{sgn}[\cos(\phi(t)/2)]\, \sin(\phi(t)/2)\,. \tag{4.19}$$

Here $\zeta = \pm 1$ is a random variable that accounts for LZ tunneling, as well as tunneling to the continuum, as discussed previously. The critical current I_m of the Majorana junction replaces I_0, the critical current of the trivial junction (the definitions in Eq. (4.14) are modified accordingly).

As a result of this replacement, the dimensionless circuit equations Eq. (4.15) are modified to

$$\begin{aligned}
\frac{\mathrm{d}\phi}{\mathrm{d}\tau} &= v\,,\\
\frac{\mathrm{d}v}{\mathrm{d}\tau} &= Q^{-2}\Big[(1+\gamma)(v_s - v - \zeta\, \mathrm{sgn}[\cos(\phi/2)]\sin(\phi/2) + i_n) - v_c + i_{n2}\Big]\,,\\
\frac{\mathrm{d}v_c}{\mathrm{d}\tau} &= \alpha Q^{-2}\Big[v_s - v - v_c - \zeta\, \mathrm{sgn}[\cos(\phi/2)]\sin(\phi/2) + i_n + i_{n2}\Big]\,.
\end{aligned} \tag{4.20}$$

As before, we may study the stable fixed points (0 state) and limit cycle (1 state) of an underlying deterministic process. There are two distinct deterministic limits: i) the junction evolves adiabatically, remaining always in its ground state. This corresponds to fixing $\zeta = 1$ in Eq. (4.20). In this case the attractors and their basins of attraction are qualitatively similar to those of the non-topological junction (Figs. 4.16 and 4.17). ii) the evolution is perfectly non-adiabatic. This corresponds to fixing $\zeta\, \mathrm{sgn}[\cos(\phi/2)] = 1$ in Eq. (4.20). An ideal topological junction (in which there is negligible hybridization between the Majorana states at the junction and those at the far ends of the wire) would be described by case ii) at any nonvanishing voltage.

The results for case ii) are plotted in Figs. 4.18 and 4.19. The analysis of the noisy dynamics in terms of phase-diffusion, switching, and running regimes applies here as well. In particular, when $v_s < v_{s2}$, it is possible for the junction to radiate at a frequency intermediate between $\omega_J/2$ and ω_J, where $\omega_J = (2e/\hbar)\overline{V}$ is the Josephson frequency, even when the junction bound state is perfectly 4π-periodic ($V_0 \to 0$ and $V_1 \to \infty$).

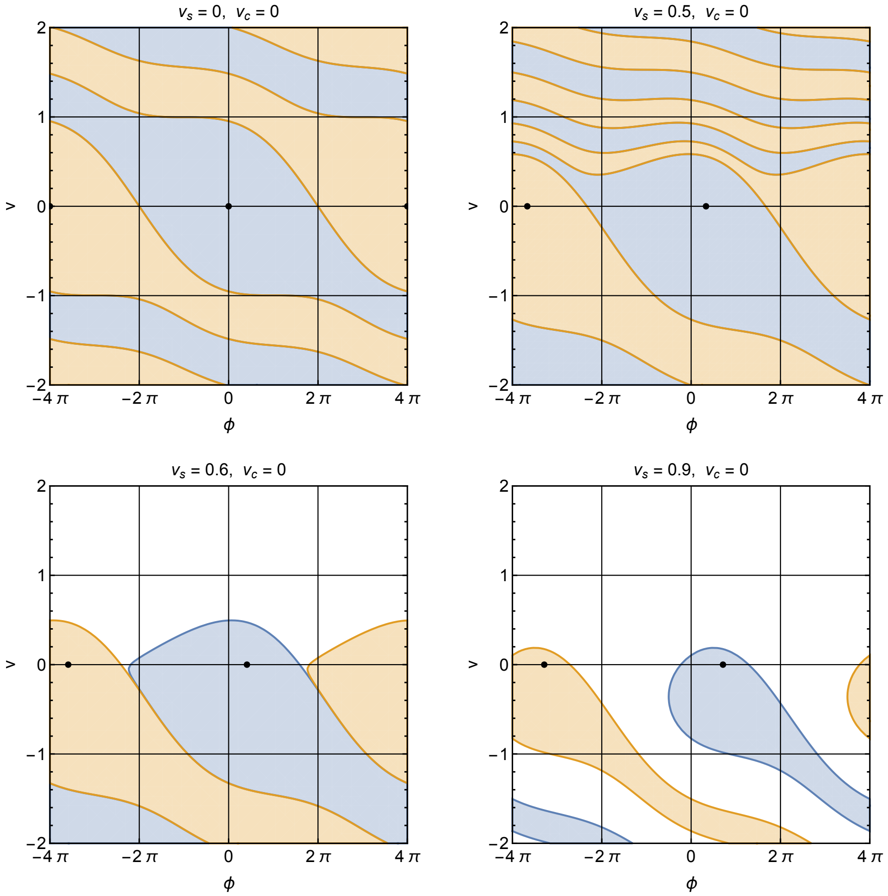

Figure 4.18: **Basins of attraction in the topological case.** Basins of attraction of Eq. (4.20) with $\zeta = +1$ on a $v_c = 0$ slice through state space, for various values of dimensionless bias voltage v_s. Other dimensionless parameters are fixed at $Q = 1.1, \alpha = 4.6, \gamma = 0.05$ (these are the approximate experimental values). The blue and orange regions are stable manifolds of 0 state attractors; every point in such a region flows to the same 0 state. Two 0 state attractors are shown (black dots). The white region is the stable manifold of the 1 state; every point in this region flows to the same periodic 1 state trajectory (not shown here). Note that the state space and all attractors are 4π-periodic in ϕ.

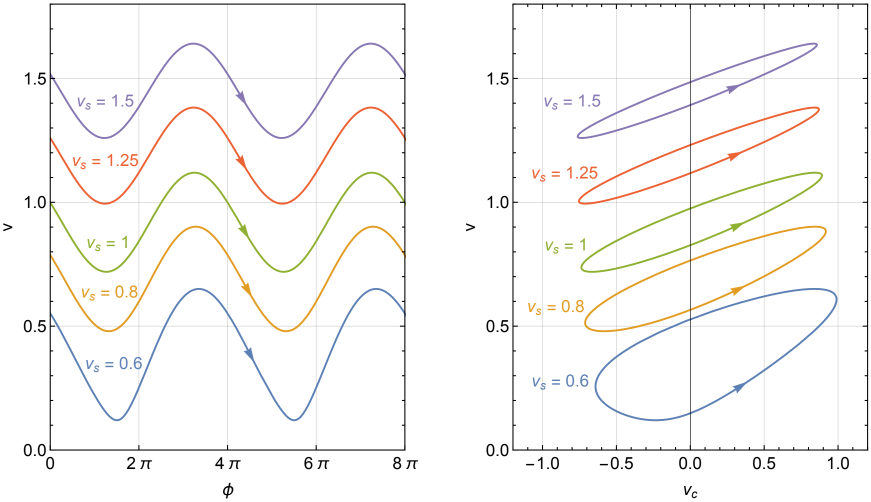

Figure 4.19: **Topological 1 state attractor.** Trajectories of the 1 state attractor for various values of dimensionless bias voltage v_s, in the topological case (Eq. (4.20) with $\zeta = +1$). The two panels show projections of the attractors onto the (ϕ, v) and (v_c, v) planes, respectively. As is clear from the left panel, ϕ increases by 4π over an orbital period. Other dimensionless parameters are fixed at $Q = 1.1$, $\alpha = 4.6$, and $\gamma = 0.05$ (these are the approximate experimental values). Note that, for these parameter values, the 1 state is only stable for $v_s \gtrsim 0.6$ (for smaller v_s, all initial points flow to a 0 state).

NUMERICAL SOLUTION OF CIRCUIT EQUATIONS

We numerically integrate the stochastic differential equations describing the circuit using the first-order Euler-Maruyama method [156]. The update rule with step size $\delta\tau$ is

$$\begin{aligned}
\phi_{j+1} &= \phi_j + v_j \delta\tau\,,\\
v_{j+1} &= v_j + Q^{-2}\Big[(1+\gamma)\big(v_s - v_j - \zeta_j s(\phi_j)\big) - (v_c)_j\Big]\delta\tau\\
&\qquad + Q^{-2}\sqrt{2\Gamma\delta\tau}\Big[(1+\gamma)X_{1,j} + \sqrt{\alpha}\,X_{2,j}\Big]\,,\\
(v_c)_{j+1} &= (v_c)_j + \alpha Q^{-2}\Big[v_s - v_j - (v_c)_j - \zeta_j s(\phi_j)\Big]\delta\tau + \alpha Q^{-2}\sqrt{2\Gamma\delta\tau}\Big[X_{1,j} + \sqrt{\alpha}\,X_{2,j}\Big]\,,
\end{aligned} \tag{4.21}$$

where $s(\phi) = \mathrm{sgn}[\cos(\phi/2)]\sin(\phi/2)$ for the topological junction, and where $X_{i,j}$ are independent identically distributed standard normal (mean 0 and variance 1) random variables. The probabilistic update rule for $\zeta = \pm 1$ takes into account quasiparticle poisoning, LZ tunneling between branches, and tunneling to the continuum:

$$P(\zeta_{j+1} = \zeta_j) = \begin{cases} (1-q)(1-p_{0j}) + q p_{0j} & \text{if} \quad \cos(\phi_j/2)\cos(\phi_{j+1}/2) < 0\,, \\ (1-q)(1-p_{1j}) + q p_{1j} & \text{if} \quad \zeta_j = -1 \quad \text{and} \quad \sin(\phi_j/2)\sin(\phi_{j+1}/2) < 0\,, \\ (1-q) & \text{otherwise}\,, \end{cases} \tag{4.22}$$

where

$$q = \frac{\Gamma_q \delta\tau}{\omega_0} \qquad p_{0j} = \exp\left(-\frac{\widetilde{v}_0}{\frac{1}{2}(v_j + v_{j+1})}\right), \quad \text{and} \qquad p_{1j} = \exp\left(-\frac{\widetilde{v}_1}{\frac{1}{2}(v_j + v_{j+1})}\right). \tag{4.23}$$

Here Γ_q is the rate of quasiparticle poisoning, and $\widetilde{v}_0 = V_0/R_{\rm eff}I_m$ and $\widetilde{v}_1 = V_1/R_{\rm eff}I_m$ are the dimensionless voltage scales for LZ tunneling between branches and to the continuum, respectively.

We estimate the PSD of $v_c(\tau)$ by applying Welch's method [157] to the simulated time series. The result is then averaged over several independent simulations with the same parameter values. The simulation step size $\delta\tau$ is chosen by requiring that the computed PSD not change significantly when $\delta\tau$ is made smaller (see Supplementary Figure 4.20).

In the case of a non-topological short junction containing a single open channel with transmission eigenvalue $\mathcal{T}$ (and thus hosting a single Andreev bound state), the update rules are still given by Eqs. (4.21), (4.22) and (4.23), but with

$$s(\phi) = \left(\frac{1+\sqrt{1-\mathcal{T}}}{2}\right)\frac{\sin\phi}{\sqrt{1-\mathcal{T}\sin^2(\phi/2)}}, \tag{4.24}$$

where $\widetilde{v}_0 = V_0/R_{\rm eff}I_0$, and $p_{1j} = 1$. In the limit $\mathcal{T} \ll 1$ with I_0 fixed, one has $s(\phi) \approx \sin\phi$, and $\widetilde{v}_0 \to \infty$ (so that $p_{0j} \approx 0$).

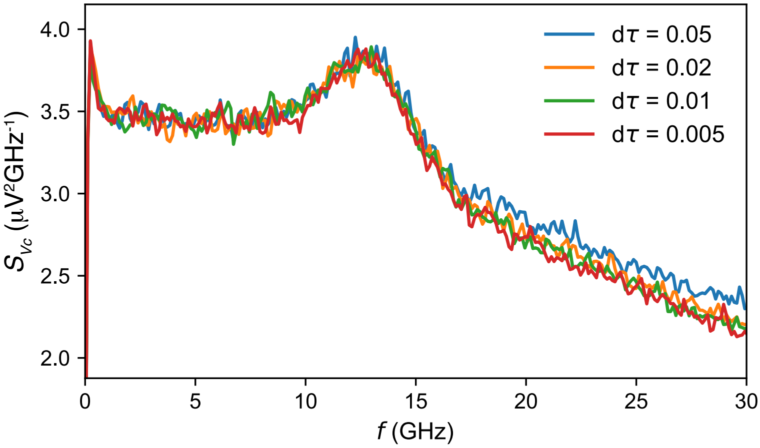

Figure 4.20: **Simulation results with varying step sizes.** Estimated PSD of $V_c(t)$ from simulations using the Euler-Maruyama update Eq. (4.21) with different step sizes $\delta\tau$, plotted versus frequency f. These results are for a trivial tunnel junction ($I_J(\phi) = I_0 \sin\phi$); circuit parameters are fixed at $r = 2.4\,\mathrm{k\Omega}$, $R_{\rm NW} = 50\,\mathrm{k\Omega}$, $R = 0.5\,\mathrm{k\Omega}$, $C = 10\,\mathrm{fF}$, $C_c = 400\,\mathrm{fF}$, $I^0_{\rm NW} = 8\,\mathrm{nA}$, $T = 150\,\mathrm{mK}$ (recall, however, that only the dimensionless ratios $\alpha, \gamma, Q, \Gamma$ appear in the equations of motion) and $\Gamma_q = 100\,\mathrm{MHz}$. The estimated PSD is essentially independent of simulation step size for $\delta\tau \lesssim 0.02$ (the deviations at larger $\delta\tau$ are likely due to aliasing of the spectrum above the Nyquist frequency). Similar results are obtained in the topological case, and for various other circuit parameter values. The simulations that were used to generate Fig. 4.4 and Supplementary Figure 4.21 were performed with a step size of $\delta\tau = 0.02$.

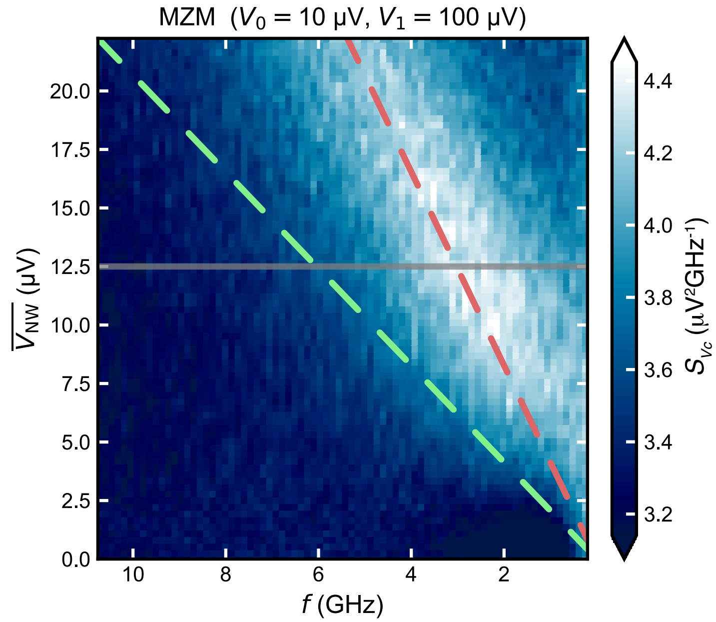

Figure 4.21: **Phase diffusion regime.** Numerically computed PSD of $V_c(t)$ for a topological junction with the indicated voltage scales for LZ tunneling between branches ($V_0 = 10\,\mu$V) and to the continuum ($V_1 = 100\,\mu$V). This plot corresponds to a zoom in of the lower right corner of Fig. 4.4c (all other circuit parameters are as specified in the Fig. 4.4c caption). Dashed green and red lines show the frequency of ideal Josephson radiation corresponding to $e^\star = 2e$ and $e^\star = e$, respectively. The horizontal gray line marks the upper boundary of the estimated phase diffusion region.

DERIVATION OF POWER SPECTRUM FOR FIXED JUNCTION VOLTAGE

If the Majorana junction is biased by a constant external voltage $V > 0$, then the phase difference across the junction increases linearly with time: $\phi(t) = \phi_0 + 2\pi\eta t$, where $\eta = (2e/h)V$. With the choice $\phi_0 = \pi$, the supercurrent at time t is given by

$$I(t)/I_m = \xi_{\lfloor \eta t \rfloor} \cos\big(\pi(\eta t - \lfloor \eta t \rfloor)\big)\,, \tag{4.25}$$

where $\lfloor z \rfloor$ denotes the integer part of z, and the random variable $\xi_n = \pm 1$ specifies the branch during the time interval $\eta t \in [n, n+1)$, i.e. between two LZ tunneling events. The probability vector

$$X_n = \begin{pmatrix} x_n^+ \\ x_n^- \end{pmatrix} = \begin{pmatrix} P(\xi_n = +1) \\ P(\xi_n = -1) \end{pmatrix} \tag{4.26}$$

evolves according to

$$X_{n+1} = \begin{pmatrix} 1-p & p \\ p & 1-p \end{pmatrix} X_n\,, \tag{4.27}$$

where $p = e^{-V_0/V}$ is the LZ tunneling probability.

The supercurrent power spectral density is defined as

$$S_I(\omega; V, V_0) = \lim_{T\to\infty} \frac{1}{T} \int_0^T \mathrm{d}t \int_0^T \mathrm{d}t' \left\langle I(t) I(t') \right\rangle e^{i\omega(t-t')} \tag{4.28}$$

(in this section, T is time rather than temperature). Using Eq. (4.25) and changing integration variables to $\tau = \eta t$,

$$S_I(\omega; V, V_0) = \lim_{T\to\infty} \frac{I_m^2}{\eta^2 T} \int_0^{\eta T} \mathrm{d}\tau \int_0^{\eta T} \mathrm{d}\tau' \left\langle \xi_{\lfloor\tau\rfloor} \xi_{\lfloor\tau'\rfloor} \right\rangle \cos(\pi(\tau - \lfloor\tau\rfloor)) \cos\big(\pi(\tau' - \lfloor\tau'\rfloor)\big)\, e^{i(\omega/\eta)(\tau-\tau')} . \tag{4.29}$$

Taking $\eta T = N$ to be a positive integer, we can write

$$\begin{aligned} S_I(\omega; V, V_0) &= \lim_{N\to\infty} \frac{I_m^2}{\eta N} \sum_{n=0}^{N-1} \sum_{n'=0}^{N-1} \int_0^1 \mathrm{d}\tau \int_0^1 \mathrm{d}\tau' \,\langle \xi_n \xi_{n'} \rangle \cos(\pi\tau) \cos\big(\pi\tau'\big)\, e^{i(\omega/\eta)(n+\tau-n'-\tau')} \\ &= \lim_{N\to\infty} \frac{I_m^2}{\eta N} \left[\sum_{n=0}^{N-1} \sum_{n'=0}^{N-1} \langle \xi_n \xi_{n'} \rangle\, e^{i(\omega/\eta)(n-n')} \right] \left| \int_0^1 \mathrm{d}\tau \cos(\pi\tau) e^{i(\omega/\eta)\tau} \right|^2 . \end{aligned} \tag{4.30}$$

One has

$$\left| \int_0^1 \mathrm{d}\tau \cos(\pi\tau) e^{i2\pi x\tau} \right|^2 = \left| \frac{x(1+e^{i2\pi x})}{2\pi(x^2 - 1/4)} \right|^2 = \frac{x^2(1+\cos 2\pi x)}{2\pi^2(x^2-1/4)^2} . \tag{4.31}$$

In the remaining term, homogeneity of the random process ξ ensures that $\langle \xi_n \xi_{n'} \rangle = \langle \xi_{n-n'} \xi_0 \rangle$. We define

$$f_n = \langle \xi_n \xi_0 \rangle . \tag{4.32}$$

Clearly, $f_0 = 1$. For $n \ge 1$, we have

$$f_n = P(\xi_n = \xi_0) - P(\xi_n = -\xi_0) . \tag{4.33}$$

By conditioning on ξ_{n-1},

$$P\big(\xi_n = \pm\xi_0\big) = (1-p) P\big(\xi_{n-1} = \pm\xi_0\big) + p P\big(\xi_{n-1} = \mp\xi_0\big) . \tag{4.34}$$

Therefore, f satisfies the recursion

$$f_{n+1} = (1-2p) f_n . \tag{4.35}$$

Since $f_0 = 1$, the solution is simply

$$f_n = (1-2p)^n . \tag{4.36}$$

Thus,

$$\begin{aligned} \lim_{N\to\infty} \frac{1}{N} \sum_{n=0}^{N-1} \sum_{n'=0}^{N-1} \langle \xi_n \xi_{n'} \rangle\, e^{i2\pi x(n-n')} &= \sum_{k=0}^{\infty} \langle \xi_k \xi_0 \rangle \left(e^{i2\pi x k} + e^{-i2\pi x k} \right) - 1 \\ &= \sum_{k=0}^{\infty} (1-2p)^k \left(e^{i2\pi x k} + e^{-i2\pi x k} \right) - 1 \\ &= \frac{1}{1-(1-2p)e^{i2\pi x}} + \frac{1}{1-(1-2p)e^{-i2\pi x}} - 1 \\ &= \frac{1-(1-2p)^2}{1+(1-2p)^2 - 2(1-2p)\cos 2\pi x} . \end{aligned} \tag{4.37}$$

Using Eqs. (4.31) and (4.37) in Eq. (4.30), we obtain

$$S_I(\omega = x \cdot 2\pi\eta; V, V_0) = \frac{I_m^2}{2\pi\eta}\left[\frac{x^2(1+\cos 2\pi x)}{\pi(x^2-1/4)^2}\right]\left[\frac{1-(1-2p)^2}{1+(1-2p)^2-2(1-2p)\cos 2\pi x}\right]. \tag{4.38}$$

Recalling that $p = e^{-V_0/V}$ and $\eta = 2eV/h$, this yields Eqs. (4.9) and (4.10).

DERIVATION OF CIRCUIT EQUATIONS

Kirchhoff's laws, applied to the circuit of Supplementary Figure 4.15, require

$$I - I_J - I_1 + I_n = I_2\,, \qquad I_2 - I_3 + I_{n2} = I_4\,, \qquad V = \widetilde{V}_1 + V_c + \widetilde{V}_2\,. \tag{4.39}$$

The current-voltage relations for the linear passive elements are

$$I = \frac{V_s - V}{r}\,, \quad I_1 = \frac{V}{R_{\mathrm{NW}}}\,, \quad I_2 = C_c\frac{\mathrm{d}\widetilde{V}_1}{\mathrm{d}t} = C_c\frac{\mathrm{d}\widetilde{V}_2}{\mathrm{d}t}\,, \quad I_3 = \frac{V_c}{R}\,, \quad I_4 = C\frac{\mathrm{d}V_c}{\mathrm{d}t}\,. \tag{4.40}$$

The ideal Josephson junction element is described by Eqs. (4.11) and (4.12):

$$\frac{\mathrm{d}\phi}{\mathrm{d}t} = \frac{2e}{\hbar}V(t)\,, \qquad I_J(t) = I_0\sin\phi(t)\,. \tag{4.41}$$

Using these relations in Eq. (4.39), we obtain

$$\begin{aligned} C_c\frac{\mathrm{d}\widetilde{V}_1}{\mathrm{d}t} &= \frac{V_s - V}{r} - I_0\sin\phi - \frac{V}{R_{\mathrm{NW}}} + I_n\,, \\ C\frac{\mathrm{d}V_c}{\mathrm{d}t} &= C_c\frac{\mathrm{d}\widetilde{V}_1}{\mathrm{d}t} - \frac{V_c}{R} + I_{n2}\,, \\ \frac{\mathrm{d}V}{\mathrm{d}t} &= \frac{\mathrm{d}V_c}{\mathrm{d}t} + 2\frac{\mathrm{d}\widetilde{V}_1}{\mathrm{d}t}\,. \end{aligned} \tag{4.42}$$

Therefore,

$$\begin{aligned} C\frac{\mathrm{d}V}{\mathrm{d}t} &= (C_c + 2C)\frac{\mathrm{d}\widetilde{V}_1}{\mathrm{d}t} - \frac{V_c}{R} + I_{n2} \\ &= \left(1 + \frac{2C}{C_c}\right)\left[\frac{V_s}{r} - \left(\frac{1}{r} + \frac{1}{R_{\mathrm{NW}}}\right)V - I_0\sin\phi + I_n\right] - \frac{V_c}{R} + I_{n2} \end{aligned} \tag{4.43}$$

and

$$C\frac{\mathrm{d}V_c}{\mathrm{d}t} = \frac{V_s}{r} - \left(\frac{1}{r} + \frac{1}{R_{\mathrm{NW}}}\right)V - I_0\sin\phi + I_n - \frac{V_c}{R} + I_{n2}\,. \tag{4.44}$$

Eqs. (4.43) and (4.44), together with Eq. (4.11), constitute the relevant equations of motion. Expressing them in terms of the quantities defined in Eq. (4.14), we arrive at the dimensionless equations of motion Eq. (4.15).

5

MULTI-ORBITAL DOUBLE QUANTUM DOT WITH SUPERCONDUCTING LEADS

Semiconductor nanowires with serial quantum dots connected to superconducting leads is a versatile platform with applications in quantum simulation and topological superconductivity. In this chapter we explore the interactions of the electron spins in a double quantum dot Josephson junction in the multi-orbital regime. We measure Yu-Shiba-Rusinov states in the weak dot-lead coupling limit and a supercurrent in the strong coupling limit. In a second device, we embed the junction in a SQUID geometry to directly measure the supercurrent amplitude and direction. As expected from theory for multi-orbital quantum dot junctions, we find – contrary to single-orbital dots – that the supercurrent can change direction within a single charge sector.

This work was performed in collaboration with R. J.J. van Gulik, D. Laroche, A. Pályi, P. Boross, G. Steffensen and A. Geresdi

5.1. INTRODUCTION

Quantum dots connected to superconducting leads allow for studying the interaction between superconductivity and single electron spins. These devices are home to a range of interesting transport phenomena, such as supercurrent reversal [52, 158], Yu-Shiba-Rusinov (YSR) states [60–62], Andreev molecules [159–161] and Kitaev chains with topologically protected states [13, 14, 80]. A common method of investigating topological states, such as Majorana zero modes, is tunnel spectroscopy [87, 162, 163]. When accidental quantum dots are present however, YSR states could mimic Majorana zero modes [62]. In this chapter, we explore the properties of YSR states and supercurrent in multi-orbital double quantum dots (DQD). We show that we can distinguish between YSR states with different electron parities and in different coupling regimes. We furthermore show that the supercurrent through an S-DQD-S junction can change direction within a charge sector.

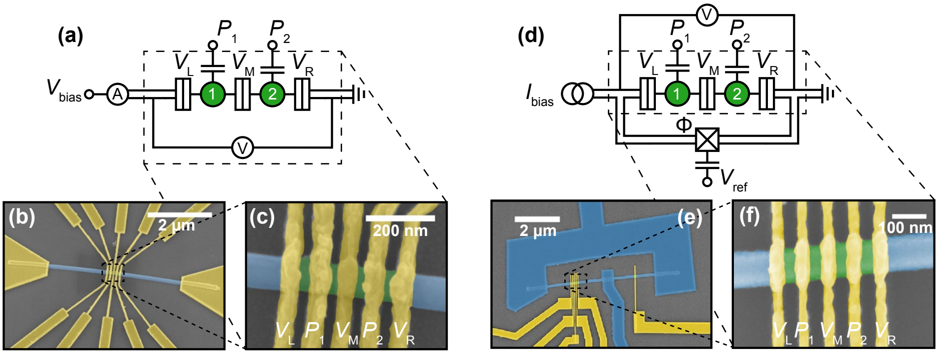

Figure 5.1: Device layouts with device 1 in **a-c** and device 2 in **d-f**. **(a)** Circuit diagram of the voltage biased S-DQD-S device. Green circles are quantum dots and the double lines indicate superconducting leads. The charge potential is controlled by P_1, P_2 and the tunnel barriers by V_L, V_M, V_R. **(b,c)** Color-enhanced electron micrograph of the full device. Superconducting Al shell of the nanowire is blue, the bare nanowire is green, Au gates and contacts are yellow. **(d)** Circuit diagram of the current biased S-DQD-S device with phase control. The superconducting (double lines) reference arm of the SQUID contains a short Josephson junction, gated by V_{ref}. **(e,f)** Color-enhanced electron micrograph of the full device. Superconducting parts of the device (Al shell of the nanowire and the NbTiN strips) are blue, the bare nanowire is green, Au gates are yellow..

The measurement data come from two different devices: a stand-alone nanowire double-quantum-dot (DQD) Josephson junction without direct control over the phase (Device 1) and a nominally identical DQD junction, that is part of a superconducting interference device (SQUID) that allows direct control over the phase (Device 2). Figure 5.1a shows the circuit of Device 1. Two quantum dots are placed in series (green discs) and are capacitively coupled to electrostatic gates (P_1,P_2) that control the charge potential. Three additional gates (V_L, V_M, V_R) control the tunnel couplings from the left lead to dot 1, between dot 1 and 2 and dot 2 to the right lead, respectively. The device is voltage biased with V_{bias} and we measure the voltage drop over the junction V in a four-terminal setup. Device 2 has a nominally identical DQD junction, that has in parallel an SNS junction with a Josephson energy tunable by an electrostatic gate V_{ref} (Figure 5.1d). This device is biased with a current source I_{bias}.

Both devices are using InAs nanowires with an epitaxial aluminum shell. The Al shell is removed where the DQD is formed by a selective wet chemical etch. The nanowires are contacted by depositing metal leads at the ends of the nanowires, made of Ti/Au (device 1, Figure 5.1b) or NbTiN (device 2, Figure 5.1e). A 10 nm dielectric layer of AlO_x is deposited by atomic layer deposition and Ti/Au electrostatic gates are evaporated on top of the normal part of the nanowire to define the DQD. On device 1 the gates are 50 nm wide, 150 nm tall and evaporated using standard physical vapor deposition, under a perpendicular angle to the substrate (Figure 5.1c). We use a multi-angle evaporation technique to conformally cover the nanowire with approximately 50 nm tall gates for device 2 (Figure 5.1f, reducing the likelihood of resist collapse that is common with high-aspect-ratio nanostructures. See section 3.1.4 for more information on this technique).

5.2. YSR STATES

The DOS of a BCS superconductor has an energy gap Δ, where no quasiparticle states are allowed. When coherently coupled to a single spinful electron, the interplay between the electron and the superconductor changes the DOS. Excitations between the doublet and singlet state of the QD will appear as in-gap states with an energy that depends on the electrostatic potential, spin of the electron and the coupling strength to the superconductor. These states are known as Yu-Shiba-Rusinov (YSR) states ζ (sometimes also called Andreev levels [62]). We investigate these YSR states in Device 1, where one of the two dots has a tunable coupling to a superconducting lead and the other dot is tuned off-resonance and is used as a tunnel probe for the QD-S system.

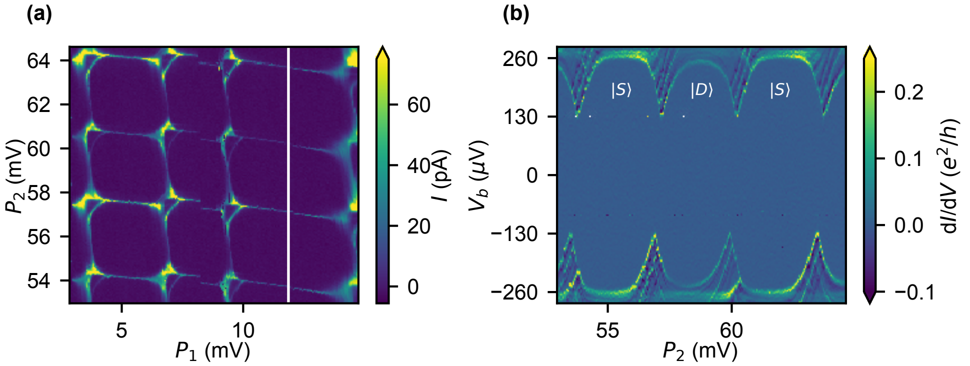

Figure 5.2: **(a)** Charge stability diagram of DQD. The peaks in current are YSR states taken at $V_b = -140\,\mu V$. The white vertical indicates the position of the scan shown in subfigure **b**. **(b)** Potential energy of the YSR dot versus V_b. YSR states (ζ) with an even-odd distinction are visible, offset by $\Delta = 130\,\mu V$ and reaching up to $\zeta = \Delta$ at $V_b = 2\Delta$.

We first establish that both dots are in Coulomb blockade by measuring a charge stability diagram (see Figure 5.2a). The diagram clearly shows a characteristic honeycomb pattern and we extract charging energies $U_1 = 1.2\,meV$ and $U_2 = 1.4\,meV$ (see Supplementary information in Chapter 5.4). Note however some unusual extra lines near the triple points. These are due to the scan being performed while the Al is in the superconducting state, implying that the lines are from YSR states instead of from Coulomb diamonds as would be the case in the normal state. Since YSR states are correlated to the expected charge of the quantum dots, the sub-gap excitations from the YSR states qualify as a good alternative for a qualitative stability diagram. The diagram is obtained at a voltage bias $V_b = -140\,\mu\text{eV}$ just above the superconducting gap $\Delta = 130\,\mu\text{eV}$.

The inter-dot coupling is tuned to $\tau = 7\,\mu\text{eV}$ such that it functions as a tunnel probe only and the interaction with the YSR dot is minimal (see supplementary figure 5.9 and table 5.1). Figure 5.2b shows a tunnel-spectroscopy scan of the YSR dot, in this case dot 2, using dot 1 as the tunnel probe. It is important to note here that the dot used as a tunnel probe is also connected to a superconducting lead. The DOS of the tunnel probe itself are convolved with the DOS of what it measures, in this case the YSR states in dot 2. This results in a shift of the YSR spectrum by Δ, which is clearly visible in Figure 5.2b.

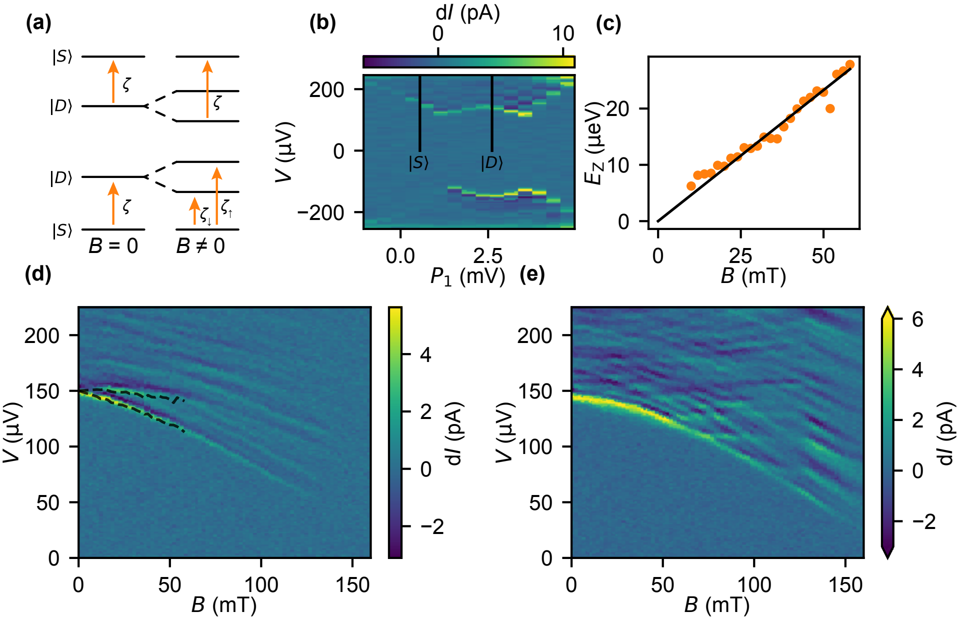

Figure 5.3: **(a)** Possible excitations (in orange) between the ground state and first excited states, at $B = 0$ (left) and $B \neq 0$ (right). The lower diagram illustrates the measurable transitions from a singlet ground state to the first excited state: $\zeta_\uparrow$ and $\zeta_\downarrow$. The upper diagram illustrates it for a doublet ground state, with only one transition. **(b)** Overview scan, the black lines denote the positions of magnetic field dependent scans in **d** and **e**. **(c)** Landé g-factor fit to Zeeman energy obtained from $\zeta_\uparrow - \zeta_\downarrow$, extracted from the data in **d**. **(d)** Magnetic-field dependent scan of the $|S\rangle$ ground state. The black dashed lines show the extracted voltages from the peak finding procedure. **(e)** Magnetic-field dependent scan of the $|D\rangle$ ground state.

For this scan, the YSR dot is weakly coupled to the superconducting lead and the states are visible as sharp peaks in conductance with an dependence on the potential controlled by the plunger gate. The shape of the YSR state depends on the parity of the quantum dot. At $P_2 \approx 55\,\text{mV}$ the quantum dot has a singlet ground state $|S\rangle$ and the doublet state energy becomes approximately equal to the superconducting gap and so the YSR state goes to Δ. Increasing P_2 lowers ζ in energy and crosses zero at the charge degeneracy point. Now in the doublet ground state $|D\rangle$ sector, ζ forms a sort of arc and does not quite reach Δ. When a metallic, instead of a superconducting, probe would be used, the positive and negative arcs would form a loop structure around $V = 0$. The maximum value of ζ in the doublet ground state sector depends on the coupling to the superconductor Γ_S, higher coupling means higher maximum ζ [60–62]. Above the YSR states we see additional states, most likely from the DOS of the probe dot.

We verify the singlet and doublet nature of the ground state by taking magnetic field dependent scans in both parity states. When the dot is in a singlet ground state, two excitations should be visible due to lifting of the degeneracy of the excited doublet state. When the dot is in a doublet ground state however, only one transition will be visible. The probability for the doublet-to-singlet transition that requires a spin flip, is too low to give measurable resonance line. Figure 5.3a illustrates the different excitations for doublet and singlet ground states. In Figure 5.3b a scan is shown with a doublet and singlet ground state visible, it shows the positions where take magnetic field dependent scans with white lines.

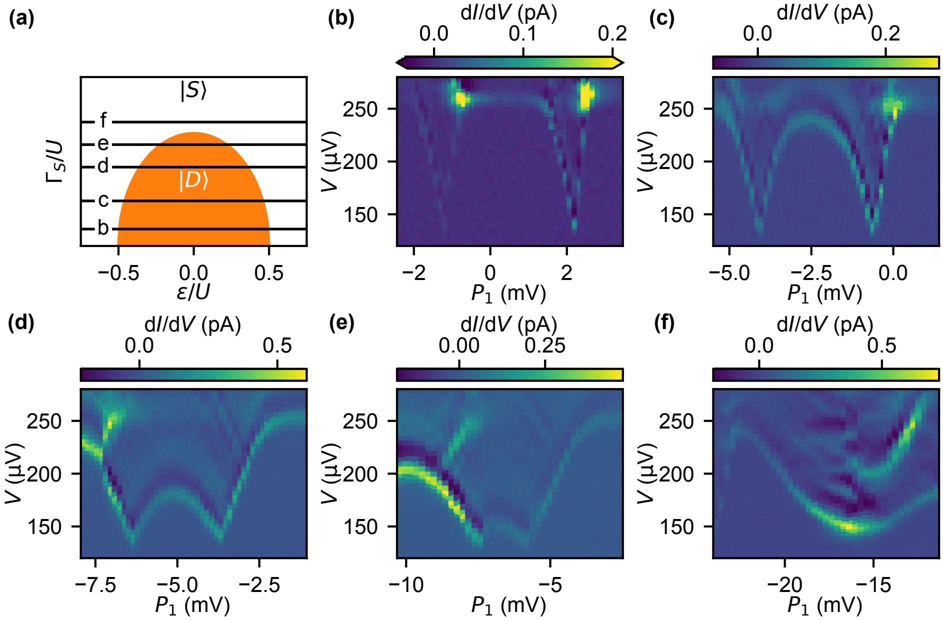

Figure 5.4: **(a)** Qualitative phase diagram of YSR QD. In the orange region the ground state is a doublet configuration and the white area represents a singlet ground state. The black lines roughly indicate the position in this parameter space of the scans in the subfigures **b-f** **(b-f)** Tunnel spectroscopy scans of the YSR QD with increasing Γ_S, where **a** has a weakest and **f** the strongest coupling to superconducting lead. The gate voltages V_L of **b-f** are −770 mV, −760 mV, −750 mV, −745 mV, −705 mV respectively. The conductance is numerically derived.

When we follow the doublet ground state sector in magnetic field (Figure 5.3d), we see the lowest resonance moving to lower energy but no splitting. This is in contrast to the scan in the singlet ground state sector, where we see a clear splitting (Figure 5.3e). By extracting the energy difference of the two resonance lines and plotting it versus magnetic field, we extract a g-factor of 8 (Figure 5.3c). The decrease in energy with increasing magnetic field that is observed for both sectors is expected from a decrease in Δ.

Competition between several energy scales determine if a singlet or a doublet ground states is energetically favorable: Δ, Γ_S, U and the detuning of the dots ϵ. Of these scales, we have easy control over Γ_S through an electrostatic gate. We use this control to reach different superconducting coupling regimes. Figure 5.4 shows five datasets with increasingly higher Γ_S. In Figure 5.4a we plot a qualitative phase diagram of the YSR QD and estimate the positions in this parameter space of the scans in the other subfigures. We do this by judging the shape of the YSR states as we increase the coupling to the superconductor Γ_S with V_L. The scan with the lowest coupling has $\Gamma_S \ll U$, as the YSR state touches the gap even in the odd sector. In the intermediate coupling regime (Figure 5.4d) we clearly see ζ crossing zero energy at $V_b = \Delta$. Moving to the last subfigure, we find ζ never crosses zero and we conclude that here $\Gamma_S > U$ [62, 69].

5.3. SUPERCURRENT

Another key phenomenon of the S-DQD-S device, is supercurrent. In an S-N-S Josephson junction, Cooper pairs are carried by Andreev bound states from one lead to another and allow a supercurrent to flow. When a quantum dot with $U > \Delta$ replaces the normal area, Coulomb repulsion and the level structure of the dot strongly affects the behavior of the supercurrent. The parity of single-level quantum dots determine the direction of the supercurrent: positive for an even and negative for an odd parity (see Ch. 6) [52, 158]. This also holds for S-DQD-S junctions, the total parity of the DQD dictates the sign of the supercurrent [53]. Here we discuss the multi-level regime, where the level spacing of the dot is small enough for higher-lying orbitals to also play an important role in transport and the simple even-odd rule is no longer universal.

With the addition of the extra levels, determining the sign of the supercurrent becomes more involved. Contributions from all levels with an appreciable tunneling probability have to be considered. Besides the breakdown of the even-odd rule, this can also lead to sign change within a charge sector. This was first observed in a single dot junction by van Dam *et al.* [52].

Figure 5.5a shows a minimal system to describe a multi-level system. In left dot we consider two levels with lead couplings $t_{\mathrm{L},1}$, $t_{\mathrm{L},2}$, while the right dot is single-level. Figure 5.5b shows a possible path the electrons can take from the left lead to the right. It is split up in the spin-up (yellow) and spin-down (green) part of a Cooper pair. Counting the number of times a spin encounters the same spin on its path N_σ, where σ is the spin, then determines the supercurrent sign for this path by evaluating $(-1)^{N_\uparrow + N_\downarrow}$ [1]. Following these simple rules for each path and adding summing all paths with their corresponding amplitudes, gives the total current. A numerical simulation is shown in Figure 5.5d. On the horizontal axis, the energy of both dots is changed simultaneously. The amplitudes of the paths depend on many electrostatic parameters of the system and determining all of them is not an easy task. Therefore this simulation serves as an example using a min-

---

[1] This approach is developed by Gorm Steffensen.

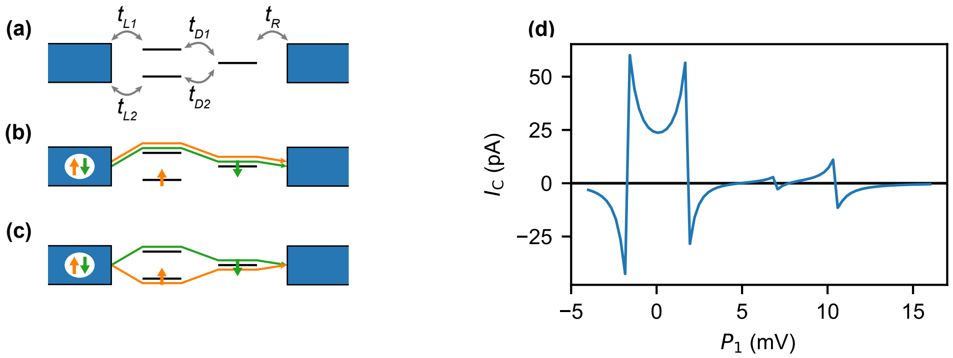

Figure 5.5: **(a)** Schematic drawing of a minimal multi-orbital S-DQD-S system. Leads are shown in blue and quantum dot levels in horizontal black lines. The arrows denote the relevant couplings. **(b,c)** An example configuration with an even number of electrons. The colors denote the spin direction, with yellow for up and green for down spin. Two situations are shown, corresponding to two different parts of a charge sector, resulting in different supercurrent signs. **(d)** Numerical simulation of the supercurrent in a multi-orbital DQD junction, with sign flips within a charge sector.

imal model that qualitatively reproduces key features of the multi-orbital supercurrent characteristics.

Figure 5.6a shows a supercurrent stability diagram of the multi-level DQD of device 1, without explicit control over the phase. The data is taken at $V = 0$, with the color scale representing differential current (with a 2 µV bias excitation). The abrupt changes in amplitude coincide with boundaries of charge sectors.

To investigate the multi-level nature of this DQD, we measure the supercurrent more carefully along two horizontal linecuts, shown in yellow (Fig. 5.6b) and red (Fig. 5.6c). In the lower panels, we plot an estimate of the critical current magnitude $|I_C|$. This is obtained by fitting the $I(V)$-curve for each plunger value with the finite temperature solution of Ivanchenko and Zil'bermann [42] for Josephson current. Note that is only an estimate, since we do not have an independent measure of the environmental impedance.

Looking at the evolution of the I_C with plunger voltage, we see a pattern very similar to that of Fig. 5.5d. Note that since we have no control over the phase we cannot directly measure a negative I_C. One might expect the critical current magnitude to still go to zero when changing sign, which is not the case in the data. This is likely due to temperature broadening effects, smoothing the transition.

To directly measure the sign of the supercurrent we switch to device 2, where we measure the switching as a function of phase over the junction. The DQD junction is connected in parallel with a regular S-N-S Josephson junction with a Josephson current much larger than that of the part of the S-DQD-S junction, thereby creating an asymmetric SQUID (see Fig. 5.1d,e). By applying a flux through the loop area we control the phase over the S-DQD-S junction (see section 2.3.1). To measure the switching current, we apply a current-bias ramp and monitor the measured voltage over the junction. When the voltage switches from zero to a finite value, we record the current bias which is equal to the switching current (see section 3.2.2).

In Figure 5.7a we plot a stability diagram with the I_{DQD}, the switching current of the

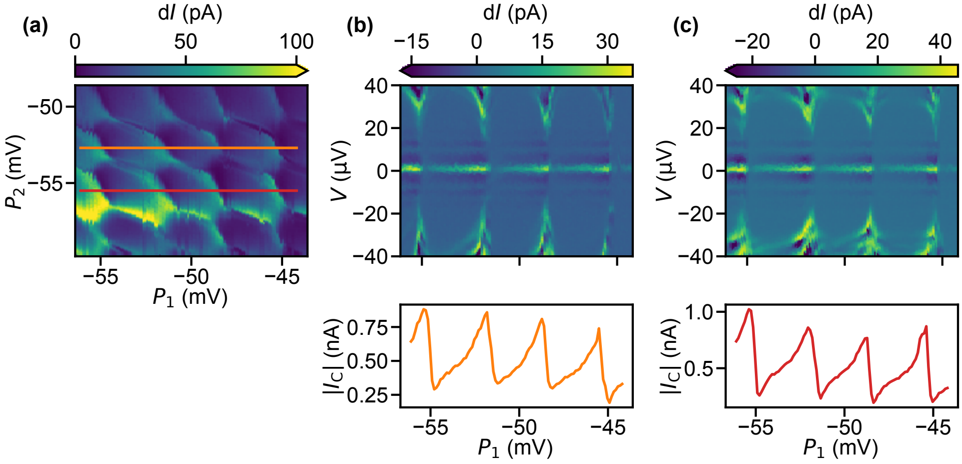

Figure 5.6: **(a)** Supercurrent charge stability diagram. Data is differential current from a 2 µV voltage-bias lock-in excitation at 78 Hz. **(b,c)** Upper panels: differential current as a function of V versus P_1. Lower panels: extracted I_C magnitude estimate from a fit to the finite temperature solution of Ivanchenko and Zil'bermann [42].

DQD. We remove the contribution of the reference arm in the SQUID by recording two datasets, with a π phase difference between them. We then get the DQD component by taking half of the difference of I_{DQD}:

$$I_{\mathrm{DQD}} = (I_{\mathrm{SW},0} - I_{\mathrm{SW},\pi})/2, \tag{5.1}$$

where $I_{\mathrm{SW,n}}$ is the average of around 20 switching currents. It is important to note that this methods is only valid when the CPR is sinusoidal.

A more reliable method is to measure the entire CPR for each plunger value and extract I_{DQD}, I_{ref} from fitting each CPR. In the upper panel of Figure 5.7c, we show the measured SQUID CPR for every point along P_2 of the blue line in subfigure **a**. Note that here, every pixel in this panel is an average of around 20 switching currents. Plotted in the lower panel, are the extracted I_{ref} and I_{DQD}. For the fits we assume a sinusoidal CPR and find an almost identical I_{DQD} when we compare it to the linecut in the upper panel of Figure 5.7b, where we used Equation 5.1 – suggesting that the CPR is indeed sinusoidal. In Figure 5.7d, we plot the fitted CPR on top of all the switching currents for two values of P_2, highlighted in subfigure **c** in green and red.

Note that I_{ref} is not completely constant, but increases in amplitude whenever the magnitude of I_{DQD} increases. This is because the two junctions are part of each other's environmental impedance. When the DQD has a higher switching current it has a lower impedance and thus less voltage fluctuation which results in a higher switching current in the reference junction.

In conclusion, we have investigated the interplay of superconductivity with the spin configuration of electrons in a DQD. We have shown the presence of YSR states and were able to confirm the distinction between doublet and singlet ground states using

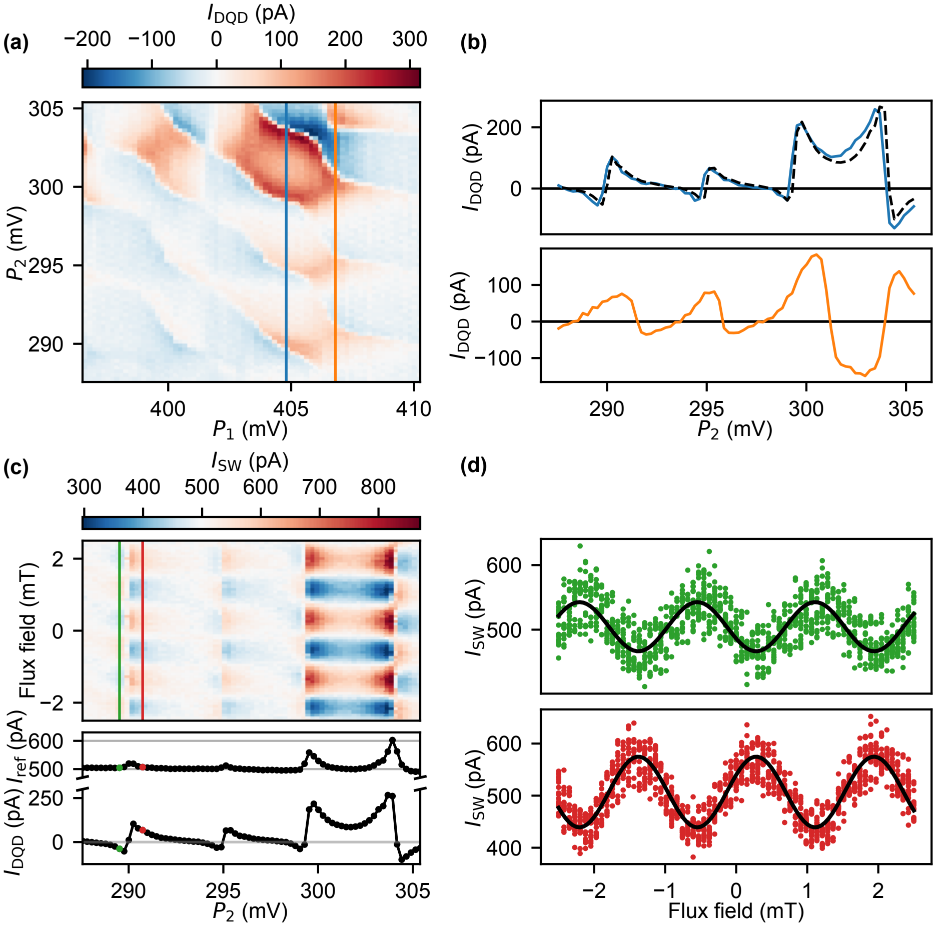

Figure 5.7: Device 2 multi-orbital supercurrent results. **(a)** Supercurrent charge stability diagram, obtained from $(I_{\mathrm{SW},0} - I_{\mathrm{SW},\pi})/2$. **(b)** Upper panel: vertical linecut (blue line in **a**) with sign changes inside charge sectors. The black dashed line is I_{DQD} extracted from a fit to the full CPR in subfigure **a**. Lower panel: vertical linecut one charge state further (orange line in **a**). **(c)** Upper panel: full CPR of the blue vertical line in **a**. Lower panel: I_{ref} and I_{DQD} extracted from fitting a sinusoidal function to the CPR. The 1σ error bars are too small to be noticeable. Two best fit examples are shown in **d**, marked in green (upper panel) and red (lower panel).

an magnetic field. We have furthermore shown control over the coupling to the leads. In addition, we have investigated the influence of the multi-orbital nature of the DQD on the supercurrent through the S-DQD-S junction, both without and with control over the phase.

5.4. SUPPLEMENTARY INFORMATION

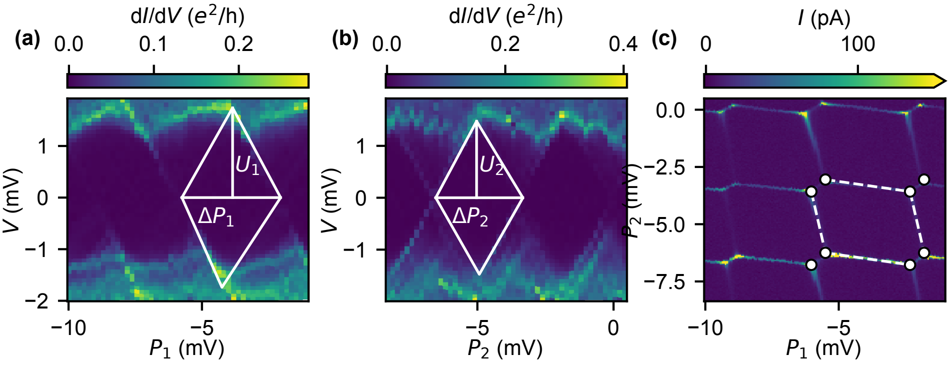

Figure 5.8: **Normal-state characterization scans.** **(a)** Coulomb diamonds of dot 1. **(b)** Coulomb diamonds of dot 2. **(c)** Charge-stability diagram.

Electrostatic parameters from device 1 are estimated both in the normal state and superconducting state. We quench superconductivity with an out-of-plane magnetic field $B_\perp = 0.5\,\mathrm{T}$. We start by extracting the lever arms α_{11} and α_{22} from Coulomb diamond scans in Figure 5.8a,b. Next we find the cross-coupling lever arms α_{21} (P_2 acting on dot 1) and α_{12} (P_1 acting on dot 2) from the stability diagram in Figure 5.8 (see Table 5.1). We assume that the lever arms stay constant in magnetic field and throughout the experiments. This is almost certainly not entirely accurate when changing the dot's potentials over a large range. However, in this chapter we are mostly concerned about order of magnitude estimates of these parameters. Therefore this approximation is sufficient.

In the data shown in Figures 5.2, 5.3 and 5.4, one dot is used as a tunnel probe for the other dot. Hence, it is important that the coupling between the dots is much smaller than the other energy scales Δ and U. Figure 5.9 shows avoided crossings at the triple points of normal-state stability diagrams, at tunnel gate values V_M equal to those used in Figures 5.2, 5.3 and 5.4. We extract the inter-dot coupling τ using a model described by a one-electron Hamiltonian [56]

$$H_{\mathrm{coupling}} = \begin{pmatrix} \epsilon_1 & \tau \\ \tau & \epsilon_2 \end{pmatrix}, \tag{5.2}$$

where ϵ_i is the on-site energy of dot i. Extracted tunnel couplings are listed in table 5.1 together with the other extracted parameters for device 1.

Device 2 is the same device as used for Chapter 6, but in a different plunger gate range. Therefore the electrostatic parameters are very similar. See 6.1 the electrostatic parameters extracted for Chapter 6.

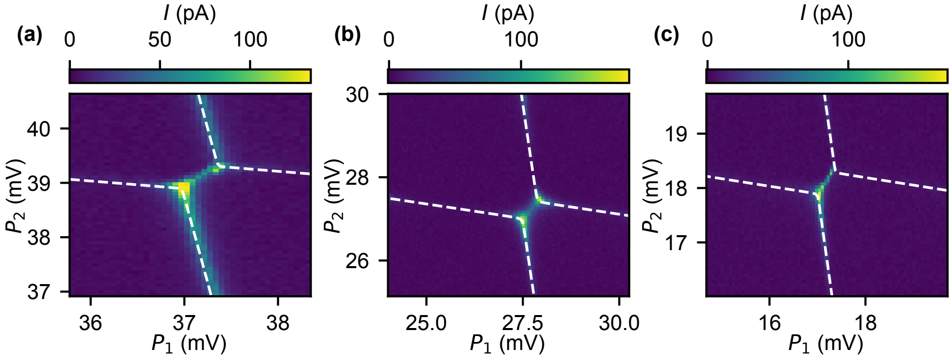

Figure 5.9: Tunnel couplings corresponding to **(a)** Figure 5.2 **(b)** Figure 5.3 **(c)** Figure 5.4.

Table 5.1: Electrostatic parameters of the device 1. τ_1, τ_2, τ_3 correspond to Figures 5.2, 5.3 and 5.4 respectively.

Quantity	Extracted value
U_1	1.2 meV
U_2	1.4 meV
U'	0.2 meV
α_{11}	0.47
α_{12}	0.074
α_{21}	0.064
α_{22}	0.461
C_m	0.018 fF
$C_{1(2)}$	0.132 fF (0.116 fF)
$C_{P_1(P_2)}$	0.043 fF (0.050 fF)
$C_{l(r)}$	0.07 fF (0.048 fF)
τ_1	7 µeV
τ_2	18 µeV
τ_3	9 µeV

6

TRIPLET-BLOCKADED JOSEPHSON SUPERCURRENT IN DOUBLE QUANTUM DOTS

D. Bouman, R. J. J. van Gulik, G. Steffensen, D. Pataki, P. Boross,
P. Krogstrup, J. Nygård, J. Paaske, A. Pályi, A. Geresdi

Serial double quantum dots created in semiconductor nanostructures provide a versatile platform for investigating two-electron spin quantum states, which can be tuned by electrostatic gating and external magnetic field. In this work, we directly measure the supercurrent reversal between adjacent charge states of an InAs nanowire double quantum dot with superconducting leads, in good agreement with theoretical models. In the even charge parity sector, we observe a supercurrent blockade with increasing magnetic field, corresponding to the spin singlet to triplet transition. Our results demonstrate a direct spin to supercurrent conversion, which can be exploited in hybrid quantum architectures coupling the quantum states of spin systems and superconducting circuits.

This chapter has been published as arXiv:2008.04375.

Semiconductor quantum dots, where the orbital and spin states of single localized electrons can be controlled [164], are one of the leading platforms for quantum information processing [165]. Specifically, double quantum dots (DQDs) connected in series [58] became the preferred physical implementation of spin [166], and spin-orbit quantum bits [167] in low-dimensional semiconductor nanodevices, such as heterostructures hosting a two-dimensional electron gas or semiconductor nanowires. In these devices, the readout of the spin quantum state relies on spin-dependent single electron tunneling processes, which then enable charge readout via direct electronic transport [164], charge sensing techniques [168], or dipole coupling to a microwave resonator [169, 170].

In a superconducting nanodevice, the dissipationless supercurrent I_S at zero voltage bias is driven by the quantummechanical phase difference φ up to a maximum amplitude, I_C, the critical current [103]. In the lowest order of tunneling, the supercurrent-phase relationship (CPR) [171] is sinusoidal, $I_S(\varphi) = I_C \sin(\varphi)$, which describes the coherent transfer of single Cooper pairs through the weak link. When the weak link is a non-magnetic tunnel barrier, a zero phase difference is energetically favorable in the absence of supercurrent, which is described by a positive critical current, $I_C > 0$. In contrast, a negative coupling yields a supercurrent reversal, $I_C < 0$, often denoted a π junction due the π phase shift in the CPR. This negative coupling has been observed in ferromagnetic weak links [172, 173], out-of-equilibrium electron systems [174] and semiconductor quantum dot junctions [175, 176].

The dependence of the critical current on the spin- and charge state of a DQD has also been addressed theoretically [74, 177–181], and the recent progress in materials science of superconductor-semiconductor hybrid nanostructures [89] enabled measurements of the amplitude of the critical current as well [182, 183], in correlation with the charge states of the DQD.

In this Letter, we report on direct measurements of the CPR through a DQD weak link formed by an electrostatically gated InAs nanowire. By employing a phase-sensitive measurement scheme, where the DQD is embedded in a superconducting quantum interference device (SQUID), we characterize the full CPR of the DQD, enabling a signful measurement of I_C. The direct observation of the supercurrent reversal in the total charge number boundaries allowed us to identify the even and odd occupied states. Finally, the magnetic-field dependence of the supercurrent amplitude in the even occupied state reveals the presence of a supercurrent blockade in the spin triplet ground state, in agreement with numerical calculations.

We built our device (Fig. 6.1) from an approximately 7 μm long InAs nanowire grown by molecular beam epitaxy, and *in-situ* partially covered by a 6 nm thick epitaxial aluminum shell with a typical superconducting gap of $\Delta \approx 200\,\mu$eV [89, 184]. We formed two segments with the aluminum layer selectively removed where the DQD and the reference arm would be defined. Next, we created the SQUID loop from a sputtered NbTiN superconducting film, and covered the device with a 10 nm thick AlO$_x$ dielectric by conformal atomic layer deposition. Finally, 40 nm wide and 50 nm thick Ti/Au gates (in yellow in Fig. 6.1a) were evaporated under three angles to ensure a conformal coverage around the wire (schematically shown in Fig. 6.1b). Five gates defined the DQD (on the right) and a single gate controlled the reference arm (on the left in Fig. 6.1c). Details on the device fabrication are shown in the Supplementary Information. All of our measurements were

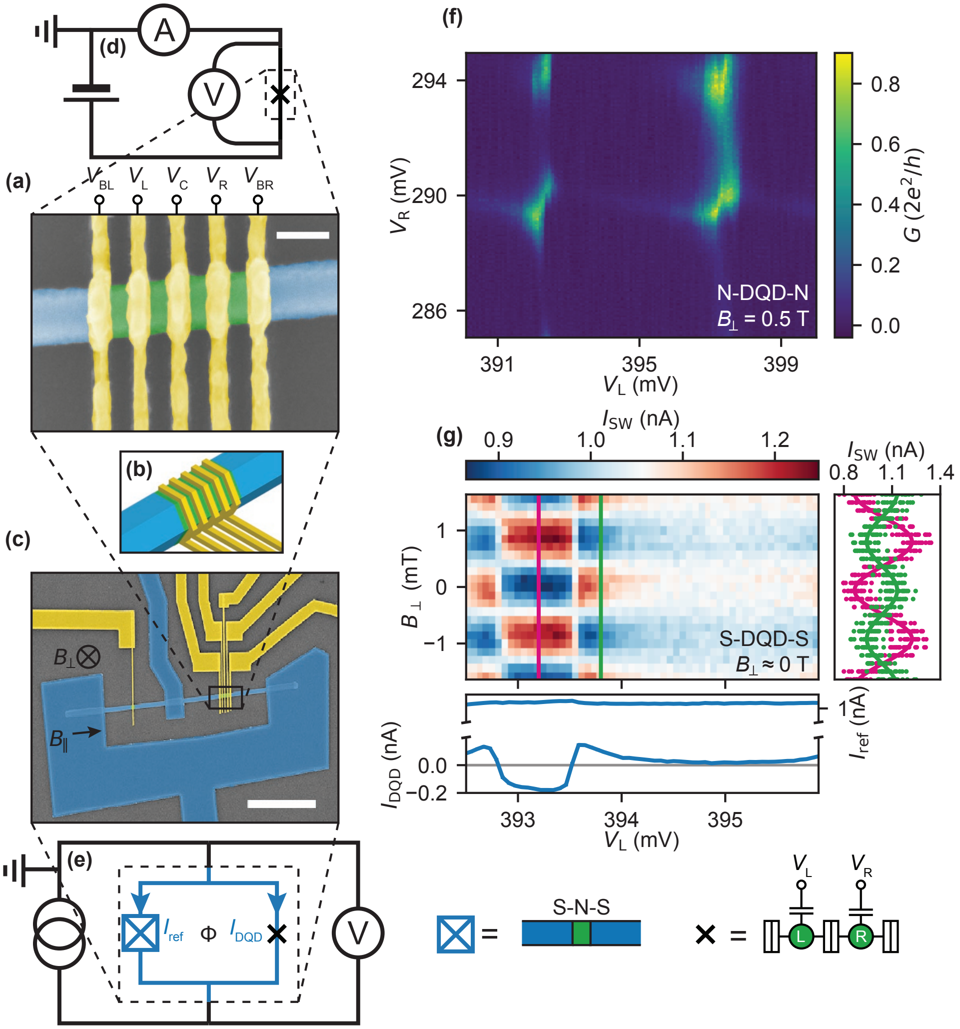

Figure 6.1: Device layout and characterization. (a) Color-enhanced electron micrograph of the nanowire DQD junction with five wrap-around gates (yellow) which provide the confining potential. The $V_{\rm BL}, V_{\rm C}$ and $V_{\rm BR}$ gate voltages define the barriers, while $V_{\rm L}$ and $V_{\rm R}$ control the number of electrons on the dots. The aluminum shell (blue) is selectively etched away in the weak link section (green denotes bare InAs). The scale bar denotes 100 nm. (b) Perspective drawing of the DQD junction highlighting the conformal gates. (c) Color-enhanced electron micrograph of the DC SQUID made of sputtered NbTiN film (in blue) with the reference junction in the left arm and the DQD junction in the right arm. The scale bar denotes 2 μm. (d) The circuit diagram for the normal-state characterization with the reference arm depleted. (e) The measurement scheme of the switching current measurements in the SQUID geometry. (f) Charge stability diagram of the DQD in the normal state at a large magnetic field $B_\perp = 0.5$ T. (g) Switching current color map through three charge states of the DQD and the flux Φ induced by a small $B_\perp$. Each pixel is an average of 18 measurements. The side panel shows all switching current data taken along the magenta and green line, respectively. The solid lines denote the sinusoidal fit yielding the signful oscillation amplitude $I_{\rm DQD}$ and offset $I_{\rm ref}$, see text. The bottom panel displays the fitted $I_{\rm ref}$ and $I_{\rm DQD}$. The DQD was tuned along the total energy axis (see the solid black line in Fig. 6.2a) and we display the corresponding $V_{\rm L}$ range on the horizontal axis.

performed in a dilution refrigerator with a base temperature of approximately 30 mK.

We first characterize the DQD with the leads driven to the normal state by a large magnetic field, $B_\perp = 0.5\,\mathrm{T}$. We measure the differential conductance $\mathrm{d}I/\mathrm{d}V$ of the DQD with the reference arm fully depleted (Fig. 6.1d). We control the coupling to the leads with the gate voltages V_{BL} and V_{BR}, and the interdot coupling is tuned by V_{C} (Fig. 6.1a). A characteristic honeycomb diagram is plotted in Fig. 6.1f, where the charge occupancy of the dots $(n_{\mathrm{L}}, n_{\mathrm{R}})$ is set by the voltages applied on the two plunger gates, V_{L} and V_{R}.

We perform the CPR measurements with the leads being superconducting and with the reference arm of the SQUID opened with its electrostatic gate so that it exhibits a higher critical current than the DQD arm. Due to this asymmetry, the phase drop over the DQD junction is determined by the magnetic flux Φ through the SQUID loop area (Fig. 6.1e) [175, 185], which is proportional to the applied magnetic field $B_\perp$. We measure the switching current I_{SW} of the SQUID by ramping a current bias in a sawtooth waveform and recording the bias current value when the junction switches to the resistive state marked by a threshold voltage drop of the order of $10\,\mu\mathrm{V}$. We show a typical dataset in Fig. 6.1g, where each pixel in the main panel is an average of 18 measurements. The right sidepanel shows the raw datapoints at two plunger gate settings denoted by the magenta and green lines in the main panel, as well as the fitted sinusoidal curves in the following functional form:

$$I_{\mathrm{SW}} = I_{\mathrm{ref}} + I_{\mathrm{DQD}} \sin\varphi, \tag{6.1}$$

where $\varphi = 2\pi(B_\perp - B_{\mathrm{o}})/B_{\mathrm{p}}$, with $B_{\mathrm{p}} \approx 1.7\,\mathrm{mT}$ being the magnetic field periodicity corresponding to a flux change equal to the superconducting flux quantum $\Phi_0 = h/2e$ and B_{o} being the offset perpendicular magnetic field. The switching current values I_{ref} and I_{DQD} represent the reference arm and the DQD junction contributions, respectively. We show these fitted values as a function of the gate voltage V_{L} in the lower subpanel of Fig. 6.1g, which displays the sign change of I_{DQD} at the charge state boundaries. We note that the change in the environmental impedance [186] causes a slight modulation of I_{ref} as well, despite the lack of any capacitive coupling between the two weak links. However, in our measurements $I_{\mathrm{ref}} > 5|I_{\mathrm{DQD}}|$ is always fulfilled, enabling a reliable observation of the supercurrent reversal in the DQD.

In Fig. 6.2a, we plot I_{DQD} as a function of the plunger gate voltages V_{L} and V_{R}, resulting in the zero magnetic field charge stability diagram of the DQD mapped by the supercurrent. Remarkably, our phase-sensitive measurement directly shows that the supercurrent reversal is associated with the change in the total charge number, and it is absent in the case of internal charge transfers with $(n_{\mathrm{L}}, n_{\mathrm{R}}) \to (n_{\mathrm{L}} \pm 1, n_{\mathrm{R}} \mp 1)$. However, $|I_{\mathrm{DQD}}|$ exhibits maxima near all charge boundaries, consistently with earlier experiments [183].

We understand this data using a two-orbital Anderson model, where each dot with an on-site charging energy U_i hosts a single spinful level at ε_i with the dot index $i = \mathrm{L}, \mathrm{R}$. In the experiment, this corresponds to a quantum dot orbital level spacing which is larger than the charging energy [175]. We consider an interdot charging energy term $U_{\mathrm{C}} n_{\mathrm{L}} n_{\mathrm{R}}$ and an effective interdot tunneling amplitude t_{C}. The tunnel coupling energies to the superconducting leads are denoted by $\Gamma_{\mathrm{L,R}}$.

We consider the leading term of the supercurrent in the weak coupling limit where $t_{\mathrm{C}}, \Gamma_{\mathrm{L}}, \Gamma_{\mathrm{R}} \ll \Delta \ll U_i$ [179, 187], and evaluate the current operator $I(\varphi) = i\frac{e}{\hbar}[H, n_{\mathrm{R}}]$, where

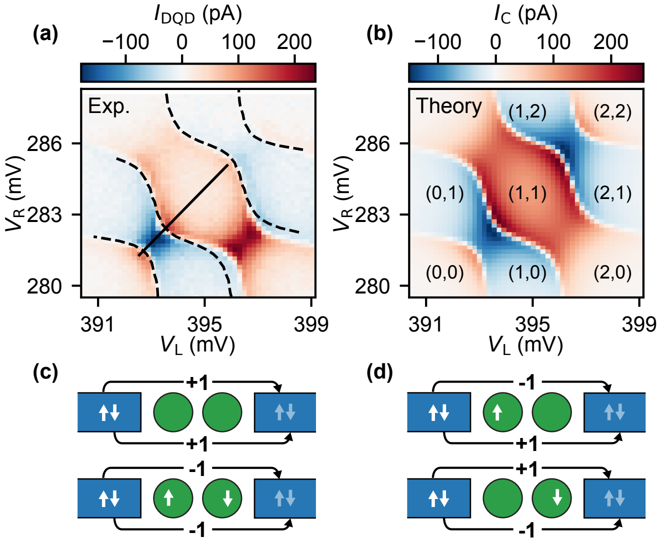

Figure 6.2: The supercurrent charge-stability diagram at zero magnetic field. (a) Colormap of the measured I_{DQD} as a function of the plunger gate voltages V_L and V_R revealing a supercurrent sign reversal between the adjacent total charge sectors. The dashed lines denote the numerically calculated charge boundaries, see the text. Measurements along the solid line are shown in Fig. 6.1g and Fig. 6.3a. (b) The ZBW calculation of the critical current I_C of the DQD using the same parameters. The charge occupation of the dots is indicated in brackets. Visual representations of a Cooper pair transfer when the DQD has an even (c) and odd charge occupation (d). The ±1 values indicate the spin permutation parity for each spin species, which yields a supercurrent reversal for an odd charge occupation of the DQD, see the text.

H is the Hamiltonian of the system at a phase difference of φ between the superconducting leads (see the Supplementary Information). We numerically evaluate $\langle I(\varphi)\rangle = I_C \sin\varphi$ to find the signful I_C. We perform a global fit of the calculated sign reversal contours (see dashed lines in Fig. 6.2a) against the experimental dataset and recover $U_L = 596.6\,\mu$eV, $U_R = 465.9\,\mu$eV, $U_C = 41.5\,\mu$eV and $t_C = 85\,\mu$eV. We match the critical current amplitude scale with the experimental data by setting $\Gamma_L = \Gamma_R = 33.2\,\mu$eV. The width of the even-odd transitions establishes an upper bound on the electron temperature of the DQD, $T < 80\,$mK. We use these parameters to display $I_C(V_L, V_R)$ in Fig. 6.2b and find a good correspondence with the experimental data using a zero bandwidth (ZBW) approximation [183, 188], see the Supplementary Information.

The observed supercurrent reversal [158, 175] is linked to the number of permutations of fermion operators required to transfer a spin-singlet Cooper pair through the DQD (see the Supplementary Information). In the weak coupling limit, this amounts to counting the number of same-spin dot electrons, which each electron in the Cooper pair crosses. Each such crossing contributes with a factor of -1 to I_C, which we illustrate for a DQD with even (Fig. 6.2c), and odd charge occupations (Fig. 6.2d). Consequently, the sign of I_C is determined by the ground-state charge parity of the DQD.

Next, we focus on the magnetic-field dependence of I_{DQD} (Fig. 6.3a) along the total energy axis (solid line in Fig. 6.2a) spanning both even and odd charge states. At

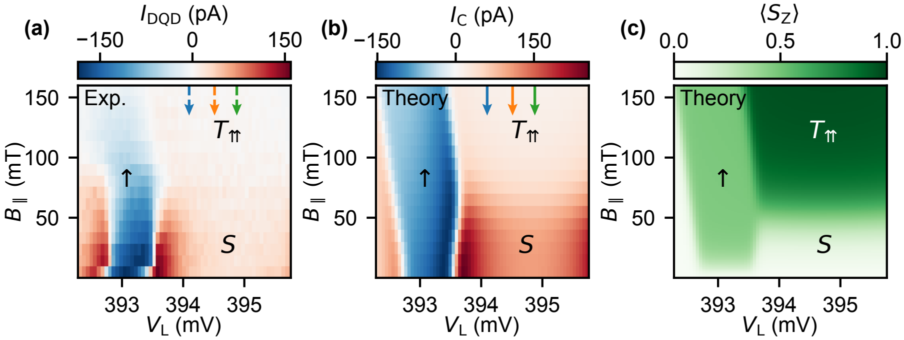

Figure 6.3: The superconducting DQD in finite magnetic fields. (a) The measured signful supercurrent oscillation amplitude I_{DQD} as a function of the total energy (see the solid line Fig. 6.2a) and magnetic field. Note the slight charge shift between the zero magnetic field line and the rest of the data. (b) The corresponding ZBW calculation of the signful critical current, see the text. (c) The calculated spin expectation value in the ground state showing the singlet to triplet transition in the even occupied state as a function of the magnetic field. In panels (b) and (c), we use the parameters extracted in Fig. 6.2b.

$B_{\parallel} = 0$, a finite t_{C} results in a singlet-triplet splitting Δ_{ST} in the even occupied $(1,1)$ charge state [164]. We model the DQD with an effective identical g-factor on both dots, which results in a spin-polarized triplet ground state above a threshold magnetic field, $B_{\mathrm{ST}} = \Delta_{\mathrm{ST}}/(g^{*}\mu_{\mathrm{B}})$. To account for spin-orbit coupling, we refine our interdot tunneling Hamiltonian to include both spin-conserving and spin-flip tunneling amplitudes, t_0 and t_{x}, resulting in an effective $t_{\mathrm{C}} = \sqrt{t_0^2 + t_{\mathrm{x}}^2}$ (see the Supplementary Information).

With a global fit to the experimental data (Fig. 6.3a,b), we extract $t_0 = 80\,\mu\mathrm{eV}$, $t_{\mathrm{x}} = 30\,\mu\mathrm{eV}$ and $g^{*} = 15.9$. This g-factor is in agreement with earlier experimental values measured on InAs quantum dots [167, 189–191] and ballistic channels with superconducting leads [184, 192]. We estimate the spin-orbit length $l_{\mathrm{SO}} = l_{\mathrm{dot}}\, t_0/(\sqrt{2}t_x) \approx 75\,\mathrm{nm}$ [193], using the gate pitch as an estimate of the dot length, $l_{\mathrm{dot}} = 40\,\mathrm{nm}$. This coupling length yields an energy scale $E_{\mathrm{SO}} = \hbar^2/(2m^{*}l_{\mathrm{SO}}^2) = 290\,\mu\mathrm{eV}$ with an effective electron mass of $m^{*} = 0.023m_e$, which is similar to earlier experimental results on semiconductor nanowires in the presence of strong electrostatic confinement [194, 195].

In Fig. 6.3c, we plot the calculated expectation value $\langle S_Z\rangle$ of the total spin z component of the DQD, which visualizes the transition between the spin singlet state $\langle S_Z\rangle = 0$ and the spin-polarized triplet state, where $\langle S_Z\rangle = 1$, as a function of the magnetic field. This transition point at B_{ST} is accompanied by a drop of the critical current in the (1,1) sector, however this sudden decrease is absent in the odd sector (see blue regions in Fig. 6.3b). We note that the gradual global decrease in I_{DQD} is consistent with the orbital effect of the magnetic field applied along the nanowire [196].

We analyze this data in Fig. 6.4, where we first find the charge state boundary at each value of $B_{\parallel}$ at $I_{\mathrm{DQD}} = 0$ (blue dots and error bars in Fig. 6.4a) and overlay the calculated boundary (black solid line, corresponding to Fig. 6.3b). We quantify $B_{\mathrm{ST}} \approx 80\,\mathrm{mT}$, which agrees consistently with the characteristic cutoff magnetic field of I_{DQD} at several plunger gate values (dots in Fig. 6.4b, colors corresponding to the arrows in Fig. 6.3a). Furthermore, we find an excellent agreement with the calculated critical current $I_{\mathrm{C}}(B)$

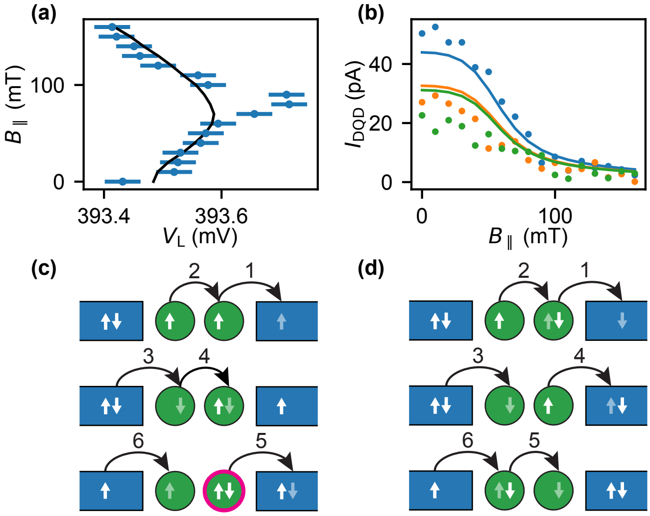

Figure 6.4: Triplet-blockaded supercurrent. (a) The measured (blue dots and error bars) and calculated (black solid line) even-odd charge boundary extracted from Fig. 6.3a and Fig. 6.3b. (b) Dots: the measured I_{DQD} at three plunger gate settings in the even (1,1) sector, see the corresponding arrows in Fig. 6.3a. Scaled theoretical values are shown as solid lines, see the text. Representative sixth order tunneling processes are shown in the $T_{\uparrow\uparrow}$ (c) and in the singlet regime (d).

(solid lines in Fig. 6.4b) with a common scaling factor of 0.29, which may stem from the reduced switching current inside the charge state due to thermal activation compared to the corresponding critical current [186].

The suppression of the Josephson supercurrent through a DQD in the spin triplet sector can be understood considering the virtual states involved in the Cooper pair transfer. Starting from the $(1,1)$ $T_{\uparrow\uparrow}$ state close to the charge boundary with the single occupation sector, we always encounter a virtual state with a double occupation on one of the dots (magenta circle in Fig. 6.4c). In the $U \gg \Delta$ limit corresponding to our experiments, this configuration is energetically unfavorable and suppresses Cooper pair tunneling. In contrast, a spin singlet starting condition can avoid this configuration (Fig. 6.4d). We finally note that the opposite limit, where $U \ll \Delta$, also leads to a triplet supercurrent blockade [74] (see the Supplementary Information), which persists with a finite residual supercurrent in the spin triplet state when $U \sim \Delta$.

In conclusion, we directly measured the supercurrent reversal associated with the even-odd charge occupation in an InAs DQD, where the large level spacing allows us to use a single orbital for each dot in our quantitative modeling. In the $(1,1)$ charge sector, we showed that the singlet to triplet transition is accompanied by a supercurrent blockade. This enables a direct spin to supercurrent conversion [192, 197] in hybrid semiconductor nanodevices [187] used for quantum information processing.

Raw datasets and computer code are available at the Zenodo repository [198].

6.1. SUPPLEMENTARY INFORMATION

6.1.1. DEVICE FABRICATION

The device is fabricated on a commercial undoped Si wafer with a 285 nm thermally grown SiO_x layer with conventional electron beam lithography methods. First, the nanowire is deterministically deposited using a micro manipulator between identification markers [92]. Next, the junctions are defined by etching the Aluminum shell for 55 s at room temperature in a photoresist developer containing 2% TMAH. The wire contacts and the SQUID loop are created by Ar plasma milling and in-situ sputtering of NbTiN.

A 10 nm thick global AlO_x gate dielectric is deposited through a low-temperature thermal Atomic layer deposition process. Wrap-around gates with a thickness of approximately 50 nm are deposited in a high-vacuum electron-beam evaporation chamber. They are deposited under three different angles to ensure conformal coverage: 60°, 0° and −60° with respect to the normal. Finally, the AlO_x is removed at the bondpads to allow easy bonding, using the same wet etching solution as used for the aluminum shell.

6.1.2. ESTIMATING ELECTROSTATIC PARAMETERS

We start characterization in the normal state by quenching superconductivity in the nanowire with a perpendicular magnetic field $B_\perp = 0.5\,\mathrm{T}$ (Fig. 6.5a). The SQUID reference junction is pinched off and by measuring the conductance at a voltage bias close to zero, we obtain the charge stability diagram of the DQD. The scan is taken around the same gate values as the data in the main text. We estimate the inter-dot lever arms from the slopes of the charge boundaries, shown as white solid lines in Fig. 6.5a.

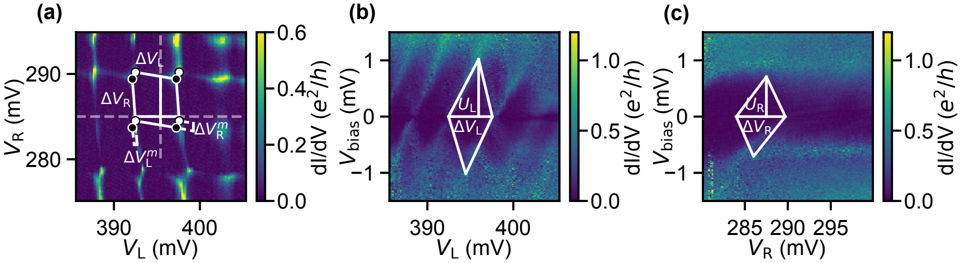

Figure 6.5: **Normal-state characterization** **(a)** Charge stability diagram taken at $B_\perp = 0.5\,\mathrm{T}$. The ranges of the Coulomb diamond scans in the other subfigures are marked by the dashed lines. **(b)** Coulomb diamond scan of quantum dot 1 with voltage bias V_{bias}. We extract $\alpha_{\mathrm{LL}} = 0.2, U_{\mathrm{L}} = 1.03\,\mathrm{meV}$. **(c)** Coulomb diamond scan of quantum dot 2. We verify $U_{\mathrm{R}} = 504\,\mu\mathrm{eV}$.

Next, we find the lever arm α_{LL} by comparing the measured height of the Coulomb diamond in Fig. 6.5b with the width in V_{L}. Combined with inter-dot lever arms, this gives us enough information to estimate the charging energies and relevant capacitances using equations 6.2 .

$$U_{\mathrm{L}} = \frac{e^2}{C_{\mathrm{L}}}\left(\frac{1}{1-\frac{C_{\mathrm{C}}^2}{C_{\mathrm{L}}C_{\mathrm{R}}}}\right), U_{\mathrm{R}} = \frac{e^2}{C_{\mathrm{R}}}\left(\frac{1}{1-\frac{C_{\mathrm{C}}^2}{C_{\mathrm{L}}C_{\mathrm{R}}}}\right), U_{\mathrm{C}} = \frac{e^2}{C_{\mathrm{C}}}\left(\frac{1}{\frac{C_{\mathrm{L}}C_{\mathrm{R}}}{C_{\mathrm{C}}^2}-1}\right), \tag{6.2}$$

where C_C is the inter-dot capacitance and $C_{L(R)} = C_{BL(BR)} + C_{V_L(V_R)} + C_C$, with $C_{BL(BR)}$ the capacitance between a dot and the nearest lead and $C_{V_L(V_R)}$ the capacitance between a dot and the nearest gate [58]. A complete list of extracted parameters is shown in Tab. 6.1. Due to the poor visibility of the Coulomb diamond scan of dot 2, we extract α_{RR} from the other parameters and verify that the resulting U_R is reasonable in Fig. 6.5c.

Table 6.1: Electrostatic parameters of the DQD device.

Quantity	Normal state	Superconducting state
U_L	1030 µeV	597 µeV
U_R	504 µeV	466 µeV
U_C	71 µeV	42 µeV
α_{LL}	0.2	0.2
α_{LR}	0.012	0.011
α_{RL}	0.014	0.013
α_{RR}	0.088	0.0124
C_C	0.022 fF	0.024 fF
$C_{L(R)}$	0.157 fF (0.321 fF)	0.270 fF (0.346 fF)
$C_{V_L(V_R)}$	0.031 fF (0.028 fF)	0.047 fF (0.039 fF)
$C_{BL(BR)}$	0.104 fF (0.271 fF)	0.199 fF (0.283 fF)

Due the non-zero g-factor of the InAs, the extracted charging energies in the normal state at $B_\perp = 0.5\,\text{T}$ are not the same as for in the superconducting state at $B_\perp \approx 0$. Therefore, we extract a separate set of parameters from the superconducting data and only use $\alpha_{LL} = 0.2$ from the normal state data and determine all other parameters independently.

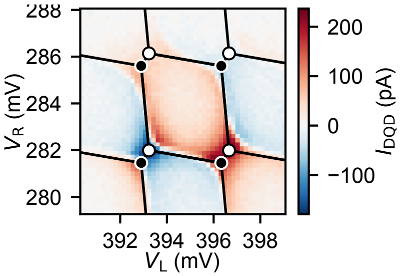

Figure 6.6: **Superconducting-state characterization (a)** Supercurrent charge stability diagram. The estimated charge-sector boundaries are shown by black solid lines.

The charge state boundaries are where the supercurrent crosses zero. We then overlay estimated charge boundaries, without considering avoided crossings due to the coupling between the quantum dots. We use $\alpha_{LL} = 0.2$ from the normal-state data and manually adjust the other parameters such that they agree with the supercurrent stability diagram (Fig. 2). We use these values for the numerical zero-bandwidth calculations shown in the main text. Tab. 6.1 lists all the electrostatic parameters extracted in the superconducting regime in the rightmost column.

6.1.3. SUPERCURRENT MODELING

In this section we will present the two approaches used to model the critical current I_C namely a zero-bandwidth (ZBW) approximation and a leading order perturbation theory in dot-lead tunneling amplitude (same approach as in supplement of Ref. 199). At sufficiently weak coupling and at zero temperature, these two approaches yield very similar critical current, I_C.

We describe the full S-DQD-S system using a serially coupled two-orbital Anderson model with superconducting (BCS) leads:

$$H = H_0 + H_\mathrm{d} + H_\mathrm{SO} + H_\mathrm{BCS} + H_\mathrm{T} \tag{6.3}$$

$$H_0 = \sum_{\sigma,i=\mathrm{L,R}} (\epsilon_i + \sigma g_i B) n_{i\sigma} + \sum_{i=\mathrm{L,R}} U_i n_{i\uparrow} n_{i\downarrow} + U_\mathrm{C}(n_{\mathrm{L}\uparrow} + n_{\mathrm{L}\downarrow})(n_{\mathrm{R}\uparrow} + n_{\mathrm{R}\downarrow}) \tag{6.4}$$

$$H_\mathrm{d} = t_0 \sum_\sigma (d^\dagger_{\mathrm{L}\sigma} d_{\mathrm{R}\sigma} + d^\dagger_{\mathrm{R}\sigma} d_{\mathrm{L}\sigma}) \tag{6.5}$$

$$H_\mathrm{SO} = \sum_{j=x,y,z} \sum_{\sigma,\sigma'} \left(i t_j \tau^j_{\sigma\sigma'} d^\dagger_{\mathrm{L}\sigma} d_{\mathrm{R}\sigma'} - i t_j \tau^j_{\sigma\sigma'} d^\dagger_{\mathrm{R}\sigma} d_{\mathrm{L}\sigma'} \right) \tag{6.6}$$

$$H_\mathrm{BCS} = \sum_{k,\sigma,i=\mathrm{L,R}} \xi_i c^\dagger_{ik\sigma} c_{ik\sigma} + \sum_{k,i=\mathrm{L,R}} \left(\Delta_i c^\dagger_{ik\uparrow} c^\dagger_{i-k\downarrow} + \Delta_i^* c_{i-k\downarrow} c_{ik\uparrow} \right) \tag{6.7}$$

$$H_\mathrm{T} = \sum_{k,\sigma,i=\mathrm{L,R}} t_i \left(c^\dagger_{ik\sigma} d_{i\sigma} + d^\dagger_{i\sigma} c_{ik\sigma} \right) \tag{6.8}$$

Here $n_{i\sigma}$ denotes the electron occupation operator for dot $i = \mathrm{L,R}$ with spin $\sigma = \uparrow, \downarrow$. t_x, t_y and t_z are interdot spin-orbit tunneling amplitudes, and τ^j is the vector of Pauli matrices [200]. Through lever arms the gating will affect ϵ_i and thereby control the ground state. For this setup all phases on tunnel couplings t_0, t_L and t_R can be gauged onto the superconducting order parameter $\Delta_\mathrm{L} = \Delta$, $\Delta_\mathrm{R} = \Delta e^{i\phi}$ where ϕ is the phase difference and $\Delta = |\Delta_\mathrm{L}| = |\Delta_\mathrm{R}|$. Corresponding to the experimental setup we consider the regime where $|\Delta| \ll U_i$ and $\Gamma_\mathrm{R}, \Gamma_\mathrm{L} \ll U_\mathrm{L}, U_\mathrm{R}, \Delta$ with $\Gamma_i = \pi \nu_\mathrm{F} |t_i|^2$ where ν_F is the normal-state density of states in the leads, assumed be constant in the relevant range around the Fermi energy.

6.1.4. ZERO-BANDWIDTH APPROXIMATION

In the zero-bandwidth approximation (ZBW), one replaces the full BCS lead with a single superconducting impurity,

$$H_\mathrm{BCS} \approx H_\mathrm{ZBW} = \sum_{i=\mathrm{L,R}} \left(\Delta_i c^\dagger_{i\uparrow} c^\dagger_{i\downarrow} + \Delta_i^* c_{i\downarrow} c_{i\uparrow} \right) \tag{6.9}$$

This kind of expansion is in principle uncontrolled in the sense that it is not an expansion in any small parameter and as such its parameters should be regarded as fitting parameters rather than physical parameters.

Within this approximation, the Hamiltonian can be readily diagonalized numerically and from the eigenenergies, E_i, the free energy can be found as,

$$F(\phi) = k_\mathrm{B} T \log \sum_i e^{-E_i/(k_\mathrm{B} T)} \tag{6.10}$$

and thereby the supercurrent can be obtained as,

$$I(\phi) = \frac{2e}{\hbar} \partial_\phi F(\phi) \tag{6.11}$$

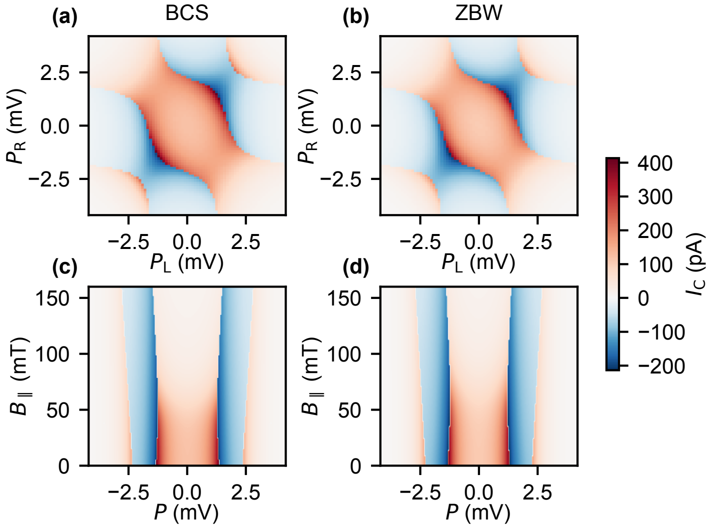

Figure 6.7: a), b) Plots of stability diagrams using fourth order perturbation theory and ZBW approximation, respectively. c), d) B-field line cuts along $P = P_L = P_R$ using BCS and ZBW description respectively. Parameters are similar to the main article $\Delta = 200$, $U_L = 595.25$. $U_R = 464.84$, $U_C = 41.41$, $t_0 = 80$, $t_x = 30$, $t_y = t_z = 0$, all in units μeV, and $g = 15.9$. The charge of the dots are determined through lever arms by $\epsilon_L = -U_L/2 - U_C - \alpha_{LL}P_L - \alpha_{LR}P_R$ and $\epsilon_R = -U_R/2 - U_C - \alpha_{RL}P_L - \alpha_{RR}P_R$ where $\alpha_{LL} = 0.2$, $\alpha_{LR} = 0.011$, $\alpha_{RL} = 0.013$ and $\alpha_{RR} = 0.124$. For the fourth order expansion we use $\Gamma_L = \Gamma_R = 33.18$ μeV while for the ZBW approximation we use the scaling $t_{L,ZBW} = t_{R,ZBW} = \sqrt{2\Gamma_L\Delta/\pi} = 65$ μeV.

From this, the critical current is found as $I_C = \max_\phi |I(\phi)|$, which is used to generate the maps of the main article.

One choice of fixing the ZBW parameters is $t_{i,\mathrm{ZBW}} = \sqrt{2\Gamma_i\Delta/\pi}$. This scaling leads to a very good quantitative match between ZBW approximation and fourth order perturbation theory for a wide range of parameters and sufficiently small values of Γ_i/U. A comparison between results from ZBW and fourth order expansion in lead coupling is shown in Fig. 6.7.

6.1.5. PERTURBATIVE EXPANSION OF I_C WITH BCS LEADS

Here we calculate the critical current I_C to lowest (4th) order in the dot-lead couplings, t_L and t_R. In general, the current is calculated as

$$I = i\frac{e}{\hbar}\sum_\sigma \langle [H, n_{R\sigma}]\rangle = \frac{2e}{\hbar}\,\mathrm{Im}\sum_\sigma \langle t_R c^\dagger_{R\sigma} d_{R\sigma}\rangle \tag{6.12}$$

and the lowest order perturbation expansion takes the form

$$\begin{aligned} I &\approx -\frac{2e}{\hbar}\frac{1}{3!}\,\mathrm{Im}\,\frac{1}{\beta}\int_0^\beta \mathrm{d}\tau_1\mathrm{d}\tau_2\mathrm{d}\tau_3\mathrm{d}\tau_4 \sum_\sigma \left\langle \mathrm{T}_\tau\left(H_T(\tau_1)H_T(\tau_2)H_T(\tau_3)t_R c^\dagger_{R\sigma}(\tau_4)d_{R\sigma}(\tau_4)\right)\right\rangle_0 \\ &= \frac{4e}{\hbar}\Delta^2\Gamma_R\Gamma_L\sin\phi\frac{1}{\beta}\int_0^\beta \mathrm{d}\tau_1\mathrm{d}\tau_2\mathrm{d}\tau_3\mathrm{d}\tau_4 f^*(\tau_1-\tau_2)f(\tau_3-\tau_4)B_{ijkl}(\tau_1,\tau_2,\tau_3,\tau_4), \end{aligned} \tag{6.13}$$

where $f(\tau) = \sum_{n=-\infty}^{\infty} \frac{e^{-i\omega_n\tau}}{\sqrt{\omega_n^2+\Delta^2}}$ with fermionic Matsubara frequencies $\omega_n = (2n+1)\pi/\beta$ and $\beta = 1/k_\mathrm{B}T$. The label 0 on the expectation value indicates that it is taken with respect to the thermal state of the decoupled dot-lead system. The important object is now $B_{ijkl}(\tau_1,\tau_2,\tau_3,\tau_4)$ which contains all information about the double dot,

$$B_{ijkl}(\tau_1,\tau_2,\tau_3,\tau_4) = \left\langle \mathrm{T}_\tau \left(d^\dagger_{\mathrm{L}\uparrow}(\tau_1) d^\dagger_{\mathrm{L}\downarrow}(\tau_2) d_{\mathrm{R}\downarrow}(\tau_3) d_{\mathrm{R}\uparrow}(\tau_4) \right) \right\rangle_0 \tag{6.14}$$

This object is conveniently evaluated in the basis of eigenstates of $H_0 + H_\mathrm{d} + H_\mathrm{SO}$, obtained numerically for a given parameter set, and the critical current is finally evaluated as $I_\mathrm{C} = I/\sin\phi$, whose sign determines if it is in a 0 or π phase.

This result is not used in the main text, and it is included here only as a check of the ZBW calculations in Fig.6.7.

6.1.6. SIGN OF THE CRITICAL CURRENT TO LEADING ORDER IN DOT-LEAD COUPLINGS

In this section, we calculate the sign of I_C to lowest order in dot-lead couplings, and demonstrate that it is determined from the double-dot ground state, using the simple rule stated in the main text. We start by rewriting Eq. (6.13) from the lowest order expansion in lead coupling,

$$\begin{aligned} I_\mathrm{C} &= \int_0^\beta \mathrm{d}\tau_1 \mathrm{d}\tau_2 \mathrm{d}\tau_3 \mathrm{d}\tau_4 g(\tau_1,\tau_2,\tau_3,\tau_4) B(\tau_1,\tau_2,\tau_3,\tau_4) \qquad (6.15)\\ &= \sum_{i,j,k,l=1}^{4} (\epsilon_{ijkl})^2 \int_0^\beta \mathrm{d}\tau_i \int_0^{\tau_i} \mathrm{d}\tau_j \int_0^{\tau_j} \mathrm{d}\tau_k \int_0^{\tau_k} \mathrm{d}\tau_l g(\tau_1,\tau_2,\tau_3,\tau_4) B_{ijkl}(\tau_1,\tau_2,\tau_3,\tau_4), \end{aligned}$$

which is a sum over all permutations of τ_i's. Here $g(\tau_1,\tau_2,\tau_3,\tau_4) = 4e/\hbar\Delta^2\Gamma_\mathrm{L}\Gamma_\mathrm{R} f^*(\tau_1 - \tau_2) f(\tau_3 - \tau_4)$ and the Levi-Civita symbol is specified with $\epsilon_{1234} = 1$. As we sum over the different permutations of operators in B_{ijkl} it no longer contains any time sorting and can be written as,

$$B_{ijkl}(\tau_1,\tau_2,\tau_3,\tau_4) = \epsilon_{ijkl} \Big\langle d_i(\tau_i) d_j(\tau_j) d_k(\tau_k) d_l(\tau_l) \Big\rangle_0 \tag{6.16}$$

where i,j,k,l specify the ordering with the definitions $d_1(\tau_1) = d^\dagger_{\mathrm{L}\uparrow}(\tau_1)$, $d_2(\tau_2) = d^\dagger_{\mathrm{L}\downarrow}(\tau_2)$, $d_3(\tau_3) = d_{\mathrm{R}\downarrow}(\tau_3)$ and $d_4(\tau_4) = d_{\mathrm{R}\uparrow}(\tau_4)$. At zero temperature, the dot system is in a definite ground state, $|g\rangle$, of the full dot Hamiltonian and

$$B_{ijkl}(\tau_1,\tau_2,\tau_3,\tau_4) = \epsilon_{ijkl} \langle g| d_i U(\tau_i,\tau_j) d_j U(\tau_j,\tau_k) d_k U(\tau_k,\tau_l) d_l |g\rangle, \tag{6.17}$$

where we have separated the trivial time evolution of the isolated dots due to H_0 from the evolution generated by $H_\mathrm{d} + H_\mathrm{SO}$, which couples the dots. The time evolution operator above is defined in the interaction picture as

$$U(\tau_i,\tau_j) = e^{-(H_0-E_\mathrm{g})\tau_i}\, \mathrm{T}_\tau\, e^{-\int_{\tau_j}^{\tau_i} \mathrm{d}\tau' \bar{H}_\mathrm{d}(\tau')} e^{(H_0-E_\mathrm{g})\tau_j}, \tag{6.18}$$

with $\bar{H}_\mathrm{d}(\tau) = e^{H_0\tau}(H_\mathrm{d} + H_\mathrm{SO})e^{-H_0\tau}$, where T_τ is the τ-ordering operator.

In Eq. (6.15) we expand the time evolution operators appearing in Eq. (6.17) to N'th order in $\bar{H}_\mathrm{d}$. From now on we will discuss generic contributions to this expansion, which we label $I^{(a,b,c)}_{\mathrm{C},ijkl}$ with $I_\mathrm{C} = \sum_{i,j,k,l=1}^{4} \sum_{a,b,c=0}^{\infty} I^{(a,b,c)}_{\mathrm{C},ijkl}$. The integers a, b and c specify the order of expansion (counting from left) of each time evolution operator in Eq. (6.17). A single N'th order $(a+b+c=N)$ contribution can, in terms of the amplitudes

$$\langle g|\mathscr{C}^{(a,b,c)}_{ijkl}|g\rangle = \epsilon_{ijkl}(-1)^N \langle g|\, d_i (H_\mathrm{d}+H_\mathrm{SO})^a d_j (H_\mathrm{d}+H_\mathrm{SO})^b d_k (H_\mathrm{d}+H_\mathrm{SO})^c d_l\, |g\rangle \tag{6.19}$$

be expressed as,

$$\begin{aligned} I^{(a,b,c)}_{\mathrm{C},ijkl} &= \int_0^\beta d\tau_i \prod_{\mu=0}^{N+2} \left(\int_0^{\tau'_\mu} d\tau'_{\mu+1} e^{-(E_\mu - E_\mathrm{g})(\tau'_\mu - \tau'_{\mu+1})} \right) g(\tau_1,\tau_2,\tau_3,\tau_4) \langle g|\mathscr{C}^{(a,b,c)}_{ijkl}|g\rangle \\ &= \frac{4e}{\hbar}\Gamma_\mathrm{L}\Gamma_\mathrm{R}|\Delta|^2 \int_\Delta^\infty \frac{d\omega}{\sqrt{\omega^2-\Delta^2}} \int_\Delta^\infty \frac{d\omega'}{\sqrt{\omega'^2-\Delta^2}} \prod_{m=1}^{n} \left(\frac{1}{E_m - E_\mathrm{g} + \omega + \omega'} \right) \\ &\quad \times \prod_{m'=1}^{n'} \left(\frac{1}{E_{m'} - E_\mathrm{g} + \omega} \right) \prod_{m''=1}^{n''} \left(\frac{1}{E_{m''} - E_\mathrm{g} + \omega'} \right) \prod_{m'''=1}^{n'''} \left(\frac{1}{E_{m'''} - E_\mathrm{g}} \right) \langle g|\mathscr{C}^{(a,b,c)}_{ijkl}|g\rangle, \end{aligned} \tag{6.20}$$

with the definition $\tau_i = \tau'_0$, $\tau_j = \tau'_{a+1}$, $\tau_k = \tau'_{a+b+2}$ and $\tau_l = \tau'_{N+3}$. In the second line $n + n' + n'' + n''' = N+3$ are positive integers whose values are specified by both the expansion in a, b and c and the ordering $ijkl$, while E_n are energies of the uncoupled charge basis H_0.

Next comes the critical statement: since fractions in Eq. (6.20) are positive, the sign is determined solely by $\mathscr{C}^{(a,b,c)}_{ijkl}$. For this to be true, the ground state energy of $H_0 + H_\mathrm{d}$, E_g, must satisfy that $E_\mathrm{g} \leq E_n$ where E_n are eigenenergies of H_0. For a hermitian matrix, A, with diagonal entries a_{nn} and minimal (maximal) eigenvalues λ_min (λ_max), the min-max theorem [201] states that $\lambda_\mathrm{min} \leq a_{nn} \leq \lambda_\mathrm{max}$. In charge basis, $H_\mathrm{d} + H_\mathrm{SO}$ only contains off-diagonal elements, and with $A = H_0 + H_\mathrm{d}$, we may therefore conclude that $E_\mathrm{g} = \lambda_\mathrm{min} < a_{nn} = E_n$, as needed. Note that this perturbation series breaks down if $E_{m'''} = E_\mathrm{g}$ in the denominator $1/(E_{m'''} - E_\mathrm{g})$. Such a denominator occurs only if $E_{m'''}$ relates to a state with ±2 electrons compared to the ground state. In such instances one would have to go to higher order in t_L, t_R.

By removing the integrals $\int_\Delta^\infty \frac{\mathrm{d}\omega}{\sqrt{\omega^2-\Delta^2}}$, setting $\omega, \omega' = \Delta$ in the denominators and using $\Gamma_i = \pi t^2_{i,\mathrm{ZBW}}/2\Delta$ one would obtain the corresponding I_C expansion for a ZBW description of the superconductors. As such, the previous and following arguments about the sign of I_C also holds for a ZBW description.

6.1.7. SIGN OF ALL CONTRIBUTIONS TO CRITICAL CURRENT

We now turn our attention to the time independent part $\mathscr{C}^{(a,b,c)}_{ijkl}$, which specifies the total sign, and we wish to show that no matter the value of a, b, c or i, j, k, l the sign of a contribution to I_C is determined by the ground state. In this subsection we neglect spin-orbit coupling, H_SO, the effect of which we discuss in a following subsection.

It is convenient to work in a spin-sorted basis definition of the many-body state $\langle 2,2| = \langle 0|\, d_{\mathrm{L}\uparrow} d_{\mathrm{R}\uparrow} d_{\mathrm{L}\downarrow} d_{\mathrm{R}\downarrow}$. With this choice, one can make use of the fact that H_d conserves spin and therefore commutes with operators of opposite spin to sort $\mathscr{C}_{ijkl}^{(a,b,c)}$ as,

$$\langle g|\mathscr{C}_{ijkl}^{(a,b,c)}|g\rangle = \sum_{n,m} \alpha_n \alpha_m^* \langle n_\uparrow|\mathscr{C}_{\uparrow,i'j'}^{(a_\uparrow b_\uparrow c_\uparrow)}|m_\uparrow\rangle\langle n_\downarrow|\mathscr{C}_{\downarrow,i''j''}^{(a_\downarrow b_\downarrow c_\downarrow)}|m_\downarrow\rangle, \tag{6.21}$$

where we have expressed the ground state as a tensor product state between the two spin sectors, $|g\rangle = \sum_n \alpha_n |n_\uparrow\rangle \otimes |n_\downarrow\rangle$, with α_n being prefactors from the diagonalization of $H_0 + H_\mathrm{d}$. The indexes of $\mathscr{C}_{\sigma,i'j'}^{(a_\sigma,b_\sigma,c_\sigma)}$ are specified by the $ijkl$ index as follows: $i', j' \in \{1,4\}$ for spin-up and $i'', j'' \in \{2,3\}$ for spin-down while ordering is the same as in $ijkl$ for each subset independently, e.g $\mathscr{C}_{3124}^{(a,b,x)}$ corresponds to $\mathscr{C}_{\uparrow,14}^{(a_\uparrow,b_\uparrow,c_\uparrow)}$ and $\mathscr{C}_{\downarrow,32}^{(a_\downarrow,b_\downarrow,c_\downarrow)}$. Finally, the powers a_σ, b_σ and c_σ denote the number of H_d operators containing spin-σ, such that $\sum_\sigma a_\sigma + b_\sigma + c_\sigma = a + b + c = N$ where we do not permute any operators of same spin in the sorting. This yields the following object, which determines the sign of each spin independently,

$$\langle n_\sigma|\mathscr{C}_{\sigma,ij}^{(a_\sigma b_\sigma c_\sigma)}|m_\sigma\rangle = \epsilon_{ij}(-1)^{a_\sigma+b_\sigma+c_\sigma}\langle n_\sigma|(H_{\mathrm{d}\sigma})^{a_\sigma} d_i (H_{\mathrm{d}\sigma})^{b_\sigma} d_j (H_{\mathrm{d}\sigma})^{c_\sigma}|m_\sigma\rangle, \tag{6.22}$$

with Levi-Civita symbols, ϵ_{ij}, defined with $\epsilon_{14} = 1$ and $\epsilon_{23} = 1$, respectively.

We will now consider a few specific spin contributions. We start with the state where both dots are void of spin-up electrons such that $|n_\uparrow\rangle = |m_\uparrow\rangle = |0,0\rangle$ where left and right number in the kets refer to the number of spin-up electrons on the left and right dots respectively. Such a contribution yields,

$$\begin{aligned}\langle 0,0|\mathscr{C}_{\uparrow,ij}^{(a_\uparrow b_\uparrow c_\uparrow)}|0,0\rangle &= \epsilon_{ij}(-1)^{a_\uparrow+b_\uparrow+c_\uparrow}\langle 0,0|(H_{\mathrm{d}\uparrow})^{a_\uparrow} d_i (H_{\mathrm{d}\uparrow})^{b_\uparrow} d_j (H_{\mathrm{d}\uparrow})^{c_\uparrow}|0,0\rangle \\ &= \delta_{i4}\delta_{j1}\delta_{a_\uparrow 0}\delta_{c_\uparrow 0}\epsilon_{41}(-1)^1 t_0^{b_\uparrow}\langle 0,0|d_{\mathrm{R}\uparrow} d_{\mathrm{R}\uparrow}^\dagger d_{\mathrm{L}\uparrow} d_{\mathrm{L}\uparrow}^\dagger|0,0\rangle \geq 0,\end{aligned} \tag{6.23}$$

where the disappearance of $H_{\mathrm{d}\uparrow}^{b_\uparrow}$ stems from the fact that the only non-zero contribution arises when $b_\uparrow$ is odd and $H_{\mathrm{d}\uparrow}^{b_\uparrow}$ contains a single $t_0 d_{\mathrm{L}\uparrow}^\dagger d_{\mathrm{R}\uparrow}$ multiplied by $(b_\uparrow - 1)/2$ back-and-forth operators of the type $t_0^2 d_{\mathrm{L}\uparrow}^\dagger d_{\mathrm{R}\uparrow} d_{\mathrm{R}\uparrow}^\dagger d_{\mathrm{L}\uparrow}$. A visual representation of such processes is shown in Fig.6.8 a). If the two dots are void of spin-up electrons, the spin-up part will therefore yield a positive sign to Eq. (6.21) to all orders of H_d.

Due to electron-hole symmetry a very similar derivation follows for the doubly occupied spin-up state,

$$\begin{aligned}\langle 1,1|\mathscr{C}_{\uparrow,ij}^{(a_\uparrow b_\uparrow c_\uparrow)}|1,1\rangle &= \epsilon_{ij}(-1)^{a_\uparrow+b_\uparrow+c_\uparrow}\langle 1,1|(H_{\mathrm{d}\uparrow})^{a_\uparrow} d_i (H_{\mathrm{d}\uparrow})^{b_\uparrow} d_j (H_{\mathrm{d}\uparrow})^{c_\uparrow}|1,1\rangle \\ &= \delta_{i1}\delta_{j4}\delta_{a_\uparrow 0}\delta_{b_\uparrow 0}\epsilon_{14}(-1)^1 t_0^{b_\uparrow}\langle 1,1|d_{\mathrm{L}\uparrow}^\dagger d_{\mathrm{R}\uparrow}^\dagger d_{\mathrm{L}\uparrow} d_{\mathrm{R}\uparrow}|1,1\rangle \geq 0,\end{aligned} \tag{6.24}$$

where a visual representation is shown in Fig.6.8 b).

The odd ground state configurations are a little more complicated, as there is more than one way of organizing operators. Consider contributions with $|n_\uparrow\rangle = |m_\uparrow\rangle = |1,0\rangle$

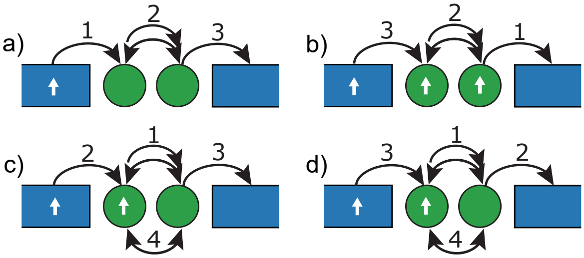

Figure 6.8: We show the paths transferring one electron across for various ground states. The numbers represent the order of operations applied to $\langle n_\uparrow|$ to reach $|n_\uparrow\rangle$. Lines with arrows in both directions indicate an integer number of back-and-forth jumps each yielding t_0^2. a) $|n_\uparrow\rangle = |0,0\rangle$, b) $|n_\uparrow\rangle = |1,1\rangle$ c), one ordering of $|n_\uparrow\rangle = |1,0\rangle$, d) another ordering of $|n_\uparrow\rangle = |1,0\rangle$

meaning one spin-up electron on the left dot,

$$\begin{aligned}\langle 1,0|\,\mathscr{C}^{(a_\uparrow b_\uparrow c_\uparrow)}_{\uparrow,ij}\,|1,0\rangle &= \epsilon_{ij}(-1)^{a_\uparrow+b_\uparrow+c_\uparrow}\langle 1,0|\,(H_{\mathrm{d}\uparrow})^{a_\uparrow} d_i (H_{\mathrm{d}\uparrow})^{b_\uparrow} d_j (H_{\mathrm{d}\uparrow})^{c_\uparrow}\,|1,0\rangle \qquad (6.25)\\ &= \delta_{b_\uparrow 0}\, t_0^{a_\uparrow+c_\uparrow}(-1)^1\Big(\delta_{i1}\delta_{j4}\epsilon_{14}\langle 1,0|\, d^\dagger_{\mathrm{L}\uparrow} d_{\mathrm{R}\uparrow} d^\dagger_{\mathrm{R}\uparrow} d_{\mathrm{L}\uparrow}\,|1,0\rangle\\ &\qquad\qquad + \delta_{i4}\delta_{j1}\epsilon_{41}\langle 1,0|\, d_{\mathrm{R}\uparrow} d^\dagger_{\mathrm{L}\uparrow} d^\dagger_{\mathrm{R}\uparrow} d_{\mathrm{L}\uparrow}\,|1,0\rangle\Big)\\ &\le 0,\end{aligned}$$

which shows that all such non-zero contributions are negative. By symmetry, exchanging spin-up with spin-down yields precisely the same signs. Similar calculations can be done for the other configurations and here we list the results:

$$\langle 0,1|\,\mathscr{C}^{(a_\sigma b_\sigma c_\sigma)}_{\sigma,ij}\,|0,1\rangle \le 0, \qquad (6.26a)$$

$$\langle 1,0|\,\mathscr{C}^{(a_\sigma b_\sigma c_\sigma)}_{\sigma,ij}\,|0,1\rangle \ge 0, \qquad (6.26b)$$

$$\langle 0,1|\,\mathscr{C}^{(a_\sigma b_\sigma c_\sigma)}_{\sigma,ij}\,|1,0\rangle \ge 0. \qquad (6.26c)$$

With these results it is straightforward to compute the sign of the critical current for a given ground state using Eq. (6.21). Here we will show some results to illustrate the methodology:

$$\langle 0,0|\,\mathscr{C}^{(a,b,c)}_{ijkl}\,|0,0\rangle = \langle 0,0|\,\mathscr{C}^{(a_\uparrow b_\uparrow c_\uparrow)}_{\uparrow,ij}\,|0,0\rangle\,\langle 0,0|\,\mathscr{C}^{(a_\downarrow b_\downarrow c_\downarrow)}_{\downarrow,ij}\,|0,0\rangle \ge 0 \qquad (6.27a)$$

$$\langle 2,2|\,\mathscr{C}^{(a,b,c)}_{ijkl}\,|2,2\rangle = \langle 1,1|\,\mathscr{C}^{(a_\uparrow b_\uparrow c_\uparrow)}_{\uparrow,ij}\,|1,1\rangle\,\langle 1,1|\,\mathscr{C}^{(a_\downarrow b_\downarrow c_\downarrow)}_{\downarrow,ij}\,|1,1\rangle \ge 0 \qquad (6.27b)$$

$$\langle \uparrow,0|\,\mathscr{C}^{(a,b,c)}_{ijkl}\,|\uparrow,0\rangle = \langle 1,0|\,\mathscr{C}^{(a_\uparrow b_\uparrow c_\uparrow)}_{\uparrow,ij}\,|1,0\rangle\,\langle 0,0|\,\mathscr{C}^{(a_\downarrow b_\downarrow c_\downarrow)}_{\downarrow,ij}\,|0,0\rangle \le 0 \qquad (6.27c)$$

$$\langle 2,\uparrow|\,\mathscr{C}^{(a,b,c)}_{ijkl}\,|2,\uparrow\rangle = \langle 1,1|\,\mathscr{C}^{(a_\uparrow b_\uparrow c_\uparrow)}_{\uparrow,ij}\,|1,1\rangle\,\langle 1,0|\,\mathscr{C}^{(a_\downarrow b_\downarrow c_\downarrow)}_{\downarrow,ij}\,|1,0\rangle \le 0 \qquad (6.27d)$$

What we have shown is that, independent of ordering and order of H_{d}, all contributions to I_{C} in Eq. (6.20) have the same sign, proving that the signs shown above must also be the sign of I_C for the respective ground states. This method can also be used to compute the sign of I_C for ground states that are not eigenstates of H_0, but eigenstates of $H_0 + H_\mathrm{d}$. Consider for example the ground state with a single electron delocalized across the dots, $|\uparrow\rangle = a\,|\uparrow,0\rangle - b\,|0,\uparrow\rangle$ where a and b have the same sign, then it follows that

$$\begin{aligned}\langle\uparrow|\mathscr{C}^{(a,b,c)}_{ijkl}\,|\uparrow\rangle = \langle 0,0|\mathscr{C}^{(a_\downarrow b_\downarrow c_\downarrow)}_{\downarrow,ij}\,|0,0\rangle \Big(&a^2\,\langle 1,0|\mathscr{C}^{(a_\uparrow b_\uparrow c_\uparrow)}_{\uparrow,ij}\,|1,0\rangle + b^2\,\langle 0,1|\mathscr{C}^{(a_\uparrow b_\uparrow c_\uparrow)}_{\uparrow,ij}\,|0,1\rangle \\ &-ab\,\langle 1,0|\mathscr{C}^{(a_\uparrow b_\uparrow c_\uparrow)}_{\uparrow,ij}\,|0,1\rangle - ab\,\langle 0,1|\mathscr{C}^{(a_\uparrow b_\uparrow c_\uparrow)}_{\uparrow,ij}\,|1,0\rangle\Big) \\ \leq 0,& \end{aligned} \tag{6.28}$$

which proves that the sign of I_C in the single electron doublet sector is negative to all orders in t_0. Using the same methodology on other ground states, we find:

$$\langle\uparrow\downarrow|\mathscr{C}^{(a,b,c)}_{ijkl}\,|\uparrow\downarrow\rangle \geq 0, \tag{6.29a}$$

$$\langle\sigma|\mathscr{C}^{(a,b,c)}_{ijkl}\,|\sigma\rangle \leq 0, \tag{6.29b}$$

$$\langle\uparrow\downarrow\sigma|\mathscr{C}^{(a,b,c)}_{ijkl}\,|\uparrow\downarrow\sigma\rangle \leq 0, \tag{6.29c}$$

$$\langle\uparrow\uparrow|\mathscr{C}^{(a,b,c)}_{ijkl}\,|\uparrow\uparrow\rangle \geq 0, \tag{6.29d}$$

for eigenstates of $H_0 + H_\mathrm{d}$ with electrons delocalized across the dots:

$$|\uparrow\downarrow\rangle = a\,|\uparrow,\downarrow\rangle + b\,|\downarrow,\uparrow\rangle - c\,|2,0\rangle - d\,|0,2\rangle\,, \tag{6.30a}$$

$$|\uparrow\downarrow\sigma\rangle = f\,|2,\sigma\rangle - g\,|\sigma,2\rangle\,, \tag{6.30b}$$

defined with positive prefactors, a, b, c, d, f, g, on all components.

Crucially for this experiment, we have shown that both a triplet ground state, $|\uparrow\uparrow\rangle$, and a singlet ground state, $|\uparrow\downarrow\rangle$, will guarantee a positive I_C. This concludes the proof that for the serial double dot, neglecting spin-orbit coupling, the sign of I_C to lowest order in dot-lead couplings is completely determined by the ground state.

Even though these derivations are quite technical, the results can be summarized as a rather simple rule: For each spin in a Cooper pair in the left lead, count the number of same-spin dot electrons it crosses to get from left to right lead. For each such same-spin crossing attribute a minus sign. The sign of I_C will the be equal to the product of all such crossing signs. This rule can be inferred from Eqs. (6.21) and (6.26), noticing that for a delocalized ground state all contributions yield the same sign as resulting from one of its localized constituents. For a serial double dot this rule clearly implies that the sign of I_C is determined by the total parity of the dots: the sign is negative for odd parity and positive for even parity, regardless of the spin configuration.

6.1.8. DISCUSSION OF SPIN-ORBIT COUPLING

So far we have established that the sign of the critical current for a double dot without spin-orbit coupling can be inferred solely from the ground state. In this subsection we discuss the possible implications of a finite spin-orbit coupling on the two quantum dots, implemented simply as a spin-dependent interdot tunneling amplitude. We begin by considering only the spin-conserving tunnel coupling, t_z, and write the total interdot tunneling Hamiltonian as

$$\begin{aligned} H_\mathrm{d} + H_\mathrm{SO} &= \sum_\sigma \left((t_0 + i\sigma t_z) d^\dagger_{\mathrm{L}\sigma} d_{\mathrm{R}\sigma} + \mathrm{h.c} \right) \\ &= t_\mathrm{eff} \sum_\sigma \left(e^{i\sigma\theta} d^\dagger_{\mathrm{L}\sigma} d_{\mathrm{R}\sigma} + \mathrm{h.c} \right) \end{aligned} \tag{6.31}$$

where t_eff is the modulus and θ the complex phase of $t_0 + i t_z$. On this system we can perform a gauge transformation $e^{i\sigma\theta} d^\dagger_{\mathrm{L}\sigma} = \tilde{d}^\dagger_{\mathrm{L}\sigma}$ which removes θ from the interdot coupling and moves it onto the left dot-lead tunneling amplitude:

$$H_{TL} = t_\mathrm{L} \sum_{k\sigma} \left(e^{i\sigma\theta} c^\dagger_{\mathrm{L}k\sigma} \tilde{d}_{\mathrm{L}\sigma} + \mathrm{h.c} \right). \tag{6.32}$$

Since the expansion in t_L, t_R in Eq. (6.13) contains two electrons of opposite spin jumping from superconductor to dot, this phase cancels out in I_C, and the only effect of t_z is simply to renormalize the interdot coupling $t_\mathrm{eff} = \sqrt{t_0^2 + t_z^2}$, leaving the sign of I_C unchanged.

Including either t_x or t_y, interdot tunneling is no longer spin conserving, and therefore disrupts the spin-sorted arguments used above to show that all contributions to I_C have the same sign. This is most easily illustrated with an example. Consider a specific term arising from the combination $H_\mathrm{SO} H_\mathrm{d} H_\mathrm{SO}$ with t_y finite:

$$H_\mathrm{SO} H_\mathrm{d} H_\mathrm{SO} = -t_y^2 t_0 d^\dagger_{\mathrm{L}\uparrow} d_{\mathrm{R}\downarrow} d^\dagger_{\mathrm{R}\downarrow} d_{\mathrm{L}\downarrow} d^\dagger_{\mathrm{L}\downarrow} d_{\mathrm{R}\uparrow} + \ldots \tag{6.33}$$

When acting on $|0,\uparrow\rangle$, this operator is equivalent to $-t_y^2 H_\mathrm{d}$. Such combinations of operators will arise in Eq. (6.19), where, for example, a contribution with $a = 1$ would contain H_d while a contribution with $a = 3$ would contain $H_\mathrm{SO} H_\mathrm{d} H_\mathrm{SO}$. As these two terms will have different signs we observe that not all contributions to I_C have the same sign.

Without any external magnetic field, one may choose the spin quantization axis to be aligned with the spin-orbit field, such that only t_z is non-zero. As such the sign of I_C is still completely determined by the ground state. With a finite external magnetic field, however, t_x and t_y components are unavoidable unless the field is carefully aligned with the spin-orbit field. In this case, I_C will sample amplitudes of different signs and the overall sign of I_C cannot be guaranteed analytically (at least we have not succeeded) since the magnitudes of the individual terms now also matter. Instead, we have done this numerically to confirm the observed signs of I_C in the plots presented in the main text. To lowest order in H_d and H_SO, it can be shown analytically, that the sign of I_C remains determined by the ground state, and that it is only higher order terms including both H_d and H_SO, such as Eq.(6.33), which yield contributions of different signs. To leading order, the sign of I_C thus remains determined by the ground state.

6.1.9. SIMPLE ARGUMENTS FOR TRIPLET BLOCKADE

In the main text, the key quantity is the critical current in a double-dot Josephson junction that is tuned to the (1,1) charge configuration. We used the term ‘triplet blockade’ for the effect that the critical current in this setup is suppressed when the ground state is

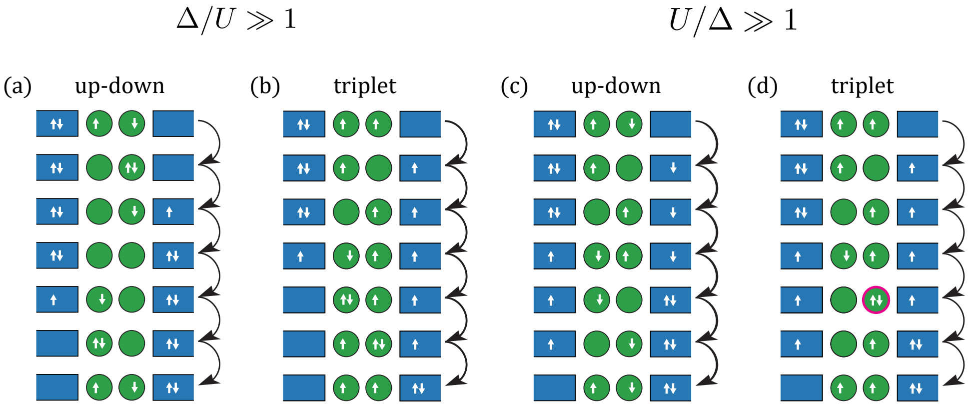

Figure 6.9: Example processes contributing to the Josephson current through the double dot. (a) Up-down process with intermediate states lacking quasiparticles, hence less penalized by a large gap $\Delta \gg U$. (b) Triplet process with intermediate states that all have at least one quasiparticle, hence more penalized by Δ. (c) Up-down process with all states having at most singly occupied quantum dots, hence exempt from Coulomb energy penalty. (d) Triplet process with an intermediate state that has a doubly occupied quantum dot and hence energetically penalized in the $U \gg \Delta$ regime.

tuned from a singlet configuration to a triplet configuration. We have shown measurement results and numerical simulations that display triplet blockade.

Here, we provide simple arguments for a strong triplet blockade in two different limiting cases: the large-gap limit, $\Delta \gg U$, and the strong-Coulomb-repulsion limit, $U \gg \Delta$. We also outline a process-counting argument that supports *partial* triplet blockade in the intermediate regime $\Delta \sim U$.

For the simple arguments, we make a number of simplifying assumptions. (1) We disregard interdot Coulomb repulsion U_C. (2) Instead of the proper singlet ground state, we address the case when the ground state holds a spin-up electron in the left dot and a spin-down electron in the right dot (the *up-down* state), (3) We describe the leads within the zero-bandwidth (ZBW) approximation. (4) We describe the Josephson current to leading order in dot-lead as well as inter-dot tunnel amplitude, assuming these to be small compared to the superconducting gap Δ and the on-site Coulomb repulsion U. With these simplifications, and following, the leading-order (6th-order) Josephson current can be described as a sum of contributions, where each contribution can be visualized as a six-step process in which a Cooper pair from one lead is transported over to the other lead. Four exemplary processes are shown in Fig. 6.9. The intermediate states of such processes are virtual states, in the sense that they have a high energy, either due to quasiparticle excitations, or due to Coulomb repulsion.

First, we revisit the case of the large-gap limit $\Delta/U \gg 1$, which was described in Ref. [74, 75]. In this case, the reason for the triplet blockade is that a triplet ground state allows only such processes whose intermediate states have one or two quasiparticles in the leads. One example is shown in Fig. 6.9b. In the 6th-order perturbative description of the ZBW model, the contribution of these processes scales as $\sim \Delta^{-5}$. In contrast, the up-down state allows for intermediate states where there are no quasiparticles in the leads;

an example is shown in Fig. 6.9a, where the 2nd, 4th and 6th states of the diagram do not have any quasiparticles. As a consequence, the contribution of such processes scale as $\sim \Delta^{-2}$. In conclusion, in the large-gap regime the ratio of the triplet and up-down critical currents is suppressed by Δ^{-3}, leading to a strong triplet blockade.

Now let us turn to the strong-Coulomb-repulsion limit $U/\Delta \gg 1$. Consider a point in the charge stability diagram in the vicinity of the boundary of the single-electron region and the (1,1) region. In this case, any intermediate state that has a DQD occupation different from 1 and 2 has a large energy penalty in the corresponding energy denominator, and hence strongly suppressed. In addition, among the processes where all states have DQD occupation 1 or 2, the ones involving a doubly occupied quantum dot also come with a large Coulomb energy penalty and hence are also suppressed.

Importantly, in the processes allowed by the triplet ground state, there is at least one intermediate state that has a doubly occupied quantum dot; for example, see Fig. 6.9d, where the right dot is doubly occupied in the 5th state. The critical current of the triplet will therefore scale as $\sim U^{-1}$. In contrast, for an up-down ground state, there is a process where the intermediate states have only singly occupied quantum dots, see Fig. 6.9c. The contribution of this process to the critical current will scale as $\sim U^{0}$. In conclusion, in the strong-Coulomb-repulsion regime the ratio of the triplet and up-down critical currents is suppressed as U^{-1}, again leading to a strong triplet blockade.

Even though we have argued for a strong triplet blockade in both limiting cases $\Delta \gg U$ and $U \gg \Delta$, it is in principle possible that the triplet critical current exceeds the up-down critical current in the intermediate regime $U \sim \Delta$. Here, we argue that this is not the case. In this regime, we estimate the ratio of the triplet and up-down critical currents from the ratio of the total number of 6th-order process. In the triplet case, the total number of allowed processes is 80, whereas the up-down state allows 320 processes in total, leading to a rough estimate of the critical current ratio of 0.25. Note that the actual critical current ratio also depends on the amplitudes of every process. Due to this estimate, we expect a partial triplet blockade in this intermediate regime.

Finally, we comment on the validity of the simplifying assumptions (1), (2) and (3) above. (1) The above considerations generalize as long as the interdot Coulomb repulsion energy U_C is moderate. The analysis of the strong-Coulomb-repulsion regime could change, e.g., if U_C would be a parameter tied to U, e.g., $U_C = U/2$, but that is beyond the scope of this work. (2) The above arguments generalize to the case when a singlet ground state is considered, instead of the up-down state. One result that is changed is the order-of-magnitude estimate of the critical current ratio in the intermediate regime $U \sim \Delta$: counting the processes of the singlet ground state yields a ratio of $80/1120 \approx 0.07$, which is even smaller than the estimate $80/320 = 0.25$ quoted above. (3) The above considerations generalize to the model with BCS leads. One technical difference is that in that model, quasiparticles have not only a spin quantum number, but also a momentum quantum number, and the contributions visualized in Fig. 6.9 have to be summed (or integrated) with respect to the quasiparticle momentum. The main difference occurring from this is that processes from BCS leads will scale with an additional Δ^2 factor which can also be accounted for in the choice of $t_{i,\mathrm{ZBW}}$. Nevertheless the Δ ratios between different processes are the same and as such the above blockade arguments also hold for BCS leads.

7

RECTIFIED CURRENT-PHASE RELATION IN AN S-DQD-S JOSEPHSON JUNCTION

In quantum dot Josephson junctions with a dot-lead coupling on the order of the charging energy and superconducting gap, competition between superconductivity and local electronic correlations gives rise to a phase-dependent charge parity. We explore this limit in a double quantum dot Josephson junction and observe an unexpected rectification of the current-phase relation, unexplained by current models. We analyze the results with a phenomenological model and discuss a possible direction for finding an explanation.

This work was performed in collaboration with R.J.J. van Gulik, A. Proutski, A. Pályi, P. Boross and A. Geresdi

7.1. INTRODUCTION

The behavior of supercurrent through a quantum dot Josephson junction depends on the relative sizes of the involved energy scales – charging energy E_C, superconducting gap Δ and dot-lead coupling Γ [52, 59, 71, 202]. In the limit of $\Gamma \ll \Delta, E_\mathrm{C}$, the charge parity of the quantum dot(s) becomes an important parameter as E_C restricts the flow of electrons to tunneling consecutively instead of in pairs. In the low-coupling limit, the supercurrent phase relation (CPR) is described by

$$I_\mathrm{S} = I_\mathrm{C} \sin(\varphi), \tag{7.1}$$

where I_C is the largest supercurrent amplitude the junction can sustain, known as the critical current and φ the phase difference between the superconducting leads. We have seen in chapter 6 how the charge parity of a single-orbital (double) quantum dot can change a standard 0-junction (as in Equation 7.1) to a π-junction by going from an even to an odd occupation. In this naming convention 0 and π refer to the offset in φ, where π results in a supercurrent reversal $I_\mathrm{C} < 0$.

In this chapter we investigate an intermediate regime, where $\Gamma \approx E_\mathrm{C} \approx \Delta$. Charge effects are still important and the even-odd effect of the quantum dot(s) charge remains. But at the transition from 0 to π, the charge becomes tunable by the phase φ. This phenomenon has been predicted and observed in single quantum dot Josephson junctions [69, 71, 203–206]. The origin can be best explained from the Andreev bound state (ABS) levels at the transition between 0 and π. For a strong enough lead coupling, the even and odd ABS overlap, crossing each other at different values for φ. When the phase is wound adiabatically, the system remains in the lowest energy level, switching parity at every ABS crossing [203].

Investigating this limit in our double quantum dot junction, we observe a CPR that does indeed appear to switch between parities – but has an even symmetry around $\varphi = 0$ and a period half of the 0 and π CPR. These observations is not explained by any of the current models. Furthermore, it suggests breaking of time-reversal symmetry, which is curious due to the magnetic field being close to zero ($B < 1\,\mathrm{mT}$). In this chapter we will analyze the observed behavior and provide a phenomenological description.

7.2. EXPERIMENTAL SETUP

The device used in this chapter consists of an InAs nanowire with an epitaxial Al shell on three of the wire's six facets (7.1a,b) [89]. A section of approximately 360 nm of the Al shell is selectively etched away to create a normal semiconductor section (shown in green). Five conformal electrostatic top gates (shown in yellow) are used to create a double quantum dot (DQD) in the semiconductor section (see Methods section 3.1.4), creating an S-DQD-S junction. A 10 nm AlO$_x$ dielectric layer galvanically isolates the gates from the nanowire. The superconducting leads are contacted to NbTiN (shown in blue), creating dc SQUID consisting of the DQD junction and a regular SNS junction.

A simplified electrical diagram of the device is drawn in Figure 7.1c, with the quantum dots depicted as green circles, connected to the superconducting leads and each other by tunnel couplings. To extract the switching current of the SQUID, the current source I_bias is driven with a sawtooth waveform while we simultaneously monitor the

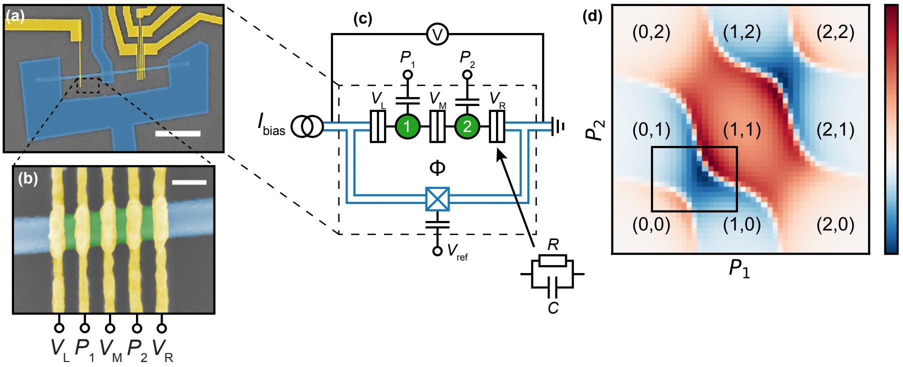

Figure 7.1: **Device layout.** Panels **(a)** and **(b)** show electron micrographs of the entire device and a zoom-in of the DQD area respectively. The false colored blue parts are superconducting, the green areas are bare InAs nanowire where the superconductor has been selectively etched away and the yellow colored parts are normal metal electrostatic gates. The quantum dots are formed by barrier gates V_L, V_M and V_R and the dot potentials by plunger gates P_1 and P_2. The scale bars are 2 µm **(a)** and 100 nm **(b)** wide. **(c)** Equivalent electrical circuit diagram of the device. **(d)** Numerical model of a DQD supercurrent charge-stability diagram. The DQD charge occupation is written in each sector. The electrostatic parameters assumed for this numerical result are extracted from this device, but in a weak QD-lead coupling limit, $\Gamma \ll \Delta, E_C$ (see Chapter 6). The experimental data in this chapter is not that limit. The rectangular inset indicates the equivalent location of the data discussed in this chapter.

voltage over the SQUID. When a finite voltage is detected, the value of I_{bias} is recorded as the switching current of the SQUID, I_{SW} (see methods section 3.2.2). The SQUID is made asymmetric with $I_{DQD} \gg I_{ref}$, the allows for direct control over the phase φ with the magnetic flux Φ through the SQUID loop (see theory section 2.3.1). This enables us to obtain the CPR of the DQD junction after subtracting I_{ref}.

The results in this chapter are obtained in a small area of the supercurrent charge stability diagram, marked in a numerical simulation of a generic DQD junction with $\Gamma \ll E_C$ in Figure 7.1d. Note that this is not completely representative for the data discussed here and only serves as a rough indication of where data is taken. The important features to consider here are the distinct areas of positive (0-junction, red) and negative (π-junction, blue) supercurrent. The shape of these areas are different due to the stronger dot-lead coupling as we will see in the results section of this chapter.

7.3. RESULTS

We focus our attention to the $0-\pi$ transitions in the marked area in Figure 7.1. We find that at these transitions, the CPR is negatively rectified and consequently has an even even symmetry around $\varphi = 0$ (Figure 7.2). This effect is most prominent in the center of the transition and decreases gradually when moving away from the transition. To analyze this effect we fit the measured switching currents to a phenomenological CPR:

$$I_{SW} = I_{ref} + I_{DQD}\sin(\varphi) - I_{anom}\left|\sin(\varphi)\right|, \tag{7.2}$$

where I_{ref} is the switching current amplitude of the reference arm, I_{DQD} is the switching current amplitude of the sinusoidal part of the DQD junction and I_{anom} of the anoma-

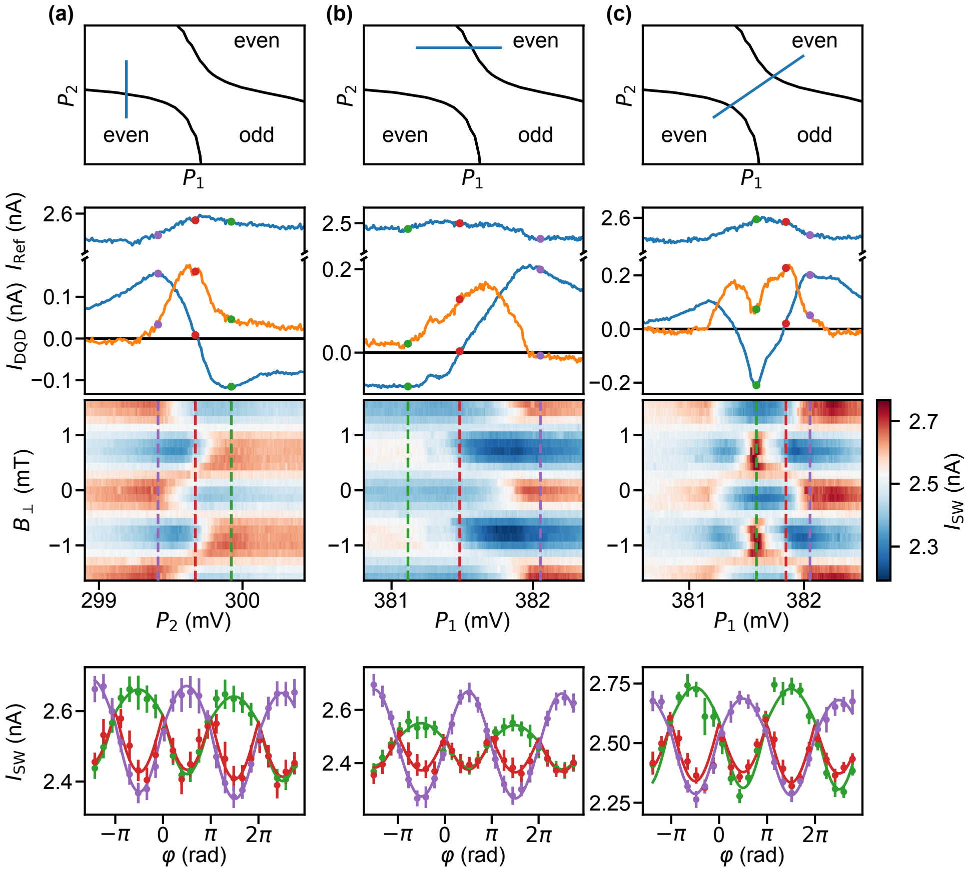

Figure 7.2: **Current-phase relation fits.** The top row contains sketches of the supercurrent charge-stability diagram with the charge parity written in the sectors. Each column corresponds a linetrace through the stability diagram, indicated by blue lines. A line along P_2 in column **(a)**, along P_1 in columns **(b)** and a diagonal line in column **(c)**. In the second row from the top we plot the switching current amplitudes obtained from the CPR fit. In blue the sinusoidal parts and the anomalous part in orange, where the upper trace is the reference arm amplitude I_{ref}, the traces below are I_{DQD} (blue) and I_{anom} (orange). The third row shows heatmaps of the average total switching current (from approximately 20 switching currents per pixel) as function of plunger gate P_1 or P_2 and $B_\perp$, which is proportional to the phase φ. In the bottom row the full CPR is plotted for three selected plunger gate voltages, denoted by same-colored dashed lines on the heatmaps and filled circles on in the second row. The filled circles are the average total switching current values, and the error bars indicate 1σ of the distribution. The solid lines are the best fits of Equation 7.2.

lous part, $\varphi = 2\pi(B_\perp - B_o)/B_p$, with $B_p \approx 1.7\,\mathrm{mT}$ the magnetic field period and B_o the offset magnetic field.. The reference junction is tuned such that $I_{\mathrm{ref}} \gtrsim 10\left(\left|I_{\mathrm{DQD}}\right| + |I_{\mathrm{anom}}|\right)$ at all times to ensure that we measure the CPR of the DQD junction only.

Figure 7.2 presents a summary of the results from fitting equation 7.2 at the different transition locations. The top row of Figure 7.2a depicts qualitative sketches of the superconducting charge-stability diagram with the DQD electron parity written inside each sector. The blue lines indicate where the data in the lower rows of each column are taken. The second row shows the evolution of the three switching current amplitudes at the $0-\pi$ transition when the changing parity of one of the quantum dots. The amplitude of the sinusoidal part of equation 7.2, I_{DQD} (plotted as a blue solid line), changes from positive to negative as we move between an even and odd parity, as expected for a single-level DQD junction (see chapter 6). Higher up in the same subfigure we plot, also in blue, the reference arm switching current I_{ref}. It stays mostly flat with a slight modulation when the junction switches from 0 to π, as expected for our asymmetric SQUID configuration. Plotted as an orange solid line is the amplitude for the anomalous part $-\left|\sin\varphi\right|$. It reaches its maximum at the center of the transition between the 0 and π region, and goes to 0 when moving away from the transition. Which shows that our phenomenological description is general enough to describe the full range in quantum dot potential energy that we measured.

The heatmaps in the middle row of Figure 7.2 show the averaged switching currents I_{SW} as a function of P_2 or P_1 and magnetic flux $B_\perp$. Note that the transition region here between the even and odd regions, spanning $370-600\,\mu\mathrm{eV}$, is significantly larger then in Figure 6.1g, where is at most $\sim 60\,\mu\mathrm{eV}$. This verifies that the quantum dots are more strongly coupled to the leads.

We fit equation 7.2 for each value of P_2 or P_1 to obtain the amplitudes in the top above. We show the complete CPR for three selected P_2 or P_1 values in the bottom row. The P_2 or P_1 values for each CPR are indicated by dashed lines on the heatmap with colors denoting each of the three characteristic CPRs: 0 phase sinusoidal (purple), π phase sinusoidal (green) and anomalous (red).

Far away from the $0-\pi$ transition the CPR is completely sinusoidal, reconfirming that that $-\left|\sin\varphi\right| \approx 0$. Moving closer to the transition point, the $-\left|\sin\varphi\right|$ contribution becomes stronger and exactly at the transition it is the only contributing term, making the CPR an even function of phase (shown in red). This effect is reproducible in both quantum dots; Figure 7.2a shows the effect as a function of P_2 (dot 2) and Figure 7.2b as a function of P_1 (dot 1). In Figure 7.2c we scan through both potentials simultaneously, along the total energy axis and observe a non-zero $-\left|\sin\varphi\right|$ contribution twice as we transition from a 0-junction to a π-junction and back to a 0-junction.

Next, we extent the gate range to cover ad two dimensional charge-stability diagram (Figure 7.3). We plot sinusoidal part I_{DQD} in Figure 7.3a, similar to the charge-stability diagram investigated in Chapter 6. In Figure 7.3b we plot the amplitude I'_{anom} for the rectified CPR parts. It shows a shape similar to I_{DQD}, but with an opposite sign and a wider transition area between the positive and negative amplitude regions. Finally we plot the ratio $I_{\mathrm{anom}}/I_{\mathrm{DQD}}$ and find that mostly the sinusoidal part dominates, but roughly half way, at the transition between the positive and negative supercurrent, the $-\left|\sin(\varphi)\right|$ component becomes a significant part and at some points the only term in the CPR.

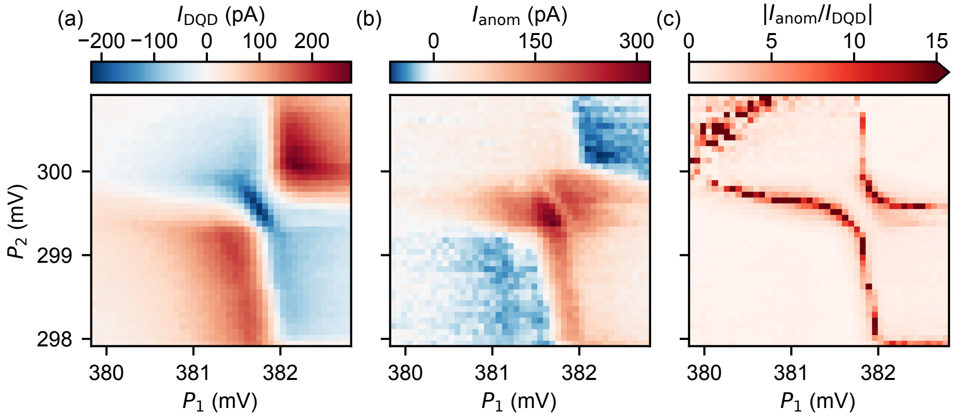

Figure 7.3: **Supercurrent charge stability diagrams.** **(a)** Sinusoidal switching current amplitude I_{DQD} **(b)** Amplitude of the anomalous I_{anom} contribution to the CPR. **(c)** Ratio between the anomalous and sinusoidal part of the CPR.

7.4. DISCUSSION

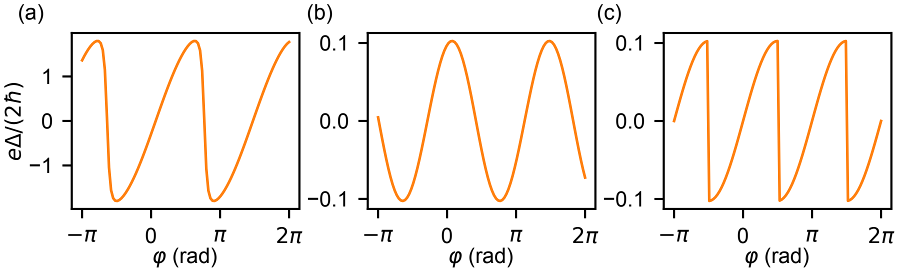

Figure 7.4: **Current-phase relations for different Josephson junctions.** **(a)** Single-channel SNS junction with a near unity transmission probability of 0.99. **(b)** Single-channel SNS junction with a low transmission probability of 0.1. **(c)** Single-channel SNS φ_0 junction with a low transmission probability of 0.1 and a phase-shift $\varphi_0 = \pi$.

To illustrate the qualitative difference of the junction behavior with existing experimental data and models in literature, we compare the measured data with CPR of three different types of SNS Josephson junctions in Figure 7.4. A non-sinusoidal CPR from highly transmitting modes in quantum dots junctions [202], shown in Figure 7.4a, does not match the shape of the red datapoints in Figure 7.2 and has an odd symmetry around $\varphi = 0$ in all orders. A low transmission junction has a sinusoidal shape, which matches shape to the data better, but retains the odd symmetry. When combined with a φ_0 junction, the CPR could have an even symmetry at φ_0 (Figure 7.4b), but besides requiring the Zeeman effect [182, 207, 208], unlikely in our setup due to $B < 1\,\mathrm{mT}$, the period of 2π is not consistent with the π periodicity of the observed CPR. In Figure 7.4c we plot an idealized zero-temperature CPR expected for a single quantum dot junction in the $\Gamma \approx E_C \approx \Delta$ regime at the transition between 0 and π [71, 72, 206]. This behavior however, is also not consistent with our observations.

For a better understanding, we start by describing the Andreev bound state energies in a single quantum dot junction using a model introduced by Vecino *et al* [203]. The model considers a symmetrically coupled dot in a strong dot-lead coupling limit $\Gamma \gg \Delta$, the ABS are described by [203]:

$$E_{A\pm} = \Delta\sqrt{\frac{\cos^2(\varphi/2) + 2E^2 + Z^2(Z^2 + \sin^2(\varphi/2)) \pm 2XS(\varphi)}{Z^2 + 2(X^2 + E^2) + 1}}, \tag{7.3}$$

$$S(\varphi) = \sqrt{Z^2\cos^2(\varphi/2) + E^2 + \sin^2(\varphi)/4},$$

where $E = \epsilon/(2\Gamma)$ with dot electrochemical potential ϵ, $X = E_{ex}/(2\Gamma)$ and E_{ex} is the so-called exchange field that represents the Coulomb interaction, finally we define $Z = \sqrt{X^2 - E^2}$.

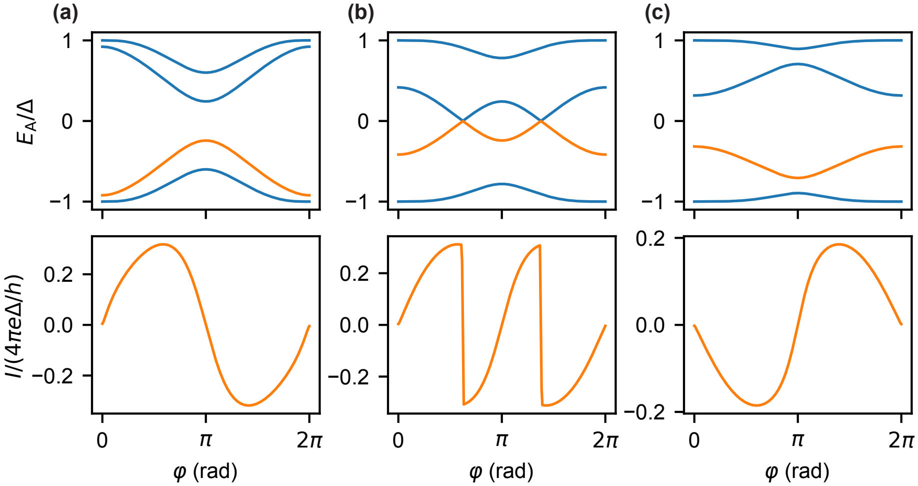

Figure 7.5: **Andreev bound states for a quantum dot junction.** Top row shows Andreev levels, bottom row the associated CPR. $E = -0.5$ for all panels. **(a)** 0-junction with $X = 0.25$. **(b)** Intermediate state with sign flips in the CPR, resulting in phase-induced parity switches. $X = 0.75$ **(c)** π-junction with $X = 1.5$.

Equation 7.3 is plotted in the top row of Figure 7.5 for different E_{ex}, representing different points in the $0-\pi$ transition. In the bottom row the we plot the CPR, $I(\varphi) = \partial E_A/\partial\varphi$, of the level with the dominant contribution (highlighted in orange). For a small $E_{ex} = 0.25$ (Figure 7.5a), the derivative of E_A yields a 0-junction, equivalent to an even occupation of the quantum dot. Increasing E_{ex} to 0.75 shows the inner ABS crossing (Figure 7.5b). This has the result that CPR changes sign at the crossings around $\varphi = \pi$, as shown by the current in the lower row. Increasing E_{ex} further enlarges the region where the supercurrent is negative and eventually the system is completely in the π state (Figure 7.5c).

Note that the finite exchange field causes a splitting of the ABS, resulting in four energy levels for a single transport channel instead of two for ABS in a regular SNS junction. Indeed, when the Coulomb interaction is turned off, $X \to 0$, we recover the regular ABS expression for an SNS junction without quantum dot with two energy levels (not shown). Lacking a satisfying microscopic explanation, we attempt to describe the effect phonologically. When our device is at the center of the $0-\pi$ transition, similar to $X = 0.75$ (Figure 7.5b), the shape of the CPR implies that the system switches parity at $\varphi = n\pi$, for integer n. This can effect can be approximated by

$$E_\mathrm{A} \propto \cos(\varphi)\,\mathrm{sgn}[\sin(\varphi)], \tag{7.4}$$

and we retrieve the CPR by taking the derivative with respect to φ:

$$I(\varphi) \propto -\left|\sin(\varphi)\right|. \tag{7.5}$$

In Figure 7.6a we plot Equation 7.4 with an orange solid line and its derivative, Equation 7.5, in solid red (Figure 7.6b). This CPR agrees well with experimental data and reproduces the key characteristics: a π period in phase, rectified to contain only negative supercurrent and it has an even symmetry around $\varphi = 0$. Indeed, this term was added to Equation 7.2 to fit the experimental data produce Figures 7.2 and 7.3.

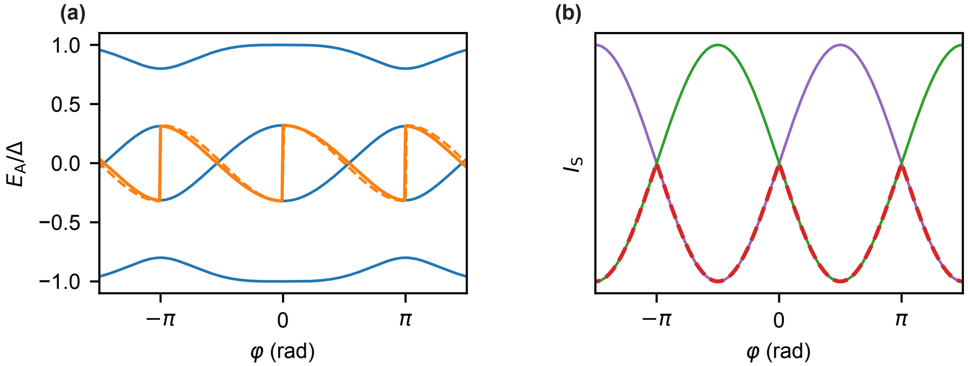

Figure 7.6: **Possible dynamics of anomalous CPR. (a)** Illustration of E_A at the transition. The system switches parity at every $\varphi = n\pi$. The orange lines indicate the main contribution to the supercurrent, where the solid line following the ABS exactly and the dashed line is Equation 7.4. **(b)** Current phase relations of the 0 (purple) state, the π (green) state and the transition state (red dashed). The red line is given by Equation 7.5.

This leaves us with the question why the system switches parity at every $\varphi = n\pi$, instead of staying in the lower ABS energy state as expected (Figure 7.5b). One possible explanation could be the conversion of bound state electrons into free quasiparticles, and vice versa, at $\varphi = n\pi/2 + 1/2$ – as described in reference 209. Note however that this non-equilibrium effect is explained through Landua-Zener transitions and requires a phase winding through a finite voltage bias. This seems unlikely in our setup due to the the slow winding we apply through the SQUID setup of our device. We suspect that a competition between the charging and superconducting energy scales could be responsible instead. This requires more detailed modeling of our device to confirm, which is beyond the scope of this thesis.

In conclusion, we have investigated the current-phase relation of a serial double quantum dot Josephson junction at the transition between 0 and π. We observe an anomalous current-phase rectification and describe it phonologically. The microscopic origin of this apparent non-equilibrium effect might be due to quasiparticles, but requires further investigation to obtain a satisfying explanation.

8

OUTLOOK

In this chapter we first explore possible new applications for the results of chapter 6. We discuss extensions of the system used in chapters 5, 6 and 7 and the characterisation of a prototype experiment performed for this purpose. In the final section, we briefly reflect on the results of chapter 4 and suggest a new direction for these type of experiments.

8.1. MEASURING SPINS WITH SUPERCURRENT

In chapter 6 we have shown that the direction of supercurrent through a single-orbital double quantum dot Josephson junction depends on the parity of the double quantum dot occupation. Furthermore, we have shown that the supercurrent becomes suppressed when the even occupation ground state changes from a spin-singlet to spin-triplet configuration. This effect could be used as a method of reading out spin qubit states.

Among quantum computation platforms, spin qubits are one of the leading candidates [210]. The field originally started with GaAs [211], but the field has since mostly moved to group IV semiconductors such as Si. Mostly for their long coherence times due to a lack of nuclear spins [212, 213]. Quantum state readout however has been a obstacle in scaling up the number of qubits. Measuring the value of a single spin is difficult due to the lack of an electrical signal and so most read-out schemes rely on converting different spin states to different charge states using Pauli's exclusion principle [55, 214]. The charge is subsequently measured using external sensors positioned in close proximity to the quantum dots containing the spins. The physical presence of these external detectors however, makes scaling up to two-dimensional-qubit arrays difficult [210]. A different readout approach couples the already existing quantum dot gates to a resonator, mitigating the traditional charge sensors [215]. By monitoring its resonance frequency, a distinction can be made between spin singlet and triplet states, using Pauli blockade. Recently, this method was improved by using an on-chip resonator, instead of an off-chip one [216]. It has the potential of overcoming the scaling limitations of traditional charge sensors, but still requires a spin-to-charge conversion.

Here we consider an alternative approach using a supercurrent. By placing the double quantum dot spin qubit in a Josephson junction, as we did in chapter 6, the supercurrent amplitude distinguishes between a singlet and a triplet configuration – making the spin-to-charge conversion unnecessary. When the spins are in a singlet configuration the number of allowed electron transfer processes that contribute to a supercurrent is approximately four times higher than for a triplet configuration. On top of that, the amplitudes for the singlet related transfer processes are significantly higher. This leads to a highly suppressed supercurrent for the triplet configuration compared to the singlet (see chapter 6).

From the perspective of superconductivity, InAs nanowires with epitaxial Al is a good candidate for a material system. Hard-gap induced superconductivity in InAs nanowires has been around now for a few years [90] and a supercurrent through single and double quantum dots has been demonstrated, in this thesis and in other works [52, 53]. Spin(-orbit) qubits have also been realised in InAs nanowires [217]. Recently, several studies have shown hard-gap superconductivity in planar geometries as well [218, 219]. From the perspective of the spin-qubit coherence times, InAs is not an optimal candidate due to the magnetic noise from uncontrolled nuclear spins present in InAs [1]. Group IV materials such as Ge and Si are gaining popularity due to a lack of these nuclear spins in abundant isotopes, resulting in significantly improved coherence times [212, 221–224]. These materials could be an alternative to InAs as high-mobility planer Ge with induced

---

[1] Although a recent study shows that these effect could be mitigated by using a notch filter approach [220]

superconductivity was recently reported [225, 226].

Another aspect to consider is the amplitude of the supercurrent. Most spin qubits are operated in the few-electron regime, in contrast to the many-electron regime in which the results from chapter 6 were obtained. Fewer electrons in the quantum dots will likely decrease the supercurrent amplitude, which makes the switching current approach less effective to determine the supercurrent amplitude. The supercurrent in chapter 6 was on the order of 10-100 pA, reaching the lower limit of what is technically possible with this method. An alternative is making the junction part of a superconducting resonator, similar to what we have done in references [197, 227]. The Josephson inductance depends on the critical current of the junctions. This inductance changes the resonance frequency of the resonator and can be measured using standard circuit QED techniques.

8.2. ANDREEV MOLECULE

In the experimental chapters of this thesis, we have presented results from single Josephson junctions in semiconductor nanowires. In an SNS junction supercurrent is carried by Andreev bound states (ABS). These bound states are fermionic modes, trapped inside the weak link and have discrete energy levels. One could see this as a type of artificial atom and a natural extension of this would be to couple this atom to one or more atoms to a molecule [159].

Apart from being an interesting new system in its own right – Andreev molecules can serve as a technological stepping stone towards realising a physical Kiteav chain [13, 14, 80]. Additionally, the junctions can each host a so-called Andreev qubit [228–230]. Coupling the two junctions could enable two-qubit gates or coherent manipulation of their energy spectra. These qubits have a key advantage over traditional spin qubit as they potentially enjoy some of the same benifits, while also being suited for long-range coherent interaction. Through spin-orbit interaction, the spin of the Andreev bound state determines the supercurrent flow [228], the supercurrent then allows for readout and manipulation through well-established circuit QED techniques [197, 227, 231].

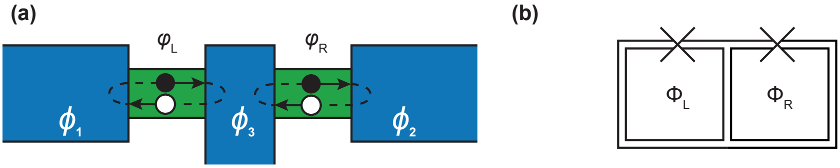

Figure 8.1: **Andreev molecule (a)** Schematic representation of an Andreev molecule made of two short Josephson junctions closely spaced together with phases $\varphi_L = \phi_1 - \phi_3$ and $\varphi_R = \phi_3 - \phi_2$. The green parts are semiconductors contacted to superconductors in blue. Andreev bound states are depicted by the electrons (black circle) and holes (white circle). **(b)** The Andreev molecule in **a** is part of two SQUID loops to control the phases of the junctions via magnetic fluxes Φ_L and Φ_R. The double lines denote superconducting connections.

The simplest Andreev molecule is composed of two SNS Josephson junctions, or atoms, spaced closely together. Figure 8.1 shows a schematic and circuit drawing of a two-junction molecule. Both junctions contain Andreev bound states and when the middle superconducting section is on the order of the superconducting coherence length, ξ, the Andreev wave functions overlap – creating the molecule. The ABS of the junctions hybridize and form avoided crossings in their spectrum. Figure 8.2 shows the spectrum as a function of the phase of the middle superconductor ϕ_3, with the other phases are kept constant at $\phi_1 = \pi$ and $\phi_2 = 3\pi/2$. At the degeneracy points of, where $\phi_3 = n\pi + \pi/2$, avoided crossings appear. The size of the gap created by the interaction, is given by $2\delta_\mathrm{D}$. The size of this gap is on the order of 10 µeV for realistic parameters with Al as a superconductor [2] and a junction separation $l = 50\,\mathrm{nm}$ [160]. Keeping the material properties constant, the energy gap depends on the junction separation and decreases exponentially with increasing separation l. In the limit of $l \gg \xi$, the energy gap disappears and the ABS in the separated junctions go back to their regular spectrum (shown by the red and green lines in Figure 8.2a).

On top of the earlier mentioned uses of an Andreev molecule, one could also envision a new type of Andreev qubit. The phase dependence of the level structure can be exploited to change excitation energies between levels. For example, one can adjust the phase such that the excitation energy falls within the reach of commercial microwave equipment and after exciting the qubit, change the splitting to frequencies where unwanted transitions are less likely to occur.

On a more fundamental note, the avoided crossing gap could be used to measure the superconducting coherence length. The relation between the gap size and the coherence length is derived in Reference [160].

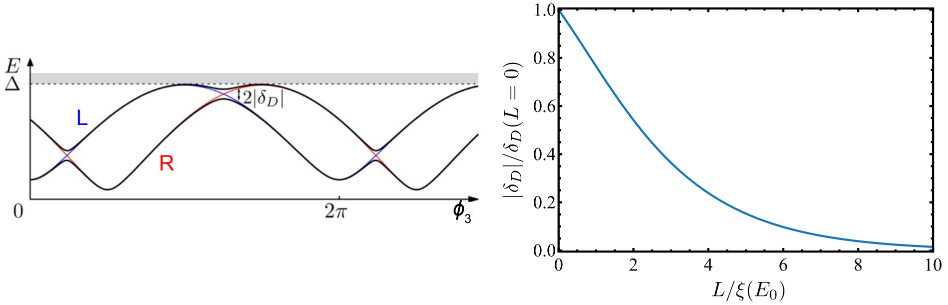

Figure 8.2: **(a)** Andreev molecule energy spectrum as a function of ϕ_3, the phases of the outer leads are kept constant at $\phi_1 = \pi$ and $\phi = 3\pi/2$. When $\xi \gg l$ the ABS of both junctions behave as isolated junctions, shown in red (left junction) and blue (right junction). If ξ is on the order of l however, a gap opens at the degeneracy points of size $2|\delta_\mathrm{D}|$. **(b)** The splitting falls of exponentially as l increases compared to ξ. Figure adapted from Reference [160].

8.2.1. MICROWAVE SPECTROSCOPY

When realising this molecule, the first step would be to measure its spectrum an observe the avoided crossings. Over the years several techniques have been used to measure the spectra of Andreev bound states. Among the most common are tunnel spectroscopy [232], superconducting resonators [197, 227, 233] and on-chip microwave spectroscopy [184, 234, 235]. In this section we will focus on a novel approach to on-chip microwave

---

[2] With superconducting gap $\Delta = 200\,\mu\mathrm{eV}$, coherence length $\xi = 96\,\mathrm{nm}$ and sheet resistance $R_\square = 1.43\,\Omega$.

spectroscopy, first introduced by the Flux Quantum Lab [3]. For an extensive study on the theoretical modelling and characteristics of this technique, we refer the reader to the thesis of Griesmar [236].

The basic principles are the same as the traditional on-chip spectroscopy method; it uses a Josephson tunnel junction both as a microwave source and detector. By voltage biasing the spectrometer junction, the ac Josephson effect generates a microwave current with frequency $f = 2eV_{\text{spec}}/h$ (see Figure 8.3). Coupled to the Andreev molecule, it will excite transitions between the even-parity Andreev levels. This energy dissipation in the spectrometer junction gives rise to a so-called inelastic Cooper tunneling current, detectable as peaks in the dc current-voltage curve of the spectrometer junction. As the peak voltage is related to the frequency of the ac current, we can measure the excitation spectrum of the molecule by scanning the current-voltage curve of the spectrometer junction (see section 2.3.3).

In previous works, the spectrometer was capacitively coupled to the Andreev junction [184, 234, 235] (see Figure 8.3a). This allowed for independent dc voltage biasing of the spectrometer junction and the Andreev junction. An important condition for this method is a good isolation of the spectrometer from circuit resonances that can crowd the measured spectrum and obscure the Andreev spectrum. In two of the publications, this was achieved by using resistive bias lines with resistances on the order of several kΩ. This has the unwanted side effect of decreasing the quality factor of the spectroscopy circuit, increasing the linewidth. Another approach is to use on-chip LC filters. While this does solve the issue of a decreased quality factor, it creates new unwanted resonances in the circuit.

The novel on-chip spectroscopy approach makes clever use of a symmetric SQUID with a magnetic flux $\Phi_{\text{spec}} = \Phi_0/2$, such that the supercurrents through the spectrometer junctions are equal and opposite. Meaning that the supercurrent circulates through the SQUID only and is effectively isolated from the external circuit. We embed the device under test, in this case an Andreev molecule, inside the SQUID loop to couple it to the spectrometer (see Figure 8.3b). This approach does not require any capacitors or on-chip isolation filters, which greatly simplifies fabrication.

There are some constraints on the size of tunnel junctions for this scheme to work. The Josephson energies of the junctions must be properly sized with respect to each other:

$$\frac{E_{\text{J,spec}}}{2} = E_{\text{J,1}} = E_{\text{J,2}}, \qquad E_{\text{J,3}} + E_{\text{J,4}} = E_{\text{J,dev}} \gg E_{\text{J,spec}}, \qquad E_{\text{J,3}} \ll E_{\text{J,4}}. \tag{8.1}$$

Symmetric spectrometer junctions ensures that the supercurrent is fully contained with the spectrometer SQUID. Asymmetry will cause the spectrometer to pick up resonances from outside the spectrometer circuit, crowding the spectrum. Next, the device Josephson energy E_{dev} must be much larger then that of the spectrometer. This ensures that the circuit can still be seen as a simple dc SQUID with predictable behaviour. Finally, the third constraint of having an asymetric SQUID at the Andreev junction, ensures control over φ_{L} through the magnetic flux Φ_{L} (see Section 2.3.1). The same condition should be used for the right Andreev junction.

---

[3] Group webpage: www.phi0.org

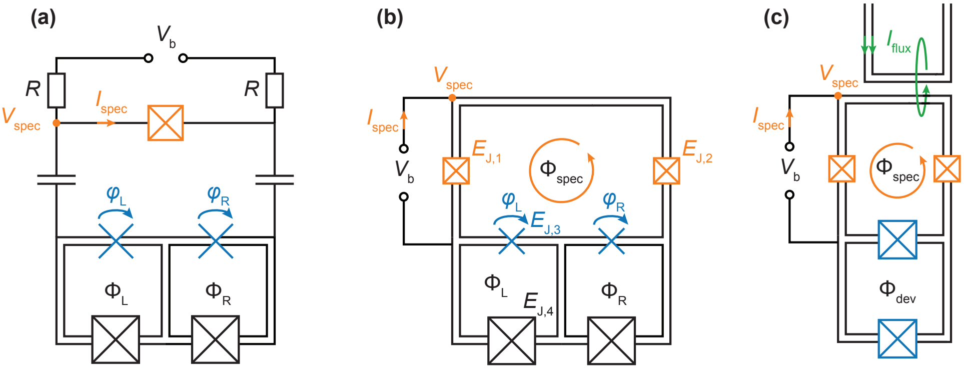

Figure 8.3: **On-chip microwave spectrometer circuits** **(a)** Traditional setup, where the spectrometer junction (orange) is capacitively coupled to the Andreev molecule (blue). By scanning the voltage-current curve of the spectrometer, $V_{\text{spec}} - I_{\text{spec}}$, excitations between the Andreev levels can be measured. The resistors R decouple the circuit from its environment to ensure a clean spectrum, these are typically on the order of tens of kΩ. The magnetic fluxes Φ_{L},Φ_{R} control the phases over the Josephson junctions $\varphi_{\text{L}} = \phi_2 - \phi_1$, $\varphi_{\text{R}} = \phi_3 - \phi_2$ respectively through asymmetric SQUIDs. **(b)** Alternative setup where two spectrometer junctions are used in a symmetric dc-SQUID arrangement. The Andreev molecule is placed inside the dc SQUID. Isolation resistors are not needed when the spectrometer SQUID is operated at $\Phi_{\text{spec}} = \Phi_0/2$, where only resonances in the Andreev molecule are excited. **(c)** Prototype version of the circuit in **b**, where the Andreev molecule is replaced by a symmetric dc SQUID made out of two tunnel junctions. At the top a flux bias line (green) is placed to control Φ_{spec} preferentially.

To test the feasibility of the new spectroscopy method, we have fabricated and measured a test setup where the Andreev molecule is replaced by a tunnel junction in the form of a symmetric SQUID arrangement for easier fabrication (see Figure 8.3c, note however that we used an external magnet to control the flux, not I_{flux}. The purpose is to test the functionality of the spectrometer approach by exciting the plasma frequency of the device SQUID. External magnetic flux Φ_{dev} controls its critical current and thus its plasma frequency, $\omega_{\text{p}} = \sqrt{2eI_{\text{C,dev}}/(\hbar C)}$ (see Section 2.3.2). The Josephson energies of the device SQUID and spectrometer junctions are $E_{\text{J,dev}} = 343.9\,\mu\text{eV}$, $E_{\text{J,spec}} = 37.2\,\mu\text{eV}$ respectively.

Figure 8.4 summarizes the results of the test setup. In subfigure **a** we plot the measured spectrometer current as a function of the voltage over the spectrometer junctions V_{spec} and external magnetic flux field B_{flux} . Note that B_{flux} is global and thus determines both Φ_{spec} and Φ_{dev} in a fixed ratio. Around $V_{\text{spec}} = 0$ we see the switching current of the spectrometer SQUID oscillating with a period of $95.8\,\mu\text{T}$ in B_{flux}, corresponding to the expected behaviour of a symmetric SQUID with a loop area of $21.6\,\mu\text{m}^2$, in agreement with the designed size. We zoom in on green line at $234\,\mu\text{V}$, where we are at the center of a resonance from outside the spectrometer circuit. The line is plotted as function of B_{flux} in Figure 8.4b. At $B_{\text{flux}} \approx 0$, supercurrent through both spectrometer junctions is equal in size and direction and so the critical current of the spectrometer SQUID is maximal. This makes the spectrometer maximally sensitive to external modes. At $B_{\text{flux}} \approx 50\,\mu\text{T}$, the flux $\Phi_{\text{spec}} = \Phi_0/2$, the point where the spectrometer supercurrent is equal and opposite to each other. Resulting in a circulating supercurrent and a minimal sensitivity to external modes. This is reflected in the strong attenuation of the spectrometer current, which means the spectrometer isolation from the external environment is working as designed. We fit the dc current data to Equation 2.35 to characterize the external mode using:

$$I = \frac{I_{\mathrm{C,spec}}^2}{2} \frac{Z_{\mathrm{ext},0}}{V_{\mathrm{spec}}},$$

where $Z_{\mathrm{ext},0} = \sqrt{L/C}$ is the characteristic impedance of the external mode with inductance L and capacitance C, and $I_{\mathrm{C,spec}}$ is the critical current of the spectrometer SQUID. The fit is shown as a dashed black line and agrees well with the data. We find $\mathrm{Re}\{Z_{\mathrm{ext},0}\} = 159.3\,\Omega$.

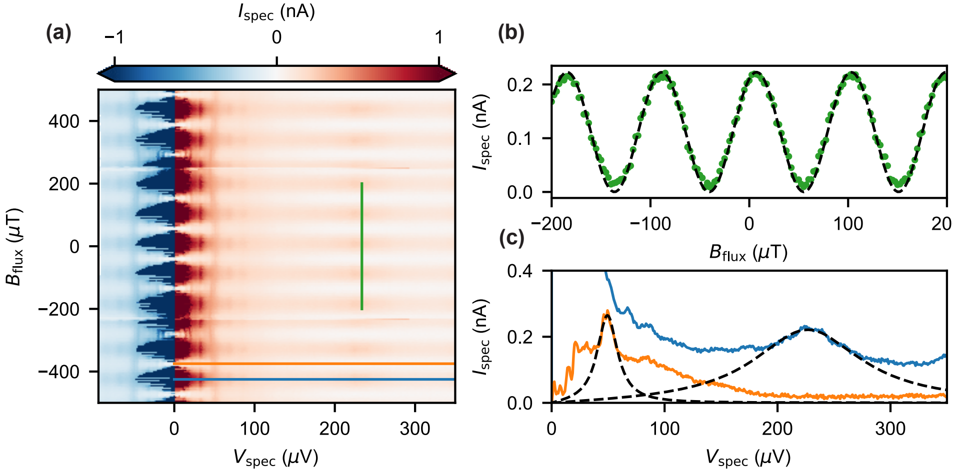

Figure 8.4: **On-chip microwave spectrometer prototype characterization (a)** Overview scan of spectrometer current I_{spec} as a function of V_{spec} and magnetic field B_{flux}. Around $V_{\mathrm{spec}} = 0$, the supercurrent oscillations of the spectrometer SQUID are visible. The breaks in the data at $|B_{\mathrm{flux}}| \approx 250\,\mu\mathrm{eV}$ are due to the low E_{J} of the device SQUID. **(b)** Spectrometer current due to an external resonance mode as a function of B_{flux}. Dashed line shows a best fit for an *RLC* circuit. **(c)** Spectrometer voltage-current curve at $\Phi_{\mathrm{spec}} = 0$ (blue) with a fit (dashed black line) to the external resonance and at the isolation setting $\Phi_{\mathrm{spec}} = \Phi_0/2$ (orange), with a fit to the plasma mode of the device SQUID (dashed black line).

In Figure 8.4c we plot two voltage-current curves of the spectrometer. Plotted in blue is the spectrometer at $\Phi_{\mathrm{spec}} = 0$ and we see the same external mode as in subfigure **b** around 230 µeV. We fit the external mode again with, this time for a frequency dependent external parallel RLC circuit impedance:

$$\mathrm{Re}\{Z_{\mathrm{ext}}(x)\} = \frac{Z_{\mathrm{ext},0} Q}{1 + \frac{Q^2}{x^2}\left(1 - x^2\right)^2}, \tag{8.2}$$

with dimensionless frequency $x = \omega/\omega_0$. The best fit results in a center frequency $f_0 = \sqrt{LC}^{-1}/(2\pi) = 113\,\mathrm{GHz}$, a quality factor $Q = R\sqrt{C/L} = 2$ and $Z_{\mathrm{ext},0} = 155\,\Omega$. The value for $Z_{\mathrm{ext},0}$ is consistent with the characteristic impedance found from the data in Figure 8.4b. The orange line is taken at $\Phi_{\mathrm{spec}} = \Phi_0/2$. Note that the external mode has disappeared and a mode around $V_{\text{spec}} = 50.6\,\mu\text{V}$ has become visible. This is the plasma mode of the device SQUID. We also fit this peak with Equation 8.2 and find $f_0 = 24.4\,\text{GHz}$, $Q = 2.3$ and $Z_{\text{int},0} = 138.9\,\Omega$, similar to values found in other on-chip microwave experiments [184, 235]. We summarize all extracted quantities in Appendix B.

These results show the feasibility of using this setup to measure the Andreev molecule spectrum. One challenge however is the need for independent control over two different fluxes (three in case of the Andreev molecule). In a typical dilution refrigerator transport setup, usually there is only a single global external magnetic field available. Independent control over multiple fluxes can be achieved by adding a flux-bias line close to the SQUID loop area, as depicted in Figure 8.3c. A large current on the order of several mA through these lines generates a local magnetic field to control the flux through the nearest SQUID loop. In typical setups this would cause a problem, as the dissipated power of these current through a resistive wire is higher then the cooling power of most dilution refridgerators at the mixing chamber. We have adressed this issue by using continuous superconducting wires up to the still level, where there is more cooling power available. This allows for large currents without heating up the mixing chaimber. In section 3.2.1 we went into more detail of the practical challanges and solutions to them.

8.3. TOWARDS A PHYSICAL KITAEV CHAIN

In chapter 4 we have reported on the observation of the 4π-periodic Josephson effect, a signature of Majorana bound states. The observed magnetic field threshold value is in the range of 175-300 mT, consistent with estimations for other publications. We were furthermore able to suppress the effect in the same device by changing the chemical potential with electrostatic gates.

Ever since the first experimental signature of Majorana states [87], several articles have reported on topologically trivial mechanisms of mimicking Majorana signatures [62, 148, 237–239]. In 2018, the possibility of so-called quasi-Majoranas was introduced [240] where local Majorana-like states can mimic many of the signatures of real Majorana states, including the fractional Josephson effect. The existence of these ‘quasi Majorana’ states and the difficulty with which they are distinguished from real Majorana states, makes one question the robustness of the current approach of creating Majoranas in semiconductor nanowire structures. Developing a topological qubit and indeed scaling up the number of qubits, requires a reliable and reproducible method for creating Majorana states.

An alternative approach is mapping a Kitaev chain onto a linear array of superconducting quantum dots. Under the right conditions, the Hamiltonian of the array becomes identical to the topological non-trivial Kitaev chain Hamiltonian with Majorana end states [13, 14, 80]. This approach allows for better control over the parameters that control the Majorana states. For example, the seperation between the Majorana states can be tuned *in situ* by adding/removing quantum dots to/from array with electrostatic gates. Additionally another set of gates can tune the superconducting coupling. See also Section 2.6.3.

From the Andreev molecule as described in the previous section, the technological step to a Kitaev chain is actually quite small. We only need to add quantum dots in the weak links of the Josephson junction and apply a magnetic field to lift the spin degeneracy. This minimal chain of two sites lacks topological protection, but is can serve as a prototype and demonstrate the feasibility of this approach [241]. In general longer chains are preferable, as they are more forgiving to variations in the parameters [14].

This easy step towards a Kiteav chain does require the inter-dot couplings t_n and p-wave pairing Δ_n to be equal, the spin-orbit length l_{SO} less or equal to the length of the quantum dots and the on-site chemical potentials of the dots $\mu_n = 0$. This last condition is trivially realized with plunger gates. The induced gap of the Al shell in InAs nanowires is typically on the order of 200 µeV, since we need a finite magnetic field for lifting the spin degeneracy, this will be a lower value when searching for Majoranas. With the use of electrostatic gates, t_n is readily tunable between 1-200 µeV, realising $t_n = \Delta_n$. Finally, the spin-orbit length typically is around $l_{\mathrm{SO}} \approx 130\,\mathrm{nm}$, which sets an upper bound on the length of the quantum dots. In chapters 5-7 we have used quantum dots with a pitch down to 60 nm, statisfying this condition.

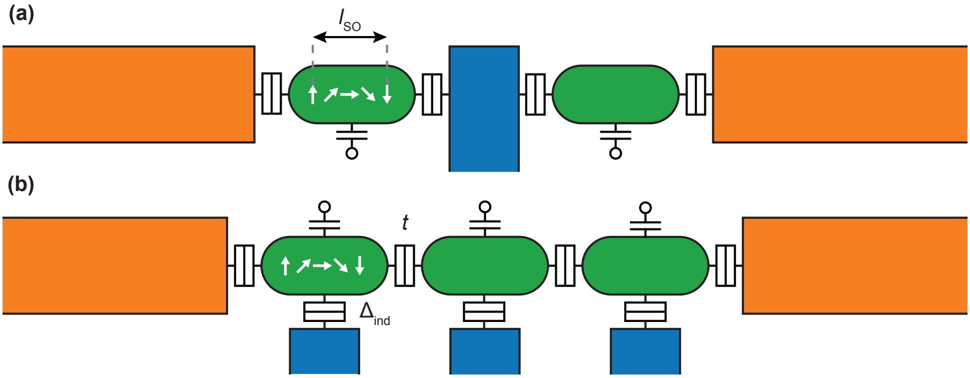

Figure 8.5: **Physical realisations of Kiteav chain (a)** Nanowire Kiteav chain with normal leads (orange) on both ends and a central superconductor (blue), coupled to single-orbital quantum dots (green) on either side. An external magnetic field lifts the spin degeneracy of the electrons in the quantum dots and spin-orbit interaction enables superconducting pairing between the quantum dots, provided that l_{SO} is smaller than the quantum dot. **(b)** 2DEG configuration where the superconducting leads are positioned on the side of the quantum dots, allowing for independent tuning of both Δ_{ind} and t. Note that Δ_{ind} is the induced s-wave pairing, not to be confused with the p-wave pairing Δ_n.

In this setup, electrons can co-tunnel via above-gap quasiparticle states in the superconductor between the dots – representing t. The superconducting lead should be smaller than the superconducting coherence length ξ, such that the pairing is induced through crossed Andreev reflection, representing Δ_n. An external magnetic field lifts the spin degeneracy and assuming the level spacing the quantum dots is much larger then the other energy scale – we have a spin polarized electron in each dot, with hopping t and pairing Δ_n. Since we have an s-wave superconductor, the pairing will be zero. To solve this, the authors of reference [241] rely on local magnetic field vectors to control the angle between the spins, tuning the pairing. In the setup of Figure 8.5a, we rely on spin-orbit interaction to give a finite pairing energy.

A downside to this approach is that there is limited independent tunablility of the normal tunneling t and the p-wave pairing energy Δ_n. As the tunnel gate controlling the coupling to the quantum dots will affect both of these parameters. The spin-orbit coupling could be varied by changing the potential landscape with the electrostatic gates, thus changing Δ_n independently. But there is no simple relation between the a gate voltage and the resulting change in spin-orbit coupling strength. This approach might still be a worthwhile endeavour as it turns out that longer chains have a relatively high tolerance for variations in t and Δ_n. An array with 5 quantum dots can still have a topological gap of around 90 µeV with t, Δ_n varying randomly between 43 and 129 µeV [14].

8.3.1. TWO DIMENSIONS

Using a two-dimensional electron gas (2DEG) as a platform allows for full independent control over t and Δ_{ind}. In a 2DEG one has the freedom to place the superconductors alongside the quantum dots instead of in-between the dots. This allows the electrostatic gates to tune Δ_{ind} (and thus Δ_n) independently from t (see Figure 8.5b).

The 2DEG platform however has its own set of challenges. The developments of inducing superconductivity and quantum dots in large spin-orbit coupling materials, such as InAs and InSb, lack behind those of VLS nanowires. The challenges arise from the fact that the 2DEG layer should be close to the surface (order of 10 nm) in order to get good-quality induced superconductivity from a superconducting layer on top. This however reduces the mobility of the electrons as surface scattering effects become more prominent.

Recently there have been reports of good-quality induced superconductivity in InAs surface 2DEGs [218, 219, 242]. There has also been progress in InSb 2DEGs, where very recently stable quantum dots were realised [243]. Induced superconductivity has also been shown in this system using NbTiN [244]. These advancements make the 2DEG platform a interesting alternative to nanowires for creating a physical Kitaev chain.

A

FABRICATION DETAILS

In this appendix we list the fabrication steps of the device measured in Chapters 5-7. Fabrication is done on 9.5 mm × 9.5 mm silicon coupons cut from a commercial 525 µm thick 4 inch intrinsic silicon wafer with a 285 nm thermally grown SiO_x layer. The lithography steps are performed with a 100 kV Raith EBPG5200. All steps are preformed at room temperature, unless stated otherwise. The lithography developer solution is stored at 7 °C. When used, it is poured into a beaker and used directly. Note that all of the steps described below are optimized to work in the Kavli nanolab cleanroom in Delft. The parameters might need adjustments for other cleanrooms.

1. **Electron-beam alignment markers**
    - Spin coating - Polymethylmethacrylaat (PMMA) 950A4 - 4000 rpm (target thickness: 200 nm)
    - Soft bake - 175 °C - 5 min
    - Electron-beam exposure - 1200 $\mu C/cm^2$
    - Development - H_2O:isopropanol (IPA) (1:3) - 7 °C - 1 min
    - N_2 dry
    - Evaporation - titanium (Ti) - 10 nm
    - Evaporation - gold (Au) - 90 nm
    - Lift off - acetone - 52 °C - 20 min
    - Rinse - IPA - 1 min
    - N_2 dry

2. **Shorting line**
   A continuous line made from aluminum that electrically shorts all ohmic nanowire contacts. This is done to protect the nanowire from electrostatic discharge.

   - Spin coating - PMMA 950A4 - 4000 rpm (target thickness: 200 nm)
   - Soft bake - 175 °C - 5 min
   - Electron-beam exposure - 1200 $\mu C/cm^2$
   - Development - H_2O:IPA (1:3) - 7 °C - 1 min
   - N_2 dry
   - Evaporation - aluminum (Al) - 50 nm
   - Lift off - acetone - 52 °C - 20 min
   - Rinse - IPA - 1 min
   - N_2 dry

3. **Deterministic deposition of nanowires**
   Nanowires are manually transferred from a growth chip to the silicon substrate as described in Chapter 3.1.1.

4. **Selective etch of nanowire shell** The superconducting aluminum shell is selectively removed for the two Josephson junctions by using a chemical wet etch as described in Chapter 3.1.2.

   - Pre-bake - 175 °C - 5 min
   - Spin coating - PMMA 950A4 - 4000 rpm (target thickness: 200 nm)
   - Soft bake - 175 °C - 5 min
   - Electron-beam exposure - 1800 $\mu C/cm^2$
   - Development - H_2O:IPA (1:3) - 7 °C - 1 min
   - Etch - MF-321 - 55 s
   - Rinse - H_2O - 10 s
   - Rinse - H_2O - 30 s
   - Rinse - H_2O - 30 s
   - Strip - acetone - 52 °C - 20 min

5. **Nanowire leads and bondpads**
   Normal metal layer for the nanowire source and drain bondpads and most of the leads. This is made from a normal metal to avoid resonant modes in the circuit.

   - Spin coating - PMMA 950A4 - 4000 rpm (target thickness: 200 nm)
   - Soft bake - 175 °C - 5 min
   - Electron-beam exposure - 1200 $\mu C/cm^2$
   - Development - H_2O:IPA (1:3) - 7 °C - 1 min
   - N_2 dry
   - Evaporation - Ti - 10 nm
   - Evaporation - Au - 50 nm
   - Lift off - acetone - 52 °C - 20 min
   - Rinse - IPA - 1 min
   - N_2 dry

6. **Superconducting arms and nanowire contacts**
   Superconducting arms connect the two Josephson junctions in parallel to form a dc SQUID one one end and connect to the normal metal leads on the other end.

   - Spin coating - PMMA 950A4 - 4000 rpm (target thickness: 200 nm)
   - Soft bake - 175 °C - 5 min
   - Electron-beam exposure - 1200 μC/cm^2
   - Development - H_2O:IPA (1:3) - 7 °C - 1 min
   - N_2 dry
   - Argon milling - 50 W - 3 min
   - Sputtering - Niobium titanium nitride (NbTiN) - 90 nm
   - Evaporation - Au - 50 nm
   - Lift off - acetone - 52 °C - 20 min
   - Rinse - IPA - 1 min
   - N_2 dry

7. **Global dielectric**
   This dielectric layer separates the electrostatic gates from the nanowire and is deposited over the entire substrate.

   - Atomic layer deposition - aluminum oxide (Al_2O_3) - 105 °C - 10 nm

8. **Gate electrodes**
   The metal for the gate electrodes is deposited under multiple angles to conformally cover the nanowires with a thickness of approximately 50 nm. See Chapter 3.1.4 for details.

   - Spin coating - PMMA 950A3 - 4000 rpm (target: 150 nm)
   - Soft bake - 175 °C - 5 min
   - Electron-beam exposure - 1200 μC/cm^2
   - Development - H_2O:IPA (1:3) - 7 °C - 1 min
   - N_2 dry
   - Evaporation - Ti - 5 nm - $-60°$
   - Evaporation - Ti - 5 nm - 60°
   - Evaporation - Au - 10 nm - 60°
   - Evaporation - Au - 10 nm - $-60°$
   - Evaporation - Au - 20 nm - 5°
   - Lift off - acetone - 52 °C - 20 min
   - Rinse - IPA - 1 min
   - N_2 dry

9. **Gate leads and bondpads**
   Due to the evaporation angle of 60° of the gate electrodes, metal is deposited on the side walls of the resist. This makes lift off difficult for large structures. The leads and bondpads for the gate electrodes are therefore done in a separate step, with a normal evaporation angle for 90°.

   - Spin coating - PMMA 950A4 - 4000 rpm (target thickness: 200 nm)
   - Soft bake - 175 °C - 5 min
   - Electron-beam exposure - 1200 μC/cm^2
   - Development - H_2O:IPA (1:3) - 7 °C - 1 min
   - N_2 dry
   - Evaporation - Ti - 10 nm
   - Evaporation - Au - 90 nm
   - Lift off - acetone - 52 °C - 20 min
   - Rinse - IPA - 1 min
   - N_2 dry

10. **Dielectric etch nanowire bondpads**
    We selectively remove the dielectric at the bondpads to facilitate wire bonding.

    - Pre-bake - 175 °C - 5 min
    - Spin coating - PMMA 950A4 - 4000 rpm (target thickness: 200 nm)
    - Soft bake - 175 °C - 5 min
    - Electron-beam exposure - 1000 μC/cm^2
    - Development - H_2O:IPA (1:3) - 7 °C - 1 min
    - Etch - MF-321 - 3 min
    - Rinse - H_2O - 10 s
    - Rinse - H_2O - 30 s
    - Rinse - H_2O - 30 s
    - Strip - acetone - 52 °C - 20 min

B

CIRCUIT PARAMETERS OF ON-CHIP MICROWAVE SPECTROSCOPY

In this appendix we list all relevant circuit parameters extracted from the on-chip microwave spectroscopy prototype device described in Section 8.2.1. These parameters help to asses the feasibility of this approach for spectroscopy, in Section 8.2.1 we aim for measuring the energy spectrum of an Andreev molecule in a nanowire. Literature values for these parameters can be found in references [184, 234, 235].

Table B.1: Extracted circuit parameters

Spectrometer SQUID		Device SQUID		External mode	
R_N (kΩ)	17.2	R_N (kΩ)	1.9		
Δ (µeV)	197.8	Δ (µeV)	197.8		
I_C (nA)	18.1	I_C (nA)	167.4		
E_J (µeV)	37.2	E_J (µeV)	343.9		
L_J (nH)	18.2	L_J (nH)	2.0		
		R (Ω)	323.4	R (Ω)	311.2
		L (nH)	0.9	L (nH)	0.2
		C (fF)	46.9	C (fF)	9.1
		f_0 (GHz)	24.5	f_0 (GHz)	113.1
		Z_0 (Ω)	138.8	Z_0 (Ω)	155.0
		Q	2.3	Q	2.0

The critical current is determined from the superconducting gap Δ and the normal-state resistance R_N with $\pi\Delta/(2eR_\mathrm{N})$. The Josephson energy is given by $\hbar I_\mathrm{C}/(2e)$ and the Josephson inductance by $\Phi_0/(2\pi I_\mathrm{C})$. The RLC resonance properties are defined as: center frequency $f_0 = 1/(2\pi\sqrt{LC})$, characteristic impedance $Z_0 = \sqrt{L/C}$ and quality factor $R\sqrt{C/L}$.

BIBLIOGRAPHY

[1] Merli, P. G., Missiroli, G. F. & Pozzi, G. On the statistical aspect of electron interference phenomena. *Am. J. Phys* **44**, 306–307 (1976).

[2] Nielsen, M. A. & Chuang, I. Quantum computation and quantum information (2002).

[3] Shor, P. W. Algorithms for quantum computation: discrete logarithms and factoring. In *Proceedings 35th annual symposium on foundations of computer science*, 124–134 (Ieee, 1994).

[4] Vandersypen, L. M. & Eriksson, M. A. Quantum computing with semiconductor spins. *Physics Today* **72**, 8–38 (2019).

[5] Devoret, M. H. & Schoelkopf, R. J. Superconducting circuits for quantum information: an outlook. *Science* **339**, 1169–1174 (2013).

[6] Terhal, B. M. Quantum error correction for quantum memories. *Reviews of Modern Physics* **87**, 307 (2015).

[7] Klitzing, K. v., Dorda, G. & Pepper, M. New method for high-accuracy determination of the fine-structure constant based on quantized Hall resistance. *Physical Review Letters* **45**, 494 (1980).

[8] Majorana, E. Teoria simmetrica dell'elettrone e del positrone. *Il Nuovo Cimento (1924-1942)* **14**, 171 (1937).

[9] Kitaev, A. Y. Unpaired Majorana fermions in quantum wires. *Physics-Uspekhi* **44**, 131 (2001).

[10] Hyart, T. *et al.* Flux-controlled quantum computation with Majorana fermions. *Physical Review B* **88**, 035121 (2013).

[11] Plugge, S., Rasmussen, A., Egger, R. & Flensberg, K. Majorana box qubits. *New Journal of Physics* **19**, 012001 (2017).

[12] Karzig, T. *et al.* Scalable designs for quasiparticle-poisoning-protected topological quantum computation with Majorana zero modes. *Physical Review B* **95**, 235305 (2017).

[13] Fulga, I. C., Haim, A., Akhmerov, A. R. & Oreg, Y. Adaptive tuning of Majorana fermions in a quantum dot chain. *New journal of physics* **15**, 045020 (2013).

[14] Sau, J. D. & Sarma, S. D. Realizing a robust practical Majorana chain in a quantum-dot-superconductor linear array. *Nature communications* **3**, 1–6 (2012).

[15] Kamerlingh Onnes, H. The resistance of pure mercury at helium temperatures. *Commun. Phys. Lab. Univ. Leiden, b* **120** (1911).

[16] Meissner, W. & Ochsenfeld, R. Ein neuer effekt bei eintritt der supraleitfähigkeit. *Naturwissenschaften* **21**, 787–788 (1933).

[17] London, F. & London, H. The electromagnetic equations of the supraconductor. *Proceedings of the Royal Society of London. Series A-Mathematical and Physical Sciences* **149**, 71–88 (1935).

[18] Landau, L. D. & Ginzburg, V. On the theory of superconductivity. *Zh. Eksp. Teor. Fiz.* **20**, 1064 (1950).

[19] Tinkham, M. *Introduction to superconductivity* (Courier Corporation, 2004).

[20] Bardeen, J., Cooper, L. N. & Schrieffer, J. R. Microscopic theory of superconductivity. *Physical Review* **106**, 162 (1957).

[21] Bogolyubov, N. A new method in the theory of superconductivity. i. *Zh. Eksp. Teor. Fiz.* **6**, 58–65 (1958).

[22] Andreev, A. Zh. e ksp. teor. fiz. 46, 1823 1964 sov. phys. *JETP* **19**, 1228 (1964).

[23] Blonder, G., Tinkham, M. & Klapwijk, T. Transition from metallic to tunneling regimes in superconducting microconstrictions: Excess current, charge imbalance, and supercurrent conversion. *Physical Review B* **25**, 4515 (1982).

[24] Beenakker, C. Quantum transport in semiconductor-superconductor microjunctions. *Physical Review B* **46**, 12841 (1992).

[25] Nazarov, Y. V., Nazarov, Y. & Blanter, Y. M. *Quantum transport: introduction to nanoscience* (Cambridge university press, 2009).

[26] Josephson, B. Possible new effect in superconducting tunneling. *Phys. Lett.* **1**, 251–253 (1962).

[27] Anderson, P. W. & Rowell, J. M. Probable observation of the Josephson superconducting tunneling effect. *Physical Review Letters* **10**, 230 (1963).

[28] Beenakker, C. & Van Houten, H. Josephson current through a superconducting quantum point contact shorter than the coherence length. *Physical review letters* **66**, 3056 (1991).

[29] Koch, J. *et al.* Charge-insensitive qubit design derived from the Cooper pair box. *Physical Review A* **76**, 042319 (2007).

[30] Hamilton, C. A., Kautz, R. L., Steiner, R. L. & Lloyd, F. L. A practical Josephson voltage standard at 1 v. *IEEE electron device letters* **6**, 623–625 (1985).

[31] Holst, T., Esteve, D., Urbina, C. & Devoret, M. Effect of a transmission line resonator on a small capacitance tunnel junction. *Physical review letters* **73**, 3455 (1994).

[32] Van Woerkom, D. J. *et al.* Josephson radiation and shot noise of a semiconductor nanowire junction. *Physical Review B* **96**, 094508 (2017).

[33] Deblock, R., Onac, E., Gurevich, L. & Kouwenhoven, L. P. Detection of quantum noise from an electrically driven two-level system. *Science* **301**, 203–206 (2003).

[34] Laroche, D. *et al.* Observation of the 4π-periodic Josephson effect in indium arsenide nanowires. *Nature communications* **10**, 1–7 (2019).

[35] Chauvin, M. *The Josephson effect in atomic contacts.* Ph.D. thesis (2005).

[36] Ambegaokar, V. & Halperin, B. Voltage due to thermal noise in the dc Josephson effect. *Physical Review Letters* **22**, 1364 (1969).

[37] Ambegaokar, V. & Halperin, B. I. Voltage due to thermal noise in the dc Josephson effect. *Phys. Rev. Lett.* **23**, 274–274 (1969).

[38] Stewart, W. Current-voltage characteristics of Josephson junctions. *Applied Physics Letters* **12**, 277–280 (1968).

[39] McCumber, D. Effect of ac impedance on dc voltage-current characteristics of superconductor weak-link junctions. *Journal of Applied Physics* **39**, 3113–3118 (1968).

[40] Fulton, T. & Dunkleberger, L. Lifetime of the zero-voltage state in Josephson tunnel junctions. *Physical Review B* **9**, 4760 (1974).

[41] van Woerkom, D. Semiconductor nanowire Josephson junctions: In the search for the Majorana (2017).

[42] Anchenko, Y. & Zil'Berman, L. The Josephson effect in small tunnel contacts. *Soviet Phys. JETP* **28** (1969).

[43] Ingold, G.-L. & Nazarov, Y. V. Charge tunneling rates in ultrasmall junctions. In *Single charge tunneling*, 21–107 (Springer, 1992).

[44] Tien, P. & Gordon, J. Multiphoton process observed in the interaction of microwave fields with the tunneling between superconductor films. *Physical Review* **129**, 647 (1963).

[45] Onac, G.-E. High frequency noise detection in mesoscopic devices (2005).

[46] van Gulik, R. J. J. Data analysis of measurement on nanodevices. *Bachelor thesis* (2015).

[47] Billangeon, P.-M., Pierre, F., Bouchiat, H. & Deblock, R. Emission and absorption asymmetry in the quantum noise of a Josephson junction. *Physical review letters* **96**, 136804 (2006).

[48] Blanter, Y. M. & Büttiker, M. Shot noise in mesoscopic conductors. *Physics reports* **336**, 1–166 (2000).

[49] Onac, E., Balestro, F., Trauzettel, B., Lodewijk, C. & Kouwenhoven, L. Shot-noise detection in a carbon nanotube quantum dot. *Physical review letters* **96**, 026803 (2006).

[50] Tarucha, S., Austing, D., Honda, T., Van der Hage, R. & Kouwenhoven, L. P. Shell filling and spin effects in a few electron quantum dot. *Physical Review Letters* **77**, 3613 (1996).

[51] Kouwenhoven, L. P., Austing, D. & Tarucha, S. Few-electron quantum dots. *Reports on Progress in Physics* **64**, 701 (2001).

[52] Van Dam, J. A., Nazarov, Y. V., Bakkers, E. P., De Franceschi, S. & Kouwenhoven, L. P. Supercurrent reversal in quantum dots. *Nature* **442**, 667–670 (2006).

[53] Saldaña, J. E. *et al.* Supercurrent in a double quantum dot. *Physical review letters* **121**, 257701 (2018).

[54] Grabert, H. & Devoret, M. H. *Single charge tunneling: Coulomb blockade phenomena in nanostructures*, vol. 294 (Springer Science & Business Media, 2013).

[55] Hanson, R., Kouwenhoven, L. P., Petta, J. R., Tarucha, S. & Vandersypen, L. M. Spins in few-electron quantum dots. *Reviews of modern physics* **79**, 1217 (2007).

[56] Ihn, T. *Semiconductor Nanostructures: Quantum states and electronic transport* (Oxford University Press, 2010).

[57] Beenakker, C. Theory of coulomb-blockade oscillations in the conductance of a quantum dot. *Physical Review B* **44**, 1646 (1991).

[58] Van der Wiel, W. G. *et al.* Electron transport through double quantum dots. *Reviews of Modern Physics* **75**, 1 (2002).

[59] De Franceschi, S., Kouwenhoven, L., Schönenberger, C. & Wernsdorfer, W. Hybrid superconductor–quantum dot devices. *Nature Nanotechnology* **5**, 703 (2010).

[60] Grove-Rasmussen, K. *et al.* Yu–shiba–rusinov screening of spins in double quantum dots. *Nature communications* **9**, 1–6 (2018).

[61] Jellinggaard, A., Grove-Rasmussen, K., Madsen, M. H. & Nygård, J. Tuning yu-shiba-rusinov states in a quantum dot. *Physical Review B* **94**, 064520 (2016).

[62] Lee, E. J. *et al.* Spin-resolved Andreev levels and parity crossings in hybrid superconductor–semiconductor nanostructures. *Nature nanotechnology* **9**, 79 (2014).

[63] Yu, L. Bound state in superconductors with paramagnetic impurities. *Acta Phys. Sin* **21**, 75–91 (1965).

[64] Shiba, H. Classical spins in superconductors. *Progress of theoretical Physics* **40**, 435–451 (1968).

[65] Rusinov, A. Superconductivity near a paramagnetic impurity. *Soviet Journal of Experimental and Theoretical Physics Letters* **9**, 85 (1969).

[66] Rusinov, A. Theory of gapless superconductivity in alloys containing paramagnetic impurities. *Sov. Phys. JETP* **29**, 1101–1106 (1969).

[67] Jellinggard, A. *Quantum Dots Coupled to a Superconductor.* Ph.D. thesis, Thesis (2016).

[68] Bauer, J., Oguri, A. & Hewson, A. Spectral properties of locally correlated electrons in a Bardeen–Cooper–Schrieffer superconductor. *Journal of Physics: Condensed Matter* **19**, 486211 (2007).

[69] Meng, T., Florens, S. & Simon, P. Self-consistent description of Andreev bound states in josephson quantum dot devices. *Physical Review B* **79**, 224521 (2009).

[70] Meng, T. Andreev bound states in Josephson quantum dot devices. *Master's thesis, Institut Néel, CNRS Grenoble* (2009).

[71] Delagrange, R. *et al.* 0-π quantum transition in a carbon nanotube Josephson junction: Universal phase dependence and orbital degeneracy. *Physical Review B* **93**, 195437 (2016).

[72] Delagrange, R. *et al.* 0- π quantum transition in a carbon nanotube Josephson junction: Universal phase dependence and orbital degeneracy. *Physica B: Condensed Matter* **536**, 211–222 (2018).

[73] Maurand, R. *et al.* First-order 0- π quantum phase transition in the kondo regime of a superconducting carbon-nanotube quantum dot. *Physical Review X* **2**, 011009 (2012).

[74] Droste, S., Andergassen, S. & Splettstoesser, J. Josephson current through interacting double quantum dots with spin–orbit coupling. *Journal of Physics: Condensed Matter* **24**, 415301 (2012).

[75] Karrasch, C., Andergassen, S. & Meden, V. Supercurrent through a multilevel quantum dot close to singlet-triplet degeneracy. *Physical Review B* **84**, 134512 (2011).

[76] Fu, L. & Kane, C. L. Josephson current and noise at a superconductor/quantum-spin-Hall-insulator/superconductor junction. *Physical Review B* **79**, 161408 (2009).

[77] Badiane, D. M., Glazman, L. I., Houzet, M. & Meyer, J. S. Ac Josephson effect in topological Josephson junctions. *Comptes Rendus Physique* **14**, 840–856 (2013).

[78] San-Jose, P., Prada, E. & Aguado, R. ac Josephson effect in finite-length nanowire junctions with Majorana modes. *Physical review letters* **108**, 257001 (2012).

[79] Pikulin, D. & Nazarov, Y. V. Phenomenology and dynamics of a Majorana Josephson junction. *Physical Review B* **86**, 140504 (2012).

[80] Zhang, P. & Nori, F. Majorana bound states in a disordered quantum dot chain. *New Journal of Physics* **18**, 043033 (2016).

[81] Datta, S. & Das, B. Electronic analog of the electro-optic modulator. *Applied Physics Letters* **56**, 665–667 (1990).

[82] Lutchyn, R. M., Sau, J. D. & Sarma, S. D. Majorana fermions and a topological phase transition in semiconductor-superconductor heterostructures. *Physical review letters* **105**, 077001 (2010).

[83] Oreg, Y., Refael, G. & Von Oppen, F. Helical liquids and Majorana bound states in quantum wires. *Physical review letters* **105**, 177002 (2010).

[84] Lutchyn, R. t. *et al.* Majorana zero modes in superconductor–semiconductor heterostructures. *Nature Reviews Materials* **3**, 52–68 (2018).

[85] Aguado, R. Majorana quasiparticles in condensed matter. *arXiv preprint arXiv:1711.00011* (2017).

[86] Leijnse, M. & Flensberg, K. Introduction to topological superconductivity and Majorana fermions. *Semiconductor Science and Technology* **27**, 124003 (2012).

[87] Mourik, V. *et al.* Signatures of Majorana fermions in hybrid superconductor-semiconductor nanowire devices. *Science* **336**, 1003–1007 (2012).

[88] Albrecht, S. M. *et al.* Exponential protection of zero modes in Majorana islands. *Nature* **531**, 206–209 (2016).

[89] Krogstrup, P. *et al.* Epitaxy of semiconductor–superconductor nanowires. *Nature materials* **14**, 400–406 (2015).

[90] Chang, W. *et al.* Hard gap in epitaxial semiconductor–superconductor nanowires. *Nature nanotechnology* **10**, 232 (2015).

[91] Zhang, H. *et al.* Quantized majorana conductance. *Nature* **556**, 74–79 (2018).

[92] Flöhr, K. *et al.* Manipulating InAs nanowires with submicrometer precision. *Review of scientific instruments* **82**, 113705 (2011).

[93] van Woerkom, D. *Majorana fermions in well aligned InSb-nanowire with superconducting and normal contacts.* Master's thesis, Delft University of Technology, Delft, Netherlands (2012).

[94] van Veen, J. *Superconducting islands and gate-based readout in semiconductor nanowires.* Ph.D. thesis, Delft University of Technology, Delft, Netherlands (2019).

[95] Carrad, D. J. *et al.* Shadow lithography for in-situ growth of generic semiconductor/superconductor devices. *arXiv preprint arXiv:1911.00460* (2019).

[96] Yasin, S., Hasko, D. & Ahmed, H. Comparison of MIBK/IPA and water/IPA as PMMA developers for electron beam nanolithography. *Microelectronic engineering* **61**, 745–753 (2002).

[97] Ocola, L. E., Costales, M. & Gosztola, D. J. Development characteristics of polymethyl methacrylate in alcohol/water mixtures: a lithography and raman spectroscopy study. *Nanotechnology* **27**, 035302 (2015).

[98] Gül, O. *et al.* Hard superconducting gap in InSb nanowires. *Nano letters* **17**, 2690–2696 (2017).

[99] Holloway, G. W., Haapamaki, C. M., Kuyanov, P., LaPierre, R. R. & Baugh, J. Electrical characterization of chemical and dielectric passivation of InAs nanowires. *Semiconductor Science and Technology* **31**, 114004 (2016).

[100] Martinis, J. M., Devoret, M. H. & Clarke, J. Experimental tests for the quantum behavior of a macroscopic degree of freedom: The phase difference across a Josephson junction. *Physical Review B* **35**, 4682 (1987).

[101] Mueller, F. *et al.* Printed circuit board metal powder filters for low electron temperatures. *Review of scientific instruments* **84**, 044706 (2013).

[102] Van Woerkom, D. J., Geresdi, A. & Kouwenhoven, L. P. One minute parity lifetime of a NbTiN Cooper-pair transistor. *Nature Physics* **11**, 547–550 (2015).

[103] Josephson, B. D. Possible new effects in superconductive tunnelling. *Phys. Lett.* **1**, 251–253 (1962).

[104] Hofheinz, M. *et al.* Bright side of the Coulomb blockade. *Phys. Rev. Lett.* **106**, 217005 (2011).

[105] Giaever, I. Detection of the ac Josephson effect. *Phys. Rev. Lett.* **14**, 904 (1965).

[106] Grimes, C., Richards, P. & Shapiro, S. Far infrared response of point-contact Josephson junctions. *Phys. Rev. Lett.* **17**, 431 (1966).

[107] Cleuziou, J.-P. *et al.* Gate-tuned high frequency response of carbon nanotube Josephson junctions. *Phys. Rev. Lett.* **99**, 117001 (2007).

[108] Doh, Y.-J. *et al.* Tunable supercurrent through semiconductor nanowires. *Science* **309**, 272–275 (2005).

[109] van Woerkom, D. J. *et al.* Josephson radiation and shot noise of a semiconductor nanowire junction. *Phys. Rev. B* **96**, 094508 (2017).

[110] Chen, J. T., Wenger, L. E., McEwan, C. J. & Logothetis, E. M. Observation of the reverse ac Josephson effect in Y-Ba-Cu-O at 240 K. *Phys. Rev. Lett.* **58**, 1972–1975 (1987).

[111] Lutchyn, R. M., Sau, J. D. & Sarma, S. D. Majorana fermions and a topological phase transition in semiconductor-superconductor heterostructures. *Phys. Rev. Lett.* **105**, 077001 (2010).

[112] Oreg, Y., Refael, G. & von Oppen, F. Helical liquids and Majorana bound states in quantum wires. *Phys. Rev. Lett.* **105**, 177002 (2010).

[113] Mourik, V. *et al.* Signatures of Majorana fermions in hybrid superconductor-semiconductor nanowire devices. *Science* **336**, 1003–1007 (2012).

[114] Das, A. *et al.* Zero-bias peaks and splitting in an Al-InAs nanowire topological superconductor as a signature of Majorana fermions. *Nature Physics* **8**, 887–895 (2012).

[115] Deng, M. T. *et al.* Anomalous zero-bias conductance peak in a Nb–InSb nanowire–Nb hybrid device. *Nano Letters* **12**, 6414–6419 (2012).

[116] Churchill, H. O. H. *et al.* Superconductor-nanowire devices from tunneling to the multichannel regime: Zero-bias oscillations and magnetoconductance crossover. *Phys. Rev. B* **87**, 241401 (2013).

[117] Deng, M. *et al.* Majorana bound state in a coupled quantum-dot hybrid-nanowire system. *Science* **354**, 1557–1562 (2016).

[118] Zhang, H. *et al.* Quantized Majorana conductance. *Nature* **556**, 74 (2018).

[119] Kwon, H.-J., Yakovenko, V. M. & Sengupta, K. Fractional AC Josephson effect in unconventional superconductors. *Low Temperature Physics* **30**, 613–619 (2004).

[120] Fu, L. & Kane, C. L. Josephson current and noise at a superconductor/quantum-spin-Hall-insulator/superconductor junction. *Phys. Rev. B* **79**, 161408 (2009).

[121] San-Jose, P., Prada, E. & Aguado, R. ac Josephson effect in finite-length nanowire junctions with Majorana modes. *Phys. Rev. Lett.* **108**, 257001 (2012).

[122] Pikulin, D. I. & Nazarov, Y. V. Phenomenology and dynamics of a Majorana Josephson junction. *Phys. Rev. B* **86**, 140504 (2012).

[123] Houzet, M., Meyer, J. S., Badiane, D. M. & Glazman, L. I. Dynamics of Majorana states in a topological Josephson junction. *Phys. Rev. Lett.* **111**, 046401 (2013).

[124] Deblock, R., Onac, E., Gurevich, L. & Kouwenhoven, L. P. Detection of quantum noise from an electrically driven two-level system. *Science* **301**, 203–206 (2003).

[125] Krogstrup, P. *et al.* Epitaxy of semiconductor-superconductor nanowires. *Nature Materials* **14**, 400–406 (2015).

[126] Higginbotham, A. *et al.* Parity lifetime of bound states in a proximitized semiconductor nanowire. *Nature Physics* **11**, 1017–1021 (2015).

[127] Albrecht, S. *et al.* Exponential protection of zero modes in Majorana islands. *Nature* **531**, 206–209 (2016).

[128] Rokhinson, L. P., Liu, X. & Furdyna, J. K. The fractional a.c. Josephson effect in a semiconductor-superconductor nanowire as a signature of Majorana particles. *Nature Physics* **8**, 795–799 (2012).

[129] Deacon, R. S. *et al.* Josephson radiation from gapless Andreev bound states in HgTe-based topological junctions. *Phys. Rev. X* **7**, 021011 (2017).

[130] Tucker, J. R. & Feldman, M. J. Quantum detection at millimeter wavelengths. *Rev. Mod. Phys.* **57**, 1055–1113 (1985).

[131] Bretheau, L., Girit, Ç. Ö., Pothier, H., Esteve, D. & Urbina, C. Exciting Andreev pairs in a superconducting atomic contact. *Nature* **499**, 312–315 (2013).

[132] Cawthorne, A. B., Whan, C. B. & Lobb, C. J. Complex dynamics of resistively and inductively shunted Josephson junctions. *Journal of Applied Physics* **84**, 1126–1132 (1998).

[133] Scheer, E., Joyez, P., Esteve, D., Urbina, C. & Devoret, M. H. Conduction channel transmissions of atomic-size aluminum contacts. *Phys. Rev. Lett.* **78**, 3535–3538 (1997).

[134] Dolan, G. J. Offset masks for lift-off photoprocessing. *Applied Physics Letters* **31**, 337–339 (1977).

[135] Ivanchenko, Y. M. & Zil'berman, L. A. The Josephson effect in small tunnel contacts. *Sov. Phys. JETP* **28**, 1272–1276 (1969).

[136] Efron, B. & Tibshirani, R. Bootstrap methods for standard errors, confidence intervals, and other measures of statistical accuracy. *Statistical Science* **1**, 54–75 (1986).

[137] van Woerkom, D. J. *et al.* Microwave spectroscopy of spinful Andreev bound states in ballistic semiconductor Josephson junctions. *Nature Physics* **13**, 876–881 (2017).

[138] Nijholt, B. & Akhmerov, A. R. Orbital effect of magnetic field on the Majorana phase diagram. *Phys. Rev. B* **93**, 235434 (2016).

[139] Potter, A. C. & Lee, P. A. Multichannel generalization of Kitaev's Majorana end states and a practical route to realize them in thin films. *Phys. Rev. Lett.* **105**, 227003 (2010).

[140] Sticlet, D., Nijholt, B. & Akhmerov, A. Robustness of Majorana bound states in the short-junction limit. *Phys. Rev. B* **95**, 115421 (2017).

[141] Spanton, E. M. *et al.* Current-phase relations of few-mode InAs nanowire Josephson junctions. *Nature Physics* **13**, 1177–1181 (2017).

[142] Goffman, M. F. *et al.* Conduction channels of an InAs-Al nanowire Josephson weak link. *New Journal of Physics* **19**, 092002 (2017).

[143] Lindner, N. H., Berg, E., Refael, G. & Stern, A. Fractionalizing Majorana fermions: Non-abelian statistics on the edges of abelian quantum Hall states. *Phys. Rev. X* **2**, 041002 (2012).

[144] Clarke, D. J., Alicea, J. & Shtengel, K. Exotic non-Abelian anyons from conventional fractional quantum Hall states. *Nature Communications* **4**, 1348 (2013).

[145] Zhang, F. & Kane, C. L. Time-reversal-invariant Z_4 fractional Josephson effect. *Phys. Rev. Lett.* **113**, 036401 (2014).

[146] Laflamme, C., Budich, J., Zoller, P. & Dalmonte, M. Non-equilibrium 8π Josephson effect in atomic Kitaev wires. *Nature Communications* **7**, 12280 (2016).

[147] Pientka, F., Kells, G., Romito, A., Brouwer, P. W. & von Oppen, F. Enhanced zero-bias Majorana peak in the differential tunneling conductance of disordered multisubband quantum-wire/superconductor junctions. *Phys. Rev. Lett.* **109**, 227006 (2012).

[148] Prada, E., San-Jose, P. & Aguado, R. Transport spectroscopy of *ns* nanowire junctions with Majorana fermions. *Phys. Rev. B* **86**, 180503 (2012).

[149] Stanescu, T. D., Tewari, S., Sau, J. D. & Das Sarma, S. To close or not to close: The fate of the superconducting gap across the topological quantum phase transition in Majorana-carrying semiconductor nanowires. *Phys. Rev. Lett.* **109**, 266402 (2012).

[150] Rainis, D., Trifunovic, L., Klinovaja, J. & Loss, D. Towards a realistic transport modeling in a superconducting nanowire with Majorana fermions. *Phys. Rev. B* **87**, 024515 (2013).

[151] Pikulin, D. I. & Nazarov, Y. V. Phenomenology and dynamics of a Majorana Josephson junction. *Phys. Rev. B* **86**, 140504 (2012).

[152] Landau, L. D. Zur Theorie der Energieubertragung. II. *Phys. Z. Sowjetunion* **2**, 1–13 (1932).

[153] Zener, C. Non-adiabatic crossing of energy levels. In *Proceedings of the Royal Society of London A: Mathematical, Physical and Engineering Sciences*, vol. 137, 696–702 (The Royal Society, 1932).

[154] Demkov, Y. N. & Osherov, V. Stationary and nonstationary problems in quantum mechanics that can be solved by means of contour integration. *Sov. Phys. JETP* **26**, 1 (1968).

[155] Kautz, R. L. & Martinis, J. M. Noise-affected i-v curves in small hysteretic Josephson junctions. *Phys. Rev. B* **42**, 9903 (1990).

[156] Gardiner, C. W. *Handbook of stochastic methods for physics, chemistry and the natural sciences.* Springer Series in Synergetics (Springer, 2004), 3 edn.

[157] Welch, P. The use of fast Fourier transform for the estimation of power spectra: a method based on time averaging over short, modified periodograms. *IEEE Transactions on audio and electroacoustics* **15**, 70–73 (1967).

[158] Spivak, B. & Kivelson, S. Negative local superfluid densities: The difference between dirty superconductors and dirty Bose liquids. *Physical Review B* **43**, 3740 (1991).

[159] Pillet, J.-D., Benzoni, V., Griesmar, J., Smirr, J.-L. & Girit, C. O. Nonlocal Josephson effect in Andreev molecules. *Nano letters* **19**, 7138–7143 (2019).

[160] Kornich, V., Barakov, H. S. & Nazarov, Y. V. Fine energy splitting of overlapping andreev bound states in multiterminal superconducting nanostructures. *Physical Review Research* **1**, 033004 (2019).

[161] Kornich, V., Barakov, H. S. & Nazarov, Y. V. Overlapping Andreev states in semiconducting nanowires: Competition of one-dimensional and three-dimensional propagation. *Physical Review B* **101**, 195430 (2020).

[162] Deng, M. *et al.* Majorana bound state in a coupled quantum-dot hybrid-nanowire system. *Science* **354**, 1557–1562 (2016).

[163] Gül, Ö. *et al.* Ballistic Majorana nanowire devices. *Nature nanotechnology* **13**, 192–197 (2018).

[164] Hanson, R., Kouwenhoven, L. P., Petta, J. R., Tarucha, S. & Vandersypen, L. M. K. Spins in few-electron quantum dots. *Rev. Mod. Phys.* **79**, 1217–1265 (2007).

[165] Loss, D. & DiVincenzo, D. P. Quantum computation with quantum dots. *Physical Review A* **57**, 120 (1998).

[166] Nowack, K. C., Koppens, F. H. L., Nazarov, Y. V. & Vandersypen, L. M. K. Coherent Control of a Single Electron Spin with Electric Fields. *Science* **318**, 1430–1433 (2007).

[167] Nadj-Perge, S., Frolov, S. M., Bakkers, E. P. A. M. & Kouwenhoven, L. P. Spin-orbit qubit in a semiconductor nanowire. *Nature* **468**, 1084–1087 (2010).

[168] Field, M. *et al.* Measurements of Coulomb blockade with a noninvasive voltage probe. *Phys. Rev. Lett.* **70**, 1311–1314 (1993).

[169] Frey, T. *et al.* Dipole Coupling of a Double Quantum Dot to a Microwave Resonator. *Phys. Rev. Lett.* **108**, 046807 (2012).

[170] Petersson, K. D. *et al.* Circuit quantum electrodynamics with a spin qubit. *Nature* **490**, 380–383 (2012).

[171] Golubov, A. A., Kupriyanov, M. Y. & Il'ichev, E. The current-phase relation in Josephson junctions. *Rev. Mod. Phys.* **76**, 411–469 (2004).

[172] Ryazanov, V. V. *et al.* Coupling of Two Superconductors through a Ferromagnet: Evidence for a π Junction. *Phys. Rev. Lett.* **86**, 2427–2430 (2001).

[173] Kontos, T. *et al.* Josephson Junction through a Thin Ferromagnetic Layer: Negative Coupling. *Phys. Rev. Lett.* **89**, 137007 (2002).

[174] Baselmans, J. J. A., Morpurgo, A. F., van Wees, B. J. & Klapwijk, T. M. Reversing the direction of the supercurrent in a controllable Josephson junction. *Nature* **397**, 43–45 (1999).

[175] van Dam, J. A., Nazarov, Y. V., Bakkers, E. P. A. M., De Franceschi, S. & Kouwenhoven, L. P. Supercurrent reversal in quantum dots. *Nature* **442**, 667–670 (2006).

[176] Delagrange, R. *et al.* 0-π quantum transition in a carbon nanotube Josephson junction: Universal phase dependence and orbital degeneracy. *Phys. Rev. B* **93**, 195437 (2016).

[177] Choi, M.-S., Bruder, C. & Loss, D. Spin-dependent Josephson current through double quantum dots and measurement of entangled electron states. *Phys. Rev. B* **62**, 13569–13572 (2000).

[178] Zhu, Y., Sun, Q. & Lin, T. Probing spin states of coupled quantum dots by a dc Josephson current. *Phys. Rev. B* **66**, 085306 (2002).

[179] Martín-Rodero, A. & Yeyati, A. L. Josephson and Andreev transport through quantum dots. *Advances in Physics* **60**, 899–958 (2011).

[180] Brunetti, A., Zazunov, A., Kundu, A. & Egger, R. Anomalous Josephson current, incipient time-reversal symmetry breaking, and Majorana bound states in interacting multilevel dots. *Physical Review B* **88**, 144515 (2013).

[181] Pokorný, V., Žonda, M., Loukeris, G. & Novotný, T. *Second Order Perturbation Theory for a Superconducting Double Quantum Dot.*

[182] Szombati, D. *et al.* Josephson ϕ_0-junction in nanowire quantum dots. *Nature Physics* **12**, 568 (2016).

[183] Estrada Saldaña, J. C. *et al.* Supercurrent in a double quantum dot. *Phys. Rev. Lett.* **121**, 257701 (2018).

[184] van Woerkom, D. J. *et al.* Microwave spectroscopy of spinful Andreev bound states in ballistic semiconductor Josephson junctions. *Nature Physics* **13**, 876–881 (2017).

[185] Della Rocca, M. L. *et al.* Measurement of the current-phase relation of superconducting atomic contacts. *Phys. Rev. Lett.* **99**, 127005 (2007).

[186] Ivanchenko, Y. & Zil'Berman, L. The Josephson effect in small tunnel contacts. *Soviet Phys. JETP* **28** (1969).

[187] De Franceschi, S., Kouwenhoven, L., Schonenberger, C. & Wernsdorfer, W. Hybrid superconductor-quantum dot devices. *Nature Nanotechnology* **5**, 703–711 (2010).

[188] Vecino, E., Martín-Rodero, A. & Yeyati, A. L. Josephson current through a correlated quantum level: Andreev states and π junction behavior. *Phys. Rev. B* **68**, 035105 (2003).

[189] Fasth, C., Fuhrer, A., Samuelson, L., Golovach, V. N. & Loss, D. Direct measurement of the spin-orbit interaction in a two-electron InAs nanowire quantum dot. *Physical review letters* **98**, 266801 (2007).

[190] Csonka, S. *et al.* Giant fluctuations and gate control of the g-factor in InAs nanowire quantum dots. *Nano letters* **8**, 3932–3935 (2008).

[191] Schroer, M. D., Petersson, K. D., Jung, M. & Petta, J. R. Field Tuning the g Factor in InAs Nanowire Double Quantum Dots. *Phys. Rev. Lett.* **107**, 176811 (2011).

[192] Tosi, L. *et al.* Spin-Orbit Splitting of Andreev States Revealed by Microwave Spectroscopy. *Phys. Rev. X* **9**, 011010 (2019).

[193] Danon, J. Spin-flip phonon-mediated charge relaxation in double quantum dots. *Phys. Rev. B* **88**, 075306 (2013).

[194] Nadj-Perge, S. *et al.* Spectroscopy of spin-orbit quantum bits in indium antimonide nanowires. *Phys. Rev. Lett.* **108**, 166801 (2012).

[195] Scherübl, Z., Fülöp, G. m. H., Madsen, M. H., Nygård, J. & Csonka, S. Electrical tuning of rashba spin-orbit interaction in multigated InAs nanowires. *Phys. Rev. B* **94**, 035444 (2016).

[196] Zuo, K. *et al.* Supercurrent interference in few-mode nanowire Josephson junctions. *Phys. Rev. Lett.* **119**, 187704 (2017).

[197] Hays, M. *et al.* Continuous monitoring of a trapped superconducting spin. *Nature Physics* 1–5 (2020).

[198] Bouman, D. *et al.* Triplet-blockaded Josephson supercurrent in double quantum dots, raw data and software (2020). URL `https://doi.org/10.5281/zenodo.3978236`.

[199] Estrada Saldaña, J. C. *et al.* Supercurrent in a double quantum dot. *Physical Review Letters* (2018).

[200] Danon, J. & Nazarov, Y. V. Pauli spin blockade in the presence of strong spin-orbit coupling. *Phys. Rev. B* **80**, 041301 (2009).

[201] Riley, K. F. & Hobson, M. P. *Essential Mathematical Methods for the Physical Sciences*, 66 (Cambridge University Press, 2011).

[202] Spanton, E. M. *et al.* Current–phase relations of few-mode InAs nanowire Josephson junctions. *Nature Physics* **13**, 1177–1181 (2017).

[203] Vecino, E., Martín-Rodero, A. & Yeyati, A. L. Josephson current through a correlated quantum level: Andreev states and π junction behavior. *Physical Review B* **68**, 035105 (2003).

[204] Karrasch, C., Oguri, A. & Meden, V. Josephson current through a single anderson impurity coupled to BCS leads. *Physical Review B* **77**, 024517 (2008).

[205] Siano, F. & Egger, R. Josephson current through a nanoscale magnetic quantum dot. *Physical review letters* **93**, 047002 (2004).

[206] Delagrange, R. *et al.* Manipulating the magnetic state of a carbon nanotube Josephson junction using the superconducting phase. *Physical Review B* **91**, 241401 (2015).

[207] Yokoyama, T., Eto, M. & Nazarov, Y. V. Anomalous Josephson effect induced by spin-orbit interaction and zeeman effect in semiconductor nanowires. *Physical Review B* **89**, 195407 (2014).

[208] Pita-Vidal, M. *et al.* A gate-tunable, field-compatible fluxonium. *arXiv preprint arXiv:1910.07978* (2019).

[209] Yeyati, A. L., Martín-Rodero, A. & Vecino, E. Nonequilibrium dynamics of andreev states in the kondo regime. *Physical review letters* **91**, 266802 (2003).

[210] Vandersypen, L. *et al.* Interfacing spin qubits in quantum dots and donors—hot, dense, and coherent. *npj Quantum Information* **3**, 1–10 (2017).

[211] Petta, J. R. *et al.* Coherent manipulation of coupled electron spins in semiconductor quantum dots. *Science* **309**, 2180–2184 (2005).

[212] Veldhorst, M. *et al.* An addressable quantum dot qubit with fault-tolerant control-fidelity. *Nature nanotechnology* **9**, 981 (2014).

[213] Yoneda, J. *et al.* A quantum-dot spin qubit with coherence limited by charge noise and fidelity higher than 99.9%. *Nature nanotechnology* **13**, 102–106 (2018).

[214] Barthel, C. *et al.* Fast sensing of double-dot charge arrangement and spin state with a radio-frequency sensor quantum dot. *Physical Review B* **81**, 161308 (2010).

[215] Colless, J. *et al.* Dispersive readout of a few-electron double quantum dot with fast rf gate sensors. *Physical review letters* **110**, 046805 (2013).

[216] Zheng, G. *et al.* Rapid gate-based spin read-out in silicon using an on-chip resonator. *Nature nanotechnology* **14**, 742–746 (2019).

[217] Nadj-Perge, S., Frolov, S., Bakkers, E. & Kouwenhoven, L. P. Spin–orbit qubit in a semiconductor nanowire. *Nature* **468**, 1084–1087 (2010).

[218] Kjærgaard, M. *et al.* Quantized conductance doubling and hard gap in a two-dimensional semiconductor–superconductor heterostructure. *Nature communications* **7**, 1–6 (2016).

[219] Kjærgaard, M. *et al.* Transparent semiconductor-superconductor interface and induced gap in an epitaxial heterostructure Josephson junction. *Physical Review Applied* **7**, 034029 (2017).

[220] Malinowski, F. K. *et al.* Notch filtering the nuclear environment of a spin qubit. *Nature nanotechnology* **12**, 16 (2017).

[221] Itoh, K. *et al.* High purity isotopically enriched 70 Ge and 74 Ge single crystals: Isotope separation, growth, and properties. *Journal of materials research* **8**, 1341–1347 (1993).

[222] Itoh, K. M. & Watanabe, H. Isotope engineering of silicon and diamond for quantum computing and sensing applications. *MRS communications* **4**, 143–157 (2014).

[223] Sigillito, A. *et al.* Electron spin coherence of shallow donors in natural and isotopically enriched germanium. *Physical review letters* **115**, 247601 (2015).

[224] Veldhorst, M. *et al.* A two-qubit logic gate in silicon. *Nature* **526**, 410–414 (2015).

[225] Hendrickx, N. *et al.* Gate-controlled quantum dots and superconductivity in planar germanium. *Nature communications* **9**, 1–7 (2018).

[226] Hendrickx, N., Franke, D., Sammak, A., Scappucci, G. & Veldhorst, M. Fast two-qubit logic with holes in germanium. *Nature* 1–5 (2020).

[227] Hays, M. *et al.* Direct Microwave Measurement of Andreev-Bound-State Dynamics in a Semiconductor-Nanowire Josephson Junction. *Phys. Rev. Lett.* **121**, 047001 (2018).

[228] Chtchelkatchev, N. M. & Nazarov, Y. V. Andreev quantum dots for spin manipulation. *Physical review letters* **90**, 226806 (2003).

[229] Padurariu, C. & Nazarov, Y. V. Theoretical proposal for superconducting spin qubits. *Physical Review B* **81**, 144519 (2010).

[230] Park, S. & Yeyati, A. L. Andreev spin qubits in multichannel rashba nanowires. *Physical Review B* **96**, 125416 (2017).

[231] Janvier, C. *et al.* Coherent manipulation of Andreev states in superconducting atomic contacts. *Science* **349**, 1199–1202 (2015).

[232] Pillet, J.-D. *Tunneling spectroscopy of the Andreev Bound States in a Carbone Nanotube*. Ph.D. thesis (2011).

[233] Tosi, L. *et al.* Spin-orbit splitting of Andreev states revealed by microwave spectroscopy. *Physical Review X* **9**, 011010 (2019).

[234] Bretheau, L., Girit, Ç., Pothier, H., Esteve, D. & Urbina, C. Exciting Andreev pairs in a superconducting atomic contact. *Nature* **499**, 312–315 (2013).

[235] Proutski, A. *et al.* Broadband microwave spectroscopy of semiconductor nanowire-based Cooper-pair transistors. *Physical Review B* **99**, 220504 (2019).

[236] Giesmar, J. *A Mesoscopic Spectrometer Based on the Josephson Effect.* Ph.D. thesis, Collège de France, Paris, France (2018).

[237] Moore, C., Zeng, C., Stanescu, T. D. & Tewari, S. Quantized zero-bias conductance plateau in semiconductor-superconductor heterostructures without topological Majorana zero modes. *Phys. Rev. B* **98**, 155314 (2018).

[238] Liu, C.-X., Sau, J. D., Stanescu, T. D. & Das Sarma, S. Andreev bound states versus Majorana bound states in quantum dot-nanowire-superconductor hybrid structures: Trivial versus topological zero-bias conductance peaks. *Phys. Rev. B* **96**, 075161 (2017).

[239] Moore, C., Stanescu, T. D. & Tewari, S. Two-terminal charge tunneling: Disentangling Majorana zero modes from partially separated Andreev bound states in semiconductor-superconductor heterostructures. *Phys. Rev. B* **97**, 165302 (2018).

[240] Vuik, A., Nijholt, B., Akhmerov, A. R. & Wimmer, M. Reproducing topological properties with quasi-Majorana states. *arXiv preprint arXiv:1806.02801* (2018).

[241] Leijnse, M. & Flensberg, K. Parity qubits and poor man's Majorana bound states in double quantum dots. *Physical Review B* **86**, 134528 (2012).

[242] Lee, J. S. *et al.* Transport studies of epi-al/InAs two-dimensional electron gas systems for required building-blocks in topological superconductor networks. *Nano letters* **19**, 3083–3090 (2019).

[243] Kulesh, I. *et al.* Quantum dots in an InSb two-dimensional electron gas. *Phys. Rev. Applied* **13**, 041003 (2020).

[244] Ke, C. T. *et al.* Ballistic superconductivity and tunable π–junctions in InSb quantum wells. *Nature communications* **10**, 1–6 (2019).

ACKNOWLEDGEMENTS

The work I presented in this thesis was not done in isolation, I have many people to thank for their help and support.

Leo and Attila, thank you for taking me on as a PhD student. Leo, I admire you for the way you lead a large group of students, combining it with your Microsoft duties and always keeping a relaxed attitude. Good luck with your future work. Attila, despite leading your group and being a busy person in general, you were not averse to getting your own hands dirty by helping out in the lab or by writing code. Your commitment to doing interesting science and throwing in a movie quote here and there, made my time working with you unforgettable. We had some frustrating moments with our 2DEG adventure, but you never lost your cool and always had a solution. I wish you all the best with your new lab and life in Sweden.

My PhD started out with the 4π project, where I learned a lot from my former mentor, David. Infamous throughout QuTech and always in for some fun. You were a great teacher with an almost endless supply of energy. We had some fun moments together and you became a valued colleague. Dominique, your help was essential in bringing our project to a good end and your advice helped me move forward with my other projects. Also outside of work we had some good times playing Ticket to Ride. I wish you good luck and happiness with your lab and family in Florida. Alex, you were not afraid to speak your mind at work, which I appreciate, and a great person to talk to in general.

Matt, thank you for always being there for a chat, for helping out with cryogenics or coding. You have been a great collegue and have became a good friend, see you around. Niko and Christine, it has been great knowing you. Your excellent nanofabrication knowledge has helped me out more then once.

While writing this final chapter of my thesis I had the pleasure to work with the cQED team. Lukas, we only worked together for a couple of months, but it quickly felt as if we have been working together for years – working with you was a great pleasure. Viel Erfolg with the Andreev Molecule project and your career. Jaap, I enjoyed our discussions on physics and stocks, good luck with measuring your ABS. Marta, great job making it onto the Wall of Fame, buddy. Arno, you have a great sense of humor. Lukas, Tess, Ruben, Arjen, Angela and Bernard, you complete this group with a great atmosphere.

Damaz, I enjoyed our discussions about Wednesdays and our efforts to improve our presenting skills. You are one of the most naturally enthusiastic presenters I know. Good luck with the final bits of your PhD. James, it was great fun having you as a colleague. Willemijn, thanks for the nice conversations. Jasper, Jouri, Michiel, Fokko, Greg, Jie, Nick, Jiying, Vukan, Lin, Tom, David, Guan, Filip, Di, Francesco, Alberto, Srijit, Ting, Qing, Christian, Prasanna, Ivan and Nikos, thank you for making Topo/QuRe the great environment that it is. I have great memories with all of you, during one of the Topo uitjes, in the cleanroom, the lab or at a conference.

Olaf, you always shared your expertise and opinion without filter, I appreciate that. We had some nice small talk and I am sure that one day you will get your hole-in-one. Jason, thanks for always being ready to help out with almost anything and I hope you will continue to share you motorcycle adventures with everyone else. Nico thanks for all the things you made, I enjoyed talking with you about cycling, machining and management philosophies. Remco and Mark, thank you for the nice conversations we have had, for your technical assistance and for staying friendly even when I kept on bugging you. Roy, Siebe and Jelle thank you for always helping out, even on short notice. Raymond, Raymond and Marijn, thank you for your electronics expertise and for sharing new ideas. Jenny, Simone, Chantal and Marja, thank you for your support. Especially Jenny, for always being ready to help me out – sometimes even on your day off.

Ruben, you have been a great student and you are partly responsible for some for the results in this thesis. You can be proud of your work and it is great to be your colleague again. Hans, you impressed me with your work and the level of understanding you reached in relatively short time.

To all the other Microsoft and QuTech people I have interacted with, including but not limited to Alessandro, Nandini, Adriaan, Sarwan, Nima and Jelmer, Sergei, Moritz, Pavel, Amrita, John, Kevin, Sebastiaan, Marina, Sarwan, Stefan, Thijs, Anne-Marije, thank you for a great time. Sophie, Udit, Kenneth and Leon, I enjoyed organizing the best uitje with you.

As with most experimental PhD's in QuTech, I spend a lot of time in the cleanroom. Thank you to all the Kavli personnel for keeping the cleanroom a nice place to work. In particular I would like to thank Arnold, Anja, Charles, Marco, Marc, Eugene, Pauline, Hozanna, Bas, Lodi and Ewan. I have also had pleasant interactions with a few people at TNO, Delphine, Nodar, Stefan, Ruud and Saurabh. Saurabh, you always made our encounters joyful. I hope we keep bumping into each other in the future.

I have had a few collaborations with research groups from around the world. I have enjoyed them, learned a great deal from them and they have been an essential part of my PhD. The first was with Max, Valla, Gijs and Kyle from Yale. We have done a few projects together and they have been very enjoyable and educational to me. Good luck with continuing these projects with Attila. For the double quantum dot Josephson junctions I have had the pleasure to work with Péter, Dávid and András. András, I admire your modesty and thoroughness, our collaboration has been essential to the project and gave us direction. When Gorm and Jens joined from Copenhagen we made even more progress and I am proud of our end result.

To my committee members, Yuli, Silvano, Lieven, Menno, Jelena, thank you for taking the time to assess my thesis and being at my defense, both virtual and in person. Thank you Damaz, James and Matt for proofreading my thesis and providing valuable input.

Kenneth, ik kijk nog altijd met veel plezier terug naar de lange dagen die we samen in de TUDelft bibliotheek hebben doorgebracht, we zijn samen een heel eind gekomen. Je bent een goede vriend geworden op wie ik kan vertrouwen. Bedankt dat je ook mijn paranimf wil zijn. Chantal, Ellen, Joost en Peter samen met jullie erbij zijn de Hippe Schakelaars compleet. Ik heb een leuke tijd met jullie gehad en ik denk niet dat ik zou zijn waar ik nu ben zonder onze gezamenlijke studie momenten. Coen en Maria, dankzij jullie heb ik de keuze gemaakt om verder te studeren. Iets waar ik jullie heel dankbaar voor ben.

Jan Willem, we kennen elkaar al erg lang en hebben veel met elkaar opgetrokken. Nog steeds ben ik blij dat we goede vrienden zijn en bedankt dat je mijn paranimf wil zijn. Samen met Jorrit en Jack hebben we met z’n vieren veel lol gehad: onvergetelijke tripjes, wielerrondes en Corona spelavonden. Ik kijk uit naar de nieuwe herinneringen die we met z’n allen gaan maken, samen met Mariëlle, Hannah en Dorian.

Papa, mama, Aron en Maico, bedankt voor jullie onvoorwaardelijke steun en voor het tonen van interesse in mijn onderzoek. Dit is erg waardevol voor mij. Rob, Engelien, Stijn, Narda en Luca, bedankt voor jullie steun en voor alle gezelligheid.

Tenslotte Anke, mijn grote liefde. Je bent er de afgelopen jaren altijd voor me geweest, ook al was het niet altijd makkelijk voor je – zonder jou was dit nooit gelukt. We hebben de afgelopen jaren veel mee gemaakt en ik ben erg gelukkig samen met jou. Op naar ons nieuwe avontuur.

CURRICULUM VITÆ

Daniël BOUMAN

13-11-1989	Born in Amstelveen, The Netherlands.
2003–2008	Secondary school Markland College, Oudenbosch
2008–2013	Bachelor of Engineering in Applied Physics The Hague University
2013–2016	Master of Science in Applied Physics Delft University of Technology *Thesis supervisor:* Prof. dr. ir. L. P. Kouwenhoven
2016–2021	PhD Research Delft University of Technology *Promotor:* Prof. dr. ir. L. P. Kouwenhoven *Copromotor:* Dr. A. Geresdi

LIST OF PUBLICATIONS

7. *Triplet-blockaded supercurrent in double quantum dots*
   D. Bouman, R. J. J. van Gulik, D. Pataki, P. Boross, A Pályi, G. Steffensen, J. Paaske, J. Nygård, P. Krogstrup, A. Geresdi
   arXiv:2008.04375.

6. *Continuous monitoring of a trapped, superconducting spin*
   M. Hays, V. Fatemi, K. Serniak, **D. Bouman**, S. Diamond, G. de Lange, P. Krogstrup, J. Nygård, A. Geresdi, M. H. Devoret
   Nature Physics **16**, 1103–1107 (2020).

5. *Observation of the* 4π*-periodic Josephson effect in indium arsenide nanowires*
   D. Laroche[†], **D. Bouman**[†], D.J. van Woerkom, A. Proutski, C. Murthy, D.I. Pikulin, C. Nayak, R. J. J. van Gulik, J. Nygård, P. Krogstrup, L. P. Kouwenhoven, A. Geresdi
   Nature Communications **10**, 245 (2019)

4. *Parity transitions in the superconducting ground state of hybrid InSb–Al Coulomb islands*
   J. Shen, S. Heedt, F. Borsoi, B. Van Heck, S. Gazibegovic, R. L. M. Op het Veld, D. Car, J. A. Logan, H. Pendharkar, S. J. J. Ramakers, G. Wang, D. Xu, **D. Bouman**, A. Geresdi, C. J. Palmstrøm, E. P. A. M. Bakkers, L. P. Kouwenhoven
   Nature Communications **9**, 4801 (2018)

3. *Direct microwave measurement of Andreev-bound-state dynamics in a semiconductor-nanowire josephson junction*
   M. Hays, G. de Lange, K. Serniak, D. J. van Woerkom, **D. Bouman**, P. Krogstrup, J. Nygård, A/ Geresdi, M/ H. Devoret
   Physical Review Letters **121**, 047001 (2018)

2. *Epitaxy of advanced nanowire quantum devices*
   S. Gazibegovic, D. Car, H. Zhang, S. C. Balk, J. A. Logan, M. W. A. de Moor, M. C. Cassidy, R. Schmits, D. Xu, G. Wang, P. Krogstrup, R. L. M. op het Veld, K. Zuo, Y. Vos, J. Shen, **D. Bouman**, B. Shojaei, D. Pennachio, J. S. Lee, P. J. van Veldhoven, S. Koelling, M. A. Verheijen, L. P. Kouwenhoven, C. J. Palmstrøm, E. P. A. M. Bakkers
   Nature **548**, 434–438 (2017)

1. *Microwave spectroscopy of spinful Andreev bound states in ballistic semiconductor Josephson junctionss*
   D. J. van Woerkom, A. Proutski, B. van Heck, **D. Bouman**, J. I. Väyrynen, L. I. Glazman, P. Krogstrup, J. Nygård, L. P. Kouwenhoven, A. Geresdi
   Nature Physics **13**, 876–881 (2017)

[†] Equal contribution.